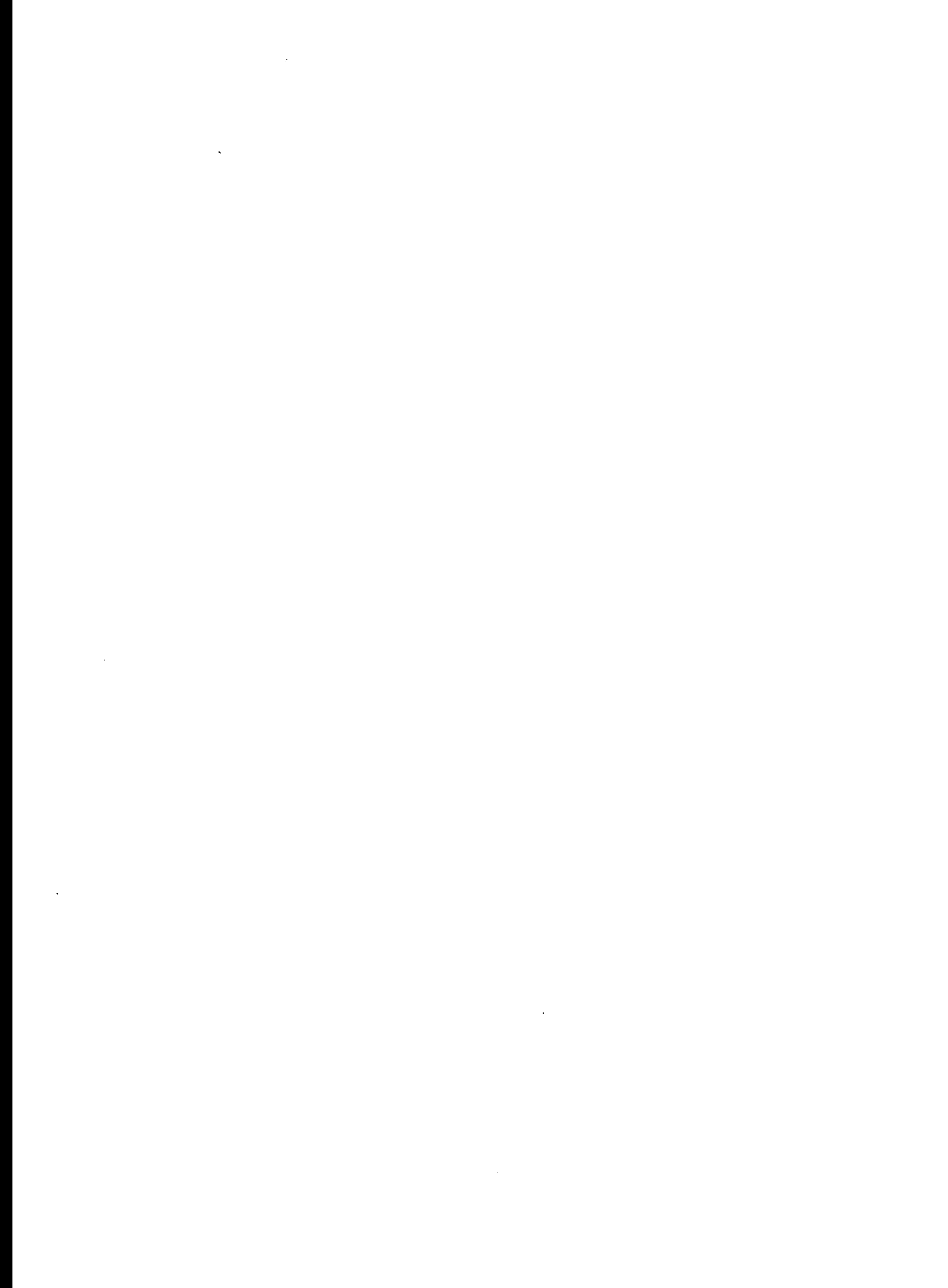


MISSILE CONFIGURATION DESIGN



MISSILE CONFIGURATION DESIGN

S. S. CHIN

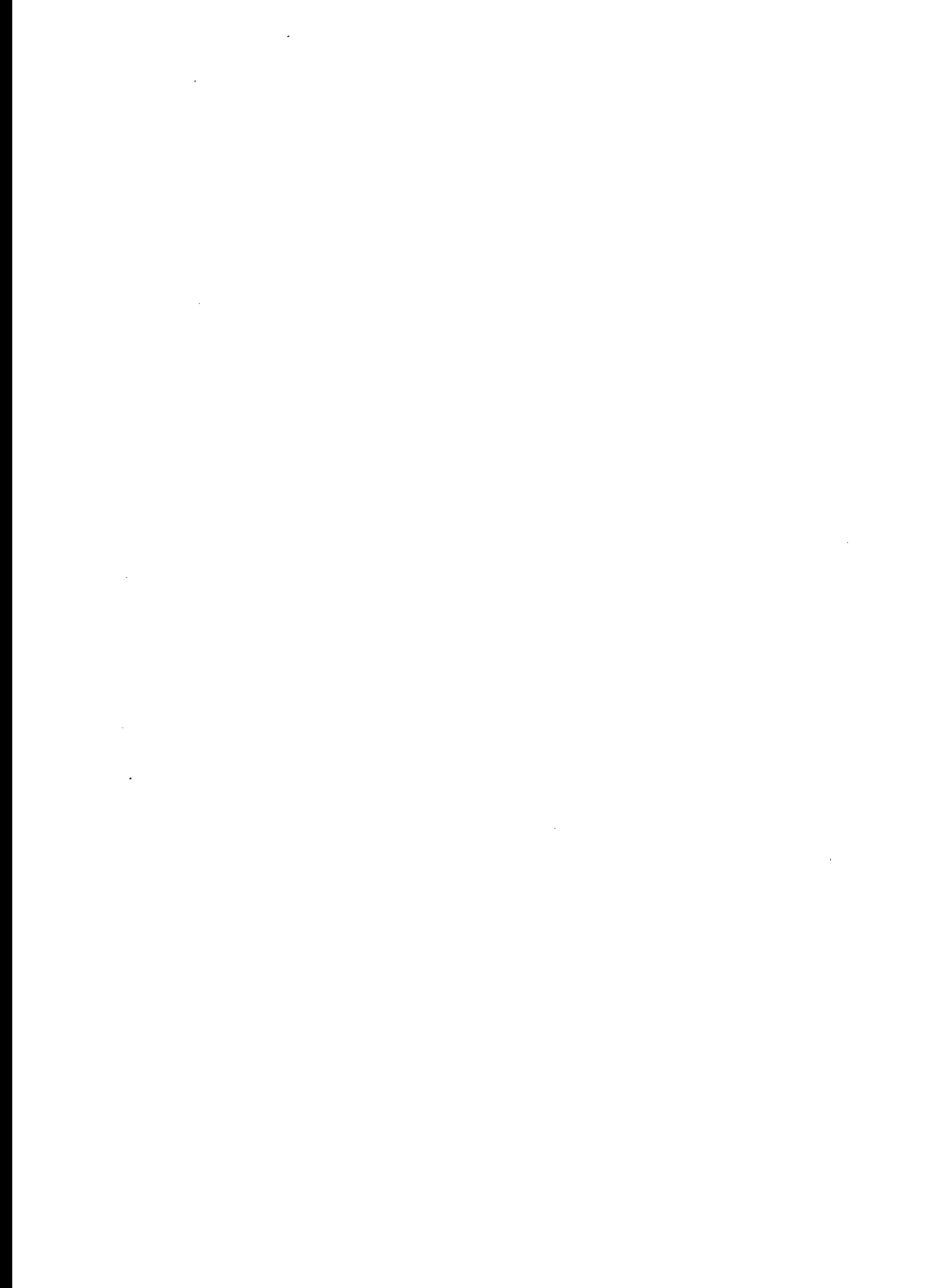
*Chief Aerodynamics Engineer
The Martin Company, Orlando, Florida*

原著者：
發行所：北門出版社
發行人：沈家駿
地 址：台北市永吉路 68 巷 19 ~ 3 號
電 話：7680934
總經銷：北門書城有限公司
地 址：台北市忠孝西路一段 209 號二樓
電 話：3822115 · 3145032
郵撥帳號：107525 號
新聞局出版登記局版台業字第 2969 號
中華民國 年 月 日
售價：NT\$ 元整

MISSILE CONFIGURATION DESIGN

Copyright © 1961 by the McGraw-Hill Book Company, Inc. Printed in the United States of America. All rights reserved. This book, or parts thereof, may not be reproduced in any form without permission of the publishers. *Library of Congress Catalog Card Number: 60-15518.*

To Ruth



PREFACE

The purpose of this book is to present some of the important basic principles involved in configuration design of guided missiles. Aerodynamic considerations are given primary emphasis in this text. Propulsion-system and structural-design aspects are also considered, since they are intimately related to the external aerodynamic configuration of the missile. The material is slanted primarily toward the aerodynamicist in preliminary design studies. It is also intended to serve as a working handbook for the aeronautical engineers in their "first assignments" in the missile industry. Aeronautical engineers who are in the "airplane-to-missile" transition phase will find this book helpful in stepping into the missile field. Finally, this book can be helpful to those engineers who are not directly concerned with external missile design, i.e., electro-mechanical and electronic missile-system engineers, in obtaining a good insight and hence some appreciation for the over-all composite missile design.

This book is an outgrowth of a company training course of The Martin Company, given by the author. The text is based largely on material developed for the afore-mentioned training class taught in several semesters during the period of 1957-1960.

Chapter 1 states some of the most important considerations involved in the over-all guided missile weapon system design. In Chap. 2 a qualitative discussion is presented on the types and classes of missiles and missile configurations together with their associated uses and their advantages and disadvantages. Chapter 3 discusses the aerodynamic characteristics of the various external configuration components to aid in the selection of these components for the design of an optimum configuration. Missile performance is treated thoroughly in Chap. 4, in which evaluation of the drag of the missile is first presented, followed by a detailed discussion of the methods of analysis of missile performance for a variety of types of missile

trajectories commonly used. The static longitudinal stability and control analysis for a simplified two degrees of freedom is presented in Chap. 5, which includes (1) model build-up of the aerodynamic derivatives involved and (2) the determination of static stability margin and load-factor capability for both forward- and rear-control configurations. Chapter 6 discusses the kinematics of the missile in maneuvering or accelerated flight and shows both analytically and graphically the effect of static stability margin on the load-factor or maneuvering capability of the missile.

Chapters 7 and 8 discuss the static directional and lateral-control design aspects of both cruciform and monowing missiles. The dynamic-stability problems are discussed in Chap. 9, which includes (1) solution of a simplified two-degree-of-freedom analysis using the classical method and (2) development and usage of transfer functions. Chapter 10 presents the method of evaluating component air loads and loading distribution for preliminary analysis. Chapter 11 discusses the general aerodynamic problems associated with missile launchings. The problem of air launching is discussed from the standpoint of safety to the parent aircraft and launch boundaries. Chapter 12 discusses the free-flight dispersion characteristics of the missile during boost and power-off flight. A simplified method is developed to predict missile drift due to cross wind during the latter phase of missile flight. Some dispersion-sensitivity factors in vacuum are derived to indicate the relative order of magnitude of various error effects. Also included in Chap. 12 is a brief discussion of the design aspects of a long-range ballistic-missile reentry body from the standpoint of heating and free-flight dispersion.

Chapter 13 discusses the fundamental principles of propulsion and the design aspects of both liquid-propellant and solid-propellant rocket motors. Finally, Chap. 14 deals with some of the more important structural-design aspects to round out the over-all missile configuration design. Several appendixes included in this volume contain derivations of equations and methods of analysis. Several methods of determining aerodynamic coefficients from flight-test data are presented in Appendix H.

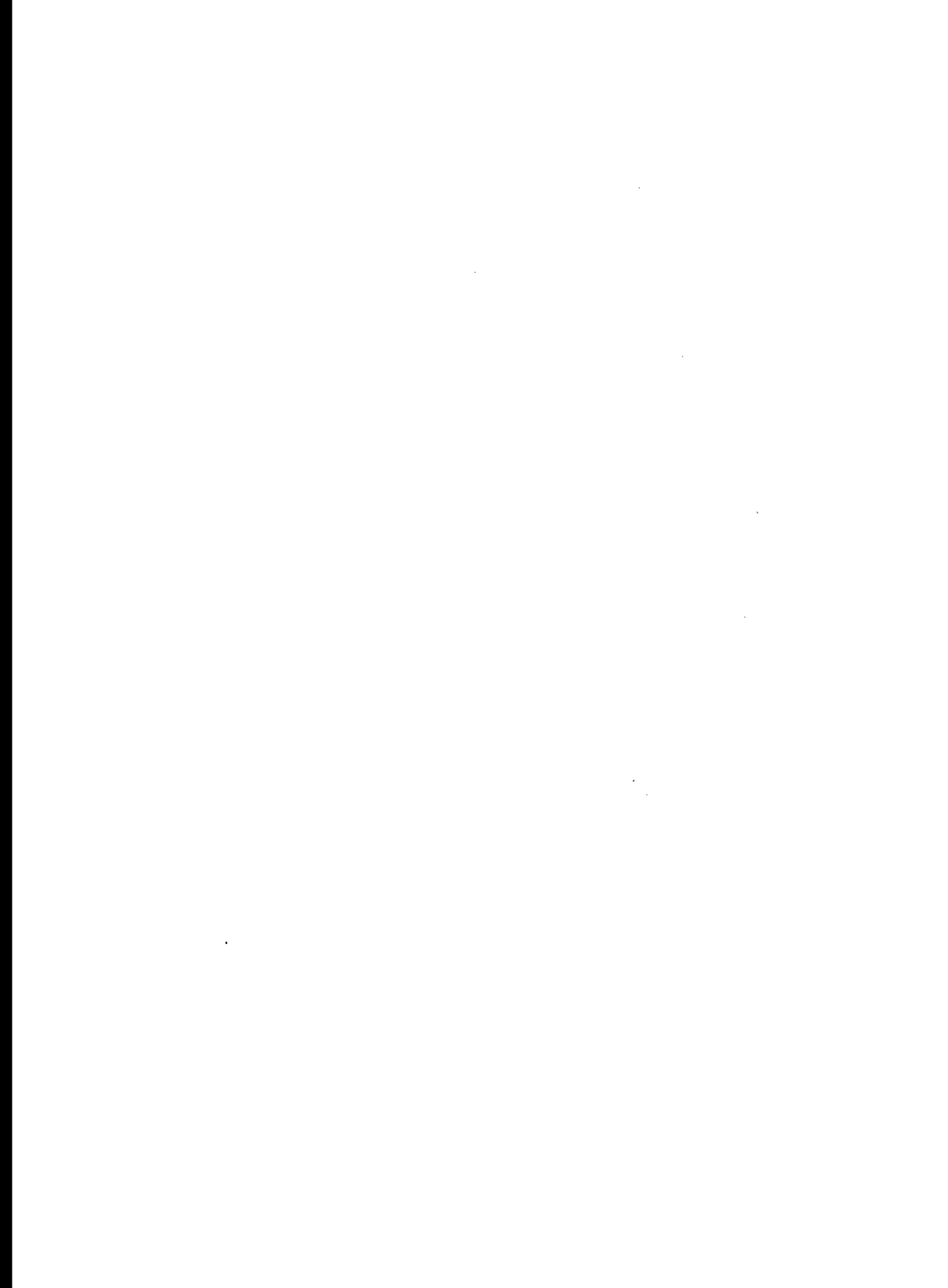
It is not the intention of this book to include comprehensive data to enable the engineer to design his configuration. In the first place, much of the essential data is classified, and secondly, it would require several volumes to include the abundance of data desirable and necessary for a reasonably efficient design. However, sufficient

references are included to assist those who are actively engaged in this challenging field of endeavor. The author believes that one of the most important assets the missile engineer must have in discharging his assignment is a sound understanding and knowledge of the fundamental principles involved in configuration design. In addition, the author also believes that the missile engineer should have a broader view, and hence a better appreciation, of the various design aspects in order to achieve a more efficient design. With these thoughts in mind, the author dedicates this book.

The author would like to express his appreciation to H. C. Sanderson, F. E. Nixon, and C. E. Hogan for their assistance, helpful suggestions, and encouragement during the writing and preparation of this book. He would also like to express his gratitude to the National Aeronautics and Space Administration (NASA) for the liberal use of their references and technical data. Many sincere thanks are due to the following associates at The Martin Company: J. E. Coster, Information Service Division; J. L. Grabber, Legal Division; C. D. Pierson, H. C. Johnson, R. T. Patterson, N. E. Singletary, C. Padera, and C. M. Bowden, Engineering Division. The author would also like to express his gratitude to Mrs. Dorothy Carrigan for her assistance in the numerical calculations and to Miss Peggy Yow, Mrs. Joyce Hartman, and Mrs. Eve Morgan for their assistance in typing the manuscript.

Finally, the author wishes to express his appreciation to his wife, who proofread the manuscript and exhibited much patience during its preparation.

S. S. Chin



CONTENTS

<i>Preface</i>	vii
1. Introduction	1
2. General Aerodynamic Design Considerations	4
2-1. Introduction	4
2-2. Classes of Missiles	4
2-3. Types of Design and Control	7
1. Wing Control	7
2. Canard Control	9
3. Tail Control	10
4. Tail-less	11
5. Body Extension	11
6. Nose-flap Control	12
7. Dorsal	12
8. Jet control	12
9. Monowing	13
10. Triform	13
11. Cruciform	14
<i>Symbols</i>	16
3. Aerodynamic Characteristics of Airframe Components	17
3-1. Introduction	17
3-2. Bodies of Revolution	18
3-3. Conical Forebody	19
3-4. Ogival Forebody	23
3-5. Hemispherical Forebody	25
3-6. Other Forebody Shapes	27
3-7. Mid-section	28
3-8. Boattail	29
3-9. Base Pressure	30
3-10. Summary of Characteristics of Bodies of Revolution	32
3-11. General Aerodynamics of Airfoil	32
3-12. Aspect Ratio	37
3-13. Wing Planform	43

3-14. Airfoil Sections	46
3-15. Wing Area	47
3-16. Subsonic Characteristics of Airfoil	49
3-17. Aerodynamic Controls	52
1. Wing Control	52
2. Canard Control	52
3. Tail Control	52
4. Lateral Controls	53
3-18. Jet Controls	53
<i>Symbols</i>	56
<i>References</i>	59
4. Missile Performance	64
4-1. Introduction	64
4-2. Friction Drag	64
4-3. Pressure Drag	67
1. Body	68
2. Wing	68
4-4. Induced Drag	69
4-5. Interference Drag	69
4-6. Boost-Glide Trajectory	70
1. Graphical Solution	70
2. Iteration Method	75
4-7. Boost-Sustain Trajectory	77
4-8. Long-range Cruise Trajectory	78
1. Maximum Speed	79
2. Rate of Climb	80
3. Time to Climb	80
4. Stall Speed	82
5. Maximum Range	82
4-9. Long-range Ballistic Trajectory	83
1. Powered Flight	84
2. Unpowered Flight	86
3. Design Considerations	88
<i>Symbols</i>	90
<i>References</i>	92
5. Static Longitudinal Stability and Control	94
5-1. Introduction	94
5-2. Two-degree-of-freedom Analysis	94
5-3. Complete Missile Aerodynamics—Forward Control	96
5-4. Static Stability Margin—Forward Control	100
5-5. Load-factor Capability—Forward Control	101
5-6. Complete Missile Aerodynamics—Rear Control	102
5-7. Static Stability Margin—Rear Control	103
5-8. Load-factor Capability—Rear Control	103
<i>Symbols</i>	104
<i>References</i>	105

6. Maneuvering Flight	107
6-1. Introduction	107
6-2. Flat Turns	107
1. Cruciform	107
2. Monowing	109
6-3. Pull-ups	110
6-4. Relationship of Maneuverability and Static Stability Margin	110
<i>Symbols</i>	112
7. Directional Stability and Control	113
7-1. Introduction	113
7-2. Cruciform Configuration	114
7-3. Body Contribution	116
7-4. Wing Contribution	116
7-5. Tail Contribution	117
7-6. Directional Control	119
<i>Symbols</i>	119
<i>References</i>	120
8. Lateral Stability and Control	121
8-1. Introduction	121
8-2. Induced Roll—Cruciform	121
8-3. Lateral Control—Cruciform	122
8-4. Special Design Considerations—Cruciform	124
8-5. Damping in Roll	125
8-6. Induced Roll—Monowing	127
8-7. Lateral Control—Monowing	127
<i>Symbols</i>	128
<i>References</i>	128
9. Dynamic Stability	130
9-1. Introduction	130
9-2. Equations of Motion	132
9-3. Classical Solution—Longitudinal Dynamics	134
1. Two Degrees of Freedom	134
2. Three Degrees of Freedom	139
9-4. Classical Solution—Lateral Dynamics	142
9-5. Transfer Function	143
1. Derivation	143
2. Application	148
<i>Symbols</i>	152
<i>References</i>	154
10. Air Loads	155
10-1. Introduction	155
10-2. Design Criteria	155
1. Forward Control	157
2. Rear Control	158

10-3. Component Air Loads	159
1. Body	159
2. Aerodynamic Surfaces	159
10-4. Component Load Distribution	160
1. Body	160
2. Aerodynamic Surfaces	162
10-5. Aerodynamic Hinge Moments	164
10-6. Aerodynamic Heating	165
<i>Symbols</i>	168
<i>References</i>	169
11. Aerodynamic Launching Problems	173
11-1. Introduction	173
11-2. Safety of Parent Aircraft—Air Launch	173
1. Missile-Aircraft Collision	174
2. Missile Structural Failure	178
11-3. Launch Boundaries—Air Launch	178
1. Launch-aircraft Trajectory	179
2. Missile Trajectory	181
3. Launch-boundary Determination	181
11-4. Consideration to Parent-aircraft Performance	182
11-5. Ground Launch	184
1. Launcher Deflection	184
2. Tip-off	184
3. Thrust and Fin Malalignment	184
4. Wind	185
11-6. Range Safety	186
11-7. Shipboard and Underwater Launches	187
<i>Symbols</i>	187
<i>References</i>	188
12. Free-flight Dispersions	190
12-1. Introduction	190
12-2. Boost Phase	191
1. Launcher Dynamics	191
2. Launcher Setting	191
3. Variation in Rocket-motor Performance	192
4. Thrust and Fin Malalignment	193
5. Surface Winds	194
12-3. Power-off Flight	195
1. Variation in Missile Characteristics	195
2. Variation in Atmospheric Density	196
3. Drift Due to Cross Winds	196
4. Determination of Over-all Free-flight Dispersion	201
12-4. Dispersion-sensitivity Factors in Vacuum	201
1. Flat Earth, Rectilinear Coordinate System	204
2. Spherical Earth, Nonrectilinear Coordinate System	206
12-5. Reentry-body Design Considerations	207
<i>Symbols</i>	208
<i>References</i>	210

13. Power-plant-design Considerations	211
13-1. Introduction	211
13-2. Types of Power Plant	211
1. Reciprocating Engine	212
2. Turbojet	213
3. Turboprop	213
4. Air Turbo Rocket	213
5. Ram Jet	214
6. Rocket	214
13-3. Fundamentals of Rocket Engines	215
1. Principles of Rocket Propulsion	215
2. General Equations	215
13-4. Rocket-motor-design Considerations	219
1. Liquid-propellant Rocket Motor	219
2. Solid-propellant Rocket Motor	221
<i>Symbols</i>	231
<i>References</i>	232
14. Structural-design Considerations	233
14-1. Introduction	233
14-2. Fundamental Structural Concepts	234
1. Dynamic Equilibrium	234
2. Linear Acceleration Due to Translation	234
3. Linear Component of Angular Acceleration	235
4. Missile-loading concept	236
14-3. Design Loads	237
1. Flight Loads	238
2. Ground Loads	238
3. Factors of Safety	238
14-4. Over-all Structural Analysis	240
14-5. Material	242
14-6. Weight and Cost	243
14-7. Types of Construction	243
1. Body	243
2. Aerodynamic Surfaces	244
<i>Symbols</i>	244
<i>References</i>	245
Appendixes	
A. <i>Determination of Radius and Volume of Tangent Ogives</i>	247
A-1. Radius	247
A-2. Volume	248
A-3. Surface Area	249
B. <i>Expression and Coordinates of Different Nose Shapes</i>	250
B-1. Power Series	250
B-2. Parabolic Series	250
B-3. Haack Series	250

<i>C. Optimum Wing Study</i>	252
C-1. C_D at $(L/D)_{\max}$	252
C-2. C_L at $(L/D)_{\max}$ or C_{Lopt}	253
C-3. $(L/D)_{\max}$	253
<i>D. Derivation of Incremental Velocity Due to Boost</i>	254
D-1. Vacuum (Drag-free Condition)	254
D-2. General Solution.	255
<i>E. Derivation of Expression for ΔV for Iteration Method</i>	257
<i>F. Determination of Downwash from Wind-tunnel-test Results</i>	258
F-1. Analytical Solution	258
F-2. Graphical Solution	259
<i>G. Determination of Damping Derivatives from Wind-tunnel-test Results</i>	260
G-1. Damping in Pitch	260
G-2. Damping in Roll	261
<i>H. Determination of Aerodynamic Derivatives from Flight-test Data</i>	263
H-1. "Pulsed Model"	263
H-2. Step-command Input	266
H-3. Forced Oscillation	268
H-4. Mach-number Determination	269
<i>Index</i>	271

CHAPTER 1

INTRODUCTION

The design of missile configurations is one of the most interesting and challenging fields—and perhaps the most complex—for the aeronautical design engineer. It requires a reasonably broad knowledge of the fundamentals of many technical specialties—aerodynamics, thermodynamics, kinematics, propulsion, structural design, etc. A quick glance at the external configurations of United States missiles indicates that these configurations (Fig. 1-1) would never have been designed if the individual design specialist—aerodynamicist, propulsion engineer, etc.—had had complete control of the final design. More often than not, the missile configuration culminates from many design compromises to achieve a final system that meets the over-all weapon requirements. In general, the optimization of design is gained by careful analysis of the following considerations:

1. Simplicity in external configuration to reduce development time and cost
2. Efficient aerodynamic control surfaces to simplify control and guidance-system circuits and to minimize servo power requirements
3. Missile range, speed, and other performance characteristics that satisfy the mission requirements
4. Adequacy of the airframe from the standpoint of stability, maneuverability, and dynamic responses
5. Simple, efficient, and highly reliable power plant
6. Low cost, producibility, and lightweight airframe construction
7. Accuracy of the control and guidance systems to accomplish the desired mission
8. Reliability of the complete weapon system as well as its individual components
9. Efficiency in packaging the various major components to facilitate check-out and replacement



SPITZER C
Surface to Air
Bomber

LACROSSE
Surface to Surface
Missile

TITAN
Surface to Surface
Missile

MINI
MOON PROBE

TALOS
Surface to Air
Bomber

TWIN AILE
MOON PROBE

VANGUARD
Surface to Air
Missile

TWIN
Surface to Surface
Missile

MINI AILE
Surface to Air
Missile

TWIN
Surface to Air
Missile

EMERALD
Surface to Surface
Missile in Production Lab
7/25/57

MINI
Surface to Air
Missile

MINI
Surface to Air
Missile

GENERAL
Surface to Surface
Missile

PULSAR
Surface to Surface
Missile

MINI
Surface to Air
Missile

MINI
Surface to Air
Missile

LETTUCE
Surface to Surface
Missile in Production Lab

TWIN
Surface to Air
Missile

JUNO
Surface to Surface
Missile

FALCON
Surface to Surface
Missile

MINI
Surface to Air
Missile

TWIN
Surface to Air
Missile

10. Degree of complexity in the preparation and delivery of the missile to accomplish its mission

It is beyond the scope of a single volume to elaborate upon all the major considerations involved in missile design. Hence this book is restricted primarily to the aerodynamic design considerations. However, since the propulsion-system and structural-design aspects are so intimately related to the external aerodynamic configuration of the missile, a brief treatise on the latter two facets is considered appropriate for the final chapters.

FIG. 1-1. Panorama of missiles (see facing page). (By permission from Remsen Advertising Agency, Inc., ©April, 1959.)

CHAPTER 2

GENERAL AERODYNAMIC DESIGN CONSIDERATIONS

2-1. INTRODUCTION

One of the primary goals of the aerodynamics design engineer is to develop a simple and yet efficient external aerodynamic configuration. As pointed out in Chap. 1, he often has to compromise his design because of many other important considerations. Consequently many types of design are evolved, each resulting from a series of design compromises. The purpose of this chapter is to discuss the various missile configurations together with their associated uses, advantages, and disadvantages.

2-2. CLASSES OF MISSILES

Most missiles may be classified into four general classes: AAM, SAM, ASM, and SSM.

The air-to-air missile (AAM) is one which is launched from one airplane against another flying aircraft or air target. This type of missile is generally of the smaller variety because of (1) the carrying capacity of the relatively small fighter aircraft and (2) the relatively short range requirements. Because of the relatively short range involved, the AAM's are usually the boost-glide type; i.e., they are boosted to their maximum speed with their own power plant and glide (or coast) the rest of the way to the target. A solid-propellant rocket motor is most frequently used on this type of missile because of its inherent simplicity, reliability, and attractive handling features. However, technical advances in prepackaged-liquid rocket motors have placed these power plants in a competitive position with the solid-propellant units, as will be discussed in Chap. 13. In some cases a boost-sustainer rocket motor is used to improve the performance characteristics of the missile. The merit of this type of rocket motor will be discussed in Chap. 13.

The aerodynamic problems associated with launching these missiles straight ahead of the parent aircraft are relatively simple. However, caution must be exercised to account for the possibility of airflow interference between the missile and airplane. This interference problem is particularly critical for high-speed launchings from highly swept-wing fighters. This problem of airplane safety and missile-launch dispersion will be discussed in detail in Chap. 11. In the special role of a bomber defense, for which the AAM may be retrolaunched or launched perpendicular to the flight direction of the bomber, detailed analysis is required to determine its launch dispersion characteristics.

The maneuverability requirement of an AAM is generally the most severe in comparison with other classes of missiles. This is due to (1) the relatively high launching speeds, (2) high target velocity and maneuverability, and (3) relatively short flight time for flight-path corrections. In addition to the severe maneuverability requirements the wide range of operating altitude presents the designer a very challenging problem. For example, the missile-maneuverability requirement generally varies linearly from sea level to some altitude and then remains at a constant value up to the maximum design altitude, as shown in Fig. 2-1. However, if the missile is designed to satisfy the low-altitude (say sea-level) maneuvering requirement with maximum control deflection the missile will not meet the high-altitude design requirement as a result of the appreciable reduction in air density, as indicated in Fig. 2-1. Hence the maximum altitude generally dictates the missile design to meet the maneuvering requirement with maximum control deflection. This results in extremely large loading at the low-altitude conditions if full control deflection is used or inadvertently realized. In order to keep the structural weight to a reasonable level and avoid excessive flight loads either the control travel must be limited as a function of operating altitude or some g -sensing device must be used to return the control surfaces to neutral or some low value.

The surface-to-air missile (SAM) is normally designed for area

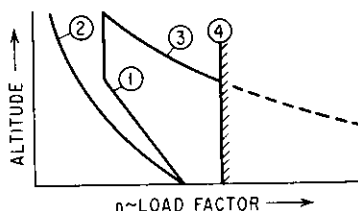


FIG. 2-1. Altitude vs. load factor (constant Mach number). (1) Requirement. (2) δ_{\max} designed for minimum altitude condition. (3) δ_{\max} designed for maximum altitude condition. (4) Structural limit.

defense against attacking aircraft or ICBM's. As a result the aerodynamic design depends upon its range, which can vary from a few miles to several hundred miles. For relatively short ranges, a single-stage solid- or liquid-propellant rocket motor is generally used. Again a boost-sustainer trajectory may be used to improve the missile performance characteristics. For longer ranges multistaging is often required in order to reduce the over-all weight of the missile. Ram jets or other air-breathing power plants prove to be advantageous from the economy and weight standpoint. Perhaps one of the chief disadvantages of using an air-breathing ram jet is that very large external and/or droppable boosters are required to boost the missile to ram-jet ignition speeds. The guidance system may vary significantly for different range requirements. For relatively short ranges, beam-riding or even infrared guidance may provide sufficient accuracy for the desired probability of kill. However, for long-range intercepts some form of homing or terminal guidance system is required to ensure an effective kill. The maneuverability requirement for this class of missile can be quite severe, particularly against fast-flying low-altitude targets. Generally this type of missile is launched vertically or at a relatively high elevation to maximize the "effective area" of the missile weapon system.

3) The air-to-surface missile (ASM) is normally designed as an offensive or tactical weapon to knock out enemy surface targets such as gun emplacements, tanks, ships, or airfields. The launching problems associated with this type of missile are similar to those associated with the straight-forward launchings of the AAM's. Again, the range of this type of missile varies from a few miles to hundreds of miles. For relatively short range missions the ASM is normally boosted off the pylon because of its relatively light weight. For long-range applications the ASM is usually dropped off the pylon, attitude-stabilized, and gradually boosted up to the required speeds. Multistaging may be beneficial for this type of missile if the range is appreciable. Careful consideration must be given to the missile-aircraft installation in order to minimize the performance degradation to the parent aircraft, particularly with the large-sized long-range ASM's. The maneuverability requirement for the ASM's is generally much lower than that for the AAM's because of the slow-moving or stationary ground targets.

4) The surface-to-surface missile (SSM) may be used in two separate roles in war. One is as a long-range offensive or retaliatory weapon; the other is for use in support of ground troops in the role of an

artillery battery. The former weapon may have a range which varies from one thousand to several thousands of miles and may fly the cruise or ballistic type of trajectory. For the latter type of trajectory, multistaging is mandatory to reduce the size of the rocket motor and the over-all weight of the missile for this mission. An indication of the gains realized by staging will be illustrated in Chap. 4. Because of their weight these missiles are always launched from their upright position on the launch pads. (The maneuverability requirement is very low, and the chief control requirement arises from wind-profile (shear) effects on the missile trajectory during its ascent.) The reentry body (in MRBM, IRBM, and ICBM applications) of such missiles is a design which merits many special considerations; it will be discussed in Chap. 12.

As an artillery weapon the SSM is normally boosted off a ground launcher and coasts to the target. In general only a moderate degree of maneuverability is required for this type of missile. In the case of an unguided missile (i.e., Honest John) the stability requirement is dictated from launch-dispersion considerations which will be detailed in Chap. 12. A special type of SSM is one which is launched from beneath the water (i.e., Polaris).

2-3. TYPES OF DESIGN AND CONTROL

Many types of external aerodynamic configurations (and modifications thereof) used for the four classes of missiles previously described are shown in Fig. 2-2. Each of these will be discussed briefly to point out the advantages and disadvantages.

1. Wing Control. (A wing-control configuration consists of a relatively large wing located close to the center of gravity of the missile and a set of tail or stabilizing surfaces at the aft end of the missile. This type of control is used mostly in an AAM because of its extremely fast response characteristics.) As shown in Fig. 2-3, instantaneous lift is developed as a result of wing deflection to provide lift for maneuvering flight. Additional lift is developed as angle of attack builds up. Control effectiveness (pitching or turning moment due to control-surface deflection) $C_{m\delta}$ from the wings is generally very low, since the lift developed is located close to the center of gravity of the missile. However, the resulting downwash has a beneficial effect on the tails since it produces a down load which provides the desired turning moment to develop angle of attack for additional lift previously mentioned. This beneficial downwash

effect on control effectiveness is readily apparent in Fig. 2-4. The wing location for a wing-control design is very critical, particularly for cases where large center-of-gravity travel occurs between launch

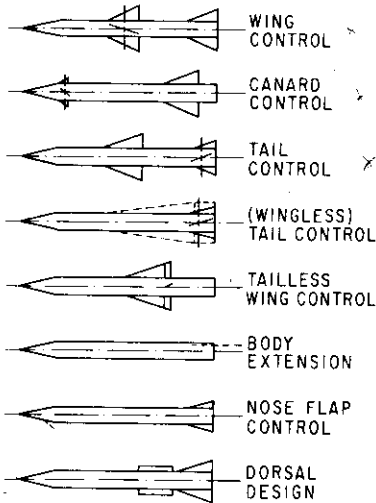


FIG. 2-2. Types of design and control.

and rocket-motor burn-out conditions. Since the wing surfaces are generally mounted very near the launch center of gravity (in order to obtain the desired degree of static stability with a reasonably small-sized tail), the forward shift in center of gravity can result in a substantial reduction in control effectiveness and hence maneuverability per unit wing deflection, as shown in Fig. 2-4.

Because of the added lift due to wing deflection the angle of attack required for a given trim lift coefficient or load factor is generally lower than that encountered in a tail control. This low value of trim angle of attack is advantageous particularly from the standpoint of inlet design for air-breathing power-plant and guidance-seeker designs. The aerodynamic hinge moments are relatively large because of the large wing area. Hence careful analysis must be made to optimize the hinge-line location for the entire range of flight Mach numbers to minimize the servo-power requirements. Lateral control may be obtained by superimposing differential wing deflections on top of the basic pitch-and-yaw deflection, thereby simplifying the servo system. However, several poor features associated with this type of control must be carefully considered before this design is selected for particular application. These are (1) relatively large loss in tail effectiveness due to downwash ϵ_a to static-stability contribution,

effect on control effectiveness is readily apparent in Fig. 2-4. The wing location for a wing-control design is very critical, particularly for cases where large center-of-gravity travel occurs between launch

and rocket-motor burn-out conditions. Since the wing surfaces are generally mounted very near the launch center of gravity (in order to obtain the desired degree of static stability with a reasonably small-sized tail), the forward shift in center of gravity can result in a substantial reduction in control effectiveness and hence maneuverability per unit wing deflection, as shown in Fig. 2-4.

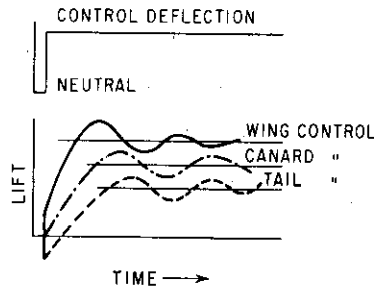


FIG. 2-3. Comparison of missile responses.

(2) nonlinear aerodynamics resulting from downwash due to both wing deflection ϵ_s and angle of attack ϵ_α , and (3) severe adverse rolling moments induced on the tail surfaces from combined effects of angle of attack and wing deflection. The latter effect will be discussed in more detail in Chap. 8.

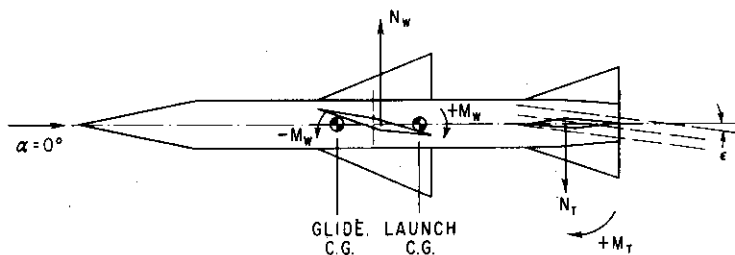


FIG. 2-4. Aerodynamics of wing control.

2. Canard Control. A canard-control configuration consists of a set of small control surfaces called canards located well forward on the body and a set of large surfaces (wing or tail) attached to the middle or aft section of the missile. In contrast to the wing-control configuration, the canards (because of their small size) do not generate a significant amount of downwash to affect the longitudinal-stability characteristics adversely. Thus relatively large static-stability margins can easily be obtained by simple changes in wing

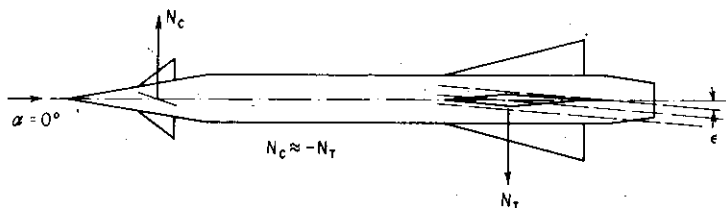


FIG. 2-5. Comparison of canard and tail loads.

location. Lift on this type of configuration is derived almost entirely from angle of attack since the lift of the canards is generally nullified by the down load on the wing caused by downwash, as shown in Fig. 2-5. One of the most attractive features in the canard configuration is the inherent simplicity of packaging due to the small size of the control system and its location in the nose. In addition, changes in center-of-gravity locations due to the design changes may

easily be accommodated by simple relocation of the wings. Since the total lifting-surface area is generally lower, the total drag and weight of the missile are reduced.

Some of the major disadvantages of the canard configuration are: (1) Roll stabilization is difficult if not impossible with the use of the canard surfaces because of their size and downwash effect on the wings. Consequently, a more complex method of providing roll control is required, i.e., wing-tip controls. (2) Relatively high control-surface rates are required to obtain the desired rate of response since angle of attack must be generated before any lift is developed, as shown in Fig. 2-3. As the result of the higher surface-rate requirement, an increase in servo-power requirement is demanded. However, the resultant servo-power requirement is generally lower than that required for the wing-control configuration. Therefore, for relatively small missiles which do not require roll-attitude stabilization, the canard configuration is probably the best over-all configuration.

3. Tail Control. (With this type of control, it is obvious that the tail deflection δ_T must be opposite in direction to the angle of attack. This feature results in relatively slow response characteristics, since

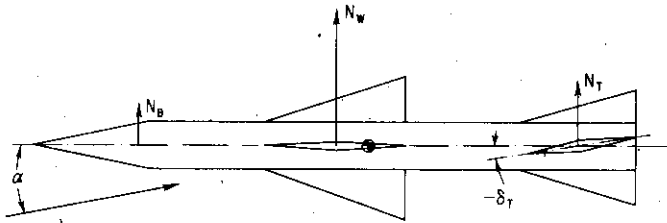


FIG. 2-6. Typical component loading—tail control.

the initial lift is in a direction opposite to the desired one, as shown in Fig. 2-3. However, it is advantageous in that the tail loads and hinge moments are kept relatively low as the total angle of attack on the tail is reduced (i.e., $\alpha_T = \alpha - \epsilon - \delta_T$). This in turn reduces the body bending to a minimum, since most of the resultant load is concentrated on the main wings located near the center of gravity, as shown in Fig. 2-6. In addition, the wing-tail interference effects are reduced, since the forward main lifting surfaces are fixed, i.e., no downwash due to wing deflection ϵ_d . Therefore, the aerodynamic characteristics are more linear than those for a wing-control design. Major disadvantages associated with this configuration are (1)

limited space at the tail end for a control mechanism if a solid rocket motor is used, and (2) deficiency of tail surfaces to provide the desired lateral control.

A special case of a tail control is one which does not have a wing. This type of configuration is restricted to missiles which require relatively low maneuverability. The body in this case provides a goodly portion of the lift with an attendant large angle of attack. This type of configuration may be used for reentry bodies which may require small flight-path guidance upon entering the sensible atmosphere. The tail size and location may be chosen to provide the desired static- and dynamic-stability characteristics to achieve a satisfactory reentry to low altitudes.

Another special case of a tail control is one in which a very low aspect ratio or arrow wing is employed. The tail in this case is really the trailing part of the wing cut out for control, as shown in Fig. 2-2. For reasons mentioned above, the aerodynamic hinge moments are generally very low. However, the trim angle of attack for this type of configuration is rather high because of the very low aspect ratio surfaces.

4. Tail-less (or Wing Control). A tail-less type of configuration involves one set of surfaces (wings) with control flaps located at the trailing edge. The chief advantage of this type of configuration is the reduced number of surfaces, which results in reduced drag and manufacturing costs. The most obvious disadvantage of this type is that the location of the wing is extremely critical. Locating the wing too far aft would provide such excessive stability as to require very large control-surface size or deflection to get the desired load factor. On the other hand, locating the wing too far forward near the center of gravity would cause a reduction in control effectiveness as well as in aerodynamic damping, which is generally required and/or desirable in most missile systems.

5. Body Extension. Another method of providing control is the profitable use of the base pressure or, rather, the pressure differential between the base and the free stream. A segment extending aft of the body into the region of differential pressure as shown in Fig. 2-7 experiences a lift force for control. Chief advantages associated with this design are (1) it has an extremely low servo-power requirement since there is no hinge moment, and (2) it is simple and compact in design. Disadvantages are (1) low maneuverability, (2) inoperability at subsonic speeds where the base pressure is practically non-existent, and (3) reversal in control between power-on and power-off

conditions due to jet effects. If positive static stability is required, flare tail configuration is readily adaptable to this type of control, since it also provides additional space at the aft end for installation of the associated control mechanisms.

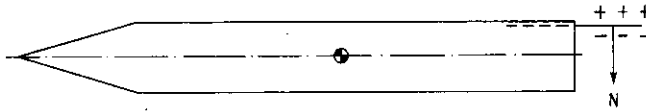


FIG. 2-7. Principle of body extension.

6. Nose-flap Control. This type of control is composed of segments of a nose section or flap extended from each of the four quadrants. When not in use they are retracted to form the nose contour. This type of control, when used with extremely low aspect ratio tail surfaces, may be suitable for air-launched missiles because of its compact design. The degree of stability required from a launching standpoint may be realized with these control surfaces retracted. However, this type of control has a rather low maneuverability characteristic and may be considered only in limited applications.

7. Dorsal. In certain applications where the over-all span of the missile is severely limited the use of "dorsal" may be necessary. Dorsal, when used in missile design, may be considered as an "aerodynamic fix" required to make up for the loss in aerodynamic efficiency due to reduction in tail aspect ratio and/or area. Since this fix is rather inefficient it may be used only in limited and specialized cases.

8. Jet Control. This type of control may be subdivided into four classes: (1) simple auxiliary jet (rocket) reactions, (2) gimbale engine and/or rocket nozzles, (3) jet vanes, and (4) jetavators. The first type of control may be used to good advantage especially on small missiles of relatively short flight duration or on reentry bodies to provide stabilization or spin (rolling velocity) to minimize dispersion in free flight. Jet or air injection over aerodynamic surfaces for augmentation may also be employed. Gimbale liquid-propellant engines have been used successfully for many years. For example, the Viking research vehicles have been successfully flown many times using this type of control during phases of flight wherein aerodynamic control is inadequate (i.e., at lift-off where the dynamic pressure is low or at extremely high altitudes where the air density

is low). Solid-propellant rocket motors, however, ordinarily cannot be gimbaled; other means of jet control must therefore be used. Swivel nozzles on this type of rocket motor (as well as on liquid-propellant rocket motors) are practical and may be employed.

In addition to the afore-mentioned jet controls, jet vanes are frequently used to provide or supplement aerodynamic controls. Although the loss of total impulse caused by these vanes submerged in the rocket-motor exhaust is relatively low (i.e., generally less than 5 per cent), the major problem is to develop a material to withstand the high temperatures for a prolonged operating period. Consideration has been given to retraction of the vanes out of the hot jet exhaust when not in operation. However, the temperature shocks associated with such a mode of operation may be equally detrimental. In addition, the complexity and added weight of the retraction mechanism are undesirable from the standpoint of reliability, cost, and missile performance. The heating problem associated with the use of jet vanes is particularly critical when high-energy solid or liquid propellants are used because of their much higher operating temperatures. Jetavators are relatively novel devices and may be used for controls. Jetavator control appears to be adequate and requires relatively low operating forces because of its low hinge moments. Under certain design conditions it may be advantageous to discard all aerodynamic stabilizing and control surfaces and rely completely on the above-mentioned jet controls. However, detailed analysis is required before one of these jet controls is selected as either a supplementary or sole means of control for a given missile-design requirement.

In addition to the above description of the various classes of missiles and types of control a few words on wing arrangements are felt necessary to close this chapter on general design considerations.

9. Monowing. The monowing arrangement is generally used on cruise-type missiles, i.e., missiles designed to cruise for relatively long ranges like manned aircraft. This type of design is generally lighter and has less drag than the cruciform configuration. The wing area and span are, however, somewhat larger. Although the monowing missile must bank to orient its lift vector in the desired direction during maneuvering flights, the response time may be sufficiently fast and acceptable from a guidance-accuracy standpoint.

10. Triform. This type of wing arrangement, which employs three panels or wings generally of equal area spaced 120° apart, is seldom used since no noticeable advantage can be realized. Results

of a brief preliminary analysis indicate that the total wing area of the triform is equal to that used on a cruciform arrangement and that consequently no noticeable change in drag may be realized. In addition, little or no weight saving will be realized, even though one less attachment or fitting is required, because the total load remains the same. Thus the increased load per panel requires heavier fitting for the triform configuration. Also, the triform panels will have a somewhat larger span with a resulting outboard shift in loading; consequently the weight per unit area increases, partially nullifying the gain in the elimination of one attachment. Triform tail arrangements may be preferred over cruciform when used in conjunction with monowing design to provide the desired degree of directional stability (see Chap. 7).

11. Cruciform. Undoubtedly the most commonly used configuration in missile design is the cruciform. There are several major advantages in the use of this type of configuration.

1. Fast response in producing lift in any direction
2. Identical pitch and yaw characteristics
3. Simpler control system as the result of item 2

One of the most important aspects associated with a cruciform design is the orientation of the tail surfaces with respect to the wing planes. Considerable experience was accumulated and experi-

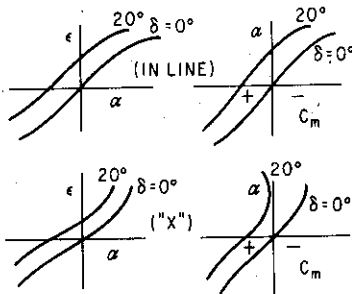


FIG. 2-8. Aerodynamic characteristics of in-line and X tail configurations.

mental data were derived in the late forties and early fifties on this subject. The significant conclusion was that an in-line tail surface provides the best over-all aerodynamic characteristics for most missile applications. This conclusion was made on the basis that:

1. Desirable stable trim conditions at high angles of attack and control-surface deflections are realized, whereas an interdigitated tail configuration results in unstable or divergent conditions.
2. Although an in-line tail configuration provides low stability at low angles of attack, this is a feature which can easily be compensated for by simple changes in the control-system gains.

To appreciate the significance of this important design aspect,

the downwash and resultant pitching-moment curves are illustrated in Fig. 2-8. The variation of downwash angle with free-stream angle of attack is the predominant factor in the determination of the complete model aerodynamic pitching-moment characteristics, since the pitching-moment curves for the body alone, body plus wing, or body plus tail configurations are, in general, relatively linear. The

TABLE 2-1. SUMMARY OF AERODYNAMIC DESIGN CHARACTERISTICS

Type of control	Advantages	Disadvantages
Wing control. . . .	Fast control Low trim α Relatively good packaging feature Beneficial downwash from canard deflection for control	High hinge moments Severe servo power required Nonlinear aerodynamics Large induced rolling moments eg travel critical High drag Large downwash decreases tail contribution to static stability
Canard control. . .	Good packaging feature Low hinge moments Fairly linear aerodynamics eg travel not critical Facilitates design changes Low drag	No simple lateral control Relatively large body bending moments High control rates required Relatively high trim α
Tail control.	Low tail loads Low tail hinge moments Low body bending moments Fairly linear aerodynamics	Slow response Negative $C_{N\delta}$ (initial force in wrong direction) Packaging problems Poor lateral control High trim α

relatively large change in downwash with angle of attack in the low region for the in-line tail configuration results from the fact that the tail is located directly in the downwash region. Consequently relatively large losses in static-stability contribution by the tail surfaces are evident in the complete model pitching moments. As the angle of attack increases to a sufficiently large value, the tail surfaces move out of this downwash region, and an increase in stability results, as shown in Fig. 2-8. For the X, or interdigitated, configuration the reverse situation is evident.

SYMBOLS

C_N	normal-force coefficient
$C_{N\delta}$	normal-force effectiveness (variation of C_N with δ) $\partial C_N/\partial \delta$
C_m	pitching-moment coefficient
$C_{m\delta}$	pitching-moment (or control) effectiveness $\partial C_m/\partial \delta$
M	pitching moment
N	normal force
α	angle of attack
ϵ	downwash angle
ϵ_α	variation of ϵ with α , $d\epsilon/d\alpha$
ϵ_δ	variation of ϵ with δ , $d\epsilon/d\delta$
δ	control-surface deflection

Subscripts

B	body
C	canard
T, t	tail
W	wing

CHAPTER 3

AERODYNAMIC CHARACTERISTICS OF AIRFRAME COMPONENTS

3-1. INTRODUCTION

Now that some of the general design aspects of guided missile configuration design have been discussed, it is necessary to get into a detailed discussion of some of the specific items or components which make up the complete missile.

As a missile flies through the air it experiences aerodynamic forces and moments. These forces, lift and drag, may be classified into two general types: (1) those due to air friction and (2) those due to pressure. The former type, i.e., drag, is created by the shearing action of the air due to its viscosity and the latter by differences in surface pressures which result in the creation of both lift and drag forces. In supersonic missile-design studies it is more convenient to consider normal forces, i.e., forces perpendicular to the missile axis, in lieu of lift forces. The reason for this is that the component section and aerodynamic lifting surfaces are generally symmetrical about the longitudinal axis or chordwise center line; the resultant aerodynamic-pressure forces on these symmetrical sections are thus normal to the longitudinal axis or wing chord. In addition, most wind-tunnel strain-gauge balance systems are arranged to measure forces normal and parallel to the longitudinal axis of the model. An additional advantage to using normal forces is in the stability analysis, as will be discussed in Chaps. 5 and 9.

Before going into the discussion of the aerodynamic characteristics of the airframe components it may be well to show the resolution of these forces. From Fig. 3-1 the following force relations are derived:

$$\begin{aligned} D &= A \cos \alpha + N \sin \alpha \\ L &= N \cos \alpha - A \sin \alpha \end{aligned} \quad (3-1)$$

$$\begin{aligned} A &= D \cos \alpha - L \sin \alpha \\ N &= L \cos \alpha + D \sin \alpha \end{aligned} \quad (3-2)$$

To reduce Eq. (3-2) into coefficient form, divide by qS and Eq. (3-3) is obtained:

$$\begin{aligned} C_A &= C_D \cos \alpha - C_L \sin \alpha \\ C_N &= C_L \cos \alpha + C_D \sin \alpha \end{aligned} \quad (3-3)$$

It is interesting to note that the value of C_A first decreases and then increases with increasing angle of attack whereas C_D always increases with angle of attack, as indicated in Fig. 3-2.

In the following discussions, the airframe is assumed to be composed of the body plus lifting and control surfaces. A brief mention

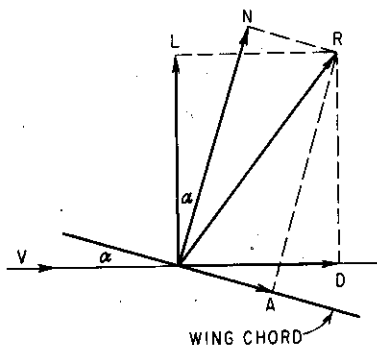


FIG. 3-1. Force resolution.

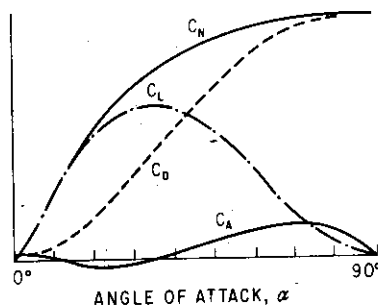


FIG. 3-2. Effect of α on C_N , C_L , C_A , and C_D .

of jet controls will also be included to complete the discussion on control characteristics.

3-2. BODIES OF REVOLUTION

The body of the missile may be divided into three major sections, the forebody, or nose; the mid-section; and the aft, or boattail, section. Forebodies may have many varieties of shapes, most common of which are conical, ogival, "power-series," or hemispherical. These shapes, shown in Figs. 3-7 and 3-11, are used primarily on missiles of supersonic speeds and are generally selected on the basis of combined aerodynamic, guidance, and structural considerations. For example, a hemispherical nose has very high drag from the aerodynamic drag or performance standpoint, but it is excellent from the standpoint of structural integrity, aerodynamic heating, and certain types of guidance (i.e., infrared). Since the pressure or wave drag may be several times that due to friction at supersonic

speeds, careful selection of the nose shape is mandatory to assure satisfactory performance and operation of the over-all system. Hence it is of interest to understand and appreciate the aerodynamic forces of these forebodies at supersonic speeds.

3-3. CONICAL FOREBODY

The supersonic aerodynamic characteristics of a conical forebody will be discussed first since many early theoretical and experimental

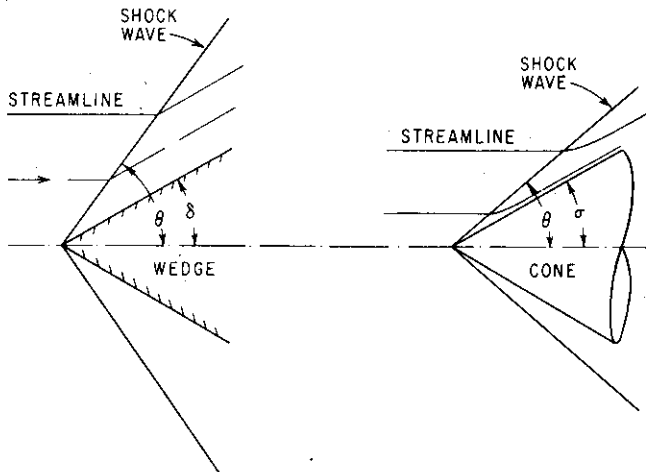


FIG. 3-3. Flow past a wedge and cone.

analyses were concentrated on this simple configuration. The supersonic flow over a cone has characteristics which are similar in appearance but markedly different in nature from those corresponding to two-dimensional flow (i.e., flow over a wedge). The similarity in appearance is that an oblique shock is formed at the tip of the wedge and apex of the cone (see Fig. 3-3). However, the flow characteristics aft of the shock wave, where the air undergoes both aerodynamic and thermodynamic changes, are noticeably different depending upon whether the flow is two-dimensional or three-dimensional as in this case of the conical nose. Briefly, these flow characteristics are (1) the shock angle, (2) streamlines or flow direction, and (3) air properties between the shock wave and surface of the body. Because the air can change direction in all planes normal to the flow instead of being restricted to just one plane as in the

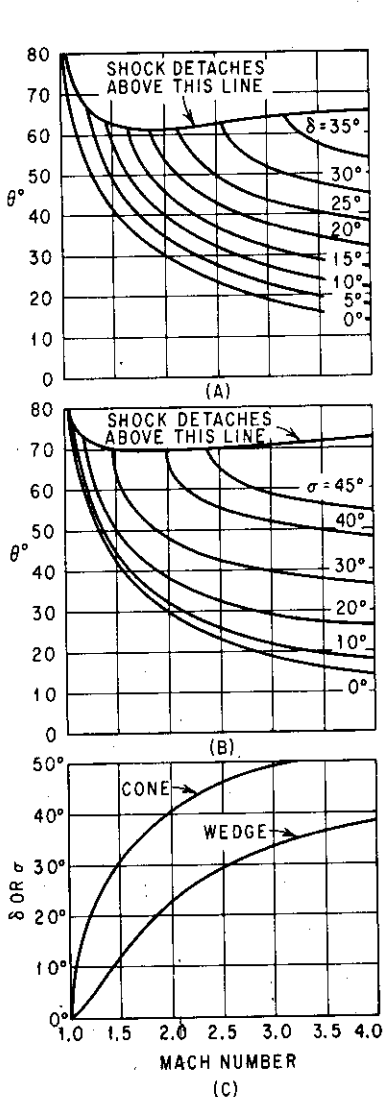


FIG. 3-4. (A) Shock-wave angle vs. Mach number in two-dimensional flow. (B) Shock-wave angle vs. Mach number for cones. (C) Detachment angle vs. Mach number for wedges and cones.

two-dimensional case, the shock angle θ for the same cone vertex angle and free-stream Mach number is noticeably less than that for the two-dimensional case (see Fig. 3-4). This corresponds to a much weaker shock, and consequently the air undergoes a smaller change in property behind the shock. The streamlines in two-dimensional flow change direction abruptly and travel in a direction parallel to the surface of the wedge, whereas in three-dimensional flow these streamlines turn gradually and approach the conical surface direction asymptotically as shown in Fig. 3-3. Finally, the density, pressure, etc., are not constant between the shock wave and the surface of the cone as they are in the case of a wedge. However, the pressure along any ray originating from the apex of the cone and hence along the cone surface is constant. This fundamental characteristic forms the basis for the well-known conical-flow theory.

The supersonic flow of air around cones at zero angle of attack has been thoroughly investigated by many experimenters, notable among whom were Taylor and Maccoll.^{1,2,*} The exact three-dimensional compressible-flow differential equations can be solved only by considering the symmetry of the cone, and thus the problem is reduced to one

* Superscript numbers indicate references listed at the end of the chapter.

in two dimensions. The resultant equation is of the second order and nonlinear and must be solved by means of an iteration process. Results derived may be found in the MIT cone tables^{3,4} and are plotted in *NACA Technical Report 1135*. Figures 3-4 and 3-5 show the shock-angle and pressure-coefficient variations with cone-geometry and Mach-number effects. These results are valid only for conditions under which the shock wave is attached to the cone. For a higher degree of accuracy the reader should consult the aforementioned references.

The pressure change between the free stream and surface of the cone—written in terms of a pressure coefficient [defined as $(p_2 - p_1)/q$ or $\Delta p/q$] as a function of Mach number—is expressed by an empirical equation within 5 per cent accuracy for semivertex cone angles up to 50° .⁶

$$\frac{p_2 - p_1}{q} = \frac{\Delta p}{q} = \left(0.083 + \frac{0.096}{M^2} \right) \left(\frac{\sigma}{10} \right)^{1.69} \quad (3.4)$$

where σ is in degrees

With the pressure defined, the drag (equivalent to axial force at zero lift or angle of attack) is simply related as

$$D = \frac{\Delta p}{q} qS = C_D qS \quad (3.5)$$

or

$$C_D = \frac{\Delta p}{q} \quad (3.6)$$

Equation (3-6) is the drag coefficient due to pressure on the cone alone and does not include base pressure or friction drag, which will be discussed in a later section.

The normal force on the cone is obtained by integrating the pressure forces in a direction normal to the center line of the conical body. The theoretical values obtained by various investigators are as follows:

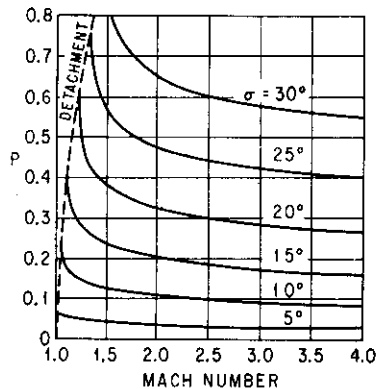


FIG. 3-5. Pressure coefficient vs. Mach number for cones.

From refs. 4 and 5, the values of C_{N_α} at $\alpha = 0^\circ$ for various cone semivertex angles and free-stream Mach numbers are shown in Fig. 3-6. Busemann⁷ in his analysis arrived at a value of $C_{N_\alpha} = 2$ per radian, which is identical to that obtained with the slender-body theory. This value is independent of the free-stream Mach number.

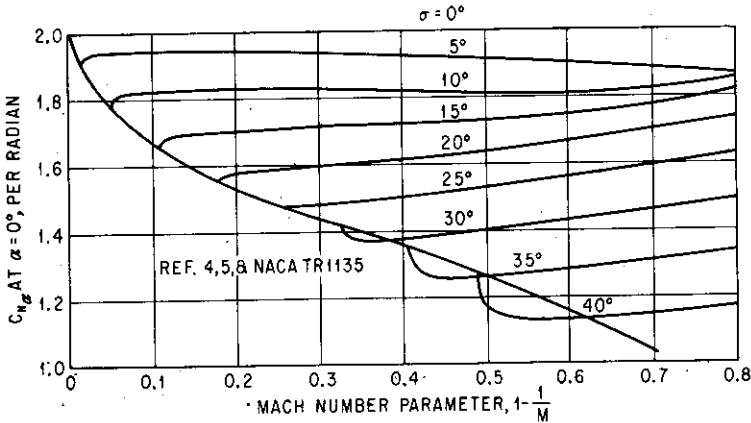


FIG. 3-6. C_{N_α} vs. Mach number parameter for cones.

Refinements made by Ferrari⁸ and Tsien⁹ resulted in the following equations:

$$C_{N_\alpha} = \frac{2 \sqrt{\left(\frac{\cot \sigma}{\sqrt{M^2 - 1}}\right)^2 - 1}}{\sqrt{M^2 - 1} \cosh^{-1} \frac{\cot \sigma}{\sqrt{M^2 - 1}}} + \sqrt{\left(\frac{\cot \sigma}{\sqrt{M^2 - 1}}\right)^2 - 1} (1 + 2 \tan^2 \sigma) \quad (3-7)$$

$$C_{N_\alpha} = \frac{2 \sqrt{\left(\frac{\cot \sigma}{\sqrt{M^2 - 1}}\right)^2 - 1}}{\sqrt{M^2 - 1} \cosh^{-1} \frac{\cot \sigma}{\sqrt{M^2 - 1}}} + \sqrt{\left(\frac{\cot \sigma}{\sqrt{M^2 - 1}}\right)^2 - 1} \quad (3-8)$$

Since the pressure is constant along the surface of the cone (conical-flow theory) the center of pressure is at the centroid of the planform area of the cone, or two-thirds of the nose length aft of the apex.

3-4. OGIVAL FOREBODY

Next the aerodynamic characteristics of the ogival forebody will be discussed, since this type of nose configuration is used more frequently than the conical nose. An ogive is similar to a cone except that the planform shape is formed by an arc of a circle instead of a straight line as shown in Fig. 3-7. A tangent ogive shown in

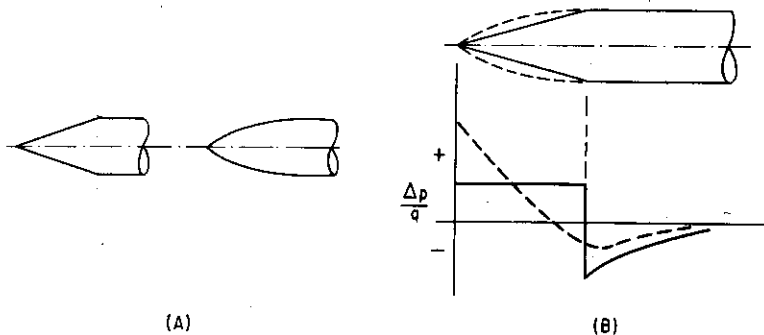


FIG. 3-7. (A) Conical and ogival nose shapes. (B) $\Delta p/q$ over cone and ogive at $\alpha = 0^\circ$.

Fig. 3-7 is one whose base is tangent to the cylindrical mid-section of the body of the missile. The ogival shape has several advantages over the conical section. These advantages are (1) slightly greater volume for a given base and length (l/d ratio), (2) a blunter nose, providing structural superiority, and (3) slightly lower drag.

Semiempirical expressions were derived by E. R. C. Miles¹⁰ for the form or pressure drag and center of pressure of the tangent ogives.

$$C_{D_p} = P \left\{ 1 - \frac{2[196(l/d)^2 - 16]}{28(M + 18)(l/d)^2} \right\} \quad (3-9)$$

$$\frac{cp}{l} = \frac{1}{2} \left[\frac{50(M + 18) + 7M^2P(5M - 18)}{40(M + 18) + 7M^2P(4M - 3)} \right] \quad (3-10)$$

where P is the pressure coefficient $\Delta p/q$ as given by Eq. (3-4). To facilitate calculation of the value of P , the ogive semivertex angle σ_o at the tip of the nose is given as

$$\sigma_o = 2 \tan^{-1} \frac{1}{2l/d} \quad (3-11)$$

It is obvious from Eq. (3-11) that the angle of the tip of the ogival nose is twice the conical value for the same length-to-diameter ratio

(see Fig. 3-8). Other characteristics of the ogival nose (i.e., radius and volume) are derived mathematically in Appendix A.

Results of an independent correlation indicate close agreement with those derived in Eq. (3-9). This will be shown quantitatively

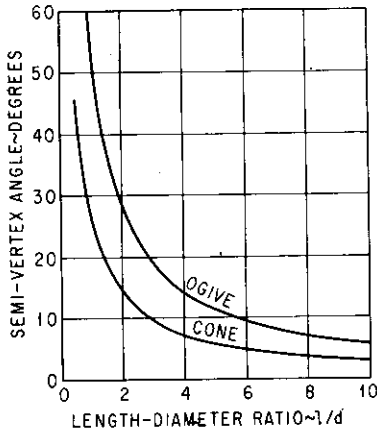


FIG. 3-8. Semivertex angle vs. length-diameter ratio for cones and ogives.

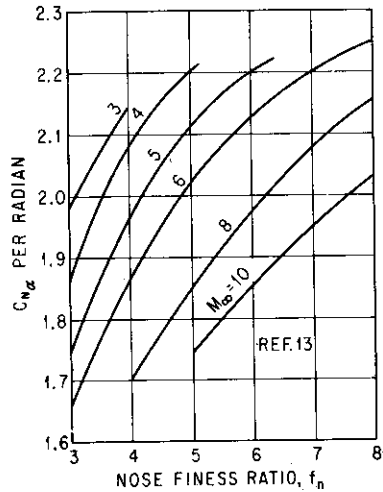


FIG. 3-9. C_{N_α} vs. nose fineness ratio.

in Chap. 4. However, the centers of pressure derived by the slender-body theory^{34,35} and by Eq. (3-10) are somewhat different, as shown below for values of l/d of 2.5 and 4.0, which correspond to semivertex angles at the tip of the ogive of 22.6 and 14.6°, respectively.

$$\frac{l}{d} = 2.5 \quad \frac{l}{d} = 4.0$$

Using Eq. (3-10),

$$\frac{c_p}{l} = 0.55 \text{ at } M = 1.5 \quad 0.59 \text{ at } M = 1.5$$

$$0.47 \text{ at } M = 3.0 \quad 0.55 \text{ at } M = 3.0$$

Using slender-body theory,^{34,35}

$$\frac{c_p}{l} = 0.46 \quad \frac{c_p}{l} = 0.47$$

and is independent of Mach number. Results from experimental tests indicate that the empirical expression yields results which are more accurate than those derived from the slender-body theory.

Many other investigators¹¹⁻²² have studied the problem of airflow over ogives and general bodies of revolutions. Syvertson and Dennis¹³ developed the second-order shock-expansion method for bodies of revolution near zero lift. This method appears to give results consistently more accurate than those obtained from other theories and is applicable over a wide range of Mach numbers and hypersonic similarity parameters, the latter defined as M/f_n where f_n is the fineness ratio of the nose. The variation of C_N with f_n for ogive-cylinder configuration is shown in Fig. 3-9 using the simplest of the three approximations available.

3-5. HEMISPHERICAL FOREBODY

This type of nose is used on some of the missiles, particularly those which use IF (infrared) seekers. This type of nose imposes an

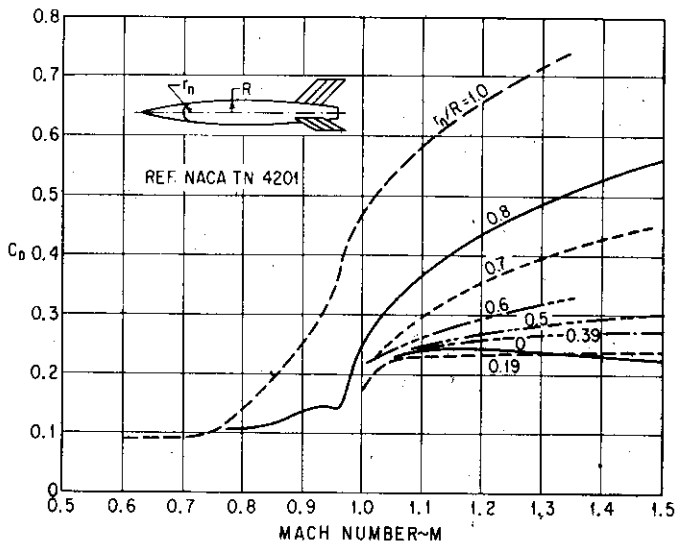


Fig. 3-10. C_D vs. Mach number for rounded-nose parabolic body.

extremely high drag penalty on the missile; i.e., wave drag may be six to seven times that of an ogive (see Fig. 3-10). The use of this

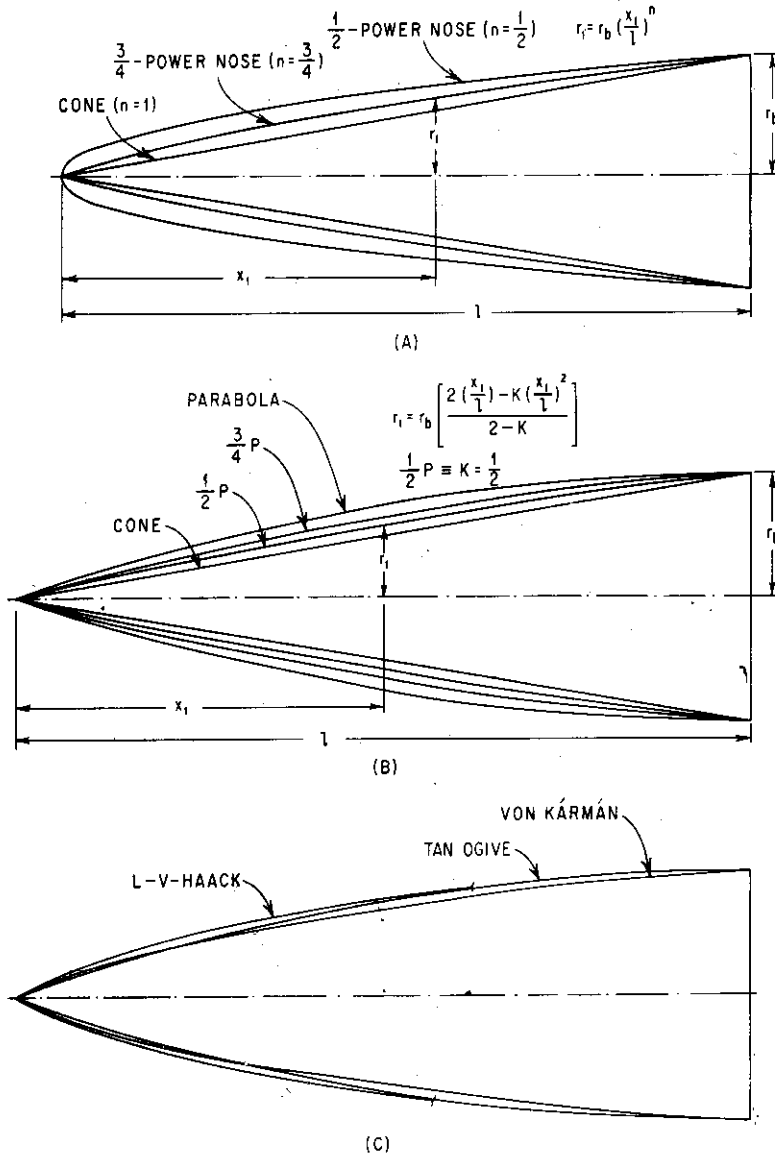


FIG. 3-11. (A) Profiles of fineness ratio, 3 noses—power series. (B) Profiles of fineness ratio, 3 noses—parabolic series. (C) Profiles of fineness ratio, 3 noses—Haack series and tangent ogive.

type of nose on missiles indicates the extent to which an aerodynamicist must compromise to achieve an optimum and feasible missile system.

3-6. OTHER FOREBODY SHAPES

Many other shapes of noses are being used on present-day missiles. The majority of these shapes may be considered as modified ogives. On some missiles, the shape of the nose section may be defined by

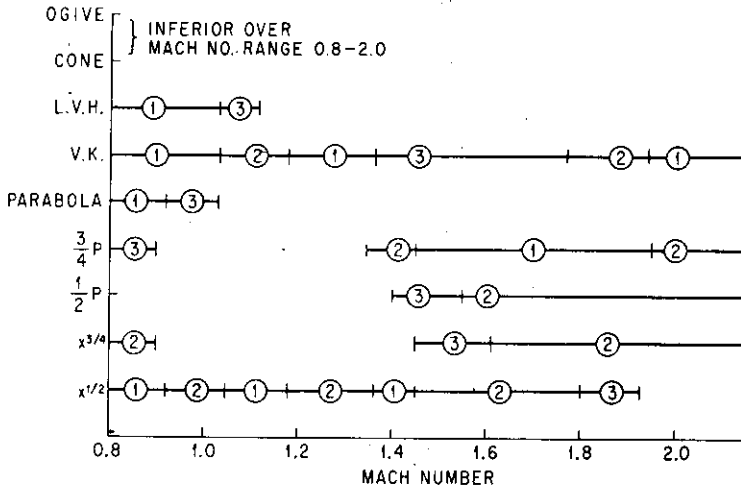


FIG. 3-12. Qualitative drag comparison of nine nose shapes (*l/d* = 3.0). (1) Best (least drag). (2) Better. (3) Good.

some elaborate expression derived purely from radar consideration, i.e., to minimize refraction and radar-beam distortion. For these peculiarly shaped nose sections, the drag may be estimated by mathematical expressions or by “eyeballing” the degree of similarity between the ogive and the shape in question. There are other types of nose shapes which were derived theoretically from aerodynamic drag consideration. Some of these are the “parabolic” or “power-series” noses (see Fig. 3-11). Another well-known one is the “Von Kármán” nose, named after its originator (see Fig. 3-11). The expression for the Von Kármán nose is

$$r = \frac{1}{\sqrt{\pi}} \sqrt{\varphi - (1/2) \sin 2\varphi} \tag{3-12}$$

where $\varphi = \cos^{-1}(1 - 2x)$

The coordinate and expressions for a variety of common nose shapes are included in Appendix B. All these have their best application (drag standpoint) at certain ranges of operating Mach numbers. A qualitative presentation of their applicability is shown in Fig. 3-12. The reader is referred to *NACA Technical Note 4201*, which has a vast collection of zero-lift-drag data on bodies of revolution. This report also contains numerous references which the reader may use to obtain additional data.

Quite frequently the aerodynamicist is asked to determine how much bluntness is acceptable for the nose of a missile, since blunting of the nose is advantageous from the standpoint of realizing better radar tracking characteristics, increasing structural strength, and alleviating the aerodynamic heating problem. The results presented in Fig. 7 of *NACA Technical Note 4201* show the effect of blunting on the drag characteristics at several Mach numbers. It can be said that the nose section may be "rounded off" for r/R values of 0.2 or less, without causing any drag penalty.

3-7. MID-SECTION

In most missile configurations, the mid-section is cylindrical in shape. This shape is advantageous from the standpoints of drag, ease of manufacturing, and load-carrying capability. The zero-lift drag ($\alpha = 0^\circ$) of a cylindrical body is caused by viscous forces (skin friction) only. At low angles of attack, a very small amount of normal force is developed on the body, and this results from the "carry-over" from the nose section. At rather large angles, some amount of normal force is developed because the cross-flow drag acts normal to the body center line. The effect of this viscous cross flow at angle of attack was reported by Allen and Perkins.²² The total normal-force coefficient is approximated by

$$C_N = 2\alpha + C_{D\alpha=90^\circ} \frac{A_p}{S} \alpha^2 \quad (3-13)$$

where A_p = planform area

S = reference area

The effects of mid-section or afterbody extension on the aerodynamic characteristics of conical and ogival nose bodies were systematically investigated experimentally by Buford²³ over a wide range of supersonic Mach numbers. These experimental data show that the effect

of afterbody extension is to increase C_N and move the center of pressure aft as a result of body carry-over and viscous cross-flow effects. It is also noted that Van Dyke's hybrid theory,¹⁹ which combines first- and second-order theories, gives results which are in reasonable agreement with these experimental results.

3-8. BOATTAIL

The tapered portion of the aft section of a body is called the boattail. The purpose of the boattail is to decrease the drag of a body which has a "squared-off" base. The latter feature has relatively large base pressure and, consequently, high drag values because of the large base area. By "boattailing" the rear portion of the body, the base area is reduced and thus a decrease in base drag is realized. However, the decrease in base drag may be partially nullified by the boattail drag.

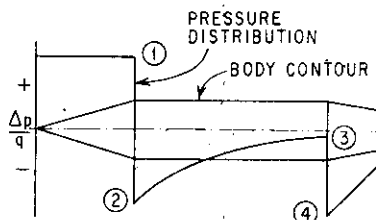


FIG. 3-13. Pressure distribution over body.

Accurate determination of boattail drag is rather difficult because of the dependence on the geometry of the fore and aft portions of the body and real-fluid effects. However, for preliminary design analysis, results from correlation of both theoretical and experimental test data should be used when available. In the absence of experimental test data, the boattail drag may be estimated by theoretical methods. One such method involves the derivation of the pressure distribution over the entire length of the body, as shown schematically in Fig. 3-13. This figure shows the familiar pressure distribution over the forward portions of the body as obtained by the Taylor-Maccoll theory and the Prandtl-Meyer equation for an expansion around a two-dimensional corner, beginning with the Mach number at point 1. The increase in pressure along the cylindrical portion can be approximated by linearized theory²⁴ to obtain the pressure at point 3. The Prandtl-Meyer equation again can be used, as before, to approximate the pressure at point 4. The boattail drag may then be obtained by integrating the pressure shown in Fig. 3-13.

Another method involves the use of the second-order theory¹⁹ to predict the boattail drag. The theoretical pressure distribution and

wave drags for conical boattails were determined with this theory by Jack⁴⁹ using the procedure detailed in *NACA Technical Note 2744*. In his theoretical investigation, he assumed that the boattail was preceded by a cylindrical body section of sufficient length to give uniform flow at the free-stream Mach number at the beginning of the boattail (i.e., free-stream static pressure at point 3 in Fig. 3-13). The results thus obtained appear to be in reasonable agreement with those derived from the theoretical method previously mentioned as well as with experimental test results as shown in Fig. 3-14

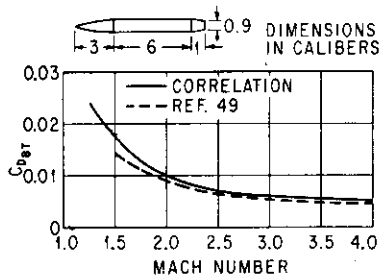


FIG. 3-14. Typical boattail drag coefficient vs. Mach number.

area. Next, the center-of-pressure travel is increased with angle of attack. Hence one must weigh these adverse factors with the drag-saving feature to decide whether or not to use boattail in a particular design. Presumably, no boattail was used on the German V-2 because of the undesirable effect of center-of-pressure travel with angle of attack.

3-9. BASE PRESSURE

At supersonic velocities the base of the body experiences a large negative pressure (relative to ambient or free-stream static pressure) resulting in a substantial increase in missile drag. An accurate determination of this base-pressure coefficient is also quite involved since it depends on many parameters, including boattail angle, Mach number, and boattail length. Chapman,²⁵ in his investigations, concluded that a strictly inviscid-fluid theory could not be employed, and consequently he developed an approximate semi-empirical theory for the real fluid-flow case. Others²⁶⁻²⁹ have

for a typical boattail configuration. For other boattail configurations, the reader is referred to Jack's report, which includes the effects of Mach number, boattail angle, area ratio, and body contours (i.e., boattail shapes).

Although boattailing is generally used, it does have some disadvantages which must be overcome. First, the lift on the boattail is destabilizing, which must be compensated by some increase in tail

analyzed the effects of individual parameters such as Reynolds number, boundary layer, and tail surfaces near the base of the body. The combined effects of several of these important parameters were compiled and correlated with test data with reasonably good success for the power-off condition (i.e., no jet exhausting from the base). For typical applications the base-pressure-coefficient variation with Mach number is shown in Fig. 3-15. The base-pressure drag coefficient C_{D_b} is related to the base-pressure coefficient as follows:

$$C_{D_b} = C_{P_b} \frac{S_b}{S} \quad (3-14)$$

where S_b = base area

S = body cross-sectional area (reference area)

C_{P_b} = base-pressure coefficient

The proper base area must be used in Eq. (3-14). For the power-off condition the total base area is used, whereas with power on, only that portion of the base shown in Fig. 3-16 is used.

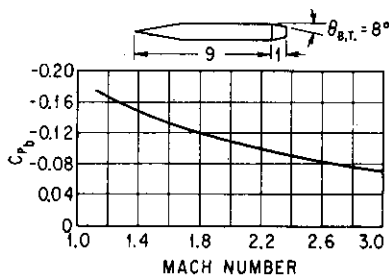


FIG. 3-15. Typical base-pressure coefficient vs. Mach number.

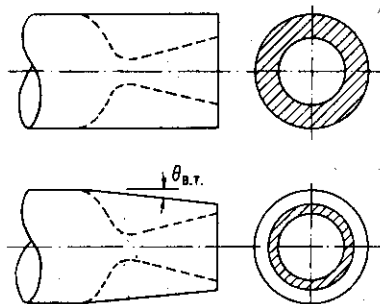


FIG. 3-16. Effective base area.

The base pressure is markedly changed by the presence of a jet emitting from the rocket motor. Limited unclassified data³⁰⁻³³ are available to determine the effects of different jet parameters such as jet pressure ratio (jet static to free-stream static pressure), nozzle angle, and base diameter. However, most of the results on jet effects on base pressure are classified, and they must be analyzed before an accurate determination of these effects can be made.

3-10. SUMMARY OF CHARACTERISTICS OF BODIES OF REVOLUTION

In summing up the aerodynamic characteristics of the complete body, the following general observations are noted:

1. The drag of the body at supersonic speeds is dependent primarily on the nose shape and the amount of boattailing.
2. Base drag is greatly affected by the presence of the jet.
3. The majority of the body lift is on the nose section of the body with a small down load on the boattail.
4. The resultant center of pressure for a conventional body varies from between 15 and 20 per cent of the body length at low angles of attack. At higher angles of attack the center of pressure of the complete body can move forward or aft of the nominal center-of-pressure location, depending on the amount of boattailing.
5. For moderate boattailing, say 7° , the center of pressure tends to shift rearward with angle of attack.
6. The nose may be "rounded off" to a value of r/R of 0.2 or less without causing any drag penalty.
7. For preliminary analysis the value of complete body C_{N_α} may be assumed to be 0.03 to 0.04 per degree for a wide range of subsonic and supersonic Mach numbers.

3-11. GENERAL AERODYNAMICS OF AIRFOIL

The next major important item in the aerodynamic missile configuration is the wing or main lifting surface. A quick glance at the various missile configurations indicates that a great variety of wing planforms or configurations are used. Undoubtedly, the wing configuration for each of these missiles was selected after detailed analyses had been conducted to optimize the configuration to the requirements of each of the complete missile weapon systems. To help in understanding the logic behind the selection of a given configuration design, the following sections are devoted to a brief discussion of the aerodynamics of different wing configurations, including the effects of airfoil section, wing planform, aspect ratio, and wing area. It is beyond the scope of this book to treat the subject of supersonic wing theory; the reader is therefore referred to the listing of the numerous reports on this subject at the end of this chapter.³⁶⁻⁴³

Perhaps one of the most useful and well-known theories used in supersonic flow over wings is the linearized theory. This theory,

derived from the exact differential equation of steady compressible flow, has the basic assumption that the body or airfoil is very thin. Other basic assumptions include the requirements that (1) the shock wave is attached to the airfoil and (2) the flow is two-dimensional, i.e., the air is deflected in only one plane perpendicular to the direction of flow. Using this simplified linear analysis, the value of $\Delta p/q$ is given:

$$\frac{\Delta p}{q} = \frac{2\delta}{\sqrt{M^2 - 1}} \quad (3-15)$$

where δ is the wedge semivertex angle, in radians. The above equation is the well-known "first-order," "linear," or "Ackeret" theory for two-dimensional flow.³⁸ Busemann⁴⁰ derived higher-order terms as constants in a series expansion as

$$\frac{\Delta p}{q} = C_1\delta + C_2\delta^2 + C_3\delta^3 + C_4\delta^4 + \dots \quad (3-16)$$

where C_1, C_2, \dots are known as Busemann constants and are defined as

$$C_1 = \frac{2}{\sqrt{M^2 - 1}} \quad (3-16a)$$

$$C_2 = \frac{2(3M^4 - 5M^2 + 5)}{5(M^2 - 1)^2} \quad (3-16b)$$

$$C_3 = \frac{10}{375(M^2 - 1)^{7/2}} (15M^8 - 68M^6 + 150M^4 - 75M^2 + 50) \quad (3-16c)$$

$$C_4 = \frac{1}{750(M^2 - 1)^5} (60M^{12} - 558M^{10} + 2,222M^8 - 2,870M^6 + 4,200M^4 - 500M^2 + 500) \quad (3-16d)$$

The above constants are for the case of an expansion wave (δ is negative) for air ($\gamma = 1.4$). For an oblique compressive wave, Eq. (3-16) becomes

$$\frac{\Delta p}{q} = C_1\delta + C_2\delta^2 + C_3^*\delta^3 + C_4^*\delta^4 + \dots \quad (3-17)$$

where

$$C_3^* = \frac{1}{75(M^2 - 1)^{7/2}} (27M^8 - 112M^6 + 270M^4 - 150M^2 + 100) \quad (3-18)$$

$$C_4^* = \frac{1}{10(M^2 - 1)C_1} [9M^2C_1(C_1C_3^* + C_2^2) - 10(M^2 - 1) \times C_2C_3^* - 14M^2C_1C_2 + \frac{4}{3}(3M^2 - 5)(3C_3^* - C_1)] \quad (3-19)$$

The numerical values of C_1 , C_2 , C_3 , and C_3^* are tabulated in Table 3-1 and plotted in Fig. 3-17.

Since the normal force on a wing is the result of difference in pressure between the upper and lower surfaces the normal-force

TABLE 3-1. BUSEMANN'S CONSTANTS

For $\gamma = 1.4$

M	C_1	C_2	C_3	C_3^*
1.2	3.015	8.307	54.03	53.22
1.4	2.041	2.919	5.80	6.13
1.6	1.601	1.950	1.937	2.153
1.8	1.336	1.618	1.144	1.280
2.0	1.155	1.467	0.934	1.016
2.5	0.873	1.320	0.943	0.947
3.0	0.707	1.269	1.112	1.155
3.5	0.596	1.245	1.309	1.387
4.0	0.516	1.232	1.513	1.621
4.5	0.456	1.224	1.719	1.854
5.0	0.408	1.219	1.925	2.086

coefficient may easily be derived. For the "first-order" linear theory the normal force is given by

$$N = (\Delta p_L - \Delta p_U)S_W \quad (3-20)$$

$$C_N = \frac{N}{qS_W} = \left(\frac{\Delta p}{q}\right)_L - \left(\frac{\Delta p}{q}\right)_U = \frac{2\delta}{\sqrt{M^2 - 1}} - \frac{-2\delta}{\sqrt{M^2 - 1}} = \frac{4\delta}{\sqrt{M^2 - 1}} \quad (3-20a)$$

For the two-dimensional wing of zero thickness the normal-force coefficient is thus

$$C_N = \frac{4\alpha}{\sqrt{M^2 - 1}} \quad (3-21)$$

$$\text{or} \quad C_{N_\alpha} = \frac{4}{\sqrt{M^2 - 1}} \equiv \frac{4}{\beta} \quad (3-22)$$

Thus the normal-force-curve slope of a wing in supersonic flow is characterized by a decrease in C_N with increasing Mach number. This is in contrast to the variation in subsonic flow where C_{N_α} varies approximately inversely as $\sqrt{1 - M^2}$, known as the Prandtl-Glauert factor.

Using a second-order degree of accuracy, the value of C_N for a two-dimensional airfoil of symmetrical double-wedge shape can readily be derived. For this condition Eq. (3-16) is reduced to

$$\frac{\Delta p}{q} = C_1 \theta + C_2 \theta^2 \quad (3-23)$$

The angle θ in Eq. (3-23) is the total local angle between the wing surface and free-stream direction. From Fig. 3-18 the values of the four regions of flow over the airfoil are

$$\begin{aligned} \theta_1 &= -\alpha + \delta & \theta_2 &= -\alpha - \delta \\ \theta_3 &= \alpha + \delta & \theta_4 &= \alpha - \delta \end{aligned} \quad (3-24)$$

By substituting Eq. (3-24) in Eq. (3-23) the pressure differential (between upper and lower surfaces) for the forward and aft sections of the airfoil as shown in Fig. 3-18 may be written as

$$\begin{aligned} \left(\frac{\Delta p}{q}\right)_F &= \left(\frac{\Delta p}{q}\right)_3 - \left(\frac{\Delta p}{q}\right)_1 = 2C_1\alpha + 4C_2\alpha\delta \\ \left(\frac{\Delta p}{q}\right)_A &= \left(\frac{\Delta p}{q}\right)_4 - \left(\frac{\Delta p}{q}\right)_2 = 2C_1\alpha - 4C_2\alpha\delta \end{aligned} \quad (3-25)$$

The normal force is the total pressure difference between the upper and lower surfaces

$$N = \left[\left(\frac{\Delta p}{q}\right)_F + \left(\frac{\Delta p}{q}\right)_A \right] S \quad (3-26)$$

where S = twice the planform area S_W . The value of C_N is thus

$$C_N = \frac{N}{qS_W} = 2C_1\alpha \quad (3-27)$$

or

$$C_{N\alpha} = 2C_1 = \frac{4}{\sqrt{M^2 - 1}} \equiv \frac{4}{\beta} \quad (3-28)$$

which is identical to the "first-order" linear theory by Ackeret for a two-dimensional airfoil of zero thickness. The value of $C_{N\alpha}$ determined by Eq. (3-27) is valid for only low angles of attack. At higher angles of attack this second-order theory must be replaced by the "exact" theory.^{42,43} However, for preliminary design analysis Eqs. (3-27) and (3-28) may be used for α up to approximately 10° .

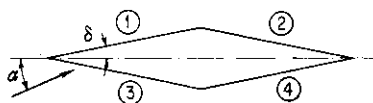


FIG. 3-18. Regions of flow—double-wedge airfoil at an angle of attack.

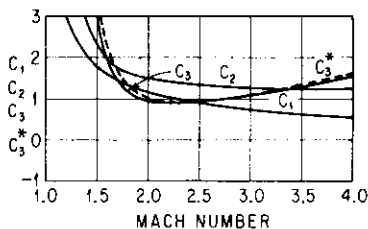


FIG. 3-17. Busemann's constants ($\gamma = 1.4$).

The form or pressure drag is the component of the pressure force in the chordwise direction at $\alpha = 0^\circ$. The pressure differential between the upper and lower surfaces may be written as

$$\begin{aligned} \left(\frac{\Delta p}{q}\right)_U &= \left(\frac{\Delta p}{q}\right)_1 - \left(\frac{\Delta p}{q}\right)_2 = 2C_1\delta - 4C_2\alpha\delta \\ \left(\frac{\Delta p}{q}\right)_L &= \left(\frac{\Delta p}{q}\right)_3 - \left(\frac{\Delta p}{q}\right)_4 = 2C_1\delta + 4C_2\alpha\delta \end{aligned} \quad (3-29)$$

The total pressure-drag coefficient is obtained by

$$C'_{D_f} = \frac{1}{2} \left[\left(\frac{\Delta p}{q}\right)_U + \left(\frac{\Delta p}{q}\right)_L \right] = 2C_1\delta = \frac{4\delta}{\sqrt{M^2 - 1}} = \frac{4\delta}{\beta} \quad (3-30)$$

On the basis of wing planform area,

$$C_{D_f} = \frac{4\delta^2}{\beta} \quad (3-31)$$

It can be seen that the wave drag of the airfoil varies as the thickness squared. Hence, in designs which require relatively large wings the thickness must be kept to a minimum to reduce the form-drag contribution.

The drag due to normal force is readily determined as follows:

$$C_{D_N} = C_N \sin \alpha \cong C_N \alpha = \frac{4\alpha^2}{\beta} = \frac{C_N^2}{C_{N\alpha}} \quad (3-32)$$

The center of pressure of a two-dimensional airfoil is at the mid-chord when the first-order linear theory is used. However, second-order linear theory must be used to obtain a more accurate center-of-pressure value. This is done first by obtaining an expression for the pitching-moment coefficient about the mid-chord $C_{m_{0.5}}$ and dividing by the normal-force coefficient C_N as shown below.

$$\begin{aligned} C_{m_{0.5}} &= \frac{M_{0.5}}{qSC} = C_N \frac{x}{C} = \left[\left(\frac{\Delta p}{q}\right)_F x_F - \left(\frac{\Delta p}{q}\right)_A x_A \right] \frac{1}{2C} \\ &= \frac{1}{2C} 0.25C(2C_1\alpha + 4C_2\alpha\delta) - 0.25C(2C_1\alpha - 4C_2\alpha\delta) \\ &= C_2\alpha\delta \end{aligned} \quad (3-33)$$

$$cP_{0.5} = \frac{C_{m_c}}{C_N} = \frac{C_2c\delta}{2C_1} \quad (3-34)$$

ahead of the mid-chord.

The above discussion has been restricted to the most simple and approximate methods for the determination of two-dimensional airfoil characteristics. Other more elaborate methods^{42,43} are available when more accurate results are desired. The latter methods involve stepwise application of the known relations for the compression through the shock wave and the expansion around a convex corner. This procedure is usually termed the "shock-expansion" method.

In most practical designs, finite-aspect-ratio wings and wings with planform other than rectangular are of interest. These features will be discussed in the following sections.

3-12. ASPECT RATIO

The above section dealt with the aerodynamic characteristics of two-dimensional airfoils, i.e., wings of infinite span or aspect ratio. In most practical cases three-dimensional airfoils are employed. In the study of airfoils in three-dimensional flow the concept of the Mach cone, a fundamental result of the linear theory, is employed. According to this concept (see Fig. 3-19) the effect of a given disturbance is felt only within the interior of a circular cone whose vertex is located at the point of disturbance and whose axis extends downstream parallel to the free-stream flow direction. The geometry of the cone is determined by the requirement that the component of the free-stream velocity normal to the surface of the cone be equal to the speed of sound in the undisturbed stream. Hence the semivertex angle of the cone is a function of the free-stream Mach number only and is given by Eq. (3-35) by inspection of Fig. 3-19.

$$\mu = \sin^{-1} \frac{c}{V} = \sin^{-1} \frac{1}{M} \quad (3-35)$$

where c = speed of sound

V = free-stream velocity

For a rectangular wing of finite aspect ratio, there will be a loss of pressure at the tips because air flows from the lower surface onto the upper surface as a result of pressure differences. These tip losses are similar in nature to those realized in subsonic-flow phenomena except that in the supersonic case these tip losses are restricted to the shaded area in Fig. 3-20. Thus it is readily apparent that the effect of aspect ratio is to decrease the over-all lift or normal-force slope of the wing. The pressure within this conical area of influence is

constant along any line radiating from the vertex of the cone created by the leading edge and wing tip and is determined^{44,45} to be

$$\frac{p - p_1}{p_\infty - p_1} = \frac{2}{\pi} \sin^{-1} \sqrt{\frac{\tan \mu'}{\tan \mu}} \quad (3-36)$$

where p = pressure at any point

p_∞ = two-dimensional value at limit of Mach cone

p_1 = free-stream static pressure

μ' = angle of any ray radiating from wing tip (see Fig. 3-21)

The variation of this pressure (loss) at the wing tip is shown in Fig.

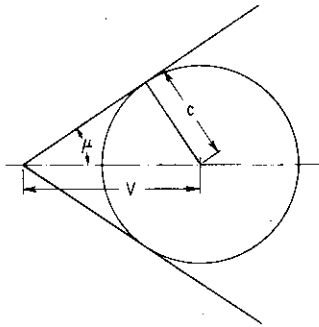


FIG. 3-19. The "Mach triangle."

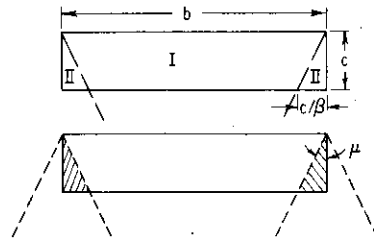


FIG. 3-20. Tip effects.

3-21. The resultant spanwise pressure distribution is shown in Fig. 3-24. Evvard⁴⁶ showed that the loss of lift due to the tips is exactly half the two-dimensional value, which yields essentially the same tip loss as calculated by Eq. (3-36) but differs slightly in the exact nature of the pressure distribution (see Fig. 3-21). Using Evvard's result, the effects of aspect ratio (i.e., tip loss) on the aerodynamic characteristics of a rectangular wing can be readily determined below.

From Fig. 3-20 it can be seen that the value of C_N for area I is given by the two-dimensional value [Eq. (3-21)].

$$C_{N_I} = \frac{4\alpha}{\beta} \quad (3-37)$$

The value of C_N at the tip sections II is

$$C_{N_{II}} = \frac{1}{2} C_{N_I} = \frac{2\alpha}{\beta} \quad (3-38)$$

The total value of C_N based on total wing area bc is therefore given by

$$C_N = \frac{4\alpha}{\beta} \frac{A_I - 2A_{II}}{A_I + 2A_{II}} + \frac{1}{2} \frac{4\alpha}{\beta} \frac{2A_{II}}{A_I + 2A_{II}} \quad (3-39)$$

Since $A_{II} = \frac{c^2}{2\beta}$ $A_I = bc - \frac{c^2}{\beta}$

Therefore, Eq. (3-39) becomes

$$C_N = \frac{4\alpha}{\beta} \frac{bc - c^2/\beta}{bc} + \frac{1}{2} \frac{4\alpha}{\beta} \frac{c^2/\beta}{bc} \quad (3-40)$$

or
$$C_N = \frac{4\alpha}{\beta} \left(1 - \frac{c}{2\beta b}\right) \quad (3-41)$$

Since $A = b/c$, Eq. (3-41) becomes

$$C_N = \frac{4\alpha}{\beta} \left(1 - \frac{1}{2A\beta}\right) \quad (3-42)$$

or
$$C_{N\alpha} = \frac{4}{\beta} \left(1 - \frac{1}{2\beta A}\right) \quad (3-43)$$

Equation (3-43) shows quantitatively the detrimental effect of aspect ratio on the normal-force-curve slope. Consequently "raked tips" (see Fig. 3-25) are sometimes used to reduce the effect of aspect ratio or tip losses. These tip losses may be completely eliminated by cutting the tips at an oblique angle equal to or somewhat greater than the Mach angle. In this case the flow over the entire wing will again be completely two-dimensional.

It is usually more convenient to use the "effective aspect ratio," defined as βA , as a common parameter. For example, the effective aspect ratio of a wing at geometric aspect ratio 3 traveling at Mach 2 is 5.2. For this case the value of $C_{N\alpha}$ is approximately 90 per cent of the two-dimensional value as shown in Fig. 3-22.

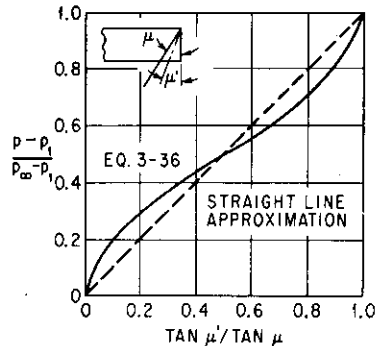


FIG. 3-21. Pressure loss due to tip effects.

By taking moments about the wing leading edge and dividing by the total force given by Eq. (3-43) the center of pressure may be shown to be

$$\frac{cp}{c} = \frac{\beta A - 2/3}{2\beta A - 1} \quad (3.44)$$

The variation of center of pressure for a rectangular wing of finite aspect ratio in supersonic flow as derived by linearized theory [Eq. (3-44)] is shown in Fig. 3-23. Since the pressure is decreased in the

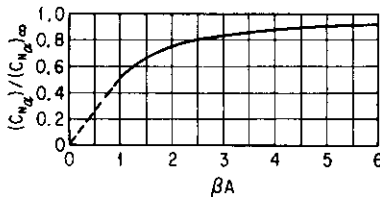


FIG. 3-22. Effect of βA on C_{N_α} —thin rectangular wing.

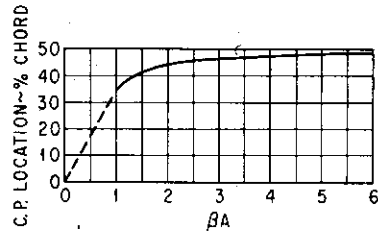


FIG. 3-23. Effect of βA on center-of-pressure location—thin rectangular wing.

region near the tips the drag of a rectangular wing of finite aspect ratio must be corrected as follows:

$$C_D = \frac{4\delta^2}{\beta} \left(1 - \frac{1}{2\beta A} \right) \quad (3.45)$$

By combining Eqs. (3-22) and (3-43) it can be shown that the drag due to normal force is given by

$$C_{D_N} = \frac{4\alpha^2}{\beta} \left(1 - \frac{1}{2\beta A} \right) \quad (3.46)$$

Equation (3-46) indicates that the effect of decreasing aspect ratio is to decrease the magnitude of the induced drag. This is in direct contrast to the case of subsonic flow, as will be shown in a later section. It is also noted that in supersonic flow induced drag is realized with an infinite-aspect-ratio wing, whereas in the subsonic case the induced drag is zero.

Strictly speaking, Eqs. (3-43) through (3-46) are derived for a flat plate (i.e., airfoil of zero thickness). The effect of airfoil thickness

will be discussed in a later section. It has been shown⁴⁷ that the value of $C_{N\alpha}$ calculated by linear theory [Eq. (3-43)] agrees quite closely with experimental data.⁴⁸ However, the chordwise pressure distribution in the two-dimensional-flow region (i.e., area I in Fig. 3-20) determined by linearized theory is noticeably different from that measured from tests particularly in the aft section of the wing, where the pressure over the upper surface is markedly lower than that predicted by theory. This discrepancy in pressure distribution may be attributed to airfoil thickness and viscous or real-fluid effects, the latter of which was assumed to be negligible in the linearized theory. As a consequence of the discrepancy in the afore-mentioned pressure distributions, the center of pressure calculated by Eq. (3-44) will be slightly forward of the actual value. In addition, the wave drag calculated by Eq. (3-45) will be lower than the actual drag, which includes viscous effects (i.e., interaction between the oblique wave and viscous boundary layer, flow separation, etc.). However, since the values of the normal-force-curve slope are in close agreement with test results, the induced drag predicted by theory [Eq. (3-46)] is generally satisfactory^{47,55} for wings with rectangular planform as well as for wings of other planforms with supersonic leading edges, a condition in supersonic flow which will be discussed in the next section.

It should be noted that Eq. (3-43) is restricted to cases where the Mach cones from the tips of the wing do not intersect each other. Hence the limiting aspect ratio is $1/\beta$. For relatively low aspect ratio or low-Mach-number flight conditions, the Mach lines from the two tips will intersect on the wing surface, resulting in an area which is influenced by both forward-tip effects as shown in Fig. 3-24. In this area, IV, the pressure decreases due to the two waves are additive and result in a substantial loss in lift. As shown in Fig. 3-24D, the length of ad equals the sum of ac and ab (i.e., $ab = cd$). The value of

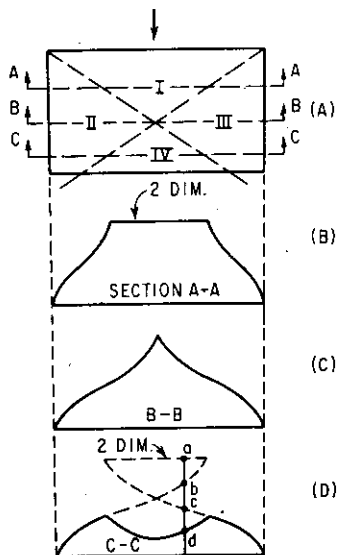


FIG. 3-24. Tip effects on low-aspect-ratio rectangular wing.

C_{N_α} for this condition of low-aspect-ratio Mach number is derived below.

$$C_{N_\alpha} = \left[\frac{4}{\beta} A_T - \frac{2}{\beta} (A_{II} + A_{IV}) - \frac{2}{\beta} (A_{III} + A_{IV}) \right] \frac{1}{A_T} \quad (3-47)$$

$$C_{N_\alpha} = \left[\frac{4}{\beta} (A_I + A_{II} + A_{III} + A_{IV}) - \frac{2}{\beta} (A_{II} + A_{III} + 2A_{IV}) \right] \frac{1}{A_T} \quad (3-47a)$$

or
$$C_{N_\alpha} = \frac{2}{\beta} \frac{2A_I + A_{II} + A_{III}}{A_T} \quad (3-48)$$

where A_T = total wing planform area.

For a given missile configuration design the aspect ratio of the aerodynamic lifting surface is primarily dependent upon the following requirements:

1. Load factor or maximum trimmed lift
2. Wing area
3. Trim angle of attack
4. Lift-to-drag L/D ratio
5. Maximum permissible span

In general, when the maneuverability and range requirements are high, it is advantageous to use a relatively large aspect ratio since the normal-force-curve slope is improved. This results in a reduction in both wing areas and trimmed angle of attack required. In addition, a higher maximum lift-to-drag ratio is realized with a high-aspect-ratio wing since $(L/D)_{\max}$ is proportional to the square root of the lift-curve slope (for a supersonic leading edge) as given below.

$$\left(\frac{L}{D} \right)_{\max} = \frac{1}{2\sqrt{C_{D_0}}} \sqrt{\frac{C_{N_\alpha}}{C_{D_0}}} \quad (3-49)$$

Equation (3-49) will be derived in Appendix C.

In some cases the optimum aspect ratio as determined from purely aerodynamic considerations must be compromised and reduced because of maximum span limitation or severe structural

loading problems. In summary the effects of increasing aspect ratio are as follows:

1. Increase $C_{N\alpha}$, C_{D_0} .
2. Increase $(L/D)_{\max}$.
3. Increase span
4. Reduce trim angle of attack
5. Reduce wing area
6. Increase structural weight
7. Negligible effect on center-of-pressure travel for $\beta A > 2$

3-13. WING PLANFORM

In addition to the basic straight-wing planform discussed in the previous section two other basic wing planforms are often used: delta and swept-back wings. There are many variations of these

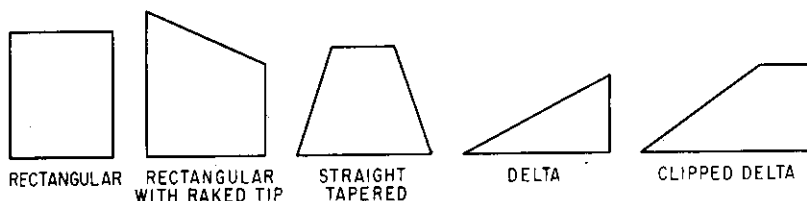


FIG. 3-25. Typical supersonic wing planforms.

three basic planforms, as shown in Fig. 3-25, each optimized for its particular application. Many advantages and disadvantages are associated with each of the three basic planforms used. Consequently a thorough study involving their aerodynamic efficiency, structural weight, and cost of manufacturing must be made before the best planform can be determined. In this section the aerodynamic characteristics of the delta and swept-back planforms are discussed and compared qualitatively with the straight-wing planform in order to provide the engineer a "feel" for selecting a wing planform.

In the analysis of wings of arbitrary planform it is important to know whether the leading (and trailing) edge is "subsonic" or "supersonic" since the pressure distribution is markedly different for each condition. The leading edge is termed "supersonic" if the normal component of the free-stream Mach number is supersonic,

i.e., leading edge ahead of the Mach line as shown in Fig. 3-26. Mathematically, a supersonic leading edge exists when $\mu < \epsilon$ where ϵ is the leading-edge angle. Other edge conditions are shown in Fig. 3-26. The theoretical pressure in the region behind a supersonic leading edge and ahead of the Mach angle increases from the two-dimensional value for no sweep [defined by Eq. (3-15)] to a value of infinity when the leading-edge sweep angle and the complement of the Mach angle are equal (i.e., a sonic leading edge). The equation for this pressure variation is given as

$$\frac{\Delta p}{q} = \frac{2\delta}{\beta\sqrt{1-n^2}} \quad (3-50)$$

where $n = k/\beta$ as shown in Fig. 3-26. As the leading-edge sweep angle is further increased a "subsonic" leading-edge condition exists and the theoretical pressure at the edge has an infinite value.

Based on the conical-flow theory first conceived by Busemann, the theoretical aerodynamic characteristics of delta or triangular wings have been studied extensively by many authors.⁵⁰⁻⁵⁴ References 6 and 50 through 54 are recommended to the reader for a

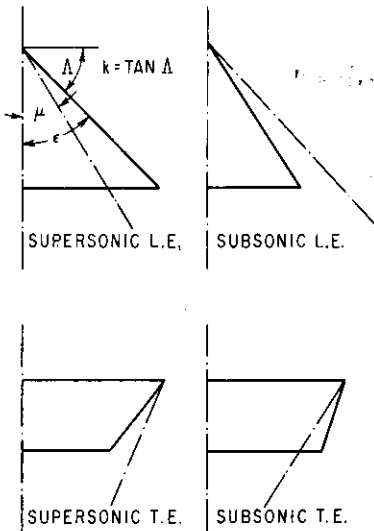


FIG. 3-26. Edge conditions.

complete treatment of this type of wing planform. For wings of arbitrary planform ref. 6 is also highly recommended. Based on the work of refs. 50 to 54 the normal-force-curve slope of the delta wing with a supersonic leading edge is shown to have the two-dimensional value of $4/\beta$. For the case of a subsonic leading edge the value becomes

$$C_{N_\alpha} = \frac{2\pi \tan \epsilon / \tan \mu}{E\beta} \quad (3-51)$$

where E is the elliptic integral of the second kind for

$$\sqrt{1 - (\tan \epsilon / \tan \mu)^2}$$

and ϵ is the triangular-wing semivertex angle shown in Fig. 3-27.

In Fig. 3-27 the ratio of $C_{N\alpha}$ to the theoretical two-dimensional value $4/\beta$ is plotted against the parameter $\tan \epsilon/\tan \mu$. Results from an extensive and systematic series of experimental tests⁵⁵ indicate that the theoretical values of $C_{N\alpha}$ are reasonably accurate for values of $\tan \epsilon/\tan \mu$ of 0.6 or below. Above this value the linear theory yields values of $C_{N\alpha}$ substantially higher than those obtained from experiment except at very large values of $\tan \epsilon/\tan \mu$. For design purposes it is recommended that experimental values of $C_{N\alpha}$ of ref. 55 be used in lieu of theoretical values. The experimental results also show that the center of area is a good approximation of the center of pressure for both subsonic and supersonic leading-edge conditions.

The effect of sweepback for a two-dimensional airfoil can be shown theoretically to be somewhat beneficial from the standpoint of improving the value of $C_{N\alpha}$ and reducing the wave drag.

Since the pressure acting on the surface is a function of the component of Mach number normal to the leading edge instead of the free-stream Mach number (i.e., $M \cos \Lambda$, where Λ is the sweep angle), the value of $C_{N\alpha}$ for the two-dimensional swept-back wing may be written as

$$(C_{N\alpha})_{\Lambda} = \frac{4 \cos \Lambda}{M^2 \cos^2 \Lambda - 1} \quad (3-52)$$

The form or wave drag may be shown to be reduced by the following factor:

$$\frac{\cos^3 \Lambda}{\sqrt{M^2 \cos^2 \Lambda - 1}}$$

Extensive experimental investigations have been conducted to determine and compare the aerodynamic characteristics of the three basic planforms (i.e., straight, delta, and swept-back wings) of finite aspect ratios for practical applications. For most preliminary designs sufficient test data and correlation of these data are available^{47,55} to evaluate the quantitative effects of planform systematically, taking into account such factors as Reynolds number and viscous fluid which are not included in the theoretical values. A

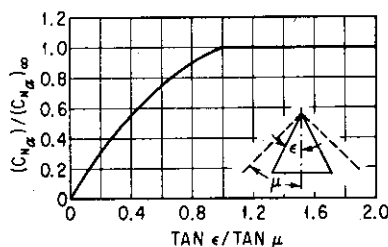


FIG. 3-27. Normal-force characteristics for delta wings.

qualitative summary based on the combined theoretical and experimental results is presented below as a guide in the selection of wing planform for design purposes. Again it must be emphasized that a thorough study involving the important factors previously mentioned (i.e., aerodynamic efficiency, structural weight, cost of manufacturing, etc.) must be conducted before the optimum planform can be determined.*

3-14. AIRFOIL SECTIONS

Since the pressure over an airfoil is primarily a function of the angle between the free-stream air direction and the surface, as previously shown, the airfoil shape or section for supersonic application is noticeably different from those sections used in the subsonic region. In general, sharp-nosed symmetrical airfoil sections of the double-wedge, modified double-wedge, or biconvex variety shown in Fig. 3-28 result in the most efficient aerodynamic design. While a sharp leading edge is desirable from the standpoint of maintaining shock attachment, thereby reducing the magnitude of the wave drag and adverse pressure gradient (conducive to separated flow), it is often necessary to round off the nose of the airfoil to minimize the aerodynamic heating effect as well as provide structural integrity to the section. From theoretical considerations a symmetrical section

* As a matter of interest to the reader, many articles written on the selection of a particular type of wing planform over the past several years may be found in the following issues of *Aviation Week*: Mar. 21, 1949; Aug. 16, 1948; Dec. 20, 1948; July 4, 1949; Sept. 17, 1951; Sept. 22, 1952; Oct. 20, 1952; Dec. 7, 1953; June 24, 1957; and July 15, 1957. Although these articles are primarily concerned with the selection of wings for manned aircraft, the fundamental problems involved in guided missile design are similar.

Supersonic aerodynamic characteristics	Wing planform		
	Straight	Delta	Swept-back
$C_{N\alpha}$	High	Low	Avg
C_{D_0}	High	Low	Avg
$(L/D)_{max}$	Low	High	Avg
C_{D_i}	Low	High	Avg
$C_{L_{max}}$	Not noticeably affected by planform ⁶⁰		
cp travel, % MAC	Large	Avg	Small
Aeroelastic effect	Small	Avg	Large

offers the minimum wave drag, but because of real (viscous) fluid effects previously mentioned, minimum wave drag is not always realized on a symmetrical section especially for the case of a relatively thick airfoil section where the linearized theory becomes less accurate.

In the final selection of airfoil shape, one must consider also the structural efficiency and manufacturing cost as well as its aerodynamic efficiency. From the latter standpoint the double wedge has the lowest drag for a given thickness ratio whereas the biconvex section has the lowest drag per unit strength.⁶ From the manufacturing standpoint the modified double wedge is preferred, where solid sections are involved, since it is easier to machine. As mentioned previously, the sharp leading (and trailing) edges may have to be rounded to provide local structural integrity as well as to minimize the aerodynamic heating effects. Generally speaking, the biconvex should be used on large wings which are not solid sections and modified double wedge should be used for smaller-sized solid wings.

The effects of blunting the trailing edge on the lift and drag characteristics of the airfoil have been investigated by many authors,⁵⁶⁻⁵⁹ notably by Chapman. The latter⁵⁶ showed that a properly designed airfoil with moderately blunt trailing edge resulted in a substantial drag reduction over a double-wedge airfoil of equal section modulus. In addition, beneficial increases in lift-curve slope and maximum L/D were obtained. The stability of the missile (or aircraft) may be improved by the use of blunt-trailing-edge wings or control surfaces since the tendency for flow separation at the aft section is minimized (i.e., adverse pressure build-up is reduced).

3-15. WING AREA

The size of the wing of a missile may be dictated by the following three important considerations:

1. Range and maneuverability requirements
2. Types of design
3. Compatibility with subsystem operation.

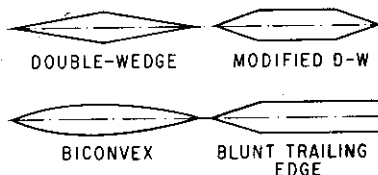


FIG. 3-28. Typical supersonic airfoil sections.

Case 1 may result in two vastly different wing sizes, depending on whether range or maneuverability is the primary factor. In the case of a long-range missile which is designed to cruise at relatively high altitudes, a relatively large wing is required to provide the desired maximum L/D . For this design the wing area is optimized when the induced drag is equal to the drag at zero lift, i.e., $C_{D_i} = C_{D_0}$ or $C_D = 2C_{D_0}$. It will be shown in Appendix C that, when this condition is realized, maximum L/D is obtained. For preliminary design studies the optimum wing area may be determined by calculating the values of C_{D_0} and C_{D_i} for three different wing sizes and determining the wing area which satisfies the condition of $C_{D_0} = C_{D_i}$. However, if maneuverability is the primary concern, which is generally the case for very short range guided missiles, the wing size will be dictated from stability and control considerations. In this case the wing area and location will be such that adequate trim load factor (defined as ratio of trim normal force to missile weight) is realized. In addition, a positive stability margin and good damping characteristics are desired in order to minimize control-system complexity. For example, consider the design of a wing of a canard-control configuration (see Fig. 2-2) designed for short range and a relatively large degree-of-maneuverability requirement. For a given fixed-wing location, too large a wing area may result in a configuration which has an excessive stability and hence may be unsatisfactory since (1) it does not meet the maneuverability requirement or (2) it requires increased canard size and hence larger and heavier servos to obtain the desired load factor. On the other hand, if the wing area is too small the design configuration may be intolerably unstable or have too low a stability margin.

The type of design also has strong influence on the wing size. For example, a wing-control design generally requires a smaller wing area than a tail-control configuration since the lift due to wing deflection for the former design is in the same direction as the main lifting force, as noted in Chap. 2. The size of the wing may also be governed by the operational requirement of the subsystem of the missile. Perhaps one of the most predominant requirements is the low trim angle of attack desired from the standpoint of inlet efficiency or radar-seeker operation. To meet this requirement the size of the wing may be larger than that required to obtain maximum L/D . In addition, a relatively large wing may be required to obtain a relatively low stall speed, particularly for missiles which are accelerated to flying speeds from a stationary ground launcher, thus reducing the size of the (external)

booster required. For this case the wing area may be determined by the following equation:

$$S = \frac{2W}{\rho V_s^2 C_{L_{\max}}} \quad (3-53)$$

where S = wing area required

W = weight of missile at end of boost (excluding weight of booster case if latter is detachable)

V_s = stall speed (or incremental speed due to booster)

$C_{L_{\max}}$ = maximum lift coefficient

The method of computing the incremental speed will be outlined in Chap. 4. In general it is desirable to accelerate the missile to a speed slightly above V_s or to increase the wing area slightly to reduce the size of the booster required.

3-16. SUBSONIC CHARACTERISTICS OF AIRFOIL

Before leaving the subject of wing and lifting surfaces, it may be of interest to mention some of the more important aerodynamic characteristics of the wing at subsonic and high subsonic speeds. In the above discussion, it was stated that the pressure or wave drag of the wing (or nose of the missile) constitutes the majority of the total drag and is a function of the shape (leading-edge angle) of the aerodynamic surface. In subsonic flow, the friction drag is over 90 per cent of the total drag force and is primarily a function of the type of flow (laminar or turbulent) and the total wetted area.

The equation for the skin-friction coefficient of a flat plate in laminar flow (known as Blasius's equation), derived from the Navier-Stokes differential equation of the motion of a viscous fluid, is

$$C_f = \frac{1.328}{\sqrt{\text{Re}}} \quad (3-54)$$

where C_f = skin-friction coefficient based on wetted area

Re = Reynolds number ($\rho VL/\mu \equiv VL/\nu$)

ρ = density of air, slug/ft³

V = free-stream velocity, fps

μ = viscosity of air, slug/ft-sec

ν = kinematic viscosity of air μ/ρ , ft²/sec

Equation (3-54) may be converted into a drag coefficient by dividing by the ratio of wetted area to reference area:

$$C_D = C_f \frac{S_{\text{wetted}}}{S_{\text{reference}}} \quad (3-55)$$

Equation (3-55) may then be used to determine the drag of any smooth aerodynamic surfaces (i.e., wing or body) in laminar incompressible flow.

For the turbulent incompressible flow case no simple theory is available or can be derived to define the complex flow characteristics in the turbulent boundary layer. Consequently, empirical or semi-empirical expressions are necessary to relate the friction coefficient

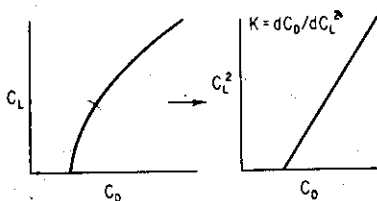


FIG. 3-29. Subsonic drag-rise factor.

with experimental results. The Kármán-Schoenherr equation has been recommended⁶¹ and is given as

$$C_f \log_{10} C_f Re = 0.242 \quad (3-56)$$

Again, Eq. (3-55) may be used to convert the friction coefficient into a drag coefficient using the value of C_f from Eq. (3-56). This will give

the drag of the airframe components in turbulent incompressible flow. The effect of compressibility in turbulent flow will be discussed in Chap. 4, which treats the problem of friction drag more fully in conjunction with the performance of the missile.

The above discussion deals with drag at zero lift or zero angle of attack for the case of a symmetrical airfoil. The induced drag or drag due to lift may be expressed as

$$C_{D_i} = KC_L^2 \quad (3-57)$$

where $K = dC_{D_i}/dC_L^2$, called the drag-rise factor, may be obtained from a plot of C_L^2 vs. C_D as shown in Fig. 3-29. For an elliptical lift distribution the value of K is $1/\pi R$. For nonelliptical lift distributions the drag-rise factor is usually written as

$$K = \frac{1}{\pi e R} \quad (3-58)$$

where e is the Oswald efficiency factor and has a value less than unity. The theoretical value of e may be evaluated by the method presented in ref. 62. However, correlation of test results of a series of 18 wings indicates that the induced-drag coefficient may be accurately expressed as

$$C_{D_i} = \frac{C_L^2}{\pi m^2 R} \quad (3-58a)$$

where m is a constant required to correlate the test results. The value

of m^2 was found to be approximately 13 per cent below the theoretical value of e .

The theoretical lift-curve slope of a thin wing of infinite aspect ratio in inviscid incompressible flow is given as

$$a_0 = 2\pi \text{ per radian} \quad (3-59)$$

The theoretical effects of aspect ratio⁶³ and sweep⁶⁴ are given by Eqs. (3-60) and (3-61) below:

$$(C_{L_\alpha})_{\Lambda=0} = \frac{Ra_0}{R+2} = \frac{2\pi}{1+2/R} \quad (3-60)$$

$$(C_{L_\alpha})_\Lambda = \frac{(R+2) \cos \Lambda}{R+2 \cos \Lambda} (C_{L_\alpha})_{\Lambda=0} \quad (3-61)$$

For low-aspect-ratio wings (i.e., wings with aspect ratio less than 2), the variation of C_L with α is nonlinear. A more accurate representation of the variation of C_L with α is given by⁶⁵

$$C_L = k\alpha^n \quad (3-62)$$

where k and n are constants and a function of aspect ratio as shown in Fig. 3-30.

The theoretical effect of compressibility is to increase the incompressible subsonic value of C_{L_α} by the Prandtl-Glauert factor $1/\sqrt{1-M^2}$. The compressibility effect on swept-back wings is given by⁶⁶

$$(C_{L_\alpha})_M = \frac{R+2 \cos \Lambda}{R\sqrt{1-M^2} \cos^2 \Lambda + 2 \cos \Lambda} (C_{L_\alpha})_{M=0} \quad (3-63)$$

The center of pressure of an airfoil in subsonic flow is generally between 20 and 25 per cent of the mean aerodynamic chord. The effect of compressibility is to shift the center of pressure forward of the quarter chord. Since airfoil thickness and section have a pronounced effect on the aerodynamic characteristics, experimental data should be used whenever possible in lieu of the theoretical results.

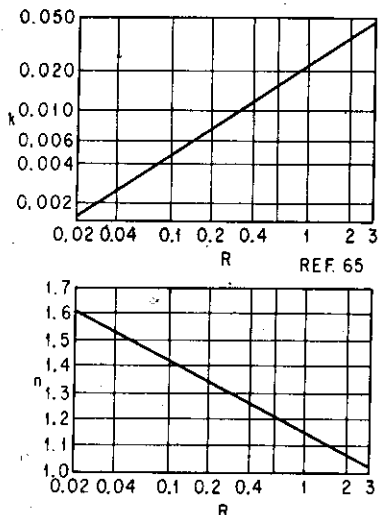


FIG. 3-30. Lift characteristics of low-aspect-ratio wings in subsonic flow.

3-17. AERODYNAMIC CONTROLS

Naturally, the type of control surface is directly associated with the type of configuration (see Fig. 2-2) in question. Perhaps the two most important design features of any type of control surface are (1) its effectiveness and (2) its hinge-moment characteristics. Control effectiveness must be large in order that its area may be kept to a minimum from the standpoint of hinge moments. The latter must be sufficiently low to make unnecessary large, heavy, and costly servos required to obtain the desired response characteristics. These two design features for the wing, canard, and tail control will be briefly discussed qualitatively below.

1. Wing Control. The control effectiveness in terms of pitching moment per unit deflection is perhaps the lowest of all three above-mentioned control surfaces. This results primarily from the extremely small moment arm normally associated with this type of control. The BW (body plus wing) configuration may actually have control reversal under certain flight or loading conditions (i.e., center of gravity ahead of wing center of pressure.) Thus the wing downwash on the rearward surfaces contributes to a large extent the resultant control effectiveness of the complete model configuration. Although the trim angle of attack may be somewhat lower, the net hinge moment of the wing control is the largest. Lateral control by differential wing deflection may be satisfactory, provided careful considerations are given to the aft surface design, as will be discussed in Chap. 8.

2. Canard Control. The control effectiveness is quite large as the result of two obvious features: (1) large canard moment arm and (2) downwash on the wing (or tail) surfaces, which can cause an almost equal amount of pitching-moment effectiveness. In addition, because of the small size, the canard has relatively low hinge moments despite the relatively large total angle of attack ($\alpha + \delta$) on the canards. This, in addition to the other features mentioned in Chap. 2, makes the canard control a very efficient aerodynamic and over-all systems design. Lateral control by differential canard deflection is completely unsatisfactory because of the low forces and moments as well as the adverse effect of downwash on the rear surfaces. Hence lateral-control devices such as wing spoilers, flaps, or tip ailerons are required for roll stabilization.

3. Tail Control. The pitching moment or control effectiveness is quite high in view of the fact that (1) the tail moment arm is generally fairly large and (2) there is no adverse downwash from deflection of

the forward surfaces. The level of hinge moment is low as a result of the relatively low resultant angle of attack. The method of solution of the tail-control effectiveness will be presented in Chap. 5 together with those previously discussed. As mentioned in Chap. 2, the use of tail control may present a critical packaging problem, especially on smaller-sized missiles. In general, lateral control by differential tail deflection is inadequate because of the relatively short moment arms as well as the large magnitude of the aerodynamic induced rolling moments from the large wings associated with this design. Consequently separate lateral-control surfaces are often required when movable tail surfaces are used for pitch control.

4. Lateral Controls. Although the previously mentioned controls (i.e., canards and tails) may be satisfactory for pitch (or yaw) control they are seldom adequate for lateral (or roll) control. Consequently separate aerodynamic control about the x , or roll, axis is required and may consist of the following types: flaps, spoilers, or wing-tip ailerons. The flap-type ailerons are generally located on the main wing-lifting surface. An excellent collection and summary of the lateral-control effectiveness of this type of control, presented in ref. 68 over a Mach-number range of 0.6 to 1.6, is recommended for preliminary design purposes. A complete bibliography⁶⁹ of control research done by the NACA (now the NASA) between 1946 and 1955 is also recommended for further study.

3-18. JET CONTROLS

Jet controls may be divided broadly into two types: those which obtain most of their effectiveness by blowing air or changing the pressure over an aerodynamic surface and those so-called (jet) reaction controls which obtain all their effectiveness by deflecting the jet-exhaust stream. The former type has received somewhat limited attention from both the theoretical and the experimental standpoint, whereas a vast amount of work has been done on the latter. Limited experimental data⁷⁰ are available on the lateral-control effectiveness of jet control using either free-stream or compressed air ejected through orifices over various portions of the wing. For configurations requiring relatively low lateral-control effectiveness this type of jet control may be satisfactorily employed.

Jet-reaction controls have been widely used, particularly on long-range ballistic missiles which, during portions of their flight, must operate at very low dynamic pressure. During lift-off and flights at

extremely high altitudes, jet-reaction control is mandatory to steer the missile on the proper flight path. Among the most common jet-reaction controls in usage are (1) simple auxiliary jets (rocket), (2) gimballed nozzles, (3) jetavators, and (4) jet vanes. Strictly speaking, the latter should be classified as an aerodynamic control since the control forces and moments are derived principally from the deflected vanes rather than from the deflected jet. The first type has been used primarily in flight testing of experimental models. Small jet rockets are used to "pulse or excite" the model to determine pitching-moment derivatives as well as the model damping characteristics. Jet rockets

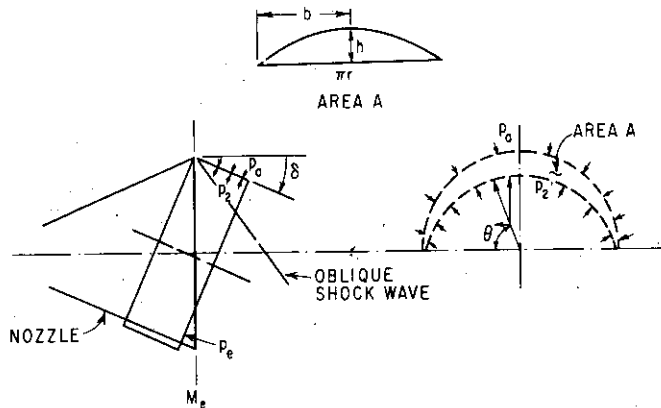


FIG. 3-31. Principle of jetavator operation.

may also be employed to provide velocity control for satellites. Gimballed nozzles may be used to provide control about all three axes with either liquid- or solid-propellant rockets. The response of this type of control is relatively low because of its inherent large inertia and hinge moments. Gimballed engines have also been used but have been restricted to liquid-propellant rockets. The disadvantages associated with this type of control are similar to those of the gimballed nozzles except that their magnitudes are greater.

A jetavator is a relatively simple jet-deflection device consisting of a right circular cylindrical ring around the diverging portion of the nozzle. The hinge line is normal to the nozzle center line when the jetavator is in the neutral position. When the jetavator is deflected, an oblique shock is produced (see Fig. 3-31), causing a large change in pressure in the jet. The pressure rise across the oblique shock p_0/p_e is a function of the jetavator deflection δ and Mach number at the exit

of the nozzle M_e and may be determined from *NACA Technical Report 1135*. The pressure in the deflected jet p_2 acts normal to the ring area A , whereas the ambient pressure p_a acts in the opposite direction. As shown in Fig. 3-31, the pertinent pressure-force components vary as the sine of the angle θ . Consequently the mean pressure force varies as the mean $\sin \theta$ (i.e., $\overline{\sin \theta}$). The resultant force of the jetavator can then be written as

$$F = \overline{\sin \theta} \left(\frac{p_2}{p_e} p_e - p_a \right) A \quad (3-64)$$

The value of mean $\sin \theta$ may be obtained by plotting $\sin \theta$ vs. ring diameter and then taking the area under the sine curve and dividing by the ring diameter. This value is $\pi/4$. The value of p_e is obtained from rocket-motor performance data. The value of p_a is obtained from atmospheric tables and must be corrected for base-pressure and jet effects. From Fig. 3-32 the normal component of the jetavator force F_y is given as

$$F_y = \frac{\pi}{4} \left(\frac{p_2}{p_e} p_e - p_a \right) A \cos \delta \quad (3-64a)$$

and the axial or drag component F_x is

$$F_x = \frac{\pi}{4} \left(\frac{p_2}{p_e} p_e - p_a \right) A \sin \delta \quad (3-64b)$$

Area A may be found by the following relationship:

$$A = \frac{4bh}{3} \quad (3-65)$$

where $b = \pi r/2$.

A single-axis jetavator will be adequate for either pitch or yaw control, whereas a full-swiveling jetavator is required where both pitch and yaw control are desired. For control about all three (pitch, yaw, and roll) axes, two nozzles, each equipped with a full-swiveling jetavator, are required.

Jet vanes are commonly used for controls about all three axes on ballistic missiles. For relatively long periods of continuous operation it is essential to use high-temperature-resistant material over a goodly portion of the vanes. In jet-vane design it is important to keep the thickness ratio to a minimum since it has been shown that the wave drag of an airfoil varies as the square of the thickness ratio. This is particularly important for conditions where the jet vanes are submerged in the jet exhaust throughout rocket-motor operation since

drag losses occur even for zero vane deflection. The aerodynamic forces on the jet vane may be calculated by the methods previously discussed using the environments of the jet (i.e., values of γ , p , and M in the jet to obtain dynamic pressure q).

The lateral (or normal) and axial components of the jet vanes F_y and F_x may be expressed with the aid of Eqs. (3-1) and (3-2) and Fig. 3-1 as follows:

$$F_y = N_{jv} \cos \delta - A_{jv} \sin \delta \quad (3-66)$$

$$F_x = A_{jv} \cos \delta + N_{jv} \sin \delta \quad (3-67)$$

The drag-loss equivalent to an impulse loss may be determined if the vane-deflection history is known during rocket-motor operation. The

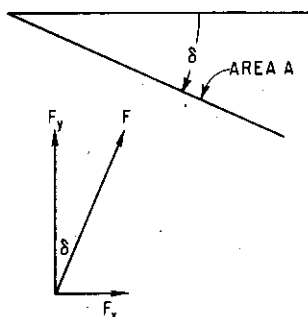


FIG. 3-32. Side view of jet-vator fores.

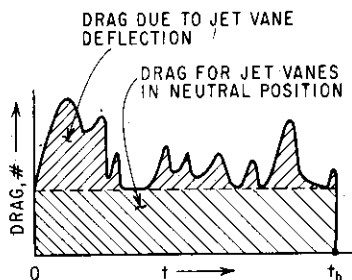


FIG. 3-33. Drag losses caused by jet vanes.

latter information can be obtained from simulation studies which determine the amount of guidance or vane deflection required for several typical flight conditions. The total drag loss I_D is then the total area under the drag-time curve (see Fig. 3-33) and can be expressed as follows:

$$I_D = - \int_0^{t_b} F_x dt \quad (3-68)$$

where t_b = total burning time of rocket motor

SYMBOLS

A	axial force, aspect ratio, area
A_p	planform area
C_A	axial-force coefficient (A/qS)
C_D	drag coefficient (D/qS)

C_{D_f}	force-drag coefficient [see Eq. (3-31)]
C_{D_i}	induced-drag coefficient
C_{D_N}	drag (coefficient) due to normal force
C_{D_0}	drag (coefficient) at zero lift
C_f	skin-friction coefficient
C_L	lift coefficient
C_N	normal-force coefficient
$C_{N\alpha}$	normal-force-curve slope (variation of C_N with α), $\partial C_N / \partial \alpha$
C_p	pressure coefficient $(p - p_0) / q_0$
C_1, C_2, C_3, \dots	Busemann constants [see Eqs. (3-16) and (3-17)]
D	drag force
E	elliptic integral of second kind [see Eq. (3-51)]
F	force
I_D	total drag loss [see Eq. (3-68)]
K	drag-rise factor, or term used in the "parabolic-series" nose (see Fig. 3-11B)
L	lift force
L/D	lift-to-drag ratio
M	Mach number
M/f_n	hypersonic similarity parameter
N	normal force
P	pressure coefficient $\Delta p / q$ or C_p [see Eq. (3-9)]; or denotes "parabolic-series" nose (see Fig. 3-11B)
R	aspect ratio, resultant force, or radius of body shown in Fig. 3-10
Re	Reynolds number [see Eq. (3-54)]
S	reference area
S_b	area of base of missile
S_w	wing planform area
V	free-stream velocity
V_s	stall speed
W	weight of missile
a_0	theoretical lift-curve slope of a thin wing of infinite aspect ratio in inviscid incompressible flow
b	wing span, or semispan of jetavator (see Fig. 3-31)
c	wing chord, speed of sound
cp	center of pressure
d	body diameter
e	Oswald efficiency factor
f_n	fineness ratio of nose l_n / d

h	projected height of jetavator (see Fig. 3-31)
k	a constant in Eq. (3-62), or tangent of leading-edge sweep angle shown in Fig. 3-26
l	length of body or nose section
l/d	length-to-diameter ratio
m	a correlation constant used in Eq. (3-58a)
n	a constant in Eq. (3-50) and defined as k/β as shown in Fig. 3-26, or exponent in defining the "power-series" nose (see Fig. 3-11A), or a constant in Eq. (3-62)
p	static pressure
Δp	pressure differential ($p - p_0$ or $p_2 - p_1$)
p_a	ambient pressure (see Fig. 3-31)
p_e	pressure at the exit of the nozzle (see Fig. 3-31)
p_0	free-stream static pressure
p_1	free-stream static pressure as used in Eq. (3-4)
p_2	static pressure on the surface of the cone as used in Eq. (3-4), or pressure in the deflected jet as shown in Fig. 3-31
q, q_0	free-stream dynamic pressure ($\frac{1}{2}\rho V^2$ or $\frac{1}{2}\gamma p M^2$)
r	local nose radius (see Fig. 3-11A and B), or dimension of the jetavator shown in Fig. 3-31
r_b	radius at the base of the nose section (see Fig. 3-11A)
r_n	nose radius (see Fig. 3-10)
t_b	burning time of the rocket motor
x	moment arm
α	angle of attack
β	$\sqrt{M^2 - 1}$
γ	specific-heat ratio of air (1.4)
δ	wedge semivertex angle (see Fig. 3-3), or jetavator deflection (see Figs. 3-31 and 3-32)
ϵ	semivertex angle of a triangular wing
θ	shock angle, or circumferential angle shown in Fig. 3-31 or boattail angle
Λ	wing leading-edge sweep angle
μ	Mach angle [see Eq. (3-35)]
μ'	angle of any ray radiating from wing tip (see Fig. 3-21)
ν	kinematic viscosity of air
ρ	density of air
σ	semivertex cone angle
σ_0	semivertex ogive angle
ϕ	a term used in Eq. (3-12)

Subscripts

<i>A</i>	aft sections of the airfoil
<i>BT</i>	boattail
<i>F</i>	forward sections of airfoil
<i>L</i>	lower surfaces of airfoil
<i>M</i>	effect of compressibility
max	maximum
<i>T</i>	total
<i>U</i>	upper surfaces of airfoil
<i>b</i>	base (section)
<i>e</i>	exit of nozzle
<i>ju</i>	jet vanes
<i>x, y</i>	coordinates shown in Fig. 3-32
Λ	with sweepback
I, II, III, IV	denote area shown in Figs. 3-20 and 3-24
1, 2, 3, 4	denote regions of airfoil in Fig. 3-18
0.5	denotes mid-chord of airfoil
∞	two-dimensional value at limit of Mach cone as used in Eq. (3-36), or two-dimensional value as used in Fig. 3-22

REFERENCES

1. Taylor, G. F., and J. W. Maccoll: The Air Pressure on a Cone Moving at High Speeds, *Proc. Roy. Soc. (London) (A)*, vol. 139, pp. 278-293, 1933.
2. Taylor, G. I., and J. W. Maccoll: The Mechanics of Compressible Fluids, Durand's "Aerodynamic Theory," vol. III, div. H, Springer-Verlag, Berlin, 1934.
3. Staff of the Computing Section, Center of Analysis (under direction of Zdeněk Kopal): Tables of Supersonic Flow around Cones, *MIT Tech. Rept. 1*, 1947.
4. Staff of the Computing Section, Center of Analysis (under direction of Zdeněk Kopal): Tables of Supersonic Flow around Yawing Cones, *MIT Tech. Rept. 3*, 1947.
5. Stone, A. H.: On Supersonic Flow Past a Slightly Yawing Cone, *J. Math. and Phys.*, vol. 27, no. 1, pp. 67-81, April, 1948.
6. Bonney, E. A.: "Engineering Supersonic Aerodynamics," McGraw-Hill Book Company, Inc., New York, 1950.
7. Busemann, A.: Aerodynamic Lift at Supersonic Speeds, lecture given at the 5th Volta Conference at Rome, published in *Luftfahrt-Forsch.*, vol. 12, no. 6, 1935 (*British ARC Rep. 2844*, Feb. 3, 1937).
8. Ferrari, C.: The Fields of Supersonic Flow around a Solid of Revolution, *Aerotecnica*, vol. 19, no. 1, 1937.
9. Tsien, H.: Supersonic Flow over an Inclined Body of Revolution, *J. Aeronaut. Sci.*, vol. 5, no. 2, pp. 480-483, October, 1938.

10. Miles, E. R. C.: "Semi-empirical Formulae for Ogives," CM-505, Applied Physics Laboratory, Johns-Hopkins University.
11. Von Kármán, T., and N. B. Moore: Resistance of Slender Bodies Moving with Supersonic Velocities with Special Reference to Projectiles, *Trans. ASME*, vol. 54, 1932.
12. Von Kármán, T.: The Problem of Resistance in Compressible Fluids, *Proc. 5th Volta Cong. Roy. Acad. Italy*, 1936.
13. Syvertson, C. A., and D. H. Dennis.: A Second-order Shock-expansion Method Applicable to Bodies of Revolution Near Zero Lift, *NACA Tech. Rept.* 1328, 1957.
14. Ferri, A.: Supersonic Flow around Circular Cones at Angles of Attack, *NACA Tech. Rept.* 1045, 1951.
15. Eggers, A. J., Jr., and R. C. Savin: A Unified Two-dimensional Approach to the Calculation of Three-dimensional Hypersonic Flows, with Application to Bodies of Revolution, *NACA Rept.* 1249, 1955 (supersedes *NACA Tech. Note* 2811).
16. Eggers, A. J., Jr., and R. C. Savin: Approximate Methods for Calculating the Flow about Nonlifting Bodies of Revolution at High Supersonic Airspeeds, *NACA Tech. Note* 2579, 1951.
17. Savin, R. C.: Application of the Generalized Shock-expansion Method to Inclined Bodies of Revolution Traveling at High Supersonic Airspeeds, *NACA Tech. Note* 3349, 1955.
18. Eggers, A. J., R. C. Savin, and C. A. Syvertson: The Generalized Shock-expansion Method and Its Application to Bodies Traveling at High Supersonic Airspeeds, *J. Aeronaut. Sci.*, vol. 22, no. 4, pp. 231-238, April, 1955.
19. Van Dyke, M. D.: First- and Second-order Theory of Super-sonic Flow Past Bodies of Revolution, *J. Aeronaut. Sci.*, vol. 18, no. 3, pp. 161-179, March, 1951.
20. Van Dyke, M. D.: A Study of Second-order Supersonic Flow Theory, *NACA Rept.* 1081, 1952 (supersedes *NACA Tech. Note* 2200).
21. Van Dyke, M. D.: A Study of Hypersonic Small-disturbance Theory, *NACA Tech. Note* 3173, 1954 (superseded by *Tech. Rept.* 1194).
22. Allen, H. J., and E. W. Perkins: A Study of Effects of Viscosity on Flow over Slender Inclined Bodies of Revolution, *NACA Tech. Rept.* 1048, 1951.
23. Buford, W. E.: The Effects of Afterbody Length and Mach Number on the Normal Force and Center of Pressure of Conical and Ogival Nose Bodies, *J. Aeronaut. Sci.*, vol. 25, pp. 103-108, February, 1958.
24. Graham, E. W.: Pressure Distribution on a Cylinder Preceded by a Cone in Axial Supersonic Flow, Douglas Aircraft Company, SM-13322, July, 1948.
25. Chapman, D. R.: An Analysis of Base Pressure at Supersonic Velocities and Comparison with Experiment, *NACA Tech. Note* 2137, July, 1950.
26. Spahr, J. R., and R. R. Dickey: Effect of Tail Surfaces on the Base Drag of a Body of Revolution at Mach Numbers of 1.5 and 2.0, *NACA Tech. Note* 2360, 1951.
27. Chapman, D. R., and E. W. Perkins: Experimental Investigation of the Effects of Viscosity on the Drag and Base Pressure of Bodies of Revolution at a Mach Number of 1.5, *NACA Tech. Rept.* 1036, 1951.

28. Bogdonoff, S. M.: A Preliminary Study of Reynolds Number Effects on Base Pressure at $M = 2.95$, *J. Aeronaut. Sci.*, vol. 19, p. 201.
29. Love, E. S.: Base Pressure at Supersonic Speeds on Two-dimensional Airfoils and on Bodies of Revolution with and without Fins Having Turbulent Boundary Layers, *NACA Tech. Note 3819*, January, 1957.
30. Chow, W. L.: On the Base Pressure Resulting from the Interaction of a Supersonic External Stream with a Sonic or Subsonic Jet, *J. Aeronaut. Sci.*, vol. 26, no. 3, pp. 176-180, March, 1959.
31. Cabbage, J., Jr.: Jet Effects on Base and Afterbody Pressures of a Cylindrical Afterbody at Transonic Speeds, *NACA Research Mem. L56C21*, May 23, 1956.
32. Cartright, E. M., Jr., and A. H. Schroeder: Investigation at Mach Number 1.91 of Side and Base Pressure Distributions over Conical Boattails without and with Jet Flow Issuing from Base, *NACA Research Mem. E51F26*, Sept. 12, 1951.
33. Englert, G. W., D. J. Vargo, and R. W. Cubbison: Effect of Jet-nozzle-expansion Ratio on Drag of Parabolic Afterbodies, *NACA Research Mem. E54B12*, Apr. 19, 1954.
34. Pitts, W. C., J. N. Nielsen, and G. E. Kaattari: Lift and Center of Pressure of Wing-body-tail Combinations at Subsonic, Transonic, and Supersonic Speeds, *NACA Tech. Rept. 1307*, 1957.
35. Spreiter, J. R.: The Aerodynamic Forces on Slender Plane- and Cruciform-wing and Body Combinations, *NACA Tech. Rept. 962*, 1950.
36. Von Kármán, T.: Supersonic Aerodynamics—Principles and Applications, *J. Aeronaut. Sci.*, vol. 14, no. 7, pp. 373-402, July, 1947.
37. Ivey, H., G. W. Stickle and A. Schuettler: Charts for Determining the Characteristics of Sharp-nose Airfoils in Two-dimensional Flow at Supersonic Speeds, *NACA Tech. Note 1143*, 1947.
38. Ackeret, J.: Air Forces on Airfoil Moving Faster than Sound, *NACA Tech. Mem. 317*, 1925
39. Taylor, G. I.: Applications to Aeronautics of Ackeret's Theory of Aerofoils Moving at Speeds Greater than That of Sound, British ARC, *R & M 1467*, 1932.
40. Busemann, A., and O. Walchner: "Airfoil Characteristics at Supersonic Speeds," RTP Translation 1786, British Ministry of Aircraft Production.
41. Lock, C. N. H.: Examples of the Application of Busemann's Formula to Evaluate the Aerodynamic Force Coefficients on Supersonic Aerofoils, British ARC, *R & M 2101*, 1949.
42. Laitone, E. V.: Exact and Approximate Solutions of Two-dimensional Oblique Flow, *J. Aeronaut. Sci.*, vol. 14, no. 1, p. 25, January, 1947.
43. Meyer, T.: Über Zweidimensionale Bewegungsvorgänge in einem Gas, das mit Überschallgeschwindigkeit strömt, *Mitt. Forschungsarb. Gebiete Ingenieurw.*, vol. 62, no. C, Berlin, 1908.
44. Snow, R. M.: Aerodynamics of Thin Quadrilateral Wings at Supersonic Speeds, *Quart. Appl. Math.*, vol. 5, no. 4, 1948.
45. Ward, G. N.: The Pressure Distribution on Some Flat Laminar Aerofoils at Incidence at Supersonic Speeds—I, Scientific Research and Experiment Airflow, Paper 30, February, 1946.
46. Evvard, J. C.: Distribution of Wave Drag and Lift in the Vicinity of Wing Tips at Supersonic Speeds, *NACA Tech. Note 1382*, July, 1947.

47. Vincenti, W.: Comparison between Theory and Experiment for Wings at Supersonic Speeds, *NACA Tech. Rept.* 1033, 1951.

48. Ferri, A.: Experimental Results with Airfoils Tested in the High-speed Tunnel at Guidonia, *NACA Tech. Mem.* 946, 1940.

49. Jack, J. R.: Theoretical Pressure Distribution and Wave Drags for Conical Boattails, *NACA Tech. Note* 2972, July, 1953.

50. Puckett, A. E.: Supersonic Wave Drag of Thin Airfoils, *J. Aeronaut. Sci.*, vol. 13, no. 9, pp. 475-484, September, 1946.

51. Puckett, A. E., and H. J. Stewart: Aerodynamic Performance of Delta Wings at Supersonic Speeds, *J. Aeronaut. Sci.*, vol. 14, no. 10, pp. 567-568, October, 1947.

52. Jones, R. T.: Thin Oblique Airfoils at Supersonic Speeds, *NACA Tech. Note* 1107, September, 1946.

53. Stewart, H. J.: The Lift of a Delta Wing at Supersonic Speeds, *Quart. Appl. Math.*, vol. IV, no. 3, pp. 246-254, October, 1946.

54. Brown, C. E.: Theoretical Lift and Drag of Thin Rectangular Wings at Supersonic Speeds, *NACA Rept.* 839, 1946 (supersedes *Tech. Note* 1183).

55. Love, E. S.: Investigation at Supersonic Speeds of 22 Triangular Wings Representing Two Airfoil Sections for Each of 11 Apex Angles," *NACA Tech. Rept.* 1238, 1955.

56. Chapman, D. R.: Reduction of Profile Drag at Supersonic Velocities by the Use of Airfoil Sections having a Blunt Trailing Edge, *NACA Tech. Note* 3503, September, 1955.

57. Chapman, D. R., and R. H. Kester: Effect of Trailing-edge Thickness on Lift at Supersonic Velocities, *NACA Tech. Note* 3504, June, 1955.

58. Morrow, J. D., and E. Katz: Flight Investigation at Mach Numbers from 0.6 and 1.7 to Determine Drag and Base Pressures on a Blunt-trailing-edge Airfoil and Drag of Diamond and Circular-arc Airfoils at Zero Lift, *NACA Tech. Note* 3548, November, 1958.

59. Morrow, J. D.: Measurements of the Effect of Trailing-edge-thickness on the Zero-lift Drag of Thin Low-aspect-ratio Wings, *NACA Tech. Note* 3550, November, 1958.

60. Gallagher, J. J., and J. N. Mueller: An Investigation of the Maximum Lift of Wings at Supersonic Speeds, *NACA Tech. Rept.* 1227, 1955.

61. Locke, F. W. S., Jr.: Recommended Definition of Turbulent Friction in Incompressible Fluids, *Bureau of Aeronautics Research Division Rept.* 1415, June, 1952.

62. DeYoung, J.: Theoretical Additional Span Loading Characteristics of Wings with Arbitrary Sweep, Aspect Ratio and Taper Ratio, *NACA Tech. Note* 1491, December, 1947.

63. Swanson, R. S., and S. M. Crandall: Lifting Surface Theory Aspect Ratio Corrections to the Lift and Hinge-moment Parameters for Full-span Elevators on Horizontal Tail Surfaces, *NACA Tech. Note* 1175, 1947.

64. Toll, T. A., and J. J. Queijo: Approximate Relations and Charts for Low Speed Stability Derivatives of Swept Wings, *NACA Tech. Note* 1581, May, 1948.

65. Locke, F. W. S.: An Empirical Study of Low Aspect Ratio Lifting Surfaces with Particular Regard to Planing Craft, *J. Aeronaut. Sci.*, March, 1949.

66. Fischer, L. R.: Approximate Corrections for the Effects of Compressibility on the Subsonic Stability Derivatives of Swept Wings, *NACA Tech. Note* 1854, April, 1949.
67. Abbott, I. H., A. E. Von Doenhoff, and L. S. Stiver, Jr.: Summary of Airfoil Data, *NACA Tech. Rept.* 824, 1948.
68. Strass, H. K., E. W. Stephens, E. M. Fields, and E. D. Schult: Collection and Summary of Flap-type-aileron Rolling Effectiveness Data at Zero Lift as Determined by Rocket-powered Model Tests at Mach Numbers between 0.6 and 1.6, *NACA Research Mem.* L55F14, Sept. 2, 1955.
69. Brewer, J. D.: Description and Bibliography of NACA Research on Wing Controls—January 1946–February 1955, *NACA Research Mem.* 54K24, Mar. 24, 1955.
70. Lowry, J. G.: Recent Control Studies, *NACA Research Mem.* L55L22a, Feb. 16, 1956.
71. Krzywoblocki, M. Z.: Aerodynamic Studies: The Forces Acting on an Air Vehicle—A Review of the Literature, *WADC Tech. Note* 56-360, pt. XVI, May, 1957 (*ASTIA AD* 130862).
72. Hall, C. F.: Lift, Drag, and Pitching Moment of Low-aspect Ratio Wings at Subsonic and Supersonic Speeds, *NACA Research Mem.* A53A30, Apr. 14, 1953.

CHAPTER 4

MISSILE PERFORMANCE

4-1. INTRODUCTION

The performance characteristics of a missile can be determined once the magnitude of the pertinent forces (i.e., thrust, drag, weight) and flight conditions are known or specified. The methods of calculating performance parameters such as maximum speed and rate of climb for cruise-type missiles are identical with those used on conventional manned aircraft. For rocket-powered missiles, particularly those which are accelerated to the desired or required speed and then decelerate or glide to their destination, a somewhat different approach to the performance evaluation is used. This chapter will be concerned with a fairly comprehensive treatment of performance of missiles designed for both long and short ranges and different modes of powered flight. In addition, methods of evaluation of drag characteristics of the missile, as well as their application, are presented in connection with missile-performance determination.

4-2. FRICTION DRAG

In incompressible flow the skin-friction coefficient depends primarily on the type of flow (i.e., laminar or turbulent) and the Reynolds number. As noted in Chap. 3, the skin-friction coefficient for laminar and turbulent flow is given as

$$C_{f_L} = \frac{1.328}{\sqrt{\text{Re}}} \quad (4-1)$$

and
$$\sqrt{C_{f_T}} \log_{10} (C_{f_T} \text{Re}) = 0.242 \quad (4-2)$$

Although Eq. (4-1) has been generally accepted as accurate for the determination of skin-friction drag in laminar flow, such flow conditions are seldom realized in actual practice except for very low values of Reynolds number (i.e., less than 1 million). For $\text{Re} > 10^6$, turbulent

flow generally prevails and Eq. (4-2) must be used. It should be noted here that a complete understanding of friction drag in turbulent flow has yet to be achieved. Recently Coles^{1,*} proposed the "universal skin-friction constants" in an attempt to predict skin friction accurately with a method of boundary-layer analysis. Results of limited experimental tests² indicate that the skin-friction coefficient approaches asymptotically a constant value at Reynolds numbers exceeding 21 million. However, until more data are obtained, it is recommended that the turbulent skin-friction coefficient be calculated by Eq. (4-2). Figure 4-1 is a plot of the skin-friction coefficient as a function of Reynolds number for laminar and turbulent flow.

For most flight conditions laminar flow prevails over the extreme forward portion of the missile wing or body, followed by completely turbulent flow over the remaining portion of the missile. The problem of drag determination has thus resolved into that of determining the transition point where turbulent flow commences. No useful theoretical methods are known to exist to determine the exact location of the transition point because of the complex nature of the flow and the interaction effects of such factors as pressure gradient, surface smoothness, and Reynolds number. Hence experience and judgment must be used to determine the transition point in most preliminary frictional-drag estimates. In general the transition point of a smooth and streamlined body may be located as far back as 30 per cent of its length. For missile application the nose tangency point of the end of the nose or forebody section as a transition point is a fairly valid assumption. For the wings turbulent flow may be assumed in preliminary drag evaluation. Once the transition is known or assumed, the next step is to calculate the skin-friction coefficient for the laminar and turbulent section of the body (or wing) as follows:

$$C_f = C_{fL} \frac{S_x}{S_t} + C_{fT} \frac{S_t - S_x}{S_t} \quad (4-3)$$

* Superscript numbers indicate references listed at the end of the chapter.

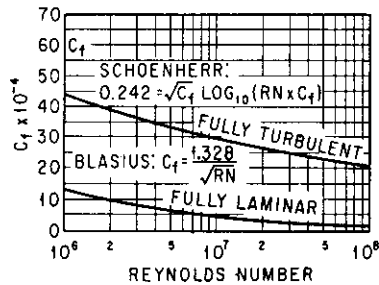


FIG. 4-1. Skin-friction coefficient vs. Reynolds number (incompressible flow).

where C_{f_L} = skin-friction coefficient in laminar flow, Re based on length x shown in Fig. 4-2

C_{f_T} = skin-friction coefficient in turbulent flow, Re based on length l

S_x = wetted area over length x

S_l = total wetted area (over length l)

Although somewhat more exact expressions are available, Eq. (4-3) is sufficiently accurate for most preliminary drag analyses.

The skin-friction-drag coefficients determined above are applicable

for condition of incompressible flow only (the effects of Mach number have been neglected). For subsonic speeds the Mach-number effects are not too pronounced. However, for the transonic and supersonic regions, the Mach-number effects become significant and cannot be ignored. For the lam-

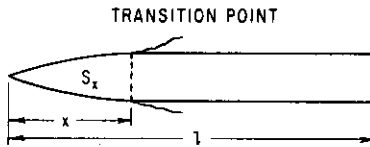


FIG. 4-2. Definition of terms for friction-drag calculation.

inar flow the effect of compressibility has been shown by a simplified theoretic approach to reduce the skin-friction coefficient by the following expression:

$$\frac{C_f}{C_{f_0}} = \left(\frac{1}{1 + 0.85M^2/5} \right)^{0.1295} \quad (4-4)$$

where C_{f_0} is the skin-friction-drag coefficient in laminar incompressible flow. Results derived by a more comprehensive theory appear to be in good agreement with those defined by Eq. (4-4). In addition, the accuracy derived by both theories is within the scatter of the test data. Figure 4-3 shows the effects of compressibility predicted by the two theories.

For turbulent flow the semiempirical mixing-length theories of Von Kármán and Prandtl have been used successfully in predicting skin friction for a flat plate at low subsonic speeds. Based on the most recent data available, the following expression appears to be most accurate in defining the effect of compressibility in turbulent flow for Mach numbers less than 1:

$$\frac{C_f}{C_{f_0}} = \frac{1}{1 + 0.08M^2} \quad (4-5)$$

When mixing theory is applied to turbulent compressible flow, numerous solutions are obtained that yield results vastly different from each other and from test data. A comprehensive bibliography of theoretical predictions of skin-friction coefficient in turbulent compressible flow may be found in ref. 3. Of all these theoretical predictions, the "extended Frankl-Voishel" theory^{4,5} appears to be one of the first to predict the compressibility effect accurately. Subsequent theories by Cope,⁶ Wilson,⁷ Tucker,⁸ and others also yield results comparable with those predicted by the extended Frankl-Voishel theory. For design purposes the latter theory is recommended, with the results shown in Fig. 4-3. The expression for the compressibility effect is given below.⁵

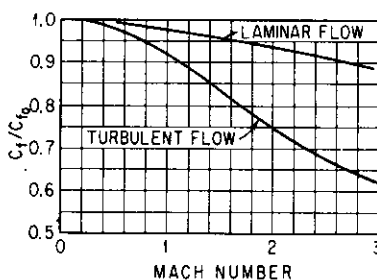


FIG. 4-3. Effect of compressibility on skin-friction coefficient.

$$\frac{C_f}{C_{f_0}} = \frac{1}{\left(1 + \frac{\gamma - 1}{2} M^2\right)^{0.467}} \quad (4-6)$$

where C_{f_0} is the skin-friction coefficient in turbulent incompressible flow.

The friction-drag coefficient is obtained by

$$C_D = C_f \frac{S_{\text{wetted}}}{S_{\text{reference}}}$$

In preliminary design studies it is recommended that the friction-drag coefficient be increased by 10 per cent to account for surface roughness and small protuberances.

4-3. PRESSURE DRAG

Pressure or form drag in subsonic flow^{9,10,11} is generally small and may be neglected in preliminary design studies. However, in the transonic and supersonic region pressure drag constitutes a great percentage of the total drag of the missile and hence must be carefully obtained before an accurate determination can be made on missile-performance capabilities. Pressure drag in the transonic region can

best be determined from experimental test data or by the transonic-area rule,¹² which is highly mathematical but can be solved on automatic computing machines. In the supersonic-speed region the pressure drag can be determined by the relationships presented in the preceding chapter.

1. Body. As previously discussed, the body-pressure drag consists of three primary parts—nose-wave drag, boattail-wave drag, and base-pressure drag. For a tangent ogive nose the wave-drag coefficient was shown [Eq. (3-9)] to be

$$C_{D_w} = P \left(1 - \frac{2[196(l/d)^2 - 16]}{28(M + 18)(l/d)^2} \right) \quad (4-8)$$

A comparison of results obtained by Eq. (4-8) and those derived from correlated test results mentioned in Chap. 3 is shown below. It can be seen that the agreement between the two sets of results is satisfactory for most preliminary design studies.

Mach No.	C_{D_w} from Eq. (4-8)	C_{D_w} from correlated data
1.3	0.115	0.124
1.5	0.101	0.106
2.0	0.095	0.095
2.5	0.094	0.093

The boattail and (power-off) base-drag coefficients may be determined from Chap. 3.

2. Wing. The theoretical wave drag of an airfoil has been shown [Eq. (3-30)] to vary as the thickness squared. For an untapered rectangular wing with a double-wedge airfoil section, the wave-drag coefficient was determined [Eq. (3-45)] to be

$$C_D = \frac{4\delta^2}{\beta} \left(1 - \frac{1}{2\beta A} \right) \quad (4-9)$$

For wings of different planform such as a delta wing, the theoretical wave drag may be obtained from the numerous references (i.e., 50 to 54 of Chap. 3) previously mentioned. However, for practical preliminary design, experimental results such as those contained in refs. 47 and 55 of Chap. 3 should be used.

4-4. INDUCED DRAG

For subsonic speeds the induced-drag coefficient may be obtained by the following empirical [Eq. (3-58a)] expression:

$$C_{Di} = \frac{C_L^2}{\pi R m^2} \quad (4-10)$$

The value of m^2 may be obtained from Chap. 3. For the high subsonic- and transonic-speed regions, experimental or correlated test results must be used in order to obtain reasonably accurate values of C_{Di} . However, for supersonic speeds the induced drag (or drag due to normal force) can be approximated fairly closely as follows:

$$C_{DN} = C_{Di} = K C_N^2 = \frac{C_N^2}{C_{N\alpha}} \quad (4-11)$$

The above expression is quite accurate, particularly for straight wings or triangular wings with supersonic leading edge. At lower supersonic speeds where subsonic leading edge is realized, "leading-edge suction" effect exists and results in a lower drag-rise factor K as shown in Fig. 4-4.

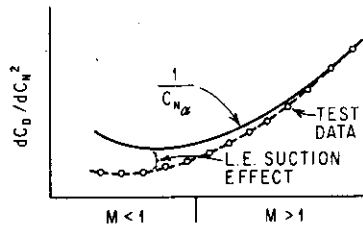


FIG. 4-4. Drag-rise factor vs. Mach number.

4-5. INTERFERENCE DRAG

Interference effects on drag in the transonic- and supersonic-speed regions are not completely understood and hence are difficult to evaluate. Theories such as the transonic- and supersonic-area rules^{12,13} are available to predict trend and with some degree of accuracy the actual magnitude of the drag of composite configurations (i.e., body plus wing, etc.). The methods and procedures on the usage of these highly mathematical theories have been greatly simplified with the aid of automatic computing equipment. In most aircraft companies the area-rule methods are programmed on automatic computers and hence the magnitude of the problem of drag (interference) evaluation is greatly reduced.

Quite frequently one must rely upon experimental results and correlations for an accurate evaluation of this interference drag. Much more effort is still necessary before a quick solution to this problem can be found.

4-6. BOOST-GLIDE TRAJECTORY

Boost-glide trajectory is defined as one in which the missile is rapidly accelerated to its maximum speed and then coasts power-off the remaining portion of its trajectory. For relatively short range missiles (i.e., AAM's, SAM's, SSM's, or ASM's described in Chap. 2), this type of trajectory is very common and warrants some consideration. Several methods are available for computing the range and velocity history of missiles employing this type of trajectory. These are (1) "short-cut" or graphical solution, (2) iteration method by manual calculations, and (3) solution of the equations of motion by automatic computing machines. If the flight path of the missile is nonlinear like that of a short-range surface-to-surface ballistic missile, the last method mentioned is recommended over the first two methods of solution. However, for certain types of missions the missile may follow a relatively linear flight path, for which case the graphical or manual iteration methods may be used. A detailed description of the latter two methods is given below.

1. Graphical Solution. This "short-cut" method has been found to be extremely useful and timesaving in the evaluation of performance characteristics for short-range missiles which follow essentially a straight flight path, i.e., level flight, diving or climbing flight trajectory. It is both desirable and convenient first to calculate the burnout condition by the analytical method and then to use the graphical solution for the power-off portion of the trajectory. The essential data which define the burnout condition are (1) missile weight, (2) velocity, and (3) range or space coordinate of the missile. The weight at burnout is readily known by subtracting the weight of the rocket-motor propellant (for an integral rocket motor) from the launch gross weight of the missile. In case of an external droppable booster the weight of the motor casing and associated attachments must also be subtracted. The velocity at burnout is the sum of the initial launch velocity and the incremental velocity due to boost ΔV_b , which may be calculated by the familiar equation shown below.

$$\Delta V_b = K' I_{sp} g \ln \frac{W_L}{W_E} - g t_b \sin \gamma_L \quad (4-12)$$

where K' = factor to account for drag effects

I_{sp} = rocket-motor specific impulse, lb-sec/lb of propellant, sec

W_L = missile launch weight, lb

W_E = missile launch weight minus propellant weight, lb

γ_L = launch attitude (assumed constant), deg

t_b = rocket-motor burning time, sec

A detailed derivation of Eq. (4-12) is presented in Appendix D. The velocity at the end of boost V_b is given as

$$V_b = V_L + \Delta V_b \quad (4-13)$$

where V_L = initial launch velocity

The distance traveled during boost S_b may be calculated by

$$S_b = \frac{V_L + V_b}{2} t_b \quad (4-14)$$

In order to calculate the value of ΔV_b , the value of K' must first be determined. This can be done by calculating ΔV_b by Eq. (4-12) by assuming $K' = 1$. The uncorrected value of ΔV_b (denoted as $\Delta V_{b_{unc}}$) thus determined is then used to determine the uncorrected end of boost velocity $V_{b_{unc}}$ using Eq. (4-13). The weighted average drag can then be determined for the $V_{b_{unc}}$ and V_L (and altitude) conditions; hence a fairly accurate value of K' is obtained. By substituting this new value of K' into Eq. (4-12) the value of ΔV_b , and hence V_b , can be readily determined. If better accuracy is desired the above process may be repeated using the second approximation of V_b to determine K' and hence ΔV_b and V_b . However, for most practical applications only one approximation is required. Having thus calculated the value of V_b , the distance traveled during boost or accelerated flight can be readily calculated by Eq. (4-14). With the conditions at burnout established one can proceed with the graphical method of evaluating the trajectory characteristics of the remaining portion of flight of the missile.

The simple case of a straight and level flight trajectory is first used to illustrate the graphical solution. The procedure involved in this graphical solution is as follows:

1. Calculate the drag of the missile as a function of velocity by the following relationship:

$$D = (C_{D_0} + KC_L^2 + C_{D_\delta} \delta_{TR})qS \quad (4-15)$$

where $C_L = W_E/qS$ (W_E is launch weight minus propellant weight, C_{D_0} is the drag coefficient due to control-surface deflection, and δ_{TR} is the control-surface deflection required for trim).

2. Plot D vs. V as shown in Fig. 4-5.
3. Establish slope n which is defined as

$$n = -\frac{\Delta V}{D} = -\frac{g \Delta t}{W} \quad (4-16)$$

where Δt is a constant.

4. Impose slope n at point A , the condition at burnout, and establish point B . $\Delta V'_1$ is the first approximation of velocity decrement

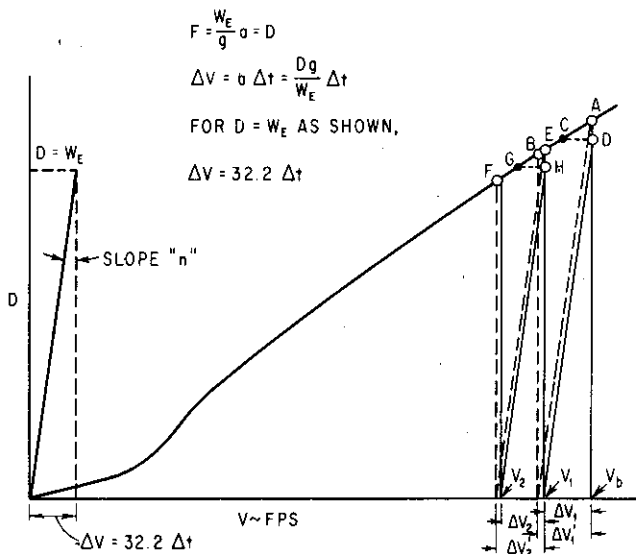


FIG. 4-5. Graphical solution—level-flight condition.

at the end of the first constant time interval Δt_1 . Since the drag at point A (assumed to be constant throughout Δt_1) is obviously higher than the average drag over Δt_1 interval, a second approximation must be made.

5. Use average drag C between A and B and again impose slope n at V_b , point D . The value of ΔV_1 thus determined is generally sufficiently accurate to establish the conditions at the end of Δt_1 (i.e., V_1 and S_1).

6. Calculate V_1 and S_1 by

$$V_1 = V_b + \Delta V_1 \quad (4-17)$$

$$S_1 = S_b + \frac{V_b + V_1}{2} \Delta t_1 \quad (4-18)$$

7. Use point *E* as the initial starting condition for the second time interval Δt_2 to determine $\Delta V'_2$.
8. Use average drag *G* between *E* and *F* and again impose *n* at V_1 (point *H*) to determine ΔV_2 .

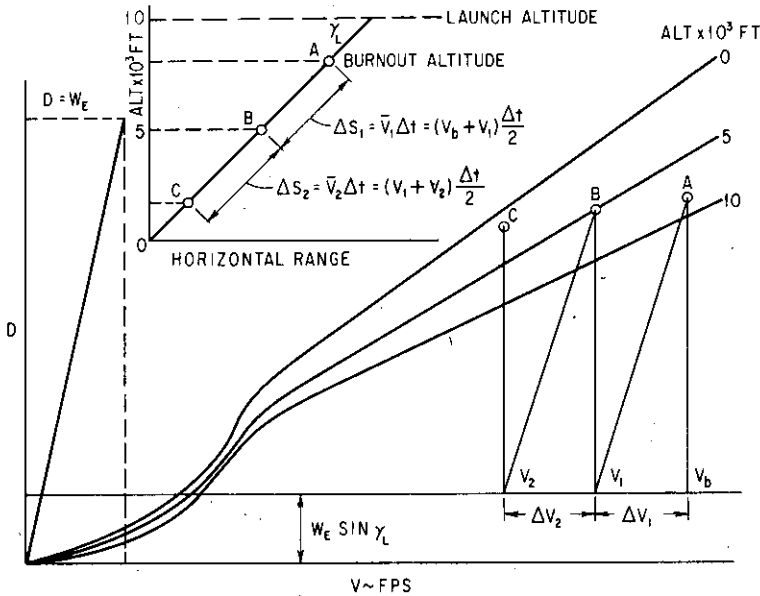


FIG. 4-6. Graphical solution—diving-flight condition.

9. Calculate V_2 and S_2 by

$$V_2 = V_1 + \Delta V_2 \quad (4-19)$$

$$S_2 = S_1 + \frac{V_1 + V_2}{2} \Delta t_2 \quad (4-20)$$

10. Repeat steps 4 through 9 until the velocity or desired range is obtained.

The diving (straight-line) flight trajectory is used next to illustrate the graphical solution. The principle involved is identical except for a few modifications to account for altitude changes and missile-weight component. The procedure involved in this case is as follows:

1. Calculate the drag of the missile as a function of velocity for a range of altitude conditions using Eq. (4-15). The value of C_L is defined in this case as $(W_E \cos \gamma_L)/qS$.
2. Plot *D* vs. *V* as shown in Fig. 4-6.
3. Establish slope *n* as before.

TABLE 4-1. SOLUTION BY ITERATION METHOD

	1	2	3	4	5	6	7	8	9	10	11	12	13
	Flight time	$M = V/c = 1/1.107$	$b = \frac{1}{2} \rho V M^2 = 1,481 M^2$	$C_{D_0} + K \left(\frac{q S_n}{W} \right)^2$	$D = (C_{D_0} + C_{D_i}) q S_n$	Rocket-motor thrust	$T - D$, lb	a , ft/sec ²	ΔV , fps	V , fps	\bar{V} , fps	ΔS , ft	ΣS , ft
	t , sec	M	q , psf	$C_{D_0} + C_{D_i}$	D , lb	T , lb	$T - D$, lb	a , ft/sec ²	ΔV , fps	V , fps	\bar{V} , fps	ΔS , ft	ΣS , ft
A	0	0.400	236	0.200	37	10,000	9,963	642	---	447.0	---	---	0
B ₁	0.1	0.459	312	0.200	49	10,000	9,951	(646)	64.4	511.4	---	---	48
B	0.1	0.459	312	0.200	49	10,000	9,951	648	64.5	512.5	479.8	48	48
C	0.2	0.490	397	0.200	63	10,000	9,937	652	65.1	577.6	545.1	55	103
D	2.0	4.00	4,000	0.320	1,005	10,000	8,995	72.4	---	1,837.0	---	---	2,284
E	2.0	4.00	4,000	0.320	1,005	0	-1,905	-81.0	---	1,837.0	---	---	2,284
F ₁	2.0	4.00	3,670	0.330	954	0	-954	(-77.0)	-79.0	1,758.0	---	---	2,464
F	3.0	4.00	3,670	0.330	954	0	-954	-76.8	-78.9	1,758.1	1,797.6	180	2,464
	4.0	4.00	3,370	0.341	905	0	-905	-72.8	-74.7	1,683.4	1,720.8	172	2,636

Flight condition: $M_L = 0.4$ at sea level. $T = 10,000$ lb. $t_0 = 2$ sec. $W_L = 500$ lb. $W_p = 100$ lb. $W_E = 400$ lb. $S_n = 0.786$ ft². Sea-level flight altitude, c (speed of sound) = 1,117 fps.

* See Eq. (4-21).

4. Shift the abscissa up by $W_E \sin \gamma_L$ as shown in Fig. 4-6.
5. Calculate conditions at burnout, V_b and S_b , using Eqs. (4-13) and (4-14).
6. Arc off S_b along the flight-path diagram shown in Fig. 4-6 and read the altitude at burnout.
7. Impose slope n at burnout condition, point A as shown.
8. Read ΔV_1 (first approximation) at the intercept of slope n with the new abscissa and calculate S_1 by Eq. (4-18).
9. Arc off S_1 on the flight-path diagram and read the new altitude (point B).
10. Compare the drag at altitude B with that at burnout altitude A . If the drag at B is approximately the same as that at A no further approximation is required, in which case point B may be used as the starting point for the next time interval Δt_2 . However, if the drag at B is significantly different from that at A , an average value of these two drags must be used for a second approximation, as was done in the illustration for the level-flight case shown in Fig. 4-5. In general, for a diving-flight straight-line trajectory no such second approximation is required.
11. Repeat steps 7 through 10 until the missile impacts or reaches the desired altitude and/or velocity.

The accuracy of the above-described graphical method may be improved by using (1) small values of Δt or (2) second or third approximations. In practice the former method is less involved and is therefore recommended.

2. Iteration Method. This method is rather tedious for manual computation. However, where only a limited number of trajectories is involved, this method may be used. A simplified boost-glide constant-altitude trajectory (similar to the first one used to illustrate the graphical method) is used here to illustrate this method of solution. The boost phase of the trajectory may be calculated by Eqs. (4-12) through (4-14). However, for purpose of illustration, the incremental velocity (and hence end of boost velocity) and distance traveled during boost will be calculated by the iteration method. The power-off flight will also be calculated by this method.

Table 4-1 presents the calculations for several time intervals during both phases of flight to illustrate the procedures involved in this method of solution for a typical level-flight trajectory. Row A in Table 4-1 represents the initial launch condition of the missile. In order to start the calculation for the first time interval (i.e., row B) the value of acceleration a in column 8 must be estimated. In the

sample calculation, a value of 646 fps was assumed and was based on the predicted behavior of the missile for the flight conditions involved. Using this assumed value of 646 fps, the pertinent information for row B can be readily determined as follows:

1. Use the average value of a from rows A and B to calculate V for column 9.
2. Next, calculate V , column 10.
3. With V thus determined, calculate M and q , columns 2 and 3.
4. Read the value of C_{D_0} from the plot of C_{D_0} vs. M and calculate C_{D_1} for the appropriate Mach number and q .
5. Calculate the drag, column 5.
6. Calculate the new value of a for row B.

From the sample calculation, the new value of a was determined to be 648 fps as compared with the previously assumed value of 646 fps; this indicates that the assumed value of 646 fps appears to be reasonably accurate. However, if increased accuracy is desired or required, a second approximation should be made using the average value between the first assumed value of 646 fps and the calculated value of 648 fps. In general, the second approximation should yield sufficiently accurate results to permit one to proceed with the iteration method as detailed below:

7. Calculate ΔV , column 9, row C, by the following expression:

$$\Delta V = 3a_{n-1} - a_{n-2} \quad (4-21)$$

where a_{n-1} and a_{n-2} are the value of acceleration for the time interval before and twice the time interval before the point in question, respectively (i.e., $a_{n-1} = 648$ and $a_{n-2} = 642$ fps in the sample calculation). Derivation of Eq. (4-21) is presented in Appendix E.

8. Calculate V , column 10, as shown in Table 4-1.
9. Calculate M and q as before (i.e., step 3).
10. Complete columns 4 through 8.
11. Calculate ΔS and ΣS , columns 12 and 13. This completes the calculations for row C.

The above steps 7 through 11 are repeated for the duration of the boost phase. Row D represents the end-of-boost condition. In order to start the power-off phase of flight, row E must be calculated for $T = 0$ condition. At this point, the time interval Δt may be changed to minimize the number of calculations required. Again, in order to start the calculation for the first time interval (i.e., row F), the value of acceleration a in column 8 must be estimated. The procedure previously outlined is then used to establish the final values for row F.

Steps 7 through 11 may then be used to determine the complete trajectory information. It should be noted that the time interval must be kept constant throughout the calculation. This limitation is readily apparent from the derivation of Eq. (4-21) in Appendix E. However, if it is found desirable to change the time interval, a restart at this point is necessary. In general, the appropriate time interval can be selected at the beginning of the computation and kept constant throughout the trajectory.

4-7. BOOST-SUSTAIN TRAJECTORY

This type of trajectory consists of a relatively short boost period followed by a sustained powered flight. The velocity in the latter phase of flight is generally constant, in which case the trajectory is termed "boost, constant, sustained" flight. Where the velocity during sustaining increases or decreases, the trajectory is termed "boost, oversustained" or "undersustained," respectively. For certain applications, the boost-sustain trajectory is preferred over the boost-glide. The main advantages are (1) reduction in the maximum Mach number required for a given range, (2) alleviation of the aerodynamic heating problem, (3) better missile aerodynamic performance due to the avoidance of high drag, and (4) simplification of the control system in that the aerodynamic gain (for a given altitude condition) is held nearly constant.

For this type of trajectory, the methods outlined in Sec. 4-5 may be used to determine the missile-performance characteristics during the boost phase of flight. For the sustained powered portion of flight either the graphical or iteration method may be used, particularly for the over- or undersustained cases. In the graphical solution the abscissa of the drag vs. velocity plot must be shifted upward by the value of the sustainer thrust (constant thrust is assumed, of course). However, for the common and simple case wherein the missile is sustained at a near constant velocity, a rather simple expression to approximate the range R traveled during this portion of flight can be derived as follows:

$$T = D$$

$$T \times t = \text{total impulse} = I = Dt \quad (4-22)$$

since

$$I = W_p I_{sp} \quad (4-23)$$

where W_p = weight of propellant

I_{sp} = propellant specific impulse

Eq. (4-22) becomes

$$W_p I_{sp} = Dt \quad (4-24)$$

since $t = R/V$ and $D = C_D \frac{1}{2} \rho V^2 S$, Eq. (4-24) can be written as

$$R = \frac{2W_p I_{sp}}{C_D \rho V S} \quad (4-25)$$

For a given sustainer propellant weight W_p , the flight time during the sustained portion of flight is

$$t = \frac{2W_p I_{sp}}{C_D \rho V^2 S} \quad (4-26)$$

or simply

$$t = \frac{R}{V} \quad (4-27)$$

The above simplified expressions [Eqs. (4-25) and (4-26)] may be used only for relatively short range missiles (i.e., $W_p \ll$ missile gross weight). For longer-range missiles, such as the conventional cruise type, somewhat more exact expressions must be used to calculate the range and flight time, as will be discussed in the next section.

It is of interest to point out that, if the missile weapon system permits, it is very advantageous from the standpoint of performance first to boost the missile up to speed, let it coast down to some lower velocity, and then sustain for the remaining portion of the trajectory. Using this technique, the high-drag region is avoided and a substantial range improvement consequently results. However, the power-plant design problems associated with this mode of flight are somewhat more severe, particularly when solid-propellant rocket motors are used. These problems will be discussed in Chap. 13.

4-8. LONG-RANGE CRUISE TRAJECTORY

The methods used to determine the performance characteristics of cruise missiles are identical with those used on conventional manned aircraft. Again, it is necessary to know the engine performance (i.e., thrust, fuel consumption, etc.), drag, and operating altitude conditions to determine the various performance parameters such as maximum speed and rate of climb. To help understand the fundamentals behind these calculations, the forces involved are illustrated in Fig. 4-7. The methods used to determine the pertinent performance parameters are discussed below.

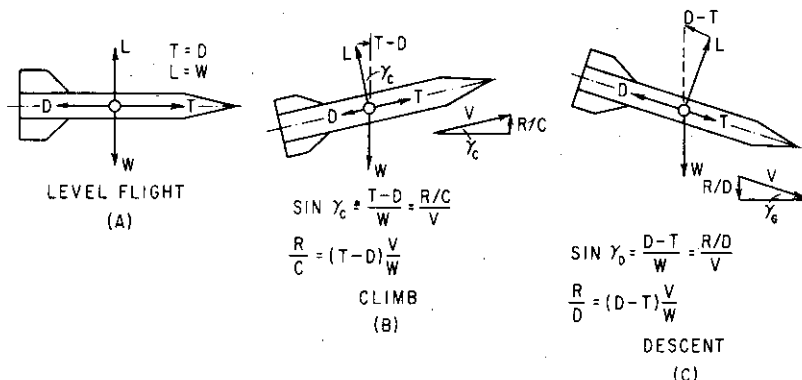


FIG. 4-7. Force diagram for various equilibrium flight conditions.

1. Maximum Speed. The maximum speed of the cruise missile for a given operating altitude is readily determined if the engine performance and missile drag characteristics are known. The latter may be calculated by the following expression:

$$D = \left[C_{D_0} + K \left(\frac{W}{qS} \right)^2 + C_{D_b} \delta_{TR} \right] qS \tag{4-28}$$

The value of drag is equivalent to the thrust required for level flight at a given constant altitude and velocity. The net thrust is obtained from the engine specification and must be corrected for installation losses such as inlet and duct losses. The resultant plot of this information is shown in Fig. 4-8 for a given altitude condition. By inspection of Fig. 4-8, the maximum speed of the missile is defined by point A, where the net thrust available is equal to the thrust required to maintain level flight. Point A is really a fictitious or theoretical V_{max} since it cannot be realized in actual flight. This is readily apparent when one considers the fact that the missile cannot accelerate to this point because the force $T - D$ required approaches zero at this point. Hence in actuality V_{max} will

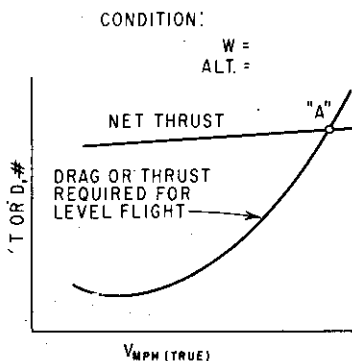


FIG. 4-8. Determination of V_{max} .

be somewhat less than that determined by this method. However, the theoretical value of V_{\max} does provide a common basis for performance comparison with other flight conditions or missile systems.

2. Rate of Climb. The expression for the rate of climb can be readily derived by inspection of Fig. 4-7 and is as follows:

$$\sin \gamma_C = \frac{T - D}{W} \quad (4-29)$$

where γ_C = flight-path angle

Since $\sin \gamma_C$ is also equal to $(R/C)/V$, Eq. (4-29) becomes

$$\frac{R}{C} = \frac{(T - D)V}{W} \quad (4-30)$$

Equation (4-30) is more commonly written as

$$\frac{R}{C} = \frac{88(T - D)V}{W} \quad (4-31)$$

where R/C is in fpm and V is in mph. The rate of climb at various speeds can be calculated using the information in Fig. 4-8 and

Eq. (4-31). The maximum rate of climb $(R/C)_{\max}$ is readily determined by plotting R/C vs. V , from which the speed for best rate of climb $V_{(R/C)\max}$ is also determined. The above steps may be repeated at other flight altitudes to determine R/C for the entire range of operating altitudes in order to determine the time to climb to various altitudes.

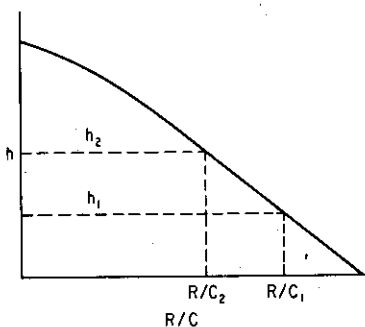


FIG. 4-9. Determination of time to climb.

may be done by adding the time increments required to climb between any two altitudes h_1 and h_2 , as shown in Fig. 4-9. In general

$$dt = \frac{dh}{dh/dt} = \frac{dh}{R/C} \quad (4-32)$$

or

$$\int_{t_1}^{t_2} dt = \int_{h_1}^{h_2} \frac{1}{R/C} dh \quad (4-33)$$

Since R/C is assumed to be linear between h_1 and h_2 , the time to climb from h_1 to h_2 may be derived from Fig. 4-9:

$$\begin{aligned} \frac{R}{C} &= \frac{R}{C_1} - \frac{R/C_1 - R/C_2}{h_2 - h_1} (h - h_1) \\ &= \frac{(R/C_1)h_2 - (R/C_2)h_1 + h(R/C_2 - R/C_1)}{h_2 - h_1} \end{aligned} \quad (4-34)$$

$$\text{or} \quad t_2 - t_1 = \Delta t = \int_{h_1}^{h_2} \frac{(h_2 - h_1) dh}{(R/C_1)h_2 - (R/C_2)h_1 + h(R/C_2 - R/C_1)} \quad (4-35)$$

$$\text{hence} \quad \Delta t = \frac{h_2 - h_1}{R/C_2 - R/C_1} \ln \frac{R/C_2}{R/C_1} \quad (4-36)$$

If very small increments in altitude are used, the following simplified expression may be used:

$$\Delta t = \frac{2(h_2 - h_1)}{R/C_1 + R/C_2} \quad (4-37)$$

The above assumes a constant speed during climb in that all the excess thrust was utilized to climb. For most modern high-performance aircraft and missiles the excess thrust is quite large so that the flight path approaches vertical. Moreover, the speed for best climb generally increases rapidly with altitude, and a programmed climbing schedule is more practical.

The optimum climbing schedule can be approximated by plotting the rate of climb vs. speed for various altitudes and drawing a straight line which most nearly goes through the maximum.

For this case a considerable percentage of the excess thrust is used to accelerate the aircraft, and a correction to the rate of climb is required. Equation (4-29) then becomes

$$\sin \gamma_C = \frac{T - D}{W} - \frac{a}{g} \quad (4-29a)$$

where a = acceleration. But

$$a = \frac{dV}{dt} = \frac{dV}{dh} \frac{dh}{dt} = \frac{dV}{dh} V \sin \gamma_C$$

and the equation of motion may be written

$$(RC)_a = \frac{(RC)_{a=0}}{1 + (V/g)(dV/dh)} \quad (4-31a)$$

where $(RC)_a$ = rate of climb in accelerated flight

$(RC)_{a=0}$ = rate of climb at constant speed

In practice, it is sufficiently accurate to use an average dV/dh from the curve previously described. The time to climb may then be computed as before, utilizing the reduced rates of climb (RC)_a.

4. Stall Speed. The stall or minimum speed of the missile may be calculated by the following expression:

$$V_S = \sqrt{\frac{2W}{C_{L_{\max}} \rho S}} \quad (4-38)$$

A typical summary plot of the above-mentioned performance parameters for the cruise missile is shown in Fig. 4-10.

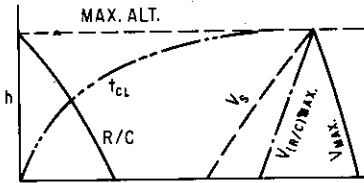


FIG. 4-10. Summary of performance.

5. Maximum Range. The maximum range of a cruise missile is the sum of the distances traversed during climb and level-flight portions of its trajectory. The distance traveled during climb may be calculated by the following equation:

$$R_{CL} = \bar{V}_{(R/C)_{\max}} t_{CL} \cos \gamma_{CL} \quad (4-39)$$

where $\bar{V}_{(R/C)_{\max}}$ = average velocity for the best rate of climb

t_{CL} = time to climb to cruise altitude

γ_{CL} = flight-path angle in climb

The range for a given level-flight condition may be readily determined by the procedures outlined below:

1. Select three or four different flight speeds and missile-weight conditions.

2. Calculate $C_L = W/qS$.

3. Determine C_D from C_D vs. C_L plot or $C_D = C_{D_0} + KC_L^2 + C_{D_0} \delta_{TR}$ at the appropriate Mach-number condition.

4. Calculate $D = C_D q S$ = thrust required.

5. Determine the engine fuel consumption, lb/hr, from the engine specifications.

6. Convert the engine fuel consumption in terms of miles per pound of fuel consumed by

$$\frac{V}{\text{lb/hr}} = \frac{\text{miles}}{\text{hr}} \times \frac{\text{hr}}{\text{lb}} = \text{miles/lb}$$

7. Plot miles/lb vs. V as shown in Fig. 4-11.

8. Read from Fig. 4-11 the maximum values of miles/lb and plot these maximum values vs. missile weight as shown in Fig. 4-12.

9. The range during cruise is the area under the curve defined in Fig. 4-12.

Steps 1 through 9 are then repeated for other flight or cruise altitudes to determine the over-all range of the missile for the various mission profiles.

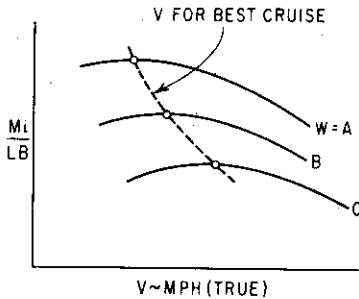


FIG. 4-11. Determination of best miles per pound and V for best cruise.

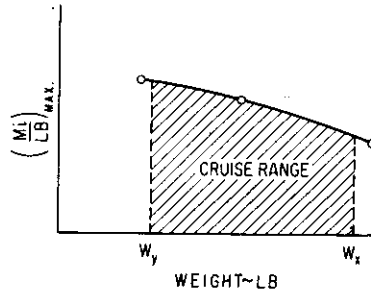


FIG. 4-12. Determination of cruise range. W_x = weight at start of cruise; W_y = weight at end of cruise.

4-9. LONG-RANGE BALLISTIC TRAJECTORY

The general nature of the trajectory flown by long-range ballistic missiles is shown in Fig. 4-13. Because of the enormous weight involved, the missile is launched vertically from the launching pad. Because of the low values of dynamic pressure during lift-off, no large control or guidance commands other than those required to keep the missile in a vertical ascent are required. As previously noted, auxiliary jet controls are used during lift-off until sufficient q is attained, whereupon aerodynamic controls are used. In certain cases, jet controls are sufficiently adequate to eliminate completely the aerodynamic control surfaces. After a few seconds

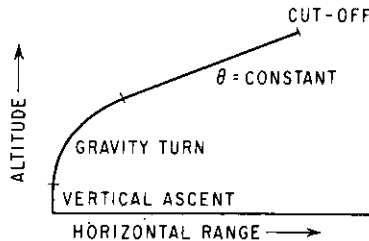


FIG. 4-13. Typical ballistic-missile trajectory during powered flight.

of vertical rise, the missile is commanded into a "gravity" (or zero-lift) turn by simply tilting the velocity vector of the missile for a short period. This "gravity" turn is continued until the missile reaches a sufficiently high altitude, at which point the missile is commanded to fly a constant-attitude trajectory as shown in Fig. 4-13. The altitude at which

the missile starts its constant-attitude flight is primarily dependent on the severity of the air loads associated during this transition phase. Powered flight is continued in this predetermined optimum attitude or angle until the required velocity is attained, whereupon thrust termination is effected. Immediately upon thrust termination, the re-entry body is separated from the last stage (in the case of multistaged configuration) and commences its free-flight ballistic trajectory to the target. The above-described trajectory may be modified somewhat by certain limitations of the guidance system in the missile.

The methods used to calculate the performance characteristics of ballistic missiles are somewhat different from those previously described in this chapter. While these methods appear to be relatively simple, careful considerations must be given to the various design and trajectory parameters in order to realize the desired optimum performance. The following sections will be concerned with the methods of calculation as well as a brief discussion of the effects on performance of several of the important design and trajectory parameters.

The problem of determining performance characteristics of ballistic missiles may be conveniently divided into two parts, powered flight and unpowered free-flight trajectories, which are discussed below.

1. Powered Flight. The equation of motion for the missile in powered flight may be written as follows:

$$\frac{W_E + W_p}{g} \frac{dV}{dt} = \frac{V_j}{g} \frac{dW_p}{dt} + A_e(p_e - p_o) - C_D \frac{1}{2} \rho V^2 S - (W_E + W_p) \sin \gamma \quad (4-40)$$

Thrust
Drag
Gravity

where W_E = weight of missile at burnout

W_p = weight of propellant

V_j = jet-exhaust velocity (gI_{sp} at SL)

A_e = nozzle exit area

p_e = nozzle exit pressure

p_o = ambient exit pressure

It is apparent that, because of the drag term, no closed solution to Eq. (4-40) is obtainable. Hence it is necessary to solve Eq. (4-40) by either of two methods: (1) the iteration method outlined in Sec. 4-6 or (2) by Eq. (4-12), by making an approximate correction for drag and gravity losses as previously outlined. One further simplification may be made in that the missile is assumed to fly a constant-rate-of-turn course instead of a "gravity" turn in actual flight. This last assumption permits one to apply an average correction readily for gravity losses [Eq. (4-12) or (4-40)] during powered flight.

TABLE 4-2. METHOD OF SOLUTION TO BALLISTIC MISSILE PERFORMANCE DURING POWERED FLIGHT

Flight time	Missile weight	$M = V/c$	$b = \frac{1}{2} \gamma p M^2$	C_{D_0}	$D = C_D q S$	$T = I_0 a_0 W^a + A_0 (d_0 - p_0)$	$T - D$	$\frac{M}{(D)(\theta)} = I_0 a_0$	$\theta \sin \beta = a_0$	Σa_0	$\Sigma v_0 + v_1 = a_0$	$\frac{z}{V} (v_0 - v_1 \sin \beta) = \Delta V$	ΔV	V , fps	ΔV , fps	θ	θ	$\frac{z}{V} (\theta + \theta) = \theta$	$\frac{z}{V} (\theta + \theta) = \theta$	$\bar{V} \sin \theta$	$\bar{V} \cos \theta$	Δh	Σh	$z/(y + 1 - u) = y$	y
t, sec	W, lb	M	q, psf	C_{D_0}	D, lb	T, lb	T - D, lb	a_0 , ft/sec ²	a_0 , ft/sec ²	Σa_0 , ft/sec ²	$\Sigma v_0 + v_1 = a_0$	ΔV , fps	ΔV , fps	V, fps	ΔV , fps	θ	θ	$\frac{z}{V} (\theta + \theta) = \theta$	$\frac{z}{V} (\theta + \theta) = \theta$	$\bar{V} \sin \theta$	$\bar{V} \cos \theta$	Δh	Σh	$z/(y + 1 - u) = y$	y
0	20,000	0	0	0.2	0	75,000	75,000	120	32	88	88	0	0	0	0	90	90	89	89	0	0	0	0	0	0
2	19,400	0.161	38	0.2	76	75,000	74,962	124	32	92	92	180 est.	180	180	88	88	88	88	88	90	90	180	180	90	90
4	18,800	0.330	159	0.2	318	75,187	74,869	128	32	96	96	188	188	368	86	86	87	87	87	274	14	548	722	451	451

Flight condition: $W_L = 20,000$ lb. $W_p = 15,000$ lb. $W_x = 5,000$ lb. $t_0 = 50$ sec. $\dot{W}_p = 300$ lb/sec. $I_0 = 250$ sec (SL).
 $S = 10$ ft². $A_0 = 5.5$ ft². $p_0 = 2,116$ psf. $\theta_0 = 40^\circ$ (from horizontal). $\dot{\theta} = 1^\circ/\text{sec}$ (assumed constant).

Flight time t, sec	p, fps at Σh	$p_0 - p$	c, fps at Σh	ΔR , ($\bar{V} \cos \theta$) Δt	ΣR , $R_{n-1} + \Delta R$
0	2,116	0	1,117	0	0
2	2,116	0	1,117	80	80
4	2,082	34	1,115	28	28

At the start of a new missile design, it is desirable to calculate the missile-performance characteristics for a few typical flight conditions using the iteration procedure previously outlined. For the type of trajectory involved, it is necessary to modify the procedure somewhat to account for the changing flight path during powered flight. The modified procedure is shown in Table 4-2. Having thus determined the general nature of the trajectory, one can make first-order approximation for other missile designs or flight conditions using Eq. (4-12) to determine the velocity of the missile at burnout. The range and altitude at burnout may be approximated by the following expressions:

$$x = V(\cos \bar{\gamma})t_b \quad (4-41)$$

$$y = V(\sin \bar{\gamma})t_b \quad (4-42)$$

Since the distance the missile traversed during powered flight is only a small percentage of the total range of the missile, Eq. (4-41) appears to be adequate. Equation (4-42) also appears to be satisfactory since inaccuracy in the determination of altitude at burnout has only a small effect on the range of the missile, as will be shown subsequently. In the above discussion, a flat earth is assumed. This assumption is valid since the traverse during powered flight is relatively small.

2. Unpowered Flight. Once the conditions at burnout are established (i.e., cutoff velocity, altitude, and angle), the range for the

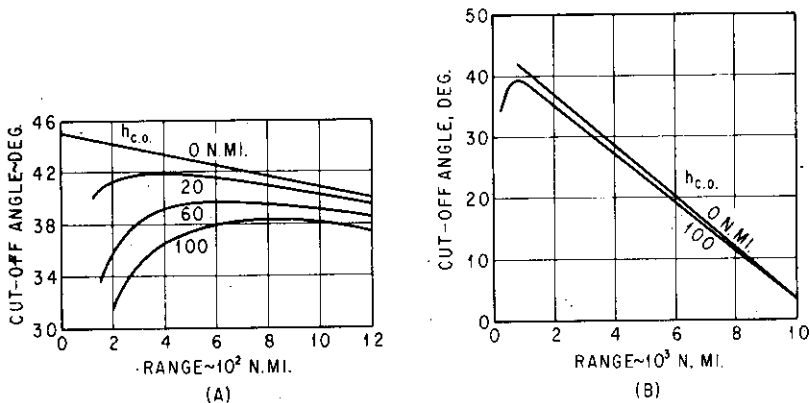


FIG. 4-14. Cutoff angle vs. range.

free-flight portion of the trajectory is readily determined. The free-flight ballistic trajectory is essentially identical to a vacuum trajectory of an object traveling within the gravitational field of a spherical non-rotating earth. The resulting trajectory is one of Kepler's planetary

ellipses with the far focus located at the center of the earth. Expressions which relate the range of the missile as a function of the various trajectory parameters, at the cutoff condition, have been used to calculate the missile-performance characteristics in free flight. The results of these calculations are shown in Fig. 4-14. The maximum range (and corresponding times of flight) shown in Fig. 4-15 were obtained by

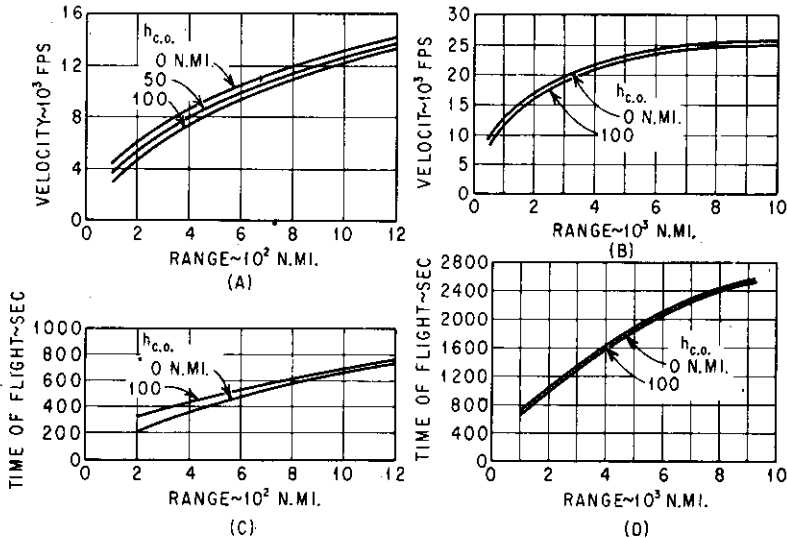


FIG. 4-15. (A and B) Velocity vs. range (optimum launch angle, free flight). (C and D) Flight time vs. range (free flight).

using the optimum-cutoff-angle information from Fig. 4-14. It is apparent from Fig. 4-15 that the cutoff velocity is the primary parameter from the standpoint of range. The cutoff altitude has only a small effect on range. This is particularly true for the long-range conditions.

By neglecting the drag effects on the range traversed during powered flight, the range of a ballistic missile was shown to be¹⁴

$$R = r_0 \varphi = 2r_0 \tan^{-1} \frac{\sin \theta_f \cos \theta_f}{(1/\bar{V}_f^2) - \cos^2 \theta_f} \tag{4-43}$$

where $\bar{V}_f = V_f/V_s =$ ratio of cutoff velocity to satellite velocity
 $\theta_f =$ angle of incidence as shown in Fig. 4-16

The optimum trajectory (defined as one yielding maximum range for

a given velocity V_f) was determined by differentiating Eq. (4-43) with respect to θ_f and equating to 0. The resulting expressions became

$$V_f^2 = 1 - \tan^2 \theta_f, \quad (4-44)$$

$$\varphi = \frac{R}{r_0} = \pi - 4\theta_f,$$

The results derived from the above equations are shown in Fig. 4-17.

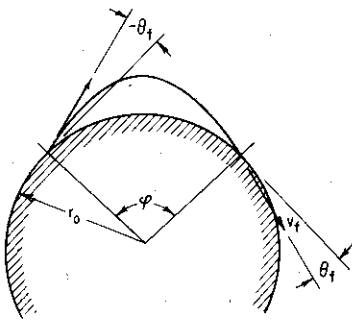


FIG. 4-16. Idealized ballistic-missile trajectory.

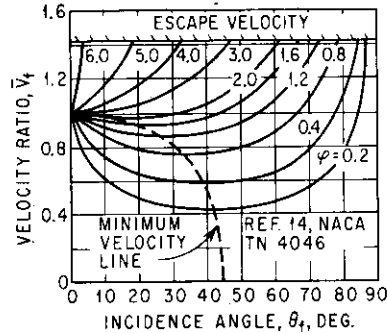


FIG. 4-17. Variation of velocity with incidence angle for various values of range of ballistic vehicles.

3. Design Considerations. Perhaps one of the most important design considerations which demand careful analysis is the requirement for rocket-motor staging. For relatively short range missiles (range less than approximately 200 miles, which varies somewhat depending upon the pay load) a single-stage rocket motor is generally adequate. However, for longer ranges, multistaging is required in order to keep the launch weight of the missile to a minimum. Also, for a given allowable launch weight, increased range is possible by multistaging. By optimizing the distribution of structures and propellant between the various stages of a multistage or "step rocket,"¹⁵⁻²³ maximum range may be realized. The pronounced effects of staging on range may readily be shown with two simplified examples presented below:

Example 1: Launch weight = 20,000 lb, top weight = 5,850 lb.

Case a: Single stage.

Total rocket-motor weight = 14,150 lb

Propellant weight = 12,000 lb

Mass ratio = 0.85

Specific impulse $I_{sp} = 240$ sec

Neglecting drag and gravity,

$$\Delta V_1 = I_{sp} g \ln \frac{W_L}{W_E} = 240 \times 32.2 \ln \frac{20,000}{8,000} = 7,070 \text{ fps}$$

Case b: Assumed two stages of equal motor weight, mass ratio, and specific impulse as above.

Weight of one rocket motor = 7,075 lb

Weight of propellant (one motor) = 6,000 lb

$$V_1 = 240 \times 32.2 \ln \frac{20,000}{20,000 - 6,000} = 2,750 \text{ fps}$$

$$\Delta V_2 = 240 \times 32.2 \ln \frac{20,000 - 7,075}{20,000 - 7,075 - 6,000} = 4,820 \text{ fps}$$

$$\Sigma V = \Delta V_1 + \Delta V_2 = 7,570 \text{ fps}$$

From the above calculation, it is seen that the maximum velocity for the two-staged missile is approximately 7 per cent greater than that using a single-stage design. Since the range varies approximately as the velocity squared, a 14 per cent increase in range is thus realized by staging. By optimizing the mass distribution, a maximum increase in range of approximately 16 per cent may be realized.

Example 2: Launch weight = 20,000 lb, top weight = 1,150 lb.

Case a: Single stage.

Total rocket-motor weight = 18,850 lb.

Propellant weight = 16,000 lb

Mass ratio = 0.85

Specific impulse I_{sp} = 240 sec

$$\Delta V = 240 \times 32.2 \ln \frac{20,000}{4,000} = 12,420 \text{ fps}$$

Case b: Assumed two stages of equal motor weight, mass ratio, and specific impulse as above.

Weight of one rocket motor = 9,425 lb

Weight of propellant (one motor) = 8,000 lb

$$\Delta V_1 = 240 \times 32.2 \ln \frac{20,000}{12,000} = 3,930 \text{ fps}$$

$$\Delta V_2 = 240 \times 32.2 \ln \frac{20,000 - 9,425}{20,000 - 9,425 - 8,000} = 10,870 \text{ fps}$$

$$\Sigma V = 14,800 \text{ fps}$$

From the above calculation, it is seen that the maximum velocity

for the two-staged design is approximately 19 per cent greater than for the single-stage design, corresponding to a 30 per cent increase in range. By optimum staging, a maximum increase in range of 67 per cent may be realized over the single-stage design. Hence it is apparent that both multistaging and optimum staging are mandatory from the standpoint of obtaining the maximum possible range for a given launch-weight condition.

Another important design consideration is the thrust level of the rocket motor. For a given total rocket-motor impulse, a high thrust level will result in a higher drag loss, whereas a low thrust level (which entails a longer burning time) may result in large losses due to gravity. Hence it is necessary to conduct a detailed analysis in order to determine the optimum level of thrust to yield the greatest incremental velocity, or range. The operating pressure of the rocket-motor units must also be carefully analyzed since an increase in mass ratio (defined as the ratio of propellant weight to total rocket-motor weight) may be realized with a low operating-chamber pressure. On the other hand, the specific impulse of the propellant (defined as the ratio of total impulse to weight of propellant) is degraded with decreasing operating pressure.

SYMBOLS

A	aspect ratio
A_e	exit area of nozzle
C_D	drag coefficient D/qS
C_{D_i}	induced-drag coefficient
C_{D_N}	drag (coefficient) due to normal force
C_{D_w}	wave-drag coefficient
C_{D_0}	drag coefficient for zero lift
C_{D_δ}	drag (coefficient) due to control-surface deflection
C_f	skin-friction-drag coefficient
C_{f_0}	skin-friction-drag coefficient for incompressible flow
C_L	lift coefficient
$C_{L_{max}}$	maximum lift coefficient
C_N	normal-force coefficient
C_{N_α}	normal-force-curve slope $\partial C_N / \partial \alpha$
D	drag forces
I	total impulse
I_{sp}	fuel specific impulse
K	drag-rise factor

K'	a factor to account for drag effects [see Eq. (4-12)]
M	Mach number
P	pressure coefficient
R	range of missile
$R/C, RC$	rate of climb
Re	Reynolds number
S	reference area, or range of missile
S_l	wetted area over length l shown in Fig. 4-2
S_x	wetted area over length x shown in Fig. 4-2.
T	thrust
V	forward speed
\bar{V}	average velocity
V_f	cutoff velocity
\bar{V}_f	ratio of cutoff velocity to satellite velocity V_f/V_s .
V_j	jet-exhaust velocity
V_S	stall speed
V_s	satellite velocity
W	weight
W_E	weight of missile in burnout condition.
W_L	weight of missile at launch
W_p	weight of propellant
a	acceleration
d	body diameter
h	altitude
h_{co}	altitude at cutoff
l	length
m	a correlation constant used in Eqs. (3-58a) and (4-10)
n	a slope used in Fig. 4-5
p_o	ambient static pressure
p_e	static pressure at the nozzle exit
q	dynamic pressure ($\frac{1}{2}\rho V^2$)
r_o	radius of the earth
t	(flight) time
t_b	burning time of rocket motor
α	angle of attack
β	$\sqrt{M^2 - 1}$
γ	specific heat of air, or flight-path angle
γ_{CL}, γ_c	flight-path angle (in climbing flight)
γ_L	launch attitude
δ	semivertex angle of leading and trailing edges of air-foil, or control-surface deflection

δ_{TR}	control-surface deflection required for trim
θ	flight path of a ballistic-missile trajectory (see Fig. 4-13)
$\bar{\theta}$	average flight-path angle [see Eqs. (4-41) and (4-42) and Table 4-2]
θ_i	angle of incidence as shown in Fig. 4-16
ρ	density of air
φ	subtended angle shown in Fig. 4-16

Subscripts

CL	in climbing flight
E	empty or burnout condition
L	launch condition, or laminar-flow condition
N	due to normal force
T	turbulent-flow condition
TR	trim condition
a	with acceleration
b	during boost or due to boost
co	cutoff condition
$n - 1, n - 2$	denote time interval before and twice the time interval before the point in question [see Eq. (4-21)]
unc	uncorrected condition
0	incompressible as used in Eq. (4-4), or zero-lift condition as used with C_D
1, 2	denote points on trajectory (see Figs. 4-5 and 4-6)

REFERENCES

1. Coles, D.: Measurements in the Boundary Layer on a Smooth Flat Plate in Supersonic Flow I. The Problem of the Turbulent Boundary Layer, *Rept. 20-69*, C.I.T. Jet Propulsion Lab., Pasadena, Calif., June 1, 1953.
2. Smith, D. W., and J. H. Walker: Skin-friction Measurements in Incompressible Flow, *NACA Tech. Note 4231*, March, 1958.
3. Chapman, D., and R. H. Kester: Measurements of Turbulent Skin Friction on Cylinders in Axial Flow at Subsonic and Supersonic Velocities, *J. Aeronaut. Sci.*, vol. 20, no. 7, July, 1953.
4. Frankl, F., and V. Voishel: Turbulent Friction in the Boundary Layer of a Flat Plate in a Two-dimensional Compressible Flow at High Speeds, *NACA Tech. Mem. 1053*, 1943.
5. Rubesin, M. W., R. C. Maydew, and S. A. Varga: An Analytical and Experimental Investigation of the Skin Friction of the Turbulent Boundary Layer on a Flat Plate at Supersonic Speeds, *NACA Tech. Note 2305*, February, 1951.
6. Cope, W. F.: The Turbulent Boundary Layer in Compressible Flow, *NPL Engr. Dept. British ARC 7634*, November, 1943.

7. Wilson, R. E.: Turbulent Boundary-layer Characteristics at Supersonic Speeds—Theory and Experiment, *J. Aeronaut. Sci.*, vol. 17, no. 9, p. 585, September, 1950.

8. Tucker, M.: Approximate Calculation of Turbulent Boundary-layer Development in Compressible Flow, *NACA Tech. Note* 2337, 1951.

9. Estabrooks, B. B.: An Analysis of the Pressure Distribution Measured on a Body of Revolution at Transonic Speeds in the Slotted Test Section of the Langley 8-ft. Transonic Tunnel, *NACA Research Mem.* L52D21a, June, 1952.

10. Cole, R. I.: Pressure Distributions on Bodies of Revolution at Subsonic and Transonic Speeds, *NACA Research Mem.* L52D30, July, 1952.

11. Young, A. D.: The Calculation of the Total Skin Friction Drags of Bodies of Revolution at Zero Incidence, R & M 1814, April, 1939.

12. Whitcomb, R. T.: A Study of the Zero-lift Drag-rise Characteristics of Wing-body Combinations Near the Speed of Sound, *NACA Research Mem.* L52H08, September, 1952.

13. Jones, R. T.: Theory of Wing-body Drag at Supersonic Speeds, *NACA Research Mem.* A53H18a, 1953.

14. Eggers, A. J., H. J. Allen, and S. E. Neice: A Comparative Analysis of the Performance of Long-range Hypervelocity Vehicles, *NACA Tech. Note* 4046, October, 1957.

15. Malina, F. J., and M. Summerfield: The Problem of Escape from the Earth by Rocket, *J. Aeronaut. Sci.*, vol. 14, pp. 471-480, August, 1947.

16. Vertregt, M.: A Method for Calculating the Mass Ratio of Step Rockets, *J. Brit. Interplanet. Soc.*, vol. 15, no. 2, p. 95, March-April, 1956.

17. Goldsmith, M.: On the Optimization of Two-stage Rockets, *Jet Propulsion*, vol. 27, pp. 415, 416, April, 1957.

18. Schurmann, E. E. H.: Optimum Staging Technique for Multistaged Rocket Vehicles, *Jet Propulsion*, vol. 27, pp. 863-865, August, 1957.

19. Weisbord, L.: A Generalized Optimization Procedure for N-staged Missiles, *Jet Propulsion*, vol. 28, pp. 164-167, March, 1958.

20. Arens, M.: On a Generalized Optimization Procedure for N-staged Missiles, *Jet Propulsion*, vol. 28, p. 766, November, 1958.

21. Subotowicz, M.: The Optimization of the N-step Rocket with Different Construction Parameters and Propellant Specific Impulses in Each Stage, *Jet Propulsion*, vol. 28, pp. 460-463, July, 1958.

22. Hall, H. H., and E. D. Zambelli: On the Optimization of Multistage Rockets, *Jet Propulsion*, vol. 28, pp. 463-465, July, 1958.

23. Weisbord, L.: Optimum Staging Technique, *ARS J.*, vol. 29, no. 6, pp. 445-446, June, 1959.

CHAPTER 5

STATIC LONGITUDINAL STABILITY AND CONTROL

5-1. INTRODUCTION

The effectiveness of a guided missile weapon system, in terms of accuracy and probability of kill, depends greatly on the response characteristics of the complete guidance, control, and airframe loop. One of the most important jobs of the aerodynamicist or configuration designer is to see that sufficient natural static and dynamic airframe stability and damping are provided in the airframe system. Once this is achieved, fewer components and "servo or electronic fixes," which require additional components, are needed to meet a given response requirement. In addition, he must design the airframe with sufficient load factor or maneuverability in order that the missile can execute reasonably low turning radii for interception with the target or flight-path correction due to launch dispersions. (Unfortunately, these two design requirements, i.e., stability and maneuverability, are conflicting in that maneuverability decreases as stability is increased.) The purpose of this chapter is to analyze some of the various aspects of missile stability and control. (Methods of analysis are presented for two general types of design: (1) forward control—where the control surfaces are located ahead of the missile center of gravity, and (2) aft control—where the control surfaces are located behind the center of gravity.)

5-2. TWO-DEGREE-OF-FREEDOM ANALYSIS

It is convenient to study the static longitudinal stability and control characteristics of a missile with the aid of a two-degree-of-freedom (one rotational and one translational motion) analysis. Constant forward

velocity is therefore assumed in this case. The equations of motion are as follows:

$$\begin{aligned} M = I\ddot{\theta} &= M_\alpha\alpha + M_\delta\delta + M_\dot{\theta}\dot{\theta} + M_{\dot{\alpha}}\dot{\alpha} + \dots \\ &= (C_{m_\alpha}\alpha + C_{m_\delta}\delta)qSd + (C_{m_\dot{\theta}}\dot{\theta} + C_{m_{\dot{\alpha}}}\dot{\alpha})\frac{qSd^2}{2V} \end{aligned} \quad (5-1)$$

and

$$\begin{aligned} F = mV\dot{\gamma} &= F_\alpha\alpha + F_\delta\delta \\ &= (C_{L_\alpha}\alpha + C_{L_\delta}\delta)qS \end{aligned} \quad (5-2)$$

Since $C_{L_\alpha} \cong C_{N_\alpha}$, Eq. (5-2) becomes

$$mV\dot{\gamma} = (C_{N_\alpha}\alpha + C_{N_\delta}\delta)qS \quad (5-2a)$$

The geometric relationship between θ , α , and γ (shown in Fig. 5-1) is expressed as

$$\theta = \alpha + \gamma \quad (5-3)$$

In steady-flight condition (i.e., missile in equilibrium), the summation of moments about the center of gravity of the missile is zero. Consequently Eq. (5-1) is equated to zero. Since the damping terms $C_{m_\dot{\theta}}$, $C_{m_{\dot{\alpha}}}$, etc., can be neglected, the pitching moment due to control-surface deflection must be balanced by that due to angle of attack. Mathematically, this equilibrium condition may be expressed as follows:

$$C_{m_\alpha}\alpha_{TR} = -C_{m_\delta}\delta \quad (5-4)$$

The condition for static stability is that the sign of C_{m_α} must be negative, i.e., a negative, or nose-down, pitching moment is realized with an increase in angle of attack or lift. Hence, when an upgust strikes a missile flying in equilibrium condition, the missile tends to nose down, or "weathercocks" in the direction of the gust. (The controllability or maneuverability of the missile is defined as the magnitude of load factor it can execute in its trimmed or equilibrium condition.) The load factor n is defined as the ratio of total trimmed normal force to the weight of the missile. In terms of the rate of change of flight-path angle $\dot{\gamma}$ the aerodynamic maneuverability of the missile may be expressed as

$$mV\dot{\gamma} = nW \quad (5-5)$$

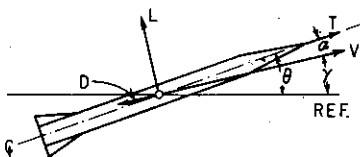


FIG. 5-1. Angle relationship.

In order to evaluate the degree of static stability and the magnitude of the maneuverability of the missile, the aerodynamic derivatives $C_{m\alpha}$, $C_{m\delta}$, etc., must first be determined. The following sections deal with the determination of these derivatives for two general types of design previously mentioned.

5-3. COMPLETE MISSILE AERODYNAMICS—FORWARD CONTROL

The aerodynamic derivatives shown in Eqs. (5-1) and (5-2) are composed of contributions from the various components of the missile.

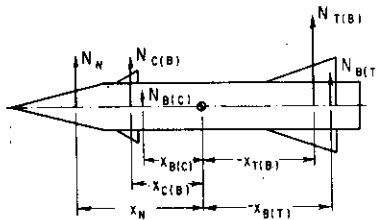


FIG. 5-2. Typical force diagram—front control.

In this section the model build-up will be analyzed for a missile which has its control surfaces placed forward of the center-of-gravity location. This type of configuration may be either the canard- or wing-control design shown in Fig. 2-2. For the purpose of illustration, the former design will be used. Since the condition of equilibrium is of

interest in this section, the damping terms will be temporarily neglected (but will be treated in Chap. 9 in the analysis of the dynamics of the missile). The model build-up equations for the pertinent aerodynamic force and moment derivatives are derived as follows:

$$N_{CM} = N_N + N_{C(B)} + N_{B(C)} + N_{T(B)} + N_{B(T)} \quad (5-6)$$

$$M_{CM} = N_N x_N + N_{C(B)} x_{C(B)} + N_{B(C)} x_{B(C)} + N_{T(B)} x_{T(B)} + N_{B(T)} x_{B(T)} \quad (5-7)$$

where N_{CM} , M_{CM} = normal force and pitching moment of the complete model or missile

N_N = normal force on nose section

$N_{C(B)}$ = normal force on canards in presence of body

$N_{B(C)}$ = normal force on body due to canard

$N_{T(B)}$ = normal force on tail in presence of body

$N_{B(T)}$ = normal force on body due to tail

x_N , $x_{C(B)}$ = moment arms (measured from center of pressure to missile center of gravity) of respective normal forces as shown in Fig. 5-2

Equations (5-6) and (5-7) may be written in coefficient form as follows:

$$(C_{N_\alpha})_{CM} \alpha q S_\pi = (C_{N_\alpha})_N \alpha q S_\pi + (C_{N_\alpha})_C \alpha K_{C(B)} q S_C + (C_{N_\alpha})_C \alpha K_{B(C)} q S_C \\ + (C_{N_\alpha})_T \alpha_T K_{T(B)} q S_T + (C_{N_\alpha})_T \alpha_T K_{B(T)} q S_T \quad (5-8)$$

$$(C_{N_\delta})_{CM} \delta q S_\pi = (C_{N_\alpha})_C \delta k_{C(B)} q S_C + (C_{N_\alpha})_C \delta k_{B(C)} q S_C \\ + (C_{N_\alpha})_T \alpha_T K_{T(B)} q S_T + (C_{N_\alpha})_T \alpha_T K_{B(T)} q S_T \quad (5-9)$$

$$(C_{m_\alpha})_{CM} \alpha q S_\pi d = (C_{N_\alpha})_N \alpha q S_\pi x_N + (C_{N_\alpha})_C \alpha K_{C(B)} q S_C x_{C(B)} \\ + (C_{N_\alpha})_C \alpha K_{B(C)} q S_C x_{B(C)} + (C_{N_\alpha})_T \alpha_T K_{T(B)} q S_T x_{T(B)} \\ + (C_{N_\alpha})_T \alpha_T K_{B(T)} q S_T x_{B(T)} \quad (5-10)$$

$$(C_{m_\delta})_{CM} \delta q S_\pi d = (C_{N_\alpha})_C \delta k_{C(B)} q S_C x_{C(B)} + (C_{N_\alpha})_C \delta k_{B(C)} q S_C x_{B(C)} \\ + (C_{N_\alpha})_T \alpha_T K_{T(B)} q S_T x_{T(B)} \\ + (C_{N_\alpha})_T \alpha_T K_{B(T)} q S_T x_{B(T)} \quad (5-11)$$

where (1) $K_{C(B)}$ and $K_{T(B)}$ are factors which account for the effect of body upwash at angles of attack ($\delta = 0^\circ$); (2) $K_{B(C)}$ and $K_{B(T)}$ are factors which account for the effect of "body carry-over" lift due to angles of attack ($\delta = 0^\circ$); (3) $k_{C(B)}$ and $k_{T(B)}$ are factors which account for body effect due to control deflection ($\alpha = 0^\circ$); (4) $k_{B(C)}$ and $k_{B(T)}$ are factors which account for body carry-over lift due to control-surface deflection; (5) subscripts CM , N , C , and T denote complete model, nose, canards, and tails, respectively; (6) the subscripts within the parentheses, i.e., $x_{C(B)}$, denote influence by the presence of the body; (7) S_C and S_T denote exposed canard and tail areas, respectively; and (8) $(C_{N_\alpha})_C$ and $(C_{N_\alpha})_T$ are based on S_C and S_T , respectively.

Since $\alpha_T = \alpha - \epsilon$ in Eqs. (5-8) and (5-10) and $\alpha_T = -\epsilon$ in Eqs. (5-9) and (5-11), Eqs. (5-8) through (5-11) become

$$(C_{N_\alpha})_{CM} = (C_{N_\alpha})_N + (C_{N_\alpha})_C [K_{C(B)} + K_{B(C)}] \frac{S_C}{S_\pi} \\ + (C_{N_\alpha})_T [K_{T(B)} + K_{B(T)}] \frac{S_T}{S_\pi} (1 - \epsilon_\alpha) \quad (5-12)$$

$$(C_{N_\delta})_{CM} = (C_{N_\alpha})_C [k_{C(B)} + k_{B(C)}] \frac{S_C}{S_\pi} + (C_{N_\alpha})_T [K_{T(B)} + K_{B(T)}] \frac{S_T}{S_\pi} (-\epsilon_\delta) \quad (5-13)$$

$$\begin{aligned}
 (C_{m_a})_{CM} = & (C_{N_a})_N \left(\frac{x}{d} \right)_N + (C_{N_a})_C K_{C(B)} \frac{S_C}{S_r} \left(\frac{x}{d} \right)_{C(B)} \\
 & + (C_{N_a})_C K_{B(C)} \frac{S_C}{S_r} \left(\frac{x}{d} \right)_{B(C)} + (C_{N_a})_T K_{T(B)} \frac{S_T}{S_r} \left(\frac{x}{d} \right)_{T(B)} (1 - \epsilon_a) \\
 & + (C_{N_a})_T K_{B(T)} \frac{S_T}{S_r} \left(\frac{x}{d} \right)_{B(T)} (1 - \epsilon_a) \quad (5-14)
 \end{aligned}$$

$$\begin{aligned}
 (C_{m_a})_{CM} = & (C_{N_a})_C k_{C(B)} \frac{S_C}{S_r} \left(\frac{x}{d} \right)_{C(B)} + (C_{N_a})_C k_{B(C)} \frac{S_C}{S_r} \left(\frac{x}{d} \right)_{B(C)} \\
 & + (C_{N_a})_T K_{T(B)} \frac{S_T}{S_r} \left(\frac{x}{d} \right)_{T(B)} (-\epsilon_a) \\
 & + (C_{N_a})_T K_{B(T)} \frac{S_T}{S_r} \left(\frac{x}{d} \right)_{B(T)} (-\epsilon_a) \quad (5-15)
 \end{aligned}$$

Since the normal force on the nose section of the body constitutes the majority of the normal force of the complete body configuration, the value of $(C_{N_a})_B$ for the complete body may be substituted in place

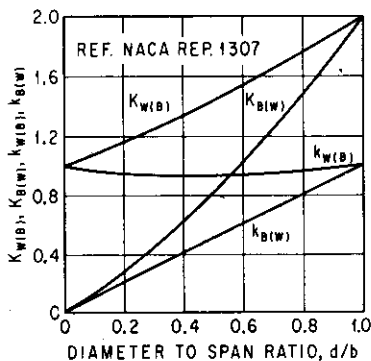


FIG. 5-3. Values of K and k based on slender-body theory.

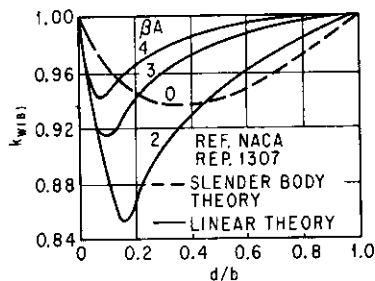


FIG. 5-4. Values of $k_{W(B)}$.

of $(C_{N_a})_N$ in Eqs. (5-12) and (5-14). The normal-force-curve slope for the canard and tail surfaces may be determined as shown in Chap. 3. The values of $K_{C(B)}$ or $K_{T(B)}$ were determined by slender-body theory^{1,2,3,*} and are shown in Fig. 5-3 as a function of diameter-to-span ratio. It is interesting to note that these values do not differ significantly from those derived by linear theory for large-aspect-ratio

* Superscript numbers indicate references listed at the end of the chapter.

wings, or those derived by Beskin's body-upwash theory.⁴ The values of $k_{C(B)}$ or $k_{T(B)}$ were also determined by slender-body theory^{1,2,3} and are shown in Fig. 5-3. These values are applicable for slender triangular wing and body combination. For rectangular wing and body combinations the results derived from exact linear theory⁵ should be used¹ (see Fig. 5-4). The values of $K_{B(C)}$ or $K_{B(T)}$ were determined primarily by the slender-body theory and are shown in Fig. 5-3. For high-aspect-ratio wings at supersonic speeds, Fig. 5-5 should be used.¹

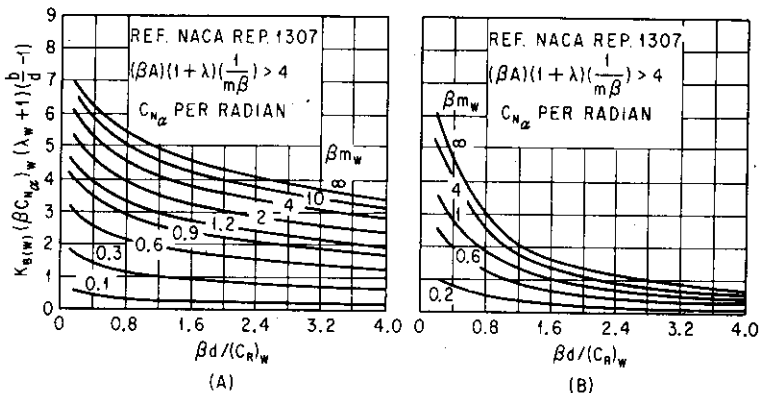


FIG. 5-5. Design charts for determining $K_{B(W)}$ for high-aspect-ratio range at supersonic speeds. (A) With afterbody. (B) No afterbody.

With the exception of the latter, these wing-body interference factors are independent of Mach number. The effect of Mach number is felt only through the values C_{N_z} of the various missile components.

The center-of-pressure location for the nose, canard, and tail may be determined by the methods presented in Chap. 3. The effect of the presence of the body on canard or tail center-of-pressure location appears to be negligible, i.e., $x_{C(B)} = x_C$. The location of the center of pressure of the normal force on the body due to canard or tail is a function of many parameters, among which are Mach number, aspect ratio, and taper ratio. Detailed design charts for the center-of-pressure location of these normal-force components may be found in *NACA Report 1307*.¹

Accurate values of ϵ_α and ϵ_δ are very difficult to determine. Theoretical methods are available⁶⁻¹¹ and may be used for preliminary design. However, whenever possible, it is recommended that experimental test results of similar or comparable configurations be used. The need for a comprehensive correlation of both theoretical and

experimental results is obvious, especially for missiles employing relatively low aspect ratio aerodynamic surfaces. Methods for evaluating downwash derivatives ϵ_α and ϵ_δ from wind-tunnel-test results are presented in Appendix F.

Typical complete model normal-force and pitch-moment curves for forward-control (canard- and wing-control) designs are shown in Figs. 5-6 and 5-7. It is seen from Fig. 5-6 that the value of C_{N_δ} is relatively low. As previously noted in Chap. 2, the down load on the tail due

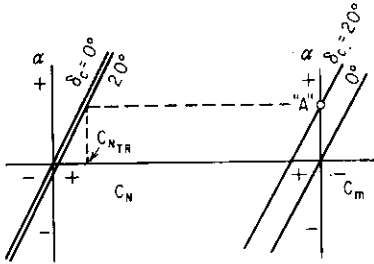


FIG. 5-6. Typical complete-model normal-force and pitching-moment curves—forward (canard) control.

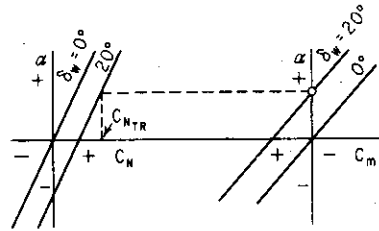


FIG. 5-7. Typical complete-model normal-force and pitching-moment curves—forward (wing) control.

to downwash from the deflected canards may partially or completely nullify the load on the deflected canards. This is readily apparent from Eq. (5-13). On the other hand, the value of C_{N_δ} is high for a wing control because of the large wing area normally associated with this design.

5-4. STATIC STABILITY MARGIN—FORWARD CONTROL

The static stability margin of a missile is defined as the distance between the center of pressure and center of gravity of the missile.

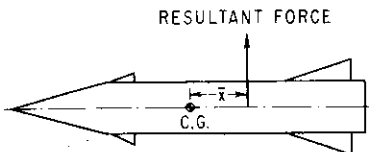


FIG. 5-8. Static stability margin.

Generally, this stability margin is defined in terms of missile body diameters since the nondimensionality factor is d , the body diameter, in lieu of the mean aerodynamic chord \bar{c} used in aircraft terminology. Once the complete missile derivatives $C_{N_\alpha}^*$ and $C_{m_\alpha}^*$ [Eqs. (5-12) and (5-14)] are known, the magnitude of the static stability

* The subscript CM is deleted since the complete model is implied.

margin may be readily calculated with the aid of Fig. 5-8. From Fig. 5-8, the following derivation of the static stability margin \bar{X}/d is made:

$$M = N\bar{X} \quad (5-16)$$

dividing by qSd , Eq. (5-16) becomes

$$C_m = C_N \frac{\bar{X}}{d} \quad (5-17)$$

differentiating with respect to α , Eq. (5-17) becomes

$$C_{m_\alpha} = C_{N_\alpha} \frac{\bar{X}}{d} \quad (5-18)$$

or

$$\frac{\bar{X}}{d} = \frac{C_{m_\alpha}}{C_{N_\alpha}} \equiv C_{m_{cN}} \quad (5-19)$$

5-5. LOAD-FACTOR CAPABILITY—FORWARD CONTROL

In order to evaluate the aerodynamic load factor or maneuvering capability of the missile, the complete model aerodynamic derivatives C_{N_α} , C_{N_δ} , C_{m_α} , and C_{m_δ} as defined by Eqs. (5-12) through (5-15) must be known. The load factor is defined mathematically as follows:

$$n = \frac{N}{W} = C_{N_{TR}} \frac{qS}{W} \quad (5-20)$$

where $C_{N_{TR}}$ = trimmed normal-force coefficient

W = weight of missile

N = normal force

The value of $C_{N_{TR}}$ may be readily determined with the aid of Fig. 5-6. The trim condition is defined as the point of zero moment, i.e., point A in Fig. 5-6. The value of $C_{N_{TR}}$ is derived as follows:

$$-C_{m_\alpha} \alpha_{TR} = C_{m_\delta} \delta \quad (5-21)$$

or

$$\alpha_{TR} = \frac{-C_{m_\delta} \delta}{C_{m_\alpha}} \quad (5-22)$$

but

$$C_{N_{TR}} = C_{N_\alpha} \alpha_{TR} + C_{N_\delta} \delta \quad (5-23)$$

Substituting Eq. (5-22) into (5-23), we get

$$C_{N_{TR}} = C_{N_\alpha} \left(-\frac{C_{m_\delta} \delta}{C_{m_\alpha}} \right) + C_{N_\delta} \delta \quad (5-24)$$

or

$$n = \left(C_{N\delta} - \frac{C_{m\delta} C_{N\alpha}}{C_{m\alpha}} \right) \delta \frac{qS}{W} \quad (5-25)$$

The load factor per unit control deflection is thus

$$\frac{n}{\delta} = \left(C_{N\delta} - C_{N\alpha} \frac{C_{m\delta}}{C_{m\alpha}} \right) \frac{qS}{W} \quad (5-26)$$

For a typical canard configuration which has a negligibly small value of $C_{N\delta}$, Eq. (5-26) becomes

$$\frac{n}{\delta} = - \left(C_{N\alpha} \frac{C_{m\delta}}{C_{m\alpha}} \right) \frac{qS}{W} \quad (5-27)$$

The above expressions are very useful in the determination of trim load factor provided that linear aerodynamics are realized. If non-linearity exists, the value of n/δ must be obtained directly from the C_N and C_m vs. α curves such as those shown in Figs. 5-6 and 5-7.

5-6. COMPLETE MISSILE AERODYNAMICS—REAR CONTROL

Another common type of design is one in which the control surfaces are located aft of the missile center of gravity. For this type of design

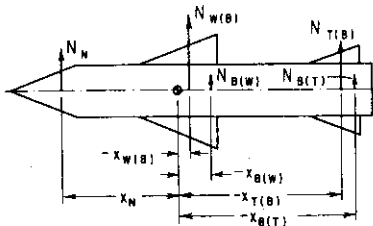


FIG. 5-9. Typical force diagram—rear control.

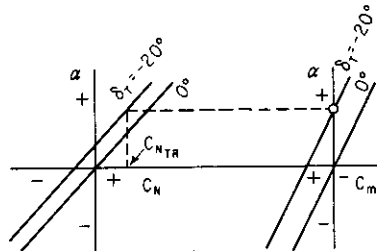


FIG. 5-10. Typical complete-model normal-force and pitching-moment curves—rear control.

the complete model or missile aerodynamics are similar to those previously discussed, as shown below. From Fig. 5-9, the forces and moments for a typical tail-control design are as follows:

$$N_{CM} = N_N + N_{W(B)} + N_{B(W)} + N_{T(B)} + N_{B(T)} \quad (5-28)$$

$$M_{CM} = N_N x_N + N_{W(B)} x_{W(B)} + N_{B(W)} x_{B(W)} + N_{T(B)} x_{T(B)} + N_{B(T)} x_{B(T)} \quad (5-29)$$

Using the procedure previously described, the following relationships are obtained:

$$(C_{N_\alpha})_{CM} = (C_{N_\alpha})_N + (C_{N_\alpha})_W [K_{W(B)} + K_{B(W)}] \frac{S_W}{S_\pi} \\ + (C_{N_\alpha})_T [K_{T(B)} + K_{B(T)}] \frac{S_T}{S_\pi} (1 - \epsilon_\alpha) \quad (5-30)$$

$$(C_{N_\delta})_{CM} = (C_{N_\alpha})_T [k_{T(B)} + k_{B(T)}] \frac{S_T}{S_\pi} \quad (5-31)$$

$$(C_{m_\alpha})_{CM} = (C_{N_\alpha})_N \left(\frac{x}{d} \right)_N + (C_{N_\alpha})_W K_{W(B)} \frac{S_W}{S_\pi} \left(\frac{x}{d} \right)_{W(B)} \\ + (C_{N_\alpha})_W K_{B(W)} \frac{S_W}{S_\pi} \left(\frac{x}{d} \right)_{B(W)} + (C_{N_\alpha})_T K_{T(B)} \frac{S_T}{S_\pi} \left(\frac{x}{d} \right)_{T(B)} (1 - \epsilon_\alpha) \\ + (C_{N_\alpha})_T K_{B(T)} \frac{S_T}{S_\pi} \left(\frac{x}{d} \right)_{B(T)} (1 - \epsilon_\alpha) \quad (5-32)$$

$$(C_{m_\delta})_{CM} = (C_{N_\alpha})_T k_{T(B)} \frac{S_T}{S_\pi} \left(\frac{x}{d} \right)_{T(B)} + (C_{N_\alpha})_T k_{B(T)} \frac{S_T}{S_\pi} \left(\frac{x}{d} \right)_{B(T)} \quad (5-33)$$

The values of the various terms appearing in Eqs. (5-30) through (5-33) may be evaluated as noted previously.

Typical complete missile aerodynamic curves of C_m and C_N vs. angle of attack for a rear-control configuration are shown in Fig. 5-10. It is readily apparent that the sign of $(C_{m_\delta})_{CM}$ is negative (δ_T is considered positive with leading edge deflected upward) for a tail-control design as previously noted in Chap. 2 (Fig. 2-6).

5-7. STATIC STABILITY MARGIN—REAR CONTROL

The static stability margin for a rear-control design may be determined in a manner similar to that previously described. The resultant expression is

$$\frac{\bar{X}}{d} = \frac{C_{m_\alpha}}{C_{N_\alpha}} \equiv C_{m_{\alpha N}} \quad (5-34)$$

which is identical to Eq. (5-19).

5-8. LOAD-FACTOR CAPABILITY—REAR CONTROL

The expression for n/δ may be derived from Fig. 5-10 using Eqs. (5-21) through (5-25). The resultant expression becomes

$$\frac{n}{\delta} = \left(C_{N_\delta} - C_{N_\alpha} \frac{C_{m_\delta}}{C_{m_\alpha}} \right) \frac{gS}{W} \quad (5-35)$$

which is identical to Eq. (5-26) for the forward-control case; the exception is that the sign of $C_{m\delta}$ for the rear-control case is negative. Hence it is apparent that the normal force due to control-surface deflection is always opposite to the resultant force. Hence it always decreases the load-factor capability of the missile.

SYMBOLS

A	aspect ratio
C_L	lift coefficient
C_m	pitching-moment coefficient
$C_{m\delta}$	static stability margin \bar{X}/d
C_N	normal-force coefficient
C_R	root chord
I	moment of inertia
$K_{B(C)}, K_{B(W)}, K_{B(T)}$	factors which account for the effect of "body carry-over" lift (or normal force) due to angle of attack
$K_{C(B)}, K_{W(B)}, K_{T(B)}$	factors which account for the effect of body upwash at angle of attack
M	(pitching) moment
$N_{B(C)}, N_{B(W)}, N_{B(T)}$	normal-force "carry-over" on the body due to aerodynamic surfaces
$N_{C(B)}, N_{W(B)}, N_{T(B)}$	normal force on the aerodynamic surfaces in the presence of the body
N_N	normal force on the nose section of the body
S	reference area
S_π	body frontal (reference) area
V	missile forward velocity
W	weight
\bar{X}	resultant center of pressure
d	body diameter
$k_{B(C)}, k_{B(W)}, k_{B(T)}$	factors which account for the effect of "body carry-over" lift (or normal force) due to control-surface deflection
$k_{C(B)}, k_{W(B)}, k_{T(B)}$	factors which account for body effect on the aerodynamic surfaces due to deflection
m	mass, or cotangent of leading-edge sweep angle (see Fig. 5-5A and B)
n	load factor
q	dynamic pressure

x	moment arm (distance between missile center of gravity and center of pressure of components)
α	angle of attack
β	$\sqrt{M^2 - 1}$
γ	flight-path angle
δ	control-surface deflection
ϵ	downwash angle
θ	missile attitude
λ	taper ratio (ratio of tip chord to root chord)

Subscripts

C	canard
CM	complete model
N	nose (or body)
W	wing
T	tail

Note: The following form is used throughout to denote aerodynamic derivatives; i.e., C_{N_α} is $\partial C_N / \partial \alpha$, C_{m_α} is $\partial C_m / \partial \alpha$, etc.

REFERENCES

1. Pitts, W. C., J. N. Nielsen, and G. E. Kaattari: Lift and Center of Pressure of Wing-body-tail Combinations at Subsonic, Transonic, and Supersonic Speeds, *NACA Rept. 1307*, 1959.
2. Spreiter, J. R.: The Aerodynamic Forces on Slender Plane- and Cruciform-wing and Body Combinations, *NACA Rept. 962*, 1950 (formerly *Tech. Notes 1662* and *1897*).
3. Morikawa, G.: Supersonic Wing-body Lift, *J. Aeronaut. Sci.*, vol. 18, no. 4, pp. 217-228, April, 1951.
4. Beskin, L.: Determination of Upwash around a Body of Revolution at Supersonic Velocities, Johns Hopkins University, Applied Physics Laboratory, *Rept. CM-251*, May 27, 1946.
5. Nielsen, J. N., and W. C. Pitts: Wing-body Interference at Supersonic Speeds with an Application to Combinations with Rectangular Wings, *NACA Tech. Note 2677*, 1952.
6. Lomax, H., L. Sluder, and M. A. Heaslet: The Calculation of Downwash behind Supersonic Wings with an Application to Triangular Plan Forms, *NACA Rept. 957*, 1950.
7. Lagerstrom, P. A., and M. E. Graham: Downwash and Sidewash Induced by Three-dimensional Lifting Wings in Supersonic Flow, Douglas Aircraft Co., Inc., *Rept. SM-13007*, April, 1947.
8. Spreiter, J. R., and A. H. Sacks: The Rolling-up of the Trailing Vortex Sheet and Its Effect on Downwash behind Wings, *J. Aeronaut. Sci.*, vol. 18, no. 1, pp. 21-32, 72, January, 1951.

9. Rogers, A. W.: Application of Two-dimensional Vortex Theory to the Prediction of Flow Fields behind Wings of Wing-body Combinations at Subsonic and Supersonic Speeds, *NACA Tech. Note 3227*, 1954.

10. Silverstein, A., and S. Katzoff: Design Charts for Predicting Downwash Angles and Wake Characteristics behind Plain and Flapped Wings, *NACA Rept. 648*, 1939.

11. Decker, J. L.: Prediction of Downwash at Various Angles of Attack for Arbitrary Tail Locations, *IAS Preprint 615*, 24th Annual Meeting, Jan. 23-26, 1956.

CHAPTER 6

MANEUVERING FLIGHT

6-1. INTRODUCTION

For certain types of missiles, such as an air-to-air missile attacking a fast-moving and maneuvering target, the maneuvering-flight characteristics are of particular interest. For the cruise-type or long-range ballistic missiles, the demand for maneuvering flight, though greatly reduced, must be satisfied in order to achieve a complete missile weapon system. The following sections deal with the maneuvering-flight characteristics of missiles with both monowing and cruciform designs. The effect of static stability margin on maneuverability or load-factor capability of the missile will be illustrated both analytically and graphically. The effect of aerodynamic damping on load-factor capability is also discussed.

6-2. FLAT TURNS

1. Cruciform. In order to change the flight path of a missile flying in an equilibrium (level or straight) flight condition, an unbalance force must be introduced. For a missile of cruciform design, this unbalance force may be obtained by deflecting the appropriate set or sets of control surfaces. As indicated in Fig. 6-1, the cruciform missile is not required to bank to produce the centripetal force for a flat turn. For the cruciform missile designed to fly with all the aerodynamic control surfaces in the "plus" (+) position during normal flight, only one set of (yaw) controls needs to be deflected to maneuver the missile in a flat turn. However, if these control surfaces are in the X position, both

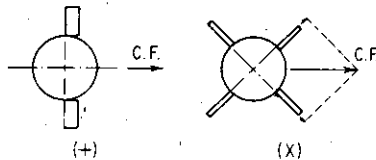


FIG. 6-1. Control deflections for "plus" and "X" designs.

sets of controls must be deflected. The magnitude of each set of control deflections is approximately 0.7 of that required for the case in which the aerodynamic surfaces are in the "plus" position.

The radius of a flat turn may be related to the forward speed and trim load-factor capability of the missile as follows:

$$\text{Centripetal force } CF = \frac{WV^2}{gR} = nW \quad (6-1)$$

or
$$R = \frac{V^2}{ng} \quad (6-2)$$

It is apparent from Eq. (6-2) that the turn radius is directly proportional to the square of the forward velocity and inversely proportional to the trim load-factor capability of the missile (also see Fig. 6-2). The turn radius can also be expressed in terms of the trim normal force (strictly speaking, it should be the lift force) as follows:

$$nW = N = C_{N_{TR}} \frac{1}{2} \rho V^2 S \quad (6-3)$$

substituting Eq. (6-3) in Eq. (6-1) or (6-2), we get

$$R = \frac{2W}{\rho g S C_{N_{TR}}} \quad (6-4)$$

For certain types of configurations, the value of $C_{N_{TR}}$ is nearly independent of Mach number.

Consequently the turn radius is nearly constant over a relatively wide Mach-number range at a given flight altitude. This feature is desirable from the standpoint of control-system design since a near-constant "aerodynamic-gain" condition is realized.

Quite frequently, it is convenient to express the maneuvering-flight characteristics of a missile in terms of the rate of change in flight-path angle $\dot{\gamma}$. From Eq. (5-5), the rate of change in flight-path angle can be written as

$$\dot{\gamma} = \frac{ng}{V} \quad (6-5)$$

or in terms of $C_{N_{TR}}$, Eq. (6-11) becomes

$$\dot{\gamma} = \frac{\rho g S V}{2W} C_{N_{TR}} \quad (6-6)$$

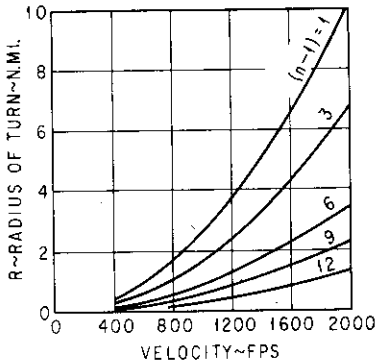


FIG. 6-2. Pull-up performance.

2. Monowing. A monowing missile must bank to produce the required centripetal force in a flat turn. Hence, from the force diagram in Fig. 6-3, the following pertinent relationships can be written:

For level flight
$$W = nW \cos \varphi \tag{6-7}$$

Centripetal force
$$CF = nW \sin \varphi = \frac{WV^2}{gR} \tag{6-8}$$

Hence, from Eqs. (6-7) and (6-8),

$$R = \frac{V^2}{g \tan \varphi} \tag{6-9}$$

and

$$n = \frac{1}{\cos \varphi} \tag{6-10}$$

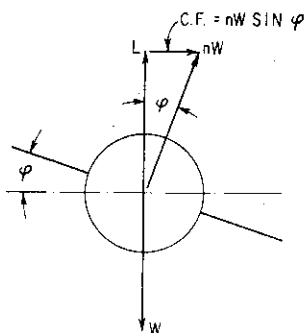


FIG. 6-3. Force diagram for a monowing missile in a flat turn.

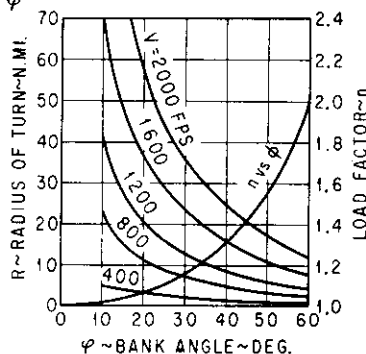


FIG. 6-4. Flat-turn performance.

The results of Eqs. (6-9) and (6-10) are shown graphically in Fig. 6-4. Equations (6-9) and (6-10) can also be expressed in terms of C_{NTR} as

$$R = \frac{2W}{\rho g S C_{NTR} \sin \varphi} \tag{6-11}$$

and

$$\frac{1}{\cos \varphi} = \frac{\rho V^2 S}{2W} C_{NTR} \tag{6-12}$$

It is interesting to note that, if the monowing missile could theoretically bank into a 90° attitude for the flat turn, Eq. (6-11) would be identical to Eq. (6-4), which is applicable for the cruciform missile.

The rate of change of flight path may be written as

$$\dot{\gamma} = \frac{ng \sin \varphi}{V} \tag{6-13}$$

or

$$\dot{\gamma} = \frac{\rho g S V \sin \varphi}{2W} C_{NTR} \tag{6-14}$$

6-3. PULL-UPS

The relationship for the turn radius for pull-ups or pitch-up maneuver from level flight is given as

$$CF = nW - W = \frac{WV^2}{gR} \quad (6-15)$$

or

$$R = \frac{V^2}{g(n-1)} \quad (6-16)$$

The rate of change in flight-path angle $\dot{\gamma}$ may be written as

$$\dot{\gamma} = g \left(\frac{\rho V}{2W} C_{N_{TR}} - \frac{1}{V} \right) \quad (6-17)$$

For pitch-down maneuvers, Eqs. (6-16) and (6-17) become

$$R = \frac{V^2}{g(n+1)} \quad (6-18)$$

and

$$\dot{\gamma} = g \left(\frac{\rho V}{2W} C_{N_{TR}} + \frac{1}{V} \right) \quad (6-19)$$

6-4. RELATIONSHIP OF MANEUVERABILITY AND STATIC STABILITY MARGIN

It was noted in Chap. 5 that the requirements for large static stability margin and great load factor or maneuvering capability are conflicting in that increasing stability margin results in a decrease in load-factor capability. The load factor per unit control deflection n/δ (assuming linear aerodynamic derivatives) given in Eq. (5-27) is expressed as

$$\frac{n}{\delta} = \left(C_{N_\delta} - \frac{C_{m_\delta}}{C_{m_{c_N}}} \right) \frac{qS}{W} \quad (6-20)$$

where

$$C_{m_{c_N}} = \frac{\partial C_m / \partial \alpha}{\partial C_N / \partial \alpha} = \frac{\bar{X}}{d}$$

in accordance with Eq. (5-19).

Since the sign of C_{m_δ} is positive and $C_{m_{c_N}}$ is negative for all practical design conditions, it is apparent from Eq. (6-20) that increasing the static stability margin $C_{m_{c_N}}$ results in a decrease in load-factor capability. This phenomenon may also be illustrated graphically as in Fig. 6-5. The solid line represents the normal-force and pitching-moment curves for a given missile design for a given static stability

margin. The dotted line represents the pitching-moment curves for a condition of greater static stability margin (i.e., a more stable missile) which could be realized by a more forward center-of-gravity location. The normal-force curves are not affected by center-of-gravity location since they are primarily a function of the external configuration. It is apparent from Fig. 6-5 that the trim angle of attack and hence the trim normal-force coefficient $C_{N_{TR}}$ is noticeably lower for the more stable missile than the corresponding values for the less stable missile. Thus, if the requirement for both a large static stability margin and a large load-factor capability exists for a given missile design, relatively large aerodynamic surfaces and/or control surfaces (i.e., larger values of C_{N_α} and C_{m_δ}) must prevail.

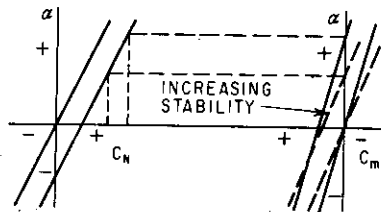


FIG. 6-5. Effect of static stability margin on trim load-factor capability.

Heretofore the effect of aerodynamic damping on the maneuverability or load-factor capability per unit control deflection has been

neglected. In actuality, aerodynamic damping, though small, is present when the missile is commanded into a maneuvering-flight trajectory. This is apparent from the equations of motion [Eqs. (5-1) and (5-2a)] and the angle relationship [Eq. (5-3)]:

$$I\ddot{\theta} = (C_{m_\alpha}\alpha + C_{m_\delta}\delta)qSd + (C_{m_\theta}\dot{\theta} + C_{m_\alpha}\dot{\alpha}) \frac{qSd^2}{2V} \quad (6-21)$$

$$mV\dot{\gamma} = (C_{N_\alpha}\alpha + C_{N_\delta}\delta)qS \quad (6-22)$$

$$\theta = \alpha + \gamma \quad (6-23)$$

For steady-state trimmed maneuvering flight, $\ddot{\theta}$ and $\dot{\alpha}$ become zero. Hence the following relationships may be written:

$$C_{m_\alpha}\alpha_{TR} + C_{m_\delta}\delta + C_{m_\theta}\dot{\theta} \frac{d}{2V} = \quad (6-24)$$

$$mV\dot{\gamma} = nW = (C_{N_\alpha}\alpha_{TR} + C_{N_\delta}\delta)qS \quad (6-25)$$

and

$$\dot{\theta} = \dot{\gamma} \quad (6-26)$$

substituting Eqs. (6-26) and (6-24), Eq. (6-25) may be expressed as

$$C_{m_\alpha}\alpha_{TR} + C_{m_\delta}\delta + C_{m_\theta} \frac{d}{2V} \left[\frac{g}{VW} (C_{N_\alpha}\alpha_{TR} + C_{N_\delta}\delta)qS \right] = 0 \quad (6-27)$$

hence
$$\alpha_{TR} = - \frac{[C_{m\delta} + C_{m\dot{\theta}}(qSdg/2V^2W)C_{N\delta}]\delta}{C_{m\alpha} + C_{m\dot{\theta}}(qSdg/2V^2W)C_{N\alpha}} \quad (6-28)$$

and
$$\frac{n}{\delta} = \left[C_{N\delta} - \frac{C_{m\delta} + C_{m\dot{\theta}}(qSdg/2V^2W)C_{N\delta}}{C_{m\alpha} + C_{m\dot{\theta}}(qSdg/2V^2W)} \right] \frac{qS}{W} \quad (6-29)$$

substituting $q = \frac{1}{2}\rho V^2$ into Eq. (6-29), we get

$$\frac{n}{\delta} = \left[C_{N\delta} - \frac{C_{m\delta} + C_{m\dot{\theta}}(\rho Sdg/4W)C_{N\delta}}{C_{m\alpha} + C_{m\dot{\theta}}(\rho Sdg/4W)} \right] \frac{qS}{W} \quad (6-30)$$

The effect of the damping term in Eq. (6-30) is to decrease the value of n/δ . For missiles with relatively high damping characteristics, the decrease in n/δ is in the order of a few per cent over that calculated by Eq. (6-20), which neglects damping. Hence, for most practical applications, the damping may be neglected in the determination of trim load factor.

SYMBOLS

CF	centripetal force
C_m	pitching-moment coefficient
$C_{m\alpha}$	static stability margin \bar{X}/d
C_N	normal-force coefficient
$C_{N\alpha}$	trim normal-force coefficient
R	turn radius
S	reference area
V	forward speed
W	weight
\bar{X}	resultant center of pressure
d	body diameter
n	load factor
q	dynamic pressure
α	angle of attack
α_{TR}	trim angle of attack
γ	flight-path angle
θ	missile attitude
ρ	air density
φ	bank angle

CHAPTER 7

DIRECTIONAL STABILITY AND CONTROL

7-1. INTRODUCTION

In Chap. 5 the longitudinal static stability and control characteristics were treated independently of those for the other two axes (i.e., yaw and roll). This was made possible by the fact that the motions in pure pitch do not produce aerodynamic forces or moments in either the yaw or roll axes. Similarly, motions in the roll and/or yaw axes do not result in aerodynamic forces or moments in the pitch plane. Strictly speaking, the motions in the yaw axis for a monowing design must be studied simultaneously with those in the roll axis. In addition, for a cruciform design, the combined pitch and yaw motions must be analyzed together with those in roll because of aerodynamic cross-coupling effects. These motions are further complicated by the existence of inertia cross-coupling effects, particularly for missiles whose moment of inertia in roll is small relative to those in pitch and/or yaw. These effects will be discussed in Chap. 9.

For the sake of clarity, the static directional stability and control characteristics in steady flight will be treated separately in this chapter. The lateral stability and control characteristics will be treated separately in Chap. 8. The problem of directional stability and control is twofold: (1) to provide static stability and adequate damping characteristics similar to those for the longitudinal axis and (2) to provide sufficient control to maintain a desired flight path or trim load-factor capability.

In the case of a cruciform design, if satisfactory pitch characteristics are obtained, then by symmetry, the yaw characteristics should also be satisfactory. In the case of the monowing design, sufficiently large stabilizing tail surfaces must be used to obtain the desired static stability and damping characteristics. The following sections deal with the contributions of the different missile components toward these desired characteristics for both monowing and cruciform designs.

Before going into the detailed discussion of the directional stability and control characteristics, it is well first to define some of the nomenclature commonly used in such an analysis (see Fig. 7-1).

1. The sideslip angle β is the angle between the velocity vector and the plane of symmetry of the missile. It is positive by definition when

the nose of the missile is pointed to the left of this velocity vector. Hence it can be seen that β is analogous to the angle of attack α for the longitudinal case.

2. The yaw angle ψ is the angle between a reference line fixed in space and the plane of symmetry. It is positive when the nose of the missile is pointed to the right of the reference direction. Hence ψ is analogous to the pitch angle θ in the longitudinal case. For steady-state conditions such as equilibrium sideslips, $\psi = -\beta$. However, for general application where the missile is not in equilibrium sideslips but is in an

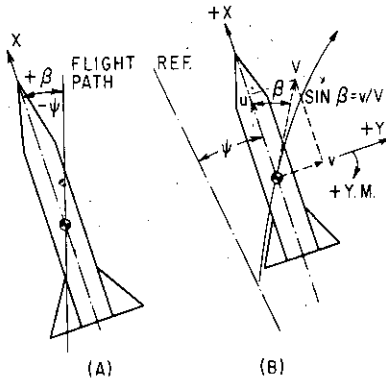


FIG. 7-1. Nomenclature for directional-stability analysis. (A) Equilibrium sideslip. (B) General sideslip.

accelerated or turning-flight maneuver, $\psi \neq -\beta$. A certain amount of confusion has arisen from the fact that some wind-tunnel data are plotted as a function of ψ instead of the more precise parameter β . Therefore, before these data can be used, the static directional-stability derivative $C_{n\psi}$ must be used as $-C_{n\beta}$, since no such derivative as $C_{n\psi}$ actually exists. The directional-stability derivative $C_{n\beta}$ is analogous to $C_{m\alpha}$ in the pitch case. Defining a positive yawing moment as one which rotates the nose of the missile to the right, the sign of $C_{n\beta}$ must be positive for static stability to exist in yaw.

7-2. CRUCIFORM CONFIGURATION

In the majority of our missile configurations, a cruciform design is used to obtain fast and equal response characteristics in both the pitch (longitudinal) and yaw (directional) axes. For this type of design, the discussions presented in Chap. 5 for the longitudinal case are applicable to the directional case. Therefore, it is considered appropriate to discuss here the pertinent relationships for combined pitch

and yaw maneuvers. From Fig. 7-2, the following angular relationships are defined:

$$\alpha = \tan^{-1} (\tan i \cos \varphi) \quad (7-1)$$

$$\beta = \tan^{-1} (\tan i \sin \varphi) \quad (7-2)$$

where φ = angle between reference plane and plane of resultant wind
 i = angle between longitudinal axis of missile and resultant wind

α and β = angle of attack and sideslip, respectively

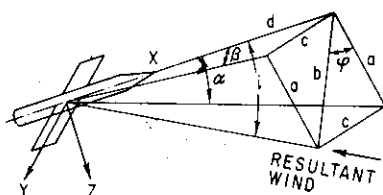


FIG. 7-2. Angle notation.

$$\tan \alpha = \frac{a}{d} \quad \tan \beta = \frac{c}{d}$$

$$a = b \cos \varphi$$

$$c = b \sin \varphi$$

$$d = b / \tan i$$

$$\tan \alpha = \cos \varphi \tan i$$

$$\tan \beta = \sin \varphi \tan i$$

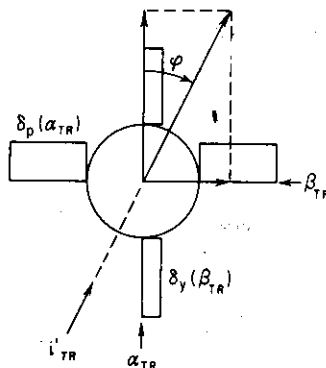


FIG. 7-3. Combined pitch and yaw maneuver.

For small angles, Eqs. (7-1) and (7-2) may be reduced to

$$\alpha \cong i \cos \varphi \quad (7-3)$$

$$\beta \cong i \sin \varphi \quad (7-4)$$

or

$$\tan \varphi \cong \frac{\beta}{\alpha} \quad (7-5)$$

Hence, for a combined maneuver which requires equal pitch and yaw commands, the orientation of the force or velocity vector will be 45° to the reference plane. If i'_{TR} is defined as the trim angle of attack for a unit load factor, then

$$\alpha \cong 0.7i'_{TR} \quad (7-6)$$

$$\beta \cong 0.7i'_{TR} \quad (7-7)$$

For other combinations of two-plane maneuvers, such as that shown in Fig. 7-3, the following relationships may be written (linear aerodynamics assumed):

$$\alpha \cong i'_{TR} \cos \varphi \quad (7-8)$$

$$\beta \cong i'_{TR} \sin \varphi \quad (7-9)$$

where φ is the desired orientation of the velocity or force vector and is specified.

7-3. BODY CONTRIBUTION

The force and moment contributions of the body consist principally of (1) those of the nose or forebody of the missile and (2) those resulting from body upwash (or sidewash) effects as described in Chap. 5. The latter effect is normally treated together with the tail contribution.

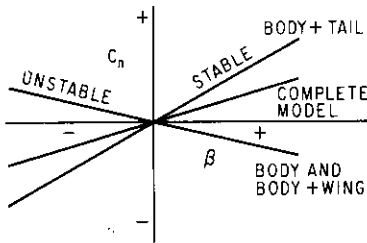


FIG. 7-4. Model build-up in directional-stability curve (monowing design).

Hence the force and moment from the nose or forebody are generally considered as the basic body contribution to the directional-stability characteristics of the missile and are essentially independent of Mach number. For large length-to-diameter ratio l/d , nose or forebody, its large destabilizing effect on directional stability is very undesirable and must be overcome by large tail surfaces. This destabilizing effect may become critical, particularly at the higher supersonic Mach numbers, since the stabilizing contribution of the tail surfaces decreases as the result of decreasing C_{N_α} with increasing Mach number. Hence it may be necessary to reduce the nose l/d to ameliorate this problem even at the sacrifice of missile performance (i.e., increase in wave drag due to foreshortened nose).

The body contribution to yawing moment can be expressed as follows:

$$(\Delta C_{n_\beta})_B = (C_{v_\beta})_B \left(\frac{x}{d} \right)_B \quad (7-10)$$

where $|(C_{v_\beta})_B| = |(C_{N_\alpha})_B|$ for a body of revolution.

Since the sign of $(C_{v_\beta})_B$ is negative (and x is positive measured forward of the center of gravity) $(\Delta C_{n_\beta})_B$ is also negative, indicating an unstable contribution as shown in Fig. 7-4.

7-4. WING CONTRIBUTION

It was noted in Chaps. 2 and 5 that, for either a wing- or tail-control design, the wing has a pronounced effect on the static longitudinal-stability and control characteristics of the missile. However, in the directional-stability and control case, the wing contribution is small,

particularly for the mid-wing design generally used on monowing missile configurations. This is apparent from the fact that, for a straight and unswept wing, the change in angle of attack due to sideslip on one side is the same as that on the opposite side. The effects of sweep, wing planforms, etc., have been extensively treated from the theoretical standpoint.^{1-5*} Except for the dihedral effects, which will be discussed in Chap. 8, the effects of the wing on the directional-stability and control characteristics are generally small and may be neglected in preliminary design studies. This is justified in the light of numerous experimental test results. It should be noted, however, that for monowing designs the effects of wing height on the body may be significant as a result of body-wing mutual interference as well as shock-wave interference, and they should be carefully analyzed in the wind tunnel.

7-5. TAIL CONTRIBUTION

The magnitude of the (vertical) tail contribution to yawing moment required is the sum of the unstable yawing moment due to the nose or forebody and that required to yield the desired static directional-stability margin. For the cruciform design, this tail contribution is identical to that determined for the pitch-stability case. However, for the monowing design the problem of determining the vertical tail contribution is complicated by several factors. Among these factors are (1) body-tail interference, (2) horizontal tail and vertical tail mutual interference, and (3) sidewash introduced by body, wing, and wing-body interference.

The tail contribution to side force and yawing moment (see Fig. 7-4) may be expressed as follows:

$$(\Delta C_{v\beta})_T = (C_{v\beta})_T \frac{S_T}{S_x} \left(1 + \frac{d\sigma}{d\beta} \right) \quad (7-11)$$

and

$$(\Delta C_{n\beta})_T = (C_{v\beta})_T \frac{S_T}{S_x} \left(1 + \frac{d\sigma}{d\beta} \right) \left(\frac{x}{d} \right)_T \quad (7-12)$$

where $(C_{v\beta})_T$ = normal-force-curve slope of vertical tail in presence of body and horizontal tail and is based on S_T (tail area)

$d\sigma/d\beta$ = rate of change in sidewash angle (see Fig. 7-5) with angle of sideslip

* Superscript numbers indicate references listed at the end of the chapter.

From the previous discussion, the complete model side-force and yawing-moment derivatives may be expressed as

$$(C_{y\beta})_{CM} = (C_{y\beta})_B + (C_{y\beta})_T \frac{S_T}{S_\pi} \left(1 + \frac{d\sigma}{d\beta}\right) \quad (7-13)$$

and

$$(C_{n\beta})_{CM} = (C_{n\beta})_B \left(\frac{x}{d}\right)_B + (C_{n\beta})_T \frac{S_T}{S_\pi} \left(1 + \frac{d\sigma}{d\beta}\right) \left(\frac{x}{d}\right)_T \quad (7-14)$$

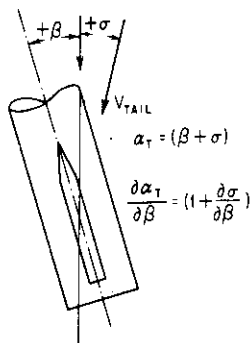


FIG. 7-5. Angle of attack on the (vertical) tail.

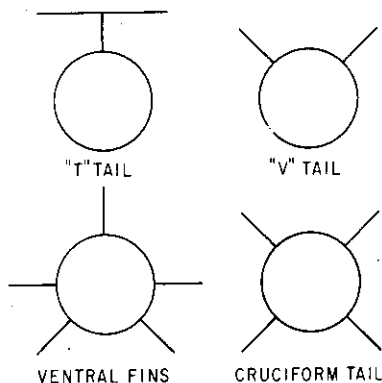


FIG. 7-6. Typical tail designs.

The static stability in yaw may be expressed as

$$\text{Static margin} = \frac{C_{n\beta}}{C_{y\beta}} = \left(\frac{\bar{X}}{d}\right)_{CM} \quad (7-15)$$

and is analogous to $C_{m\alpha}/C_{N\alpha}$ for the longitudinal case. Hence for a given static stability requirement the vertical-tail size may be determined with the aid of Eqs. (7-13) through (7-15).

It will be recalled from Chap. 3 that the normal-force-curve slope of an aerodynamic lifting surface decreases with increasing Mach number in the supersonic region. Therefore, it is apparent that the static stability margin (and control) characteristics deteriorate with increasing Mach number. Consequently, the area of the vertical tail of a monowing design may become extremely large in order to satisfy the stability requirement in the high-Mach-number regions. The tail span for such a large area may be impractical from the standpoint of structural efficiency, physical-span limitation (particularly for air-launched missiles), and aerodynamic cross-coupling effects. In order to circumvent this design inefficiency, several types of tail design may

be used. These include the T tail, V tail, ventral fins, and cruciform X tails as shown in Fig. 7-6. From the standpoint of keeping the span to a minimum, the latter design is optimum. Ventral fins may also be used advantageously, particularly for cases where the pitch angle of attack is relatively large, which results in fuselage blanketing of the top portion of the vertical tail.

7-6. DIRECTIONAL CONTROL

For a cruciform design the primary requirement of directional control is to assure that adequate load-factor capability is realized in the yaw plane. As previously mentioned, if the pitch-control characteristics are satisfactory, the yaw control should also be adequate. If linear aerodynamics are assumed, the control deflections for combined pitch and yaw maneuvers may be readily determined. Since the control-surface deflection is proportional to the trim angle of attack (or sideslip) as expressed in Eq. (5-22), the pitch-and-yaw-control deflections δ_p and δ_y may be related with the aid of Eq. (7-3) as follows:

$$\tan \varphi \sim \frac{\delta_y}{\delta_p} \quad (7-16)$$

Hence
$$\delta_p \cong \delta' \cos \varphi \quad (7-17)$$

$$\delta_y \cong \delta' \sin \varphi \quad (7-18)$$

where δ' is defined as the control-surface deflection required for a unit load factor in a single plane with i'_{TR} as its corresponding trim angle of attack [see Eqs. (7-8) and (7-9)].

For a monowing configuration, the primary requirement of directional control is to maintain zero sideslip. Rudder is generally preferred over the all-movable vertical tail. This results from the fact that the hinge moment and consequently servo-power requirement is minimized and that only a portion of the vertical tail surface is needed to provide the desired control. In general, detailed analysis of the dynamics of the missile about both the yaw and roll axes must be performed before the exact requirement for direction control can be established.

SYMBOLS

C_m	pitching-moment coefficient
C_n	yawing-moment coefficient
C_y	side-force coefficient

S	body frontal (reference) area
V	resultant forward velocity
\bar{X}	resultant center of pressure
YM	yawing moment
d	body diameter
i	angle between the longitudinal axis of the missile and the resultant wind
i'_{TR}	trim angle of attack for a unit load-factor length
l	length
u	velocity along the X axis
v	velocity along the Y axis
x	distance between missile center of gravity and center of pressure
α	angle of attack
β	angle of sideslip
δ	control-surface deflection
δ'	control-surface deflection for unit load factor in a single plane
σ	sidewash angle
φ	angle between reference plane and plane of resultant wind
ψ	yaw angle

Subscripts

B	body
CM	complete model
T	tail
p	pitch
y	yaw

REFERENCES

1. Harmon, S. M.: Stability Derivatives of Thin Rectangular Wings at Supersonic Speeds. Wing Diagonals ahead of Tip Mach Lines, *NACA Rept.* 925, 1949.
2. Ribner, H. S.: The Stability Derivatives of Low-aspect-ratio Triangular Wings at Subsonic and Supersonic Speeds, *NACA Tech. Note* 1423, 1947.
3. Ribner, H. S., and F. S. Malvestuto, Jr.: Stability Derivatives of Triangular Wings at Supersonic Speeds, *NACA Rept.* 908, 1948.
4. Moeckel, W. E.: Effect of Yaw at Supersonic Speeds on Theoretical Aerodynamic Coefficients of Thin Pointed Wings with Several Types of Trailing Edge, *NACA Tech. Note* 1549, 1948.
5. Jones, A. L., and A. Alksne: A Summary of Lateral-stability Derivatives Calculated for Wing Plan Forms in Supersonic Flow, *NACA Rept.* 1052, 1949.
6. Love, E. S.: Supersonic Wave Interference Affecting Stability, *NACA Tech. Note* 4358, September, 1958.

CHAPTER 8

LATERAL STABILITY AND CONTROL

8-1. INTRODUCTION

Since there is no natural static stability about the lateral axis such as that associated with either the longitudinal or directional axis, intelligent inputs, such as those from the human pilot in the airplane or the automatic pilot or control-system sensor in the missile, are necessary to control the lateral attitude and/or motion of the airframe. The absence of the human pilot from the missile airframe-control system has to a certain extent simplified the problem of lateral stability and control. Hence the problem is one which deals primarily with the determination of the nature and magnitude of the induced rolling moments and lateral-control effectiveness of the missile. The following sections present some of the more important design aspects with regard to realizing acceptable lateral-stability and control characteristics for both cruciform and monowing configuration.

8-2. INDUCED ROLL—CRUCIFORM

Perhaps the one most difficult parameter to determine accurately is the induced rolling-moment characteristics of a cruciform missile. These rolling moments arise whenever the missile simultaneously executes pitch and yaw maneuvers which are unequal in magnitude. Such maneuvers result in unequal or asymmetric flow patterns over the aerodynamic lifting surfaces, and consequently rolling moments are "induced" on the airframe. An illustration of the general effects causing induced rolling moments is presented in Fig. 8-1 for a wing-control configuration. It can be seen that these effects may be divided into four general classes: (1) tip effect, (2) root effect, (3) body-blanketing effect, and (4) downwash effect. Of these, the most important effect results from the downwash on the tail surfaces. Because of the complex nature of the flow pattern under combined

maneuvers, any attempt to evaluate these rolling moments must, by necessity, be only approximate and quite lengthy. Hence, in most preliminary design analyses, the determination of this parameter is omitted, since it is most conveniently evaluated in the wind tunnel. However, the designer should bear in mind the importance of these induced rolling moments in the determination of a satisfactory and adequate lateral-control system.

8-3. LATERAL CONTROL— CRUCIFORM

The exact magnitude of the lateral-control effectiveness required is not easily determined since it depends chiefly on the magnitude of the induced rolling moments. However, from the standpoint of control-system simplification, it is desirable to provide sufficient lateral control to overcome the aerodynamic induced rolling moments and also those due to surface malalignments encountered throughout the entire missile flight régime of speed and angle of attack and yaw. However, in some cases, it may be necessary to incorporate a more complicated lateral-control system to compensate for a less efficient aerodynamic lateral control in order to simplify the pitch-and-yaw-control systems and consequently result in a more optimum over-all missile system. Such a case may be one in which the main movable wing (or tail) surfaces are used for both pitch or yaw and roll control in lieu of a separate set of lateral-control surfaces such as ailerons or tip controls.

In the selection of a lateral-control system the following important design considerations must be taken into account: (1) control effectiveness, (2) hinge moments, and (3) complexity in terms of structural design and control-system design. For a canard configuration (see Fig. 2-2), the canard surfaces are completely inadequate for lateral control primarily because of (1) the small surface area and its short moment arm and (2) the induced rolling moments from the aft surfaces

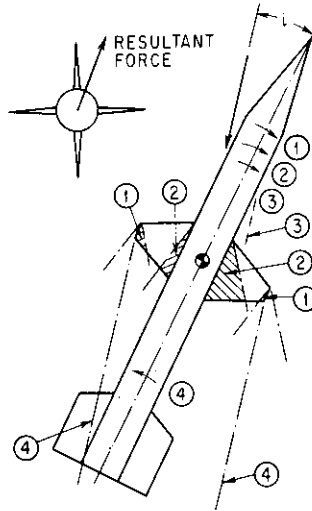


FIG. 8-1. Effects causing induced roll. (1) Tip effect. (2) Root effect. (3) Blanketing effect. (4) Downwash effect.

due to downwash effects. For this type of design, a separate set of lateral controls such as wing-tip ailerons is needed. For a wing-control configuration the movable wing surfaces may be used as lateral-control devices if proper design is realized. As illustrated in Fig. 8-2, the opposing rolling moments from the tail surfaces may be of sufficient magnitude to nullify completely the effectiveness of the wing surfaces even for single-plane maneuvers; hence roll reversal may result. These opposing rolling moments may also be considered as induced rolling moments and are present in addition to those due to combined maneuvers previously described. By proper design, adequate lateral-control effectiveness may be realized from the movable wings. These design considerations will be discussed in a latter section. For a tail-control configuration, the lateral-control effectiveness obtained by differential tail deflections may be marginal because of (1) the downwash from the wing due to angle of attack and (2) the relatively short moment arm for producing rolling moments.

The magnitude of the lateral-control effectiveness obtained by differential wing or tail deflection is also difficult to determine because of the effect of downwash. This is particularly so for combined maneuvering conditions where knowledge of the magnitude of the lateral-control effectiveness (as well as the induced rolling moments) is most desirable. Hence its determination must also be made in the wind tunnel. For the more simplified lateral-control devices, such as wing-tip ailerons, spoilers, or flaps, sufficient experimental data^{1,2,3,*} may be available to permit a preliminary determination of its control effectiveness.

The adequacy of the lateral-control effectiveness may be determined from wind-tunnel-test results by plotting the rolling-moment coefficient C_l vs. i (defined in Chap. 6) for the complete model configuration with and without lateral-control surface deflections superimposed on various combined maneuvers (i.e., different ϕ 's) as shown in Fig. 8-3. The "trim" point A is the maximum value of i for which lateral control is adequate to trim out the induced rolling moments. If the magnitude of i thus obtained is greater than that anticipated in the required combined pitch and yaw maneuver (including the effect of dynamic overshoot), the lateral-control effectiveness is deemed satisfactory. However, if the magnitude of i is less than that anticipated in flight, lateral control appears inadequate. In such a case, several alternatives may be taken: (1) restrict the magnitude of the combined pitch and yaw maneuver, thereby restricting the effectiveness of the missile

* Superscript numbers indicate references listed at the end of the chapter.

weapon system; (2) modify the pitch-and-yaw-control system to reduce the dynamic overshoot of the airframe or i ; and (3) modify the configuration. The selection of one or a combination of these alternatives depends on the degree of lateral-control deficiency.

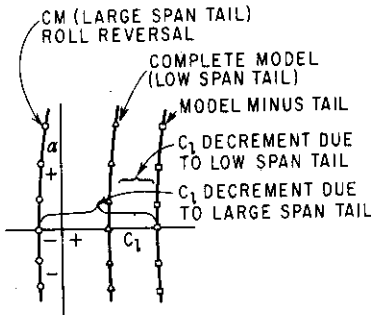


FIG. 8-2. Effect of tail on roll-control effectiveness (single-plane maneuver).

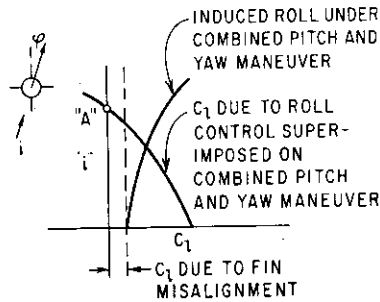


FIG. 8-3. Lateral-control effectiveness when superimposed on combined pitch and yaw maneuver.

8-4. SPECIAL DESIGN CONSIDERATIONS—CRUCIFORM

In view of the complexity of the lateral stability and control problem, certain design practices should be observed during the preliminary or development phase of a missile project in order that satisfactory lateral characteristics may be realized. From the standpoint of keeping the aerodynamic induced rolling moments to a minimum, the span of the tail surface is perhaps the one most important design one must consider. From Fig. 8-1, it is apparent that, for a given wing configuration, the majority of the tail surface is directly affected by the wing downwash. Consequently, a reduction in tail span will materially decrease the roll moment arm and hence the induced rolling moment. The reduction in span has the added advantage that the aspect ratio is reduced, thereby decreasing the lift-curve slope. The latter is, however, a disadvantage from the standpoint of tail effectiveness in that its contribution to the static longitudinal (or directional) stability is also decreased. Hence a relatively large increase in tail area is necessary. The angle of attack should also be kept relatively low in order to avoid the large induced rolling moments generally associated with large values of i , as shown in Fig. 8-3. This may be accomplished by (1) increasing the static longitudinal and directional stability margin and (2) restricting the dynamic overshoot of the angle of attack and/or yaw

by proper control-system design. The former method has the disadvantage in that relatively large aerodynamic surfaces are required to satisfy the maneuverability required (see Sec. 6-4). On the other hand, the second method requires a somewhat more complicated and hence less reliable control system.

From the standpoint of lateral-control effectiveness, separate wing-tip-aileron roll control appears to be the most effective. However, structural and control-system design is somewhat more involved. The hinge moments associated with this type of control appear to be reasonably low. The use of the main wing surfaces for roll control may be acceptable, provided that proper tail design is realized. The hinge line for this type of control must be carefully selected to minimize the hinge moments. The use of the tail surfaces for roll control is generally avoided since it is generally marginal because of its small area and small roll moment arm. For tail-control design (see Fig. 2-2) a separate set of lateral controls on the wing tip is therefore more acceptable.

8-5. DAMPING IN ROLL

In the study of the (dynamic) lateral motion of the missile, the damping-in-roll characteristics must be known. This damping term arises primarily from lift and moment from the wing (or tail) surfaces whenever the missile develops a rolling velocity. The effect of such a rolling velocity is to induce an angle of attack which varies linearly along the span as shown in Fig. 8-4 and can be expressed as

$$\Delta\alpha \cong \frac{v_t}{V} = \frac{py}{V} \quad (8-1)$$

where $\Delta\alpha$ = induced angle of attack at point y along span

V_t = tangential velocity (equal to py)

p = rolling velocity, radians/sec

V = missile forward speed

Consequently the damping-in-roll derivative may be derived as follows:

$$\mathcal{L} = -N\bar{y} = \int_{-b/2}^{b/2} (C_{N_\alpha})_1 \Delta\alpha yqc \, dy \quad (8-2)$$

where \mathcal{L} = rolling moment

N = normal force

\bar{y} = resultant roll moment arm

$(C_{N_\alpha})_1$ = section normal-force coefficient

c = local chord at span y (see Fig. 8-5)

By using common missile terminology, the rolling-moment coefficient C_l is defined as

$$C_l = \frac{\mathcal{L}}{qS_r d} \quad (8-3)$$

Defining C_{l_p} as $\partial C_l / \partial (pd/2V)$ and combining Eqs. (8-2) and (8-3), we get

$$C_{l_p} = \frac{2}{S_r d^2} \int_{-b/2}^{b/2} (C_{N_a})_1 cy dy \quad (8-4)$$

The magnitude of the damping in roll depends primarily on the aspect ratio, planform, and Mach number and has been determined

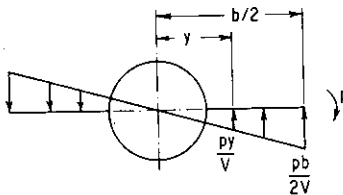


FIG. 8-4. Spanwise variation of induced angle of attack caused by rolling velocity.

both theoretically and experimentally.⁴⁻¹⁶ For preliminary design, the experimental results should be used wherever possible because of the limitations imposed on most of the theoretical treatments. In general, the experimental values of C_{l_p} are somewhat lower than those predicted by theory and may be attributed to such effects as wing thickness, body interference, and possible aeroelasticity. In the conversion of either the theoretical or experimental results, extreme care must be exercised to assure that proper units or definitions are adhered to. This is particularly important for configurations (i.e., cruciform wing or tail control) which have several aerodynamic surfaces contributing to roll damping. For preliminary design, the damping in roll for four equal wing panels may be assumed to be twice the value of the two panels. This assumes no mutual wing interference. The tail contribution may also be assumed to be independent of the wing interference (i.e., downwash effects). However, experimental results indicate that such a method generally yields values

of C_{l_p} which are somewhat larger than the actual value since the downwash decreases the tail contribution to roll damping. For certain applications where a "tight" roll control is required to assure the

both theoretically and experimentally.⁴⁻¹⁶ For preliminary design, the experimental results should be used wherever possible because of the limitations imposed on most of the theoretical treatments. In general, the experimental values of C_{l_p} are somewhat lower than those predicted by theory and may be attributed to such effects as wing thickness, body interference, and possible aeroelasticity.

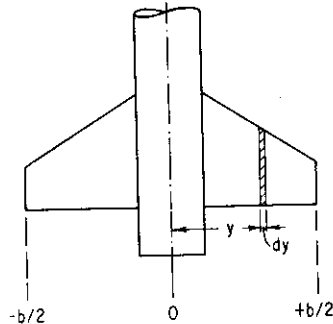


FIG. 8-5. Strip integration for C_{l_p} .

desired guidance accuracy, it is desirable to determine the roll-damping term experimentally. This may be accomplished in the wind tunnel with a scaled-down model or by flight-testing a full-scale model.

8-6. INDUCED ROLL—MONOWING

The induced-roll problem for the monowing configuration is substantially less severe than that associated with the cruciform configuration previously described. This results primarily from the following differences in the basic design of the monowing and cruciform configurations: (1) the omission of one set of wings or control surfaces for the monowing design, (2) the bank-to-turn feature, and (3) the separate set of lateral controls generally employed on the monowing configuration. The omission of one set of wings results in a drastic reduction in induced rolling moments since the asymmetric flow due to downwash is essentially eliminated. The bank-to-turn feature, however, does result in a nominal amount of flow asymmetry and hence induced rolling moments, the magnitude of which is generally acceptable. Finally, the use of a separate set of lateral-control surfaces such as wing-tip ailerons generally provides adequate roll-control effectiveness over the entire flight regime.

In the analysis of the (dynamic) lateral (and directional) stability characteristics, the rolling moment due to sideslip C_{l_β} is one of the most influential parameters. This factor is often referred to as the effective dihedral effect and has a finite value even for wings with no geometric dihedral angle. For this condition of no geometric dihedral, the rolling moment due to sideslip in supersonic flow is the result of an increase in lift within the Mach cone from the leading wing tip coupled with a corresponding decrease from the trailing wing tip. The magnitude of C_{l_β} has been determined theoretically for various wing planforms^{4,17,18} and may be used for preliminary design analysis. However, these values should be checked by wind-tunnel tests, particularly when geometric dihedral or cathedral (negative dihedral) is used.

Generally speaking, excessive effective dihedral may result in highly oscillatory motion which must be artificially damped by the lateral-control-system servo loop.

8-7. LATERAL CONTROL—MONOWING

As previously mentioned, a separate set of lateral-control surfaces is generally used in a monowing design. This stems from the fact that

the canards or tail surfaces which are usually employed for pitch control on this type of design are generally inadequate for lateral control. The most common types of lateral control used are (1) flaps, (2) spoilers, and (3) wing-tip ailerons. A detailed analysis in terms of their lateral-control effectiveness,¹⁻³ hinge-moment characteristics, and design complexities must be made before an optimum lateral-control configuration can be realized.

SYMBOLS

C_l	rolling-moment coefficient
C_{l_p}	damping-in-roll coefficient
$(C_{N_x})_l$	section normal-force coefficient
\mathcal{L}	rolling moment
N	normal force
S_π	body frontal (reference) area
V	forward speed
c	local chord
d	body diameter
p	rolling velocity
q	dynamic pressure
v_t	tangential velocity py
y	spanwise distance measured from center line of missile
\bar{y}	resultant spanwise roll moment arm
α	angle of attack
β	angle of sideslip
φ	angle between reference plane and plane of resultant wind

REFERENCES

1. Strass, H. K., E. W. Stephens, E. M. Fields, and E. D. Schult: Collection and Summary of Flap-type-aileron Rolling Effectiveness Data at Zero Lift as Determined by Rocket-powered Model Test at Mach Numbers between 0.6 and 1.6. *NACA Research Mem.* L55F14, Sept. 2, 1955.
2. Brewer, J. D.: Description and Bibliography of NACA Research on Wing Controls. January 1946-February 1955. *NACA Research Mem.* 54K24, Mar. 24, 1955.
3. Lowry, J. G.: Recent Control Studies. *NACA Research Mem.* L55L22a, Feb. 16, 1956.
4. Harmon, S. M.: Stability Derivatives at Supersonic Speeds of Thin Rectangular Wings with Diagonals ahead of Tip Mach Lines. *NACA Rept.* 925, 1949 (supersedes *NACA Tech. Note* 1706).
5. Malvestuto, F. S., Jr., K. Margolis, and H. S. Ribner: Theoretical Lift

and Damping in Roll at Supersonic Speeds of Thin Sweptback Tapered Wings with Streamwise Tips, Subsonic Leading Edges, and Supersonic Trailing Edges, *NACA Rept.* 970, 1950 (supersedes *NACA Tech. Note* 1860).

6. Tosti, L. P.: Low-speed Static Stability and Damping-in-roll Characteristics of Some Swept and Unswept Low-aspect-ratio Wings, *NACA Tech. Note* 1468, October, 1947.

7. Ribner, H. S.: Damping in Roll of Cruciform and Some Related Delta Wings at Supersonic Speeds, *NACA Tech. Note* 2285, 1951.

8. Piland, R. O.: Summary of the Theoretical Lift, Damping-in-roll, and Center-of-pressure Characteristics of Various Wing Plan Forms at Supersonic Speeds, *NACA Tech. Note* 1977, October, 1949.

9. Adams, G. J.: Theoretical Damping in Roll and Rolling Effectiveness of Slender Cruciform Wings, *NACA Tech. Note* 2270, January, 1951.

10. Hedgepeth, J. M., and R. J. Kell: Rolling Effectiveness and Aileron Reversal of Rectangular Wings at Supersonic Speeds, *NACA Tech. Note* 2067.

11. Adams, G. J., and D. W. Dugan: Theoretical Damping Roll and Rolling Moment Due to Differential Wing Incidence for Slender Cruciform Wings and Wing-body Combinations, *NACA Tech. Rept.* 1088, 1952.

12. Bleviss, Z. O.: Some Roll Characteristics of Cruciform Delta Wings at Supersonic Speeds, *J. Aeronaut. Sci.*, vol. 18, no. 5, pp. 289-297, May, 1951.

13. Michael, W. H.: Analysis of the Effects of Wing Interference on the Tail Contributions to the Rolling Derivatives, *NACA Rept.* 1086, 1952.

14. Stone, D. G.: A Collection of Data for Zero-lift Damping-in-roll of Wing-body Combinations as Determined with Rocket-powered Models Equipped with Roll-torque Nozzles, *NACA Tech. Note* 3955, April, 1957.

15. Polhamus, E. C.: A Simple Method of Estimating the Subsonic Lift and Damping in Roll of Sweptback Wings, *NACA Tech. Note* 1862, 1949.

16. Bland, W. M., Jr., and A. E. Dietz: Some Effects of Fuselage Interference, Wing Interference, and Sweepback on the Damping in Roll of Untapered Wings as Determined by Techniques Employing Rocket-propelled Vehicles, *NACA Research Mem.* L51D25, 1951.

17. Jones, A. L., J. R. Spreiter, and A. Alksne: The Rolling Moment Due to Sideslip of Triangular, Trapezoidal, and Related Plan Forms in Supersonic Flow, *NACA Tech. Note* 1700, September, 1948.

18. Ribner, H. S., and F. S. Malvestuto, Jr.: Stability Derivatives of Triangular Wings at Supersonic Speeds, *NACA Tech. Note* 1572, May, 1948.

CHAPTER 9

DYNAMIC STABILITY

9-1. INTRODUCTION

(Since the accuracy or effectiveness of a guided missile depends greatly on the dynamics of the missile, particularly during the terminal phase of its flight, it is often desirable to predict its flight dynamics in the early preliminary-design phase to assure that a reasonably satisfactory missile configuration is realized.) In this chapter, the problems associated with the dynamics of the airframe as well as the pertinent equations of motion are discussed. In addition, derivations of few of the more commonly used transfer equations are included for automatic-control analysis.

A missile is a free body with six degrees of freedom, translational and rotational motions about the X , Y , and Z axes. In addition, with free controls, each freed control surface permits another degree of freedom for the rotation of the control about its hinge line. In general, the control surfaces on missiles are "locked" in place by the control actuators and are not free to move under the influence of inertia or external aerodynamic applied forces or moments. Hence, in most missile dynamic analyses, six degrees of freedom are adequate. The dynamic-stability characteristics can be evaluated by solution of the appropriate set of equations of motion for each degree of freedom. Each of these equations can be treated independently only if motions along and about one axis under consideration do not result in forces or moments about another axis. Such a case may be motions in pure pitch or roll.

In general, the response characteristics of a missile (or any dynamic system), when disturbed from equilibrium, consist of four modes. These modes may be either oscillatory or nonoscillatory (i.e., aperiodic), damped or undamped, as shown in Fig. 9-1. These oscillations correspond to the natures of the roots of the differential equations of motion. This can be illustrated by considering a simple harmonic equation:

$$A\ddot{\theta} + B\dot{\theta} + C\theta = K \quad (9-1)$$

By substituting the operator p to denote differentiation with respect to time p^2 for the second derivative, etc., Eq. (9-1) becomes

$$(p^2A + pB + C)\theta = K \quad (9-2)$$

The term $(p^2A + pB + C)$ equated to zero is called the characteristic equation. The roots of this characteristic equation may be found by the binomial theorem as follows:

$$P_{1,2} = \frac{-B \pm \sqrt{B^2 - 4AC}}{2A} \quad (9-3)$$

The solution consists of a "characteristic solution" and a "particular solution." The former solution is determined by the roots of the characteristic equation [Eq. (9-3)] whereas the latter solution is determined by the forcing function. For the case illustrated, the latter is K . The complete solution is the sum of the characteristic and particular solution and may be expressed as

$$\theta = a_1e^{p_1t} + a_2e^{p_2t} + K \quad (9-4)$$

where a_1 and a_2 are determined by the initial conditions.

From Eq. (9-3), the value of the roots p_1 and p_2 may be one of the following possibilities:

1. Two positive real roots
2. Two negative real roots
3. One positive and one negative real root
4. Conjugate complex root with positive real parts
5. Conjugate complex root with negative real parts

It is apparent that a positive real root indicates a divergent motion since e^{p_1t} [in Eq. (9-4)] increases with time whereas a negative real root indicates a convergent motion since e^{p_2t} decreases with time. A complex root indicates oscillatory motion. The latter type of motion is damped if the real part of the root is negative and undamped for a positive real root.

A higher-order differential equation may be conveniently factored into quadratic terms similar to those just discussed. Hence a complicated motion consists of many modes which can be superimposed to

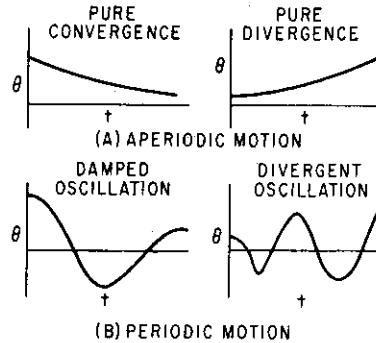


FIG. 9-1. Typical modes of motion.

form the total resultant motion. Such an example is the longitudinal equation of motion which results in a quartic differential equation which can be factored into two quadratics. In this case, two distinct modes are obtained: one short period which is heavily damped and one long period which is very lightly damped and is commonly known as the phugoid motion. These motions will be discussed further in Sec. 9-3.

9-2. EQUATIONS OF MOTION

The equations of motion of a missile with controls fixed may be derived from Newton's second law of motion, which states that the rate of change of momentum of a body is proportional to the summation of forces applied to the body and that the rate of change of the moment of

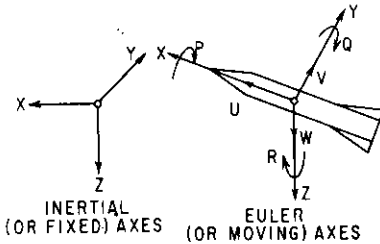


FIG. 9-2. Axes systems.

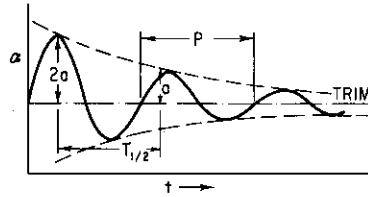


FIG. 9-3. Typical longitudinal short-period oscillation.

momentum is proportional to the summation of moments applied to the body. Mathematically, this law of motion may be written as

$$\begin{aligned} \Sigma F_x &= \frac{d(mU)}{dt} & \Sigma M_x &= \frac{dh_x}{dt} \\ \Sigma F_y &= \frac{d(mV)}{dt} & \Sigma M_y &= \frac{dh_y}{dt} \\ \Sigma F_z &= \frac{d(mW)}{dt} & \Sigma M_z &= \frac{dh_z}{dt} \end{aligned} \quad (9.5)$$

where ΣF_x , ΣF_y , and ΣF_z = summation of forces along x , y , and z axis (see Fig. 9-2)

ΣM_x , ΣM_y , and ΣM_z = summation of moments about the x , y , and z axis

h_x , h_y , and h_z = moments of momentum about x , y , and z axis

The moment of momentum h_x , h_y , and h_z may be written in terms of the

moments of inertia and products of inertia and angular velocities P , Q , and R of the missile as follows:

$$\begin{aligned} h_x &= PI_x - QI_{xy} - RI_{xz} \\ h_y &= QI_y - RI_{yz} - PI_{xy} \\ h_z &= RI_z - PI_{xz} - QI_{yz} \end{aligned} \quad (9-6)$$

Substituting Eq. (9-6) into (9-5) and assuming m is a constant, we get

$$\begin{aligned} \Sigma F_x &= \frac{m dU}{dt} \\ \Sigma F_y &= \frac{m dV}{dt} \\ \Sigma F_z &= \frac{m dW}{dt} \end{aligned} \quad (9-7)$$

$$\begin{aligned} \Sigma M_x &= \dot{P}I_x + PI_x - \dot{Q}I_{xy} - Q\dot{I}_{xy} - \dot{R}I_{xz} - RI_{xz} \\ \Sigma M_y &= \dot{Q}I_y + Q\dot{I}_y - \dot{R}I_{yz} - R\dot{I}_{yz} - \dot{P}I_{xy} - P\dot{I}_{xy} \\ \Sigma M_z &= \dot{R}I_z + R\dot{I}_z - \dot{P}I_{xz} - P\dot{I}_{xz} - \dot{Q}I_{yz} - Q\dot{I}_{yz} \end{aligned}$$

It is readily apparent that Eqs. (9-7), which are the equations of motion written about an inertial or fixed axis, are extremely cumbersome and must be modified before the motion of the missile can be conveniently analyzed. Hence a moving-axis system called the Eulerian axes is commonly used. This axis system is a right-hand system of orthogonal coordinate axes whose origin is at the center of gravity of the missile and whose orientation is fixed with respect to the missile (see Fig. 9-3). The two main reasons for the use of the Eulerian axes in the dynamic analysis of the airframe are (1) the velocities along these axes are identical to those measured by instruments mounted in the missile and (2) the moments and products of inertia are independent of time. Consequently, Eqs. (9-7) may be rewritten about the Eulerian axes as

$$\begin{aligned} \Sigma F_x &= m(\dot{U} + QW - RV) \\ \Sigma F_y &= m(\dot{V} + RU - PW) \\ \Sigma F_z &= m(\dot{W} + PV - QU) \\ \Sigma M_x &= \dot{P}I_x - \dot{Q}I_{xy} - \dot{R}I_{xz} + QR(I_z - I_y) - PQI_{xz} - Q^2I_{zy} \\ &\quad + R^2I_{yz} + PRI_{xy} \\ \Sigma M_y &= \dot{Q}I_y - \dot{R}I_{yz} - \dot{P}I_{xz} + PR(I_x - I_z) - QRI_{zy} - R^2I_{xz} \\ &\quad + P^2I_{xz} + PQI_{xz} \\ \Sigma M_z &= \dot{R}I_z - \dot{P}I_{xy} + PQ(I_y - I_x) - PRI_{yz} - P^2I_{xy} + Q^2I_{xy} + QRI_{xz} \end{aligned} \quad (9-8)$$

For a monowing configuration, the xz plane is a plane of symmetry. Consequently $I_{yz} = I_{xy} = 0$. Hence Eq. (9-8) may be simplified as follows:

$$\begin{aligned}
 \Sigma F_x &= m(\dot{U} + QW - RV) \\
 \Sigma F_y &= m(\dot{V} + RU - PW) \\
 \Sigma F_z &= m(\dot{W} + PV - QU) \\
 \Sigma M_x &= \dot{P}I_x + QR(I_z - I_y) - I_{xz}(\dot{R} + PQ) \\
 \Sigma M_y &= \dot{Q}I_y + PR(I_x - I_z) + I_{xz}(P^2 - R^2) \\
 \Sigma M_z &= \dot{R}I_z + PQ(I_y - I_x) - I_{xz}(\dot{P} - QR)
 \end{aligned} \tag{9-9}$$

For a cruciform configuration, further simplifications may be made since (1) the xy plane (as well as the xz) is also a plane of symmetry (i.e., $I_{xz} = 0$) and (2) the moment of inertia about the y axis is generally equal to that about the z axis (i.e., $I_y \approx I_z$). Hence the resultant simplified equations are

$$\begin{aligned}
 \Sigma F_x &= m(\dot{U} + QW - RV) \\
 \Sigma F_y &= m(\dot{V} + RV - PW) \\
 \Sigma F_z &= m(\dot{W} + PV - QU) \\
 \Sigma M_x &= \dot{P}I_x \\
 \Sigma M_y &= \dot{Q}I_y + PR(I_x - I_z) \\
 \Sigma M_z &= \dot{R}I_z + PQ(I_y - I_x)
 \end{aligned} \tag{9-10}$$

Detailed derivations of these classical equations of motion may be found in many published works.^{1-6*}

9-3. CLASSICAL SOLUTION—LONGITUDINAL DYNAMICS

Quite frequently it is desirable to evaluate the dynamic characteristics of the airframe alone (with controls locked) in order to determine the type and complexity of the autopilot or control system required to realize a satisfactory complete missile system. The following sections deal with the classical method of analysis for the longitudinal dynamics in two and three degrees of freedom.

1. Two Degrees of Freedom. For this simplified two-degree-of-freedom longitudinal dynamic analysis, Eq. (9-10) reduces to the following expressions:

$$\Sigma F_z = m(\dot{W} - QU) \tag{9-11}$$

$$\Sigma M_y = \dot{Q}I_y \tag{9-12}$$

* Superscript numbers indicate references listed at the end of the chapter.

Since $\dot{W} = U\dot{\alpha}$ and substituting $\dot{\theta}$ for Q , Eqs. (9-11) and (9-12) become

$$\Sigma F_z = mU(\dot{\alpha} - \dot{\theta}) \quad (9-13)$$

$$\Sigma M_y = I_y \ddot{\theta} \quad (9-14)$$

Since $\theta = \alpha + \gamma$ (9-15)

Eq. (9-13) becomes

$$\Sigma F_z = -mU\dot{\gamma} \quad (9-16)$$

For most simplified analyses such as this, it is common to reverse the sign convention by denoting F_z as positive when it is directed upward and also to use V as the missile forward velocity in lieu of U used in the complete six-degree-of-freedom analysis. With these changes made, Eqs. (9-14) and (9-16) become

$$I_y \ddot{\theta} = \Sigma M_y = M_\alpha \alpha + M_\delta \delta + M_\theta \dot{\theta} + M_{\dot{\alpha}} \dot{\alpha} + M_{\dot{\delta}} \dot{\delta} \quad (9-17)$$

$$mV\dot{\gamma} = \Sigma F_z = N_\alpha \alpha + N_\delta \delta \quad (9-18)$$

Dividing Eq. (9-17) by I_y and Eq. (9-18) by mV , we get

$$\ddot{\theta} = m_\alpha \alpha + m_\delta \delta + m_\theta \dot{\theta} + m_{\dot{\alpha}} \dot{\alpha} + m_{\dot{\delta}} \dot{\delta} \quad (9-19)$$

and $\dot{\gamma} = f_\alpha \alpha + f_\delta \delta$ (9-20)

where $m_\alpha = M_\alpha/I_y$, $f_\alpha = N_\alpha/mV$, etc.

Equations (9-19) and (9-20) may be solved by using the Heaviside factor, i.e., $\theta = \theta_0 e^{\lambda t}$, $\dot{\theta} = \lambda \theta_0 e^{\lambda t}$, $\ddot{\theta} = \lambda^2 \theta_0 e^{\lambda t}$, etc. Hence, using this factor and factoring out $\theta_0 e^{\lambda t}$ from Eqs. (9-17), (9-19), and (9-20), we get

$$\lambda^2 \theta = m_\alpha \alpha + m_\delta \delta + \lambda m_\theta \theta + \lambda m_{\dot{\alpha}} \alpha + \lambda m_{\dot{\delta}} \delta \quad (9-21)$$

$$\lambda \gamma = f_\alpha \alpha + f_\delta \delta \quad (9-22)$$

Since the above equations are homogeneous, the determinant of their coefficient is equal to zero. Rearranging the terms, the following determinant is obtained:

$$\begin{vmatrix} 1 & -1 & 1 \\ (m_\alpha + \lambda m_{\dot{\alpha}}) & \lambda(m_\theta - \lambda) & 0 \\ f_\alpha & 0 & -\lambda \end{vmatrix}$$

By expanding this determinant, the following quadratic is obtained:

$$\lambda[\lambda^2 - (m_\theta + m_{\dot{\alpha}} - f_\alpha)(m_\alpha + f_\alpha m_\theta)] = 0 \quad (9-23)$$

Substituting,

$$B = -(m_{\dot{\theta}} + m_{\alpha} - f_{\alpha}) \quad (9-24)$$

and

$$C = -(m_{\alpha} + f_{\alpha} m_{\dot{\theta}}) \quad (9-25)$$

we get

$$\lambda(\lambda^2 + B\lambda + C) = 0 \quad (9-26)$$

or

$$\lambda_{1,2} = \frac{-B \pm \sqrt{B^2 - 4C}}{2} \quad (9-27)$$

and

$$\lambda_3 = 0 \quad (9-28)$$

The roots λ_1 and λ_2 , which are the only roots of interest in this analysis, may be expressed in the complex form

$$\lambda_{1,2} = -\xi \omega_n \pm i \omega_n \sqrt{1 - \xi^2} \quad \lambda_{1,2} = -\xi_1 \pm i \eta_{1,2} \quad (9-29)$$

The period P and time to damp to half amplitude $T_{1/2}$ (see Fig. 9-3) may be calculated by the following equations:

$$P = \frac{2\pi}{\eta} \quad \text{sec} \quad (9-30)$$

$$T_{1/2} = \frac{\ln 2}{\xi} \quad \text{sec} \quad (9-31)$$

It is apparent from Eq. (9-31) that the time to damp to half amplitude is dependent upon the value of ξ or B in Eq. (9-24). Since the value of B is primarily a function of the damping characteristics of the airframe (i.e., $M_{\dot{\theta}}$ and M_{α}), it is appropriate to discuss here the source and magnitude of these damping terms before going into the three-degree-of-freedom analysis.

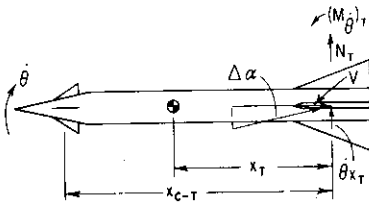


FIG. 9-4. Tail contribution to damping in pitch.

$(M_{\dot{\theta}})$. This is a damping moment which arises from the pitching velocity $\dot{\theta}$ of the missile and is commonly known as the damping in pitch. From Fig. 9-4, it is seen that, as a result of missile rotation about the center of gravity, an angle of attack is induced at the tail (or any other aerodynamic component, i.e., nose, canard, or wing). The resultant force and hence moment is in a direction which opposes the rotation of the missile; hence the term damping arises and has a negative sign. In most missile configurations, the tail surfaces contribute

the largest portion to the complete model damping.) The magnitude of this damping in pitch may be determined as follows:

$$\Delta M_T = -N_T x_T = -(C_{N_\alpha})_T [K_{T(B)} + K_{B(T)}] \Delta \alpha_T q S_T x_T \quad (9-32)$$

where $K_{T(B)}$ and $K_{B(T)}$ are the body-tail interference factors discussed in Chap. 5.

It has been assumed in Eq. (9-32) that the damping due to the tail surfaces includes the body-carry-over normal force, i.e., $(C_{N_\alpha})_T K_{B(T)}$ and that the center of pressure of this part of the normal force is the same as that on the tail surfaces. For preliminary-design purposes, this assumption appears to be adequate, particularly for configurations with tail surfaces located near or at the end of the body (i.e., little or no afterbody). This assumption is used throughout the entire derivation of the complete model damping in pitch. In this derivation a canard-control design is used. The error introduced by the above assumption is negligible since the canard contribution to damping is of secondary importance.

Dividing Eq. (9-32) by $q S_T d$, we get

$$\Delta C_{m_T} = -(C_{N_\alpha})_T [K_{T(B)} + K_{B(T)}] \Delta \alpha_T \frac{S_T}{S_\pi} \left(\frac{x}{d} \right)_T \quad (9-33)$$

The induced angle of attack due to pitching velocity $\dot{\theta}$ is

$$\Delta \alpha_T = \tan^{-1} \frac{\dot{\theta} x_T}{V} \quad (9-34)$$

or, for small values of $\Delta \alpha_T$,

$$\Delta \alpha_T \cong \frac{\dot{\theta} x_T}{V} \quad (9-35)$$

Substituting Eq. (9-35) into (9-33), we get

$$\Delta C_{m_T} = -(C_{N_\alpha})_T [K_{T(B)} + K_{B(T)}] \frac{\dot{\theta}}{V} \frac{S_T}{S_\pi} \frac{x_T^2}{d} \quad (9-36)$$

Defining

$$C_{m_{\dot{\theta}}} = \frac{\partial C_m}{\partial (\dot{\theta} d / 2V)} \quad (9-37)$$

we get

$$C_{m_{\dot{\theta}}} = -2(C_{N_\alpha})_T [K_{T(B)} + K_{B(T)}] \frac{S_T}{S_\pi} \left(\frac{x}{d} \right)_T^2 \quad (9-38)$$

(It is apparent from Eq. (9-38) that the tail contribution to damping in pitch varies directly with the tail area and as the square of the tail length. Hence it is much more effective to increase the length of the

tail than to increase the tail area to obtain increased damping.) Moreover, tail area has the disadvantage of increased weight and drag. The complete model damping in pitch is the sum of the contributions from the nose, canard, and tail surfaces and may be expressed as

$$(C_{m\dot{\theta}})_{CM} = - \left\{ 2(C_{N\alpha})_B \left(\frac{x}{d} \right)^2 + 2(C_{N\alpha})_C [K_{C(B)} + K_{B(C)}] \frac{S_C}{S_r} \left(\frac{x}{d} \right)^2 + 2(C_{N\alpha})_T [K_{T(B)} + K_{B(T)}] \frac{S_T}{S_r} \left(\frac{x}{d} \right)^2 \right\} \quad (9-39)$$

M_α . This damping term arises because of the time lag in the canard downwash getting to the tail surfaces (in the case of a wing- or tail-control design, the lag in the wing downwash getting to the tail surfaces is used). Since $\alpha_T = \alpha - \epsilon$ and $\epsilon = (d\epsilon/d\alpha)\alpha$,

$$\epsilon = \frac{d\epsilon}{d\alpha} \left(\alpha - \frac{d\alpha}{dt} \Delta t \right) \quad (9-40)$$

where Δt is the time it takes the air to go from the canard to the tail, i.e., $\Delta t = x_{C-T}/V$. Hence the damping moment due to this downwash lag is

$$M_T = -(C_{N\alpha})_T [K_{T(B)} + K_{B(T)}] \alpha_T q S_T x_T \quad (9-41)$$

Substituting Eq. (9-40) into Eq. (9-41), we get

$$M_T = -(C_{N\alpha})_T [K_{T(B)} + K_{B(T)}] \left[\alpha - \frac{d\epsilon}{d\alpha} \left(\alpha - \frac{d\alpha}{dt} \frac{x_{C-T}}{V} \right) \right] q S_T x_T \quad (9-42)$$

Dividing Eq. (9-42) by $q S_r d$, we get

$$C_{m\dot{\theta}} = -(C_{N\alpha})_T [K_{T(B)} + K_{B(T)}] \left[\alpha - \epsilon_\alpha \left(\alpha - \dot{\alpha} \frac{x_{C-T}}{V} \right) \right] \frac{S_T}{S_r} \frac{x_T}{d} \quad (9-43)$$

Defining

$$C_{m\dot{\alpha}} = \frac{\partial C_m}{\partial (\dot{\alpha} d / 2V)} \quad (9-43a)$$

we get $C_{m\dot{\alpha}} = -2(C_{N\alpha})_T [K_{T(B)} + K_{B(T)}] \frac{S_T}{S_r} \frac{x_T}{d} \epsilon_\alpha \frac{x_{C-T}}{d}$ (9-44)

Equation (9-44) is applicable for a canard-control design. For a wing-control design (see Fig. 2-2) where the wing is located at or near the center of gravity of the missile, the following simplification may be made since the length x_{W-T} is approximately equal to x_T .

$$C_{m\dot{\alpha}} = -2(C_{N\alpha})_T [K_{T(B)} + K_{B(T)}] \frac{S_T}{S_r} \left(\frac{x}{d} \right)^2 \epsilon_\alpha \quad (9-45)$$

(It is apparent that $C_{m\dot{\alpha}}$ is of secondary importance since the value of ϵ_x is generally low. This is particularly true for the case of the canard-control design.)

Another damping which is similar in nature to $C_{m\dot{\alpha}}$ is $C_{m\dot{\delta}}$. The latter is generally negligible because of the very low value of ϵ_δ as shown in Eq. (9-46) below for the canard-control design.

$$C_{m\dot{\delta}} = -2(C_{N_\alpha})_T [K_{T(B)} + K_{B(T)}] \frac{S_T}{S_r} \frac{x_T}{d} \epsilon_\delta \frac{x_{C-T}}{d} \quad (9-46)$$

A note of caution is injected here that, in most airplane applications, these dynamic rotary derivatives are expressed as $\partial(\)/\partial(\theta\dot{c}/2V)$ where \bar{c} is the aerodynamic chord of the wing. However, in most missile analysis, these derivations are expressed as $\partial(\)/\partial(\theta\dot{d}/2V)$ and hence the added factor of $(d/2V)$ must appear in all the damping coefficients such as those shown in Eq. (5-1) and subsequent equations where these damping coefficients occur.

The values of these aerodynamic damping or rotary derivatives $C_{m\dot{\delta}}$, $C_{m\dot{\alpha}}$, and $C_{m\dot{\beta}}$ may be readily determined from the static derivatives, i.e., C_{N_α} , C_{m_α} , etc., obtained from wind-tunnel-test results. The method of calculation is presented in Appendix G. A summary of the pitch-damping derivatives of complete airplane and missile configurations as measured in flight at transonic and supersonic speeds is presented in ref. 7.

2. Three Degrees of Freedom. In the analysis of longitudinal dynamics with three degrees of freedom, the equation relating the change in missile forward speed, i.e., $\Sigma F_x = m(\dot{U})$ from Eq. (9-10), is used in addition to Eqs. (9-17) and (9-18). The characteristic equation for this case may be solved by the same procedure used previously for the two-degree-of-freedom analysis. The resultant characteristic equation is the familiar quartic as shown below.

$$A\lambda^4 + B\lambda^3 + C\lambda^2 + D\lambda + E = 0 \quad (9-47)$$

The coefficients A, B, \dots are a function of the aerodynamic derivatives, mass, and moment of inertia of the missile. If all the coefficients of λ are positive, no positive real roots exist and hence no pure divergence will be exhibited in the dynamic motion of the missile. When the combination of coefficients $(BCD - AD^2 - B^2E)$, known as Routh's discriminant,⁸ is positive, the motion is stable. A zero value for Routh's discriminant indicates neutral stability whereas a negative value indicates a divergent (undamped) oscillation for one of the modes. If any of the coefficients is negative, a pure divergent or increasing oscillatory motion in one of the modes is present.

In general it is of interest to determine the roots of the characteristic equation in order that the periods of the motion and the damping characteristics may be determined. Of the many available methods of solution for the roots, the method by Lin⁹ appears to be the easiest. In this method the form of one of the quadratics is assumed and the second quadratic is determined by division as indicated below.

$$\lambda^4 + B'\lambda^3 + C'\lambda^2 + D'\lambda + E' = 0 \quad (9-48)$$

where $B' = B/A$, $C' = C/A$, etc. The first trial quadratic is assumed to be

$$\lambda^2 + \frac{D'}{C'}\lambda + \frac{E'}{C'}$$

and is used as a divisor as shown below:

$$\lambda^2 + \frac{D'}{C'}\lambda + \frac{E'}{C'} \left) \begin{array}{r} \lambda^4 + B'\lambda^3 + C'\lambda^2 + D'\lambda + E' \\ \underline{x \quad x \quad x} \\ \quad x \quad x \quad D'\lambda \\ \quad \underline{x \quad x \quad x} \\ \qquad R_1 \quad R_2 \quad E' \\ \qquad \underline{x \quad x \quad x} \\ \qquad \qquad x \quad x \text{ (remainder)} \end{array}$$

In the division process shown above, if there is a remainder, the first trial quadratic assumed, $\lambda^2 + (D'/C')\lambda + (E'/C')$, is not a factor of the quartic. In this case, a second trial quadratic must be assumed. It is of the following form:

$$\lambda^2 + \frac{R_2}{R_1}\lambda + \frac{E'}{R_1}$$

and is derived from the result of the first division previously shown. If the frequencies of the two oscillatory modes are considerably different (such is the case in the longitudinal dynamic motions) this method will converge on the second or third try. This is illustrated by a sample calculation shown in Table 9-1 for the following quartic:

$$\lambda^4 + 3.05\lambda^3 + 5.12\lambda^2 + 0.0412\lambda + 0.0205 = 0$$

Before proceeding with Lin's method of determining the roots of the quartic, a quick check should be performed to determine qualitatively the nature of the dynamic motion. Since all the coefficients are positive, no divergent motion is present. The value of Routh's discriminant is calculated to be

$$(3.05)(5.12)(0.0412) - (1)(0.0412)^2 - (3.05)^2(0.0205) > 0$$

TABLE 9-1. SAMPLE QUARTIC SOLUTION BY LIN'S METHOD⁹

Sample quartic: $\lambda^4 + 3.05\lambda^3 + 5.12\lambda^2 + 0.0412\lambda + 0.0205 = 0$

First trial quadratic: $\lambda^2 + \frac{0.0412}{5.12}\lambda + \frac{0.0205}{5.12} = \lambda^2 + 0.00805\lambda + 0.00401$

$$\lambda^2 + 0.00805\lambda + 0.00401 \sqrt{\frac{\lambda^4 + 3.05\lambda^3 + 5.12\lambda^2 + 0.0412\lambda + 0.0205}{\lambda^2 + 0.01\lambda^3 + 0.00\lambda^2}}$$

$$\frac{3.04\lambda^3 + 5.12\lambda^2 + 0.0412\lambda}{3.04\lambda^3 + 0.02\lambda^2 + 0.0122\lambda}$$

$$\frac{5.10\lambda^2 + 0.0290\lambda + 0.0205}{5.10\lambda^2 + 0.0410\lambda + 0.0205}$$

$$- 0.0120\lambda + 0$$

Second trial quadratic: $\lambda^2 + \frac{0.0290\lambda}{5.10} + \frac{0.0205}{5.10} = \lambda^2 + 0.00569\lambda + 0.00402$

$$\lambda^2 + 0.00569\lambda + 0.00402 \sqrt{\frac{\lambda^4 + 3.05\lambda^3 + 5.12\lambda^2 + 0.0412\lambda + 0.0205}{\lambda^4 + 0.01\lambda^3 + 0.00\lambda^2}}$$

$$\frac{3.04\lambda^3 + 5.12\lambda^2 + 0.0412\lambda}{3.04\lambda^3 + 0.02\lambda^2 + 0.0122\lambda}$$

$$\frac{5.10\lambda^2 + 0.0290\lambda + 0.0205}{5.10\lambda^2 + 0.0290\lambda + 0.0205}$$

$$\frac{0}{0}$$

$$\therefore (\lambda^2 + 0.00569\lambda + 0.00402)(\lambda^2 + 3.04\lambda + 5.10) = 0$$

$$\lambda_{1,2} = \frac{-0.00569 \pm \sqrt{(0.00569)^2 - 4(0.00402)}}{2} = -0.00285 \pm 0.063j$$

$$P_{1,2} = \frac{2\pi}{0.063} = 99.6 \text{ sec}, (T_{1/2})_{1,2} = \frac{0.693}{0.00285} = 243 \text{ sec}$$

$$\lambda_{3,4} = \frac{-3.04 \pm \sqrt{(3.04)^2 - 4(5.10)}}{2} = \pm 1.52 \pm 1.67j$$

$$P_{3,4} = \frac{2\pi}{1.67} = 3.76 \text{ sec}, (T_{1/2})_{3,4} = \frac{0.693}{1.52} = 0.456 \text{ sec}$$

Since the value of Routh's discriminant is positive and greater than zero, a stable motion is anticipated.

The results derived from Table 9-1 indicate the roots for the two modes

$$\lambda_{1,2} = -0.00285 \pm 0.063j$$

$$\lambda_{3,4} = -1.52 \pm 1.67j$$

where $j = \sqrt{-1}$, an imaginary number. The period and time to

damp to half amplitude for the two modes [using Eqs. (9-30) and (9-31)] are

$$P_{1,2} = \frac{2\pi}{0.063} = 99.6 \text{ sec}$$

$$(T_{1/2})_{1,2} = \frac{0.693}{0.00285} = 243 \text{ sec}$$

$$P_{3,4} = \frac{2\pi}{1.67} = 3.76 \text{ sec}$$

$$(T_{1/2})_{3,4} = \frac{0.693}{1.52} = 0.456 \text{ sec}$$

From the above results, it is seen that the longitudinal dynamic motion in three degrees of freedom consists of two distinct and separate modes: a long-period oscillation which is lightly damped and a very-short-period heavily damped oscillation. The former mode, called the phugoid, is of interest on cruise-type missiles whereas the short-period motion is usually more important on short-range missiles such as an AAM.

9-4. CLASSICAL SOLUTION—LATERAL DYNAMICS

The dynamic motions of a monowing missile about its lateral and directional (x and z) axes may be conveniently analyzed by assuming a three-degree-of-freedom study. The equations involved are [from Eq. (9-10)]

$$\begin{aligned} \Sigma F_y &= m(\dot{V} + UR) && \Sigma \text{ side force} \\ \Sigma M_z &= I_z \dot{R} - I_{xz} \dot{P} && \Sigma \text{ yawing moment} \\ \Sigma M_x &= I_x \dot{P} - I_{xz} \dot{R} && \Sigma \text{ rolling moment} \end{aligned} \quad (9-49)$$

In the above analysis, constant forward speed and no pitching motions are assumed. It is emphasized, however, that in most dynamic analysis of this kind, careful considerations must be given to the inertia cross-coupling effects whenever pitching motions are present. These cross-coupling effects arise from the fact that the roll moment of inertia of a missile is generally small relative to the pitch or yaw moments of inertia, i.e., $(I_y - I_z)$ and $(I_x - I_z)$ in Eq. (9-10) are large. In such cases, a more complete analysis involving five or six degrees of freedom must be conducted on automatic computing equipment.

Substituting $\beta \cong V/U$, $\dot{V} = U\dot{\beta}$, $R = \dot{\psi}$, and $P = \dot{\phi}$ (see Fig. 9-5), Eq. (9-49) becomes

$$\begin{aligned} \Sigma F_y &= mU(\dot{\psi} + \dot{\beta}) \\ \Sigma M_y &= I_z \ddot{\psi} - I_{xz} \ddot{\phi} \\ \Sigma M_x &= I_x \ddot{\phi} - I_{xz} \ddot{\psi} \end{aligned} \quad (9-50)$$

Equation (9-50) may be solved by the method previously described for the longitudinal case.

In the analysis of the flight dynamics of the missile, the dynamics of the missile airframe alone are only part of the over-all system. The response of the control and autopilot systems must be included in order to determine the response of the over-all missile system. The study of the complete missile dynamics is most conveniently made with the Laplace-transform and transfer-function technique discussed in the next section.

9-5. TRANSFER FUNCTION

1. Derivation. A transfer function is the ratio of output to input of a linear system and is expressed in the Laplace transform variable s . The Laplace transform is a mathematical technique involving the use of the transform variable s , which is a complex variable of the form $\sigma + j\omega$, where σ is the real part and $j\omega$ is the imaginary part ($j = \sqrt{-1}$). For example, suppose the angle θ varies as a function of time and is expressed as $\theta(t)$. The Laplace transform of this function is $\theta(s)$ or $\theta(s) = \mathcal{L} \theta(t)$, where \mathcal{L} denotes application of the transform integral. The Laplace transform of a function of the time $\mathcal{L}f(t)$ is of the following form:

$$\mathcal{L}f(t) \equiv F(s) = \int_0^{\infty} e^{-st}f(t) dt,$$

where $F(s)$ is a function of the transform variable s .

The transfer functions of the missile airframe without control and autopilot are usually expressed as the ratio of the rate of change of angle of attack, flight-path angle, etc., as an output to control-surface deflection δ . For example,

$$\dot{\gamma} = \frac{K}{s^2 + 2\zeta\omega s + \omega^2} \delta \quad (9-51)$$

is the aerodynamic transfer function of the second order which relates the rate of change of flight-path angle to control-surface deflection.

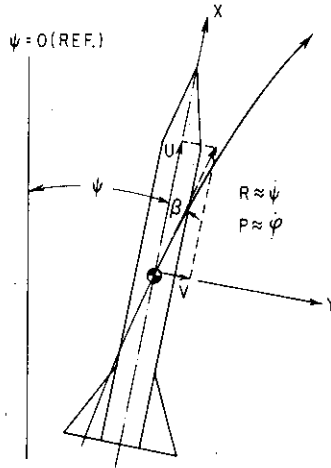


FIG. 9-5. Nomenclature for lateral-directional dynamic analysis.

In most preliminary-design studies, a two-degree-of-freedom analysis is adequate in the evaluation of the response characteristics of the airframe in conjunction with those of the autopilot and control system for pitch and/or yaw motions for the cruciform design. For the lateral-directional motions of a monowing design, a three-degree-of-freedom analysis involving Eq. (9-50) may be used. In each case, a constant forward speed is assumed regardless of the actual velocity profile of the missile. Linear aerodynamics are also assumed in these analyses.

In the development of the transfer functions for the longitudinal motions, the gravity term $W \cos \theta$ may be conveniently omitted since it represents an initial input or condition which can be biased (i.e., by fixed control-surface deflection). Since only the disturbed or perturbation motions are of interest, the initial conditions may be assumed to be zero. However, where flight kinematics (i.e., missile displacement relative to the inertial axes) are involved, the gravity terms must be accounted for. The equations of motion involved in the derivation of the transfer functions for the longitudinal case are

$$I_y \ddot{\theta} = \Sigma M_y = M_\alpha \alpha + M_\delta \delta + M_{\dot{\theta}} \dot{\theta} + M_{\dot{\alpha}} \dot{\alpha} + M_{\dot{\delta}} \dot{\delta} \quad (9-52)$$

$$mV \dot{\gamma} = \Sigma F = N_\alpha \alpha + N_\delta \delta \quad (9-53)$$

$$\theta = \alpha + \gamma \quad (9-54)$$

where V is used in lieu of U to denote missile forward velocity, and m is the mass of the missile and is assumed to be a constant or

$$I_y \ddot{\theta} = C_{m_\alpha} \alpha q S d + C_{m_\delta} \delta q S d + C_{m_{\dot{\theta}}} \dot{\theta} \frac{q S d^2}{2V} + C_{m_{\dot{\alpha}}} \dot{\alpha} \frac{q S d^2}{2V} + C_{m_{\dot{\delta}}} \dot{\delta} \frac{q S d^2}{2V} \quad (9-55)$$

$$mV \dot{\gamma} = C_{N_\alpha} \alpha q S + C_{N_\delta} \delta q S \quad (9-56)$$

Dividing Eq. (9-52) by I_y and Eq. (9-53) by mV ,

$$\ddot{\theta} = m_\alpha \alpha + m_\delta \delta + m_{\dot{\theta}} \dot{\theta} + m_{\dot{\alpha}} \dot{\alpha} + m_{\dot{\delta}} \dot{\delta} \quad (9-57)$$

$$\dot{\gamma} = f_\alpha \alpha + f_\delta \delta \quad (9-58)$$

where $m_\alpha = M_\alpha / I_y, \dots$ etc.

$f_\alpha = N_\alpha / mV, \dots$ etc.

Rearranging and letting $s = d/dt$ and $s^2 = d^2/dt^2$, Eqs. (9-57), (9-58), and (9-54) become

$$(1)\alpha + (-1)\theta + (1)\gamma = 0 \quad (9-59)$$

$$(m_\alpha + sm_\alpha)\alpha + (sm_\delta - s^2)\theta + (0)\gamma = -(m_\delta + m_\delta s)\delta \quad (9-60)$$

$$(f_\alpha)\alpha + (0)\theta + (-s)\gamma = (-f_\delta)\delta \quad (9-61)$$

Solving Eqs. (9-59) through (9-61) by determinants, we get

$$\gamma = \frac{\begin{vmatrix} 1 & -1 & 0 \\ m_\alpha + sm_\alpha & s(m_\delta - s) & -(m_\delta + m_\delta s)\delta \\ f_\alpha & 0 & -f_\delta\delta \end{vmatrix}}{\begin{vmatrix} 1 & -1 & 1 \\ m_\alpha + sm_\alpha & s(m_\delta - s) & 0 \\ f_\alpha & 0 & -s \end{vmatrix}}$$

$$= \frac{[-sf_\delta(m_\delta - s) + f_\alpha(m_\delta + m_\delta s) - f_\delta(m_\alpha + sm_\alpha)]\delta}{-s^2(m_\delta - s) - sf_\alpha(m_\delta - s) - s(m_\alpha + sm_\alpha)} \quad (9-62)$$

The transfer function γ/δ is thus

$$\frac{\gamma}{\delta} = \frac{f_\delta s^2 + (f_\alpha m_\delta - f_\delta m_\delta - f_\delta m_\alpha)s + (f_\alpha m_\delta - f_\delta m_\alpha)}{s[s^2 - (m_\delta - f_\alpha + m_\alpha)s - (m_\alpha + f_\alpha m_\delta)]} \quad (9-63)$$

Defining $\Delta = [s^2 - (m_\delta - f_\alpha + m_\alpha)s - (m_\alpha + f_\alpha m_\delta)]$ (9-64)

$$\frac{\gamma}{\delta} = \frac{f_\delta s^2 + (f_\alpha m_\delta - f_\delta m_\delta - f_\delta m_\alpha)s + (f_\alpha m_\delta - f_\delta m_\alpha)}{s\Delta} \quad (9-65)$$

Since $\dot{\gamma} = s\gamma$, the transfer function $\dot{\gamma}/\delta$ becomes

$$\frac{\dot{\gamma}}{\delta} = \frac{f_\delta s^2 + (f_\alpha m_\delta - f_\delta m_\delta - f_\delta m_\alpha)s + (f_\alpha m_\delta - f_\delta m_\alpha)}{\Delta} \quad (9-66)$$

Similarly,

$$\theta = \frac{\begin{vmatrix} 1 & 0 & 1 \\ (m_\alpha + sm_\alpha) & -(m_\delta + m_\delta s) & 0 \\ f_\alpha & -f_\delta\delta & -s \end{vmatrix}}{\Delta}$$

$$= \frac{s(m_\delta + m_\delta s) - f_\delta(m_\alpha + sm_\alpha) + f_\alpha(m_\delta + m_\delta s)}{s\Delta} \quad (9-67)$$

or $\frac{\theta}{\delta} = \frac{m_\delta s^2 + (m_\delta - f_\delta m_\alpha + f_\alpha m_\delta)s + (f_\alpha m_\delta - f_\delta m_\alpha)}{s\Delta}$ (9-68)

and

$$\frac{\dot{\theta}}{\delta} = \frac{m_{\delta}s^2 + (m_{\delta} - f_{\delta}m_{\alpha} + f_{\alpha}m_{\delta})s + (f_{\alpha}m_{\delta} - f_{\delta}m_{\alpha})}{\Delta} \quad (9-69)$$

$$\alpha = \frac{\begin{vmatrix} 0 & -1 & 1 \\ -(m_{\delta} + m_{\delta}s) & s(m_{\theta} - s) & 0 \\ -f_{\delta}\delta & 0 & -s \end{vmatrix}}{s\Delta} = \frac{[s(m_{\delta} + m_{\delta}s) + f_{\delta}s(m_{\theta} - s)]\delta}{s\Delta} \quad (9-70)$$

$$\text{or} \quad \frac{\alpha}{\delta} = \frac{(m_{\delta} - f_{\delta})s + (m_{\delta} + f_{\delta}m_{\theta})}{\Delta} \quad (9-71)$$

$$\text{and} \quad \frac{\dot{\alpha}}{\delta} = \frac{(m_{\delta} - f_{\delta})s^2 + (m_{\delta} + f_{\delta}m_{\theta})s}{\Delta} \quad (9-72)$$

Other transfer functions may be derived as follows:

$$\frac{\alpha}{\gamma} = \frac{\alpha}{\delta} \times \frac{\delta}{\gamma} = \frac{[(m_{\delta} - f_{\delta})s + (m_{\delta} + f_{\delta}m_{\theta})]s}{f_{\delta}s^2 + (f_{\alpha}m_{\delta} - f_{\delta}m_{\theta} - f_{\delta}m_{\alpha})s + (f_{\alpha}m_{\delta} - f_{\delta}m_{\alpha})} \quad (9-73)$$

$$\frac{\alpha}{\theta} = \frac{\alpha}{\delta} \times \frac{\delta}{\theta} = \frac{[(m_{\delta} - f_{\delta})s + (m_{\delta} + f_{\delta}m_{\theta})]s}{m_{\delta}s + (m_{\delta} - f_{\delta}m_{\alpha} + f_{\alpha}m_{\delta})s + (f_{\alpha}m_{\delta} - f_{\delta}m_{\alpha})} \quad (9-74)$$

$$\frac{\gamma}{\theta} = \frac{\gamma}{\delta} \times \frac{\delta}{\theta} = \frac{f_{\delta}s^2 + (f_{\alpha}m_{\delta} - f_{\delta}m_{\theta} - f_{\delta}m_{\alpha})s + (f_{\alpha}m_{\delta} - f_{\delta}m_{\alpha})}{m_{\delta}s^2 + (m_{\delta} - f_{\delta}m_{\alpha} + f_{\alpha}m_{\delta})s + (f_{\alpha}m_{\delta} - f_{\delta}m_{\alpha})} \quad (9-75)$$

For a highly maneuverable missile where $n \gg 1$, the following approximate transfer function of n/δ may be expressed as

$$\frac{n}{\delta} = \frac{V\dot{\gamma}}{g\delta} = \frac{V}{g} \left[\frac{f_{\delta}s^2 + (f_{\alpha}m_{\delta} - f_{\delta}m_{\theta} - f_{\delta}m_{\alpha})s + (f_{\alpha}m_{\delta} - f_{\delta}m_{\alpha})}{\Delta} \right] \quad (9-76)$$

Let

$$\begin{aligned} a &= f_{\delta} \\ b &= f_{\delta}m_{\theta} + f_{\delta}m_{\alpha} - f_{\alpha}m_{\delta} \\ c &= f_{\alpha}m_{\delta} - f_{\delta}m_{\alpha} \\ d &= f_{\delta}m_{\theta} + m_{\delta} \\ e &= m_{\alpha} - f_{\alpha} + m_{\theta} \\ h &= m_{\alpha} + m_{\theta}f_{\alpha} \\ i &= f_{\delta}m_{\alpha} - m_{\delta} - f_{\alpha}m_{\delta} \\ l &= m_{\delta} \\ (b - i) &= m_{\delta} + f_{\delta}m_{\theta} \\ (l - a) &= m_{\delta} - f_{\delta} \end{aligned} \quad (9-77)$$

The above transfer functions become

$$\frac{\gamma}{\delta} = \frac{as^2 - bs + c}{s(s^2 - es - h)} \quad (9-78)$$

$$\frac{\dot{\gamma}}{\delta} = \frac{as^2 - bs + c}{(s^2 - es - h)} \quad (9-79)$$

$$\frac{\theta}{\delta} = \frac{ls^2 - is + c}{s(s^2 - es - h)} \quad (9-80)$$

$$\frac{\dot{\theta}}{\delta} = \frac{ls^2 - is + c}{(s^2 - es - h)} \quad (9-81)$$

$$\frac{\alpha}{\delta} = \frac{(l-a)s + (b-i)}{(s^2 - es - h)} \quad (9-82)$$

$$\frac{\dot{\alpha}}{\delta} = \frac{(l-a)s^2 + (b-i)s}{(s^2 - es - h)} \quad (9-83)$$

$$\frac{\alpha}{\gamma} = \frac{\alpha}{\delta} \times \frac{\delta}{\gamma} = \frac{s[(l-a)s + (b-i)]}{as^2 - bs + c} \quad (9-84)$$

$$\frac{\alpha}{\theta} = \frac{\alpha}{\delta} \times \frac{\delta}{\theta} = \frac{s[(l-a)s + (b-i)]}{ls^2 - is + c} \quad (9-85)$$

$$\frac{\gamma}{\theta} = \frac{\gamma}{\delta} \times \frac{\delta}{\theta} = \frac{as^2 - bs + c}{ls^2 - is + c} \quad (9-86)$$

$$\frac{n}{\delta} = \frac{V\dot{\gamma}}{g\delta} = \frac{V[as^2 - bs + c]}{g[s^2 - es - h]} \quad (9-87)$$

The aerodynamic transfer function is usually expressed in the following general form, i.e.,

$$\frac{\dot{\gamma}}{\delta} = \frac{K}{s^2 + 2\zeta\omega s + \omega^2} \quad (9-88)$$

where K/ω^2 is the aerodynamic static "gain" of the system and $(s^2 + 2\zeta\omega s + \omega^2)$ is the characteristic equation. In this case, $\omega = \sqrt{-h}$ and is defined as the undamped natural frequency of the missile. The term ζ equal to $(-e/2\omega)$ is the damping constant of the (airframe) system and is defined as the ratio of the actual damping of the airframe to critical damping. The value of the critical damping for a second-order linear system, such as that expressed by Eq. (9-88), is one. By

solving for the roots in the characteristic equation, the period and time to damp to half amplitude of the dynamic motion are determined as shown below.

$$s_{1,2} = \frac{-2\zeta\omega \pm \sqrt{4\zeta^2\omega^2 - 4\omega^2}}{2} \quad (9-89)$$

or
$$s_{1,2} = -\zeta\omega \pm \sqrt{-\omega^2(1 - \zeta^2)} = (\xi + i\eta) \quad (9-90)$$

[see Eq. (9-29)]

$$P_{1,2} = \frac{2\pi}{\eta} = \frac{2\pi}{\sqrt{-\omega^2(1 - \zeta^2)}} \cong \frac{2\pi}{\omega} \quad \text{sec} \quad (9-91)$$

$$(T_{1/2})_{1,2} = \ln \frac{2}{\xi} = \frac{0.693}{\zeta\omega} \quad (9-92)$$

The transfer function for rolling motion in a single degree of freedom is readily derived as follows:

$$\begin{aligned} I_x \dot{p} &= \mathcal{L}_p p + \mathcal{L}_\delta \delta \\ &= C_{l_p} p \frac{qSd^2}{2V} + C_{l_\delta} \delta qSd \end{aligned} \quad (9-93)$$

$$\dot{p} = l_p p + l_\delta \delta \quad (9-94)$$

where $l_p = \frac{\mathcal{L}_p}{I_x}$ and $l_\delta = \frac{\mathcal{L}_\delta}{I_x}$

Let $s = \frac{d}{dt}$

then $sp - l_p p = l_\delta \delta \quad (9-95)$

or $\frac{p}{\delta} = \frac{l_\delta}{s - l_p} \quad (9-96)$

2. Application. The transfer functions derived above may be used to determine the dynamic-response characteristics of the airframe (i.e., open loop) together with those associated with the autopilot and control system. Several methods which are available and used by the servomechanical engineers include the Nyquist technique and the root-locus method. These methods are extensively discussed in many published works (i.e., refs. 10 to 14). For the purpose of this

volume, a simple example is worked up to illustrate the usefulness of the transfer function in a frequency-response study.

The illustrative problem involves the determination of the proper time lag of the control system in order to prevent the missile from attaining an excessively high dynamic overshoot whenever the frequency of the sinusoidal input approaches the undamped natural frequency (denoted as ω_n in lieu of ω used previously) of the missile. In this example, a typical canard configuration is used in order to simplify the calculation. Since the values of $C_{N\delta}$, $C_{m\dot{\alpha}}$, and $C_{m\delta}$ for this type of design are relatively low, they are assumed to be zero. The resultant transfer function of α/δ is simply

$$\frac{\alpha}{\delta} = \frac{m_\delta}{s^2 - (m_\theta - f_\alpha)s - (m_\alpha - m_\theta f_\alpha)} \quad (9-97)$$

For the condition investigated,

$$\frac{\alpha}{\delta} = \frac{300}{s^2 + 8.00s + 1,600} \quad (9-98)$$

Substituting $j\omega = s$ where $j = \sqrt{-1}$, an imaginary number, this transfer function can be rewritten as

$$\frac{\alpha}{\delta} = \frac{300}{(-\omega^2 + 1,600 + 8.00j\omega)} \quad (9-99)$$

$$\begin{aligned} \text{or } \frac{\alpha}{\delta} &= \frac{300}{(-\omega^2 + 1,600 + 8.00j\omega)} \frac{(-\omega^2 + 1,600) - 8.00j\omega}{(-\omega^2 + 1,600) - 8.00j\omega} \\ &= \frac{\overset{\text{(real part)}}{(-300\omega^2 + 480,000)} - \overset{\text{(imaginary part)}}{2,400j\omega}}{(-\omega^2 + 1,600)^2 + (8.00\omega)^2} \end{aligned} \quad (9-99a)$$

Since the amplitude is equal to the square root of the sum of the squares of the real and imaginary parts, i.e., $A = \sqrt{r^2 + i^2}$, we get

$$A = \frac{\sqrt{(-300\omega^2 + 480,000)^2 + (2,400\omega)^2}}{(-\omega^2 + 1,600)^2 + (8.00\omega)^2} \quad (9-100)$$

Substituting various values of the input frequency ω_i we get the following amplitude or dynamic overshoot ratio A/A_0 , where A_0 is the amplitude at $\omega_i = 0$ radians/sec.

ω_i	ω_i/ω_n	A	$A/A_0 = \text{overshoot ratio}$
0	0	0.183 = A_0	1.00
10	0.250	0.200	1.09
20	0.500	0.248	1.32
30	0.750	0.405	2.15
37	0.925	0.802	4.27
38	0.950	0.878	4.67
39	0.975	0.932	4.96
40	1.000	0.938	4.99
41	1.005	0.888	4.72
42	1.050	0.802	4.27
45	1.125	0.539	2.87
50	1.25	0.305	1.61

In the above example, the value of α/δ (i.e., trim angle of attack per degree of control deflection) for the static condition is 0.183 and

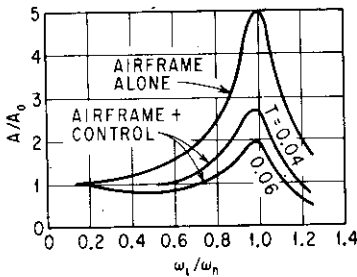


FIG. 9-6. Frequency-response characteristics of airframe and control system.

is obtained from $\omega_i = 0$ condition. This value is often referred to as the static gain of the system. The above results, plotted in Fig. 9-6, indicate that, as the frequency of the input approaches the undamped natural frequency of the missile, the dynamic gain or overshoot ratio A/A_0 increases considerably since the damping constant ζ for the sample configuration is low [i.e., $\zeta = 0.09$ from Eqs. (9-88) and (9-98)]. Since the above results do not include the time lag in the

servo-control system, the above values of the amplitude ratio are valid for the air-frame loop only.

The effect of the servo loop on the combined airframe-control-system (see Fig. 9-6) response characteristics must be taken into account. This may be done conveniently by assuming that the servo has the response characteristics of a first-order linear system whose transfer function of δ_0/δ_i may be expressed as follows:

$$\frac{\delta_0}{\delta_i} = \frac{1}{1 + Ts} \quad (9-101)$$

where T is a time constant (i.e., time required for δ_0 to reach 63 per cent of its final value). Substituting $s = j\omega$, Eq. (9-101) becomes

$$\begin{aligned} \frac{\delta_0}{\delta_i} &= \frac{1}{1 + Ts} = \frac{1}{1 + Ts} \times \frac{1 - Ts}{1 - Ts} \\ &= \frac{1}{1 + jT\omega} \times \frac{1 - jT\omega}{1 - jT\omega} = \frac{1 - jT\omega}{1 + T^2\omega^2} \end{aligned} \quad (9-102)$$

The value of the amplitude ratio for the control system A_c may be calculated by the same method used previously.

$$A_c = \sqrt{r^2 + i^2} = \frac{\sqrt{1 + (T\omega)^2}}{1 + T^2\omega^2} = \frac{\sqrt{1 + T^2\omega^2}}{1 + T^2\omega^2} = \frac{1}{\sqrt{1 + T^2\omega^2}} \quad (9-103)$$

ω_i	ω_i/ω_n	A_c for ($T = 0.04$)	A_c for ($T = 0.06$)	$(A/A_0)(A_c)$ for ($T = 0.04$)	$(A/A_0)(A_c)$ for ($T = 0.06$)
0	0	1	1	1.000	1.000
10	0.250	0.929	0.857	1.014	0.936
20	0.500	0.780	0.640	1.029	0.845
30	0.750	0.640	0.486	1.375	1.045
37	0.925	0.565	0.413	2.410	1.762
38	0.950	0.555	0.404	2.590	1.885
39	0.975	0.545	0.397	2.705	1.970
40	1.000	0.530	0.384	2.640	1.915
41	1.005	0.526	0.378	2.480	1.783
42	1.050	0.517	0.369	2.208	1.575
45	1.125	0.488	0.348	1.400	0.999
50	1.250	0.448	0.316	0.725	0.512

The transfer function of α/δ for the combined servo-airframe open loop may be expressed as

$$\frac{\alpha}{\delta_i} = \frac{\delta_0}{\delta_i} \times \frac{\alpha}{\delta_0} = \frac{1}{1 + Ts} \frac{m_s}{s^2 - (m_{\delta} - f_a)s - (m_x - m_{\delta}f_a)} \quad (9-104)$$

Hence it is apparent that the servo lag T attenuates the dynamic overshoot by the factor A_c . These effects are shown in Fig. 9-6. From Fig. 9-6, the time lag of the servo may be selected to prevent the missile from exceeding the designed dynamic overshoot under the most

severe input condition. Assume that the structural design overshoot ratio is 2.0; it is apparent from Fig. 9-6 that the desired time lag of the control system must be approximately 0.06 sec.

SYMBOLS

A	amplitude
A_c	amplitude ratio for the control system
A_0	amplitude at $\omega_i = 0$
A/A_0	overshoot ratio
A, B, C, D, E, K	general constants in Eqs. (9-1), (9-2), and (9-47)
B, C	constants in Eqs. (9-24) and (9-25)
B', C', D', E'	general constants in Eq. (9-48)
C_l	rolling-moment coefficient
C_m	pitching-moment coefficient
C_N	normal-force coefficient
F	force
$F(s)$	function of the transform variable s
I	moment of inertia
$K_{B(C)}, K_{B(T)}$	see Symbols in Chap. 5
$K_{C(B)}, K_{T(B)}$	see Symbols in Chap. 5
\mathcal{L}	rolling moment
$\mathcal{L}f(t)$	Laplace transform of a function of time $F(s)$
M	moment
N	normal force
P	period of oscillation
P, Q, R	angular velocities about the X, Y, Z axes (see Fig. 9-2)
S	reference area
T	time constant of first-order control system [see Eq. (9-101)]
$T_{1/2}$	time to damp to half amplitude
U, V, W	velocities along the X, Y, Z axes (see Fig. 9-2)
W	weight of missile
a, b, c, \dots	constants defined in Eq. (9-77), also in Fig. 9-3
a_1, a_2	constants defined in Eq. (9-4)
d	body diameter
f	N/mV [see Eq. (9-58)]
h	moments of momentum
i	imaginary number in the complex form
j	an imaginary number, $\sqrt{-1}$

$j\omega$	imaginary part of a complex variable
I_y	\mathcal{L}_y/I_x [see Eq. (9-94)]
m	mass, also M/I_y [see Eq. (9-57)]
n	load factor
p	rolling velocity, also operator to denote differentiation with respect to time
$p_{1,2}$	roots of the characteristic equation [see Eq. (9-3)]
q	dynamic pressure
s	Laplace operator
t	time
Δt	time it takes the air to go from the canard to the tail [see Eq. (9-40)]
x	moment arm
x_{C-T}	distance between canard and tail surfaces (see Fig. 9-4)
α	angle of attack
β	angle of sideslip
γ	flight-path angle
Δ	denominator as defined in Eq. (9-64)
δ	control-surface deflection
ϵ	downwash angle
ζ	damping constant defined as the ratio of the actual damping of the airframe to critical damping [see Eq. (9-88)]
η	term used in Eqs. (9-29), (9-30), and (9-91)
θ	missile attitude ($\alpha + \gamma$)
$\lambda_{1,2}$	roots of the characteristic equation [see Eq. (9-27)]
ξ	term used in Eqs. (9-29), (9-31), and (9-92)
σ	real part of a complex variable (see Sec. 9-5)
φ	roll (or bank) angle
ψ	yaw angle
ω, ω_n	undamped natural frequency of missile
ω_i	input frequency
Subscripts	
B	body
C	canard
T	tail
x, y, z	about the X, Y, Z axes
π	body frontal area (i.e., S_π)
0	initial condition
1, 2	conditions other than zero

REFERENCES

1. Dynamics of the Airframe, BuAer Rept. AE-61-4II, Bureau of Aeronautics, Navy Department, September, 1952.
2. Perkins, C. D., and R. E. Hage: "Airplane Performance Stability and Control," John Wiley & Sons, Inc., New York, 1950.
3. Jones, B. M.: Dynamics of the Airplane, Durand's "Aerodynamic Theory," vol. V, Div. N, Springer-Verlag, Berlin, 1935.
4. Synge, J. L., and B. A. Griffith,: "Principles of Mechanics," 3d ed., McGraw-Hill Book Company, Inc., New York, 1959.
5. Goldstein, H.: "Classical Mechanics," Addison-Wesley Publishing Company, Reading, Mass., 1950.
6. Webster, A. G.: "The Dynamics of Particles and of Rigid, Elastic, and Fluid Bodies," Hafner Publishing Company, New York, 1950.
7. Gillis, C. L., and R. Chapman, Jr.: Summary of Pitch-damping Derivatives of Complete Airplane and Missile Configurations as Measured in Flight at Transonic and Supersonic Speeds, NACA Research Mem. L52K20, Jan. 22, 1953.
8. Routh, E. J.: "Dynamics of a System of Rigid Bodies," 3d ed., Macmillan & Co., Ltd., London, 1877.
9. Lin, S.: A Method of Successive Approximations for Evaluating the Real and Complex Roots of Cubic and Higher-order Equations, *J. Math. and Phys.*, vol. 20, no. 3, August, 1941.
10. Nixon, F. E.: "Principles of Automatic Controls," Prentice-Hall, Inc., Englewood Cliffs, N.J., 1953.
11. Brown, G. S., and D. P. Campbell: "Principles of Servomechanisms," John Wiley & Sons, Inc., New York, 1948.
12. Methods of Analysis and Synthesis of Piloted Aircraft Flight Control Systems, BuAer Rept. AE-61-4I, Bureau of Aeronautics, Navy Department, March, 1952.
13. Savant, C. J., Jr.: "Basic Feedback Control System Design," McGraw-Hill Book Company, Inc., New York, 1958.
14. Thaler, G. J., and R. G. Brown: "Servomechanism Analysis," McGraw-Hill Book Company, Inc., New York, 1953.

CHAPTER 10

AIR LOADS

10-1. INTRODUCTION

In most preliminary analyses, one is required to estimate the air loads on the missile and its components in order for the structural and stress engineers to "rough out" the detailed design of the various external components such as skin gauge on the nose and body or wing thickness. Since detailed design criteria are generally not specified at this stage of design, one must examine several conditions of flight which include both trim and dynamic flight conditions. These missile flight conditions may be examined by the methods discussed previously, particularly in Chap. 5 and 9. In addition to the air loads, the aerodynamic hinge moments are of interest for the determination of the type and capacity of the servo system for actuating the aerodynamic movable surfaces. Finally, thermal loading or aerodynamic heating must be estimated in order to determine the optimum type of material and construction for the airframe. This chapter is devoted to a discussion of some of the approaches and methods of analysis associated with the general aerodynamic air loads, load distribution, and heating problems.

10-2. DESIGN CRITERIA

A missile is often designed to operate over a wide range of speed, altitude, and dynamic pressure q conditions. Hence care must be exercised in selecting the correct or critical design loading condition or conditions for stress analyses. Since the aerodynamic loading on the missile is expressed as

$$N = C_{N_\alpha} \alpha q S = C_{N_\alpha} \alpha^{1/4} \gamma p M^2 S \quad (10-1)$$

it is necessary to examine not only the individual terms C_{N_α} , α , M , etc.,

in Eq. (10-1) but also the product of these terms. Each of these terms is discussed below.

1. C_{N_α} . As discussed in Chap. 3, the normal-force-curve slope is a function of Mach number. In the supersonic case C_{N_α} varies approximately inversely as $\sqrt{M^2 - 1}$. Hence it is evident that the maximum value of C_{N_α} encountered in flight does not necessarily result in maximum aerodynamic loading.

2. α . In general, the maximum value of angle of attack including dynamic overshoot, gusts, etc., will result in the critical loading condition provided the product of $C_{N_\alpha} q$ is a maximum.

3. p . The effect of decreasing static pressure or increasing altitude is to decrease the aerodynamic loading on a missile. However, for medium- or long-range ballistic missiles, the effect of increasing altitude is generally overcompensated by the Mach-number increase such that the q is a maximum at the higher altitude (see Fig. 10-1) and hence results in maximum loading at altitude. For other types of missiles, the lowest operating altitude generally results in the maximum loading.

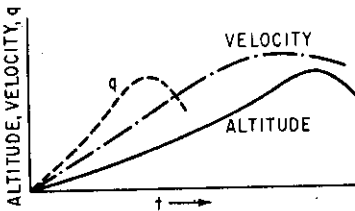


FIG. 10-1. Altitude, velocity, and dynamic pressure vs. time.

4. M . The effect of the Mach number is twofold: it decreases the value of C_{N_α} as previously mentioned and increases the dynamic pressure. Since the latter effect is more pronounced in that q varies as the Mach number squared, the general net effect of the Mach number is to increase the aerodynamic loading on the missile. An exception to this case may be one in which the control system is inadequate in overcoming the aerodynamic hinge moment of the control surfaces. In such a case, the restricted control deflection results in a lower trim or dynamic overshoot α and hence may result in a lower loading condition at the higher operating Mach numbers. The type of servo used in this case is commonly called the "proportional-torque" servo which "proportions" the loading of the missile as a function of the aerodynamic hinge moments on the control surfaces.

5. Dynamic pressure q . In the majority of the cases, maximum q results in the maximum air loads. In a very few cases, maximum loading may occur at somewhat lower values of q . One such may be the case in which the maximum speed of the missile is slightly supersonic, where C_{N_α} may be significantly reduced. In such a case the high

subsonic speed with its attendant rise in $C_{N\alpha}$ may result in maximum loading even though maximum q is not yet attained.

From the above discussion, it is apparent that careful analysis must be made of the various factors involved before the maximum aerodynamic loading condition can be determined. Now that the effects of Mach number, altitude, q , etc., have been discussed the various missile flight attitudes (i.e., trim and out-of-trim conditions) must be examined next. These flight attitudes are described below for two common types of design: (1) forward canard or wing control and (2) rear or tail control.

1. Forward Control. The flight attitudes for this type of design are shown in Fig. 10-2 and are discussed below.

A. This is the condition which exists immediately after the forward movable control surfaces are deflected hard over onto their stops. Actually this condition rarely exists since it takes a finite time to reach maximum deflection, at which time some nominal angle of attack would have been developed. However, assuming $\alpha = 0$, maximum positive pitching acceleration occurs at point **A**.

B. This is the trimmed condition of the missile, since $C_m = 0$. Generally, this condition does not result in maximum design loads.

C. This is the maximum dynamic overshoot condition which results in maximum aerodynamic loads on the body and control (movable wings or canards) surfaces. The amount of overshoot depends primarily on the amount of aerodynamic damping and control-surface response characteristics as discussed in Chap. 9. For low aerodynamic damping and very fast control-surface (rates) responses, this overshoot can be many times that of the trimmed value **B**. In a given design, the response and overshoot loading must often be compromised.

D. This is a transient condition in which the forward movable control surfaces are returned to neutral at the peak of the dynamic overshoot condition. This condition may often result in maximum tail loads since the angle of the tail is at a maximum because of the absence of downwash.

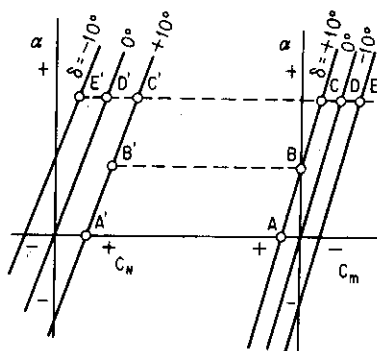


FIG. 10-2. Flight conditions for airloads analysis—forward control.

E. Again this is a transient condition similar to *A*, *C*, and *D*. This condition obviously results in maximum negative pitching acceleration.

2. Rear Control. The flight attitudes for a rear-control design are shown in Fig. 10-3 and are similar to those shown in Fig. 10-2 for the forward-control design. However, because of the negative value of C_{m_0} , as pointed out in Sec. 5-8 the corresponding points A^1 , B^1 , C^1 , etc., on the C_N vs. α curves are located differently from those of Fig. 10-2.

- A.* Same as for the forward-control design.
B. Same as for the forward-control design.

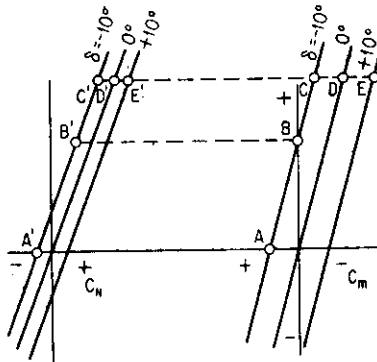


FIG. 10-3. Flight conditions for airloads analysis—rear control.

load (i.e., $\alpha_T = \alpha_W - \epsilon + \delta_T$) as well as maximum negative pitching acceleration are encountered in this condition.

The above conditions are generally more severe than the actual conditions the missile experiences since it requires a finite time for the control surfaces to deflect from one position to the next, during which time the angle of attack is changing in a direction so as to alleviate the loading problem. Hence, if a more refined definition of the dynamic conditions is desired, a simplified transient response study should be conducted.

Although maximum air loads on the various components seldom occur during any one flight attitude or condition, these components must be designed to withstand their respective maximum loads. It is very important, then, to investigate all these five (and possibly other) flight conditions and evaluate the loads and angular accelerations. The previously described conditions (i.e., *A*, *B*, *C*, etc.) should also be made for the range of center-of-gravity locations of the missile. The

C. This is the maximum dynamic overshoot condition which results in maximum loads on the body and forward fixed (wing) aerodynamic surfaces.

D. This is a transient condition in which the movable tail-control surfaces are returned to neutral at the peak of the overshoot condition. Large tail load is generally associated with this condition.

E. This transient condition is similar to that for the forward-control case. Maximum tail

effect of gust should be factored in the loads analysis. This may be done by increasing the angle of attack by an incremental value defined below:

$$\Delta\alpha_g \cong \frac{V_g}{V} \quad (10-2)$$

where $\Delta\alpha_g$ = angle of attack due to gust
 V_g = gust velocity

The methods of evaluating the aerodynamic loads, loading distributions, and hinge moments are discussed next. Inertia loading will be discussed in Chap 14..

10-3. COMPONENT AIR LOADS

1. Body. As discussed in Chap. 3, the majority of the body load for the body-alone configuration is concentrated at the forebody or nose section. Therefore, the total load on the forebody may be approximated as

$$N_N = (C_{N_\alpha})_B \alpha_B q S_B \quad (10-3)$$

Owing to wing and/or tail-body interference effects, additional loads are incurred on the body because of the presence of these aerodynamic surfaces. For a forward-control design (i.e., a canard control) the "carry-over" load from the canards on the body [from Eqs. (5-8) and (5-9)] is

$$N_{B(C)} = (C_{N_\alpha})_C [K_{B(C)} \alpha_C + k_{B(C)} \delta_C] q S_C \quad (10-4)$$

The load on the body caused by the tail surfaces is

$$N_{B(T)} = (C_{N_\alpha})_T K_{B(T)} (\alpha - \epsilon) q S_T \quad (10-5)$$

For a rear-control (i.e., tail-control) design, the interference loads due to the forward fixed wing and movable tail surfaces may be written [see Eqs. (5-30) and (5-31)] as

$$N_{B(W)} = (C_{N_\alpha})_W K_{B(W)} \alpha_W q S_W \quad (10-6)$$

$$N_{B(T)} = (C_{N_\alpha})_T [K_{B(T)} (\alpha - \epsilon) + k_{B(T)} \delta_T] q S_T \quad (10-7)$$

2. Aerodynamic Surfaces. The normal force on the aerodynamic surfaces may also be calculated with the aid of Eqs. (5-8), (5-9), (5-30), and (5-31) for the forward- and rear-control design. For the

former type of design, the forward (i.e., canard) control-surface load is

$$N_{C(B)} = (C_{N_\alpha})_C [K_{C(B)} \alpha_C + k_{C(B)} \delta_C] q S_C \quad (10-8)$$

For the aft (tail) surfaces, the load is

$$N_{T(B)} = (C_{N_\alpha})_T K_{T(B)} (\alpha - \epsilon) q S_T \quad (10-9)$$

For an aft (tail) control design, the load on the forward fixed wing surfaces is

$$N_{W(B)} = (C_{N_\alpha})_W K_{W(B)} \alpha_W q S_W \quad (10-10)$$

The load on the movable tail surfaces is

$$N_{T(B)} = (C_{N_\alpha})_T [K_{T(B)} (\alpha - \epsilon) + k_{T(B)} \delta_T] q S_T \quad (10-11)$$

The load on small movable control surfaces such as flaps and ailerons is generally obtained from test data. However, for preliminary design analysis, the load on these surfaces may be estimated by first analyzing the nature and magnitude of its pressure distribution, which is discussed in the following section.

10-4. COMPONENT LOAD DISTRIBUTION

1. Body. The theoretical pressure distribution and hence loading characteristics of a body of revolution at zero angle of attack may be predicted by many different methods.^{1-5,13*} Comparison of the results obtained by the different theoretical methods indicates excellent agreement with those obtained experimentally.⁶⁻⁸ Figure 10-4 shows the typically close agreement between the theoretical and experimental results for a common body of revolution of $l/d = 10$ with a three-caliber tangent ogive forebody.

For inclined bodies of revolution, many theoretical methods⁹⁻¹³ are also available for the determination of the pressure distribution over their entire length. However, since these methods are based primarily on potential-flow theories, viscous and cross-flow compressibility effects were neglected. Hence these theoretical results could not be expected to agree exactly with those obtained from experiments which include these viscous effects. Figure 10-5 shows a typical comparison of the theoretical and experimental results. It can be seen that, as the angle of attack increases, flow separation due to viscous effects is a major cause of the discrepancy between the theoretical and experimental results.

* Superscript numbers indicate references listed at the end of the chapter.

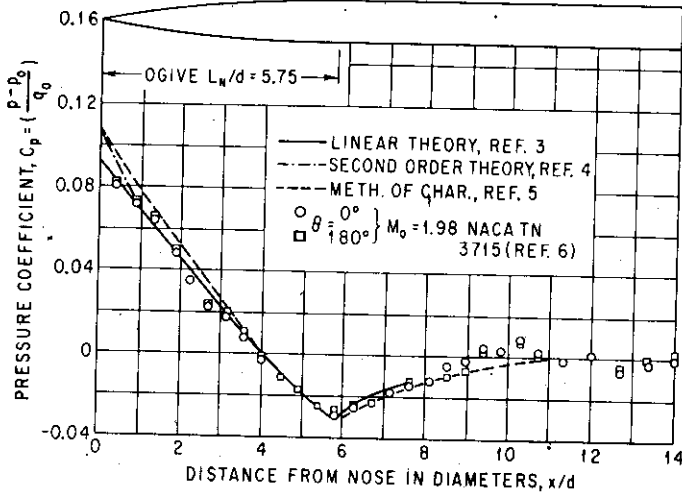


Fig. 10-4. Comparison of theoretical and experimental C_p at $\alpha = 0^\circ$.

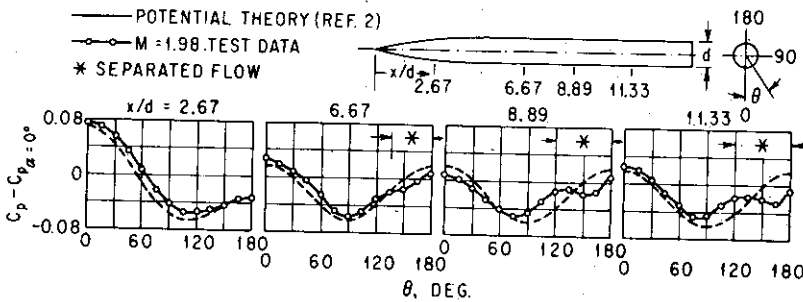


Fig. 10-5. Comparison of theoretical and experimental circumferential distribution of lifting pressure at $\alpha = 8^\circ$. (NACA Tech. Note 3715.)

Once the peripheral pressure distribution is determined for the various stations along the body (such as those shown in Fig. 10-5), the local normal-force coefficient per inch may be determined as follows:

$$C_n = \frac{2r}{S_r} \int_0^\pi C_p \cos \theta \, d\theta \quad (10-12)$$

where r = radius of the body

S_r = reference area

$C_p = (p - p_0)/q_0$

The value of C_n is next plotted vs. body station as shown in Fig. 10-6. Integration of the area under this curve yields the total normal-force

coefficient C_N on the complete-body configuration. The center of pressure is determined by taking the summation of the moments of area and dividing by the summation of the area of Fig. 10-6.

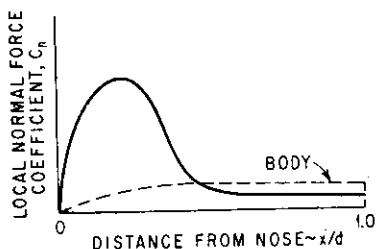


FIG. 10-6. Variation of local normal-force coefficient with body station.

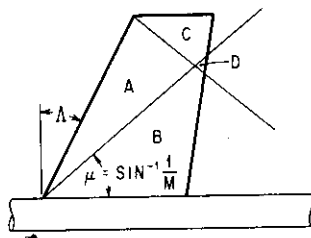


FIG. 10-7. Definition of regions for air-loads analysis.

2. Aerodynamic Surfaces. For preliminary analysis, the load on the aerodynamic surfaces may be assumed to be concentrated at the quarter chord at subsonic speeds and close to the mid-chord at supersonic speeds, as pointed out in Chap. 3. For detailed analysis, however, actual loading distribution is needed. This need may be fulfilled by either (1) using pressure-distribution data on a similar or identical configuration or (2) estimating the loading distribution by theoretical means. The latter approach for the determination of load distribution at supersonic speeds is presented below.

Figure 10-7 shows a typical wing planform with its Mach lines to represent a given flight Mach-number condition. In the application of the linear theory the following four important assumptions are made: (1) attached shock (i.e., sharp leading edge), (2) relatively low angles of attack ($\alpha < 10^\circ$), (3) relatively thin airfoil, and (4) supersonic leading edge (i.e., $\mu > \Lambda$). The relationships for the local pressure coefficient C_p defined as $(p_{\text{upper}} - p_{\text{lower}})/q$, for the different areas A, B, etc., are

$$C_{p(A)} = \frac{4\alpha}{\sqrt{\beta^2 - k^2}} \quad (10-13)$$

$$C_{p(B)} = \frac{8\alpha}{\pi\sqrt{\beta^2 - k^2}} \left[\frac{\pi}{2} - \sin^{-1} \sqrt{\frac{n^2 - t_1^2}{1 - t_1^2}} \right] \quad (10-14)$$

$$C_{p(C)} = \frac{4\alpha(a+1)}{\pi\beta\sqrt{a}} \tan^{-1} \sqrt{\frac{-2a\beta y_2}{(1+a)(x_2 + \beta y_2)}} \quad (10-15)$$

and

$$C_{p(D)} = C_{p(B)} + C_{p(C)} - C_{p(A)} \quad (10-16)$$

where α is the local angle of attack and must be corrected for body upwash effects. The local angle of attack at any spanwise wing location r may be related to the body radius R and the free-stream angle of attack α_0 as¹⁴

$$\alpha = \alpha_0 \left[1 + \left(\frac{R}{r} \right)^2 \right] \quad (10-17)$$

$$\beta = \sqrt{M^2 - 1} \quad (10-18a)$$

$$k = \tan \Lambda \quad (10-18b)$$

$$n = \frac{k}{\beta} \quad (10-18c)$$

$$t_1 = \frac{ky_1}{x_1} \quad (10-18d)$$

(See Fig. 10-8.)

$$a = \frac{\beta + k}{\beta - k} \quad (10-18e)$$

Using the above relationships, the chordwise pressure distribution may be readily calculated for several spanwise wing stations such as

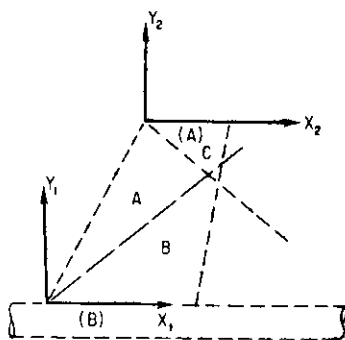


FIG. 10-8. Definition of coordinate systems for air-loads analysis.

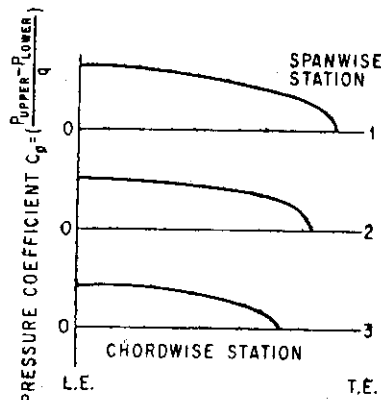


FIG. 10-9. Typical chordwise pressure distribution.

those shown in Fig. 10-9. The spanwise loading distribution and total load may be calculated as follows:

1. Integrate the area under the curves in Fig. 10-9:

$$N'(\text{lb/in.}) = FC_p c q \quad (10-19)$$

where F is a scale factor (i.e., if 1 in. = one unit of C_p and 1 in. = 2 in. span, then $F = 1 \times 2 = 2$).

2. Plot N' vs. spanwise stations (see Fig. 10-10) to get the spanwise distribution.

3. Integrate the area under Fig. 10-10 to obtain the total normal force N .

A comprehensive treatment of the spanwise load distributions for a variety of wing planforms at supersonic speeds may be found in refs. 15 to 17. For subsonic speeds, refs. 18 and 19 should be consulted.

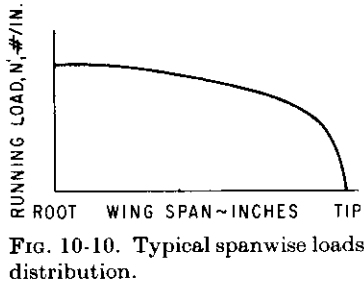


FIG. 10-10. Typical spanwise loads distribution.

Quite frequently, after the component loads and their locations have been determined, the summation of forces may not agree with the total load (or load factor), or the summation of moments about the center of gravity is not zero (for trimmed-flight condition), or the predetermined angular acceleration

(out-of-trim condition) does not result. Hence it will be necessary to adjust either the individual component loads and/or locations to satisfy these predetermined values. Which component load or load location to be modified or adjusted to satisfy these predetermined values depends upon the magnitude or accuracy of these loadings. Hence, if the load of a particular component (say the wing, for instance) is much larger than that on other components, only slight modification of its magnitude and/or its location is required. Or, if the accuracy of the load or its location on a particular component is questionable, then modification should be made on that particular load or location.

10-5. AERODYNAMIC HINGE MOMENTS

Since the size and capacity of the servomechanism is dependent directly upon the magnitude of the hinge moments associated with the aerodynamic surfaces to which it is linked, it is important to be able to predict the approximate magnitude of the hinge moments for the critical flight conditions. Several flight conditions of Mach number, control-surface deflection, angle of attack, and dynamic pressure must be investigated since these parameters affect both the magnitude of the normal force and its center-of-pressure location. When only

supersonic speeds are concerned, maximum hinge moments generally occur at the highest supersonic Mach number, q , α , and δ condition.

Several methods may be used to estimate the magnitude of the hinge moment for preliminary analysis. These are (1) estimation of the load and center-of-pressure location, (2) integration of pressure-distribution data, and (3) use of hinge-moment data of similar configuration. The first method mentioned may be expressed mathematically (for a movable wing) as

$$(HM)_\alpha = (C_{N_\alpha})_W K_{W(B)} (x_{HL} - \bar{x}_\alpha) q S_W \quad (10-20)$$

and
$$(HM)_\delta = (C_{N_\alpha})_W k_{W(B)} (x_{HL} - \bar{x}_\delta) q S_W \quad (10-21)$$

where $(HM)_\alpha$ = hinge moment due to α , etc.

x_{HL} = hinge-line location

\bar{x}_α = center of pressure due to α

\bar{x}_δ = center of pressure due to δ

The values of \bar{x}_α and \bar{x}_δ for the wing-alone configuration (see Chap. 3) may be used since the body effect on the wing center of pressure appears to be negligible.

Another method of determining hinge moment is by integrating the theoretical pressure distribution as previously described to determine the load and chordwise center-of-pressure location. Since this method is rather tedious, it is generally not recommended for the sole purpose of hinge-moment determination. However, in the process of getting the loading distribution, the hinge moment may be also determined by this method. Perhaps the most direct method is to use experimental hinge-moment data of similar configurations. Theoretical values of hinge moments for trailing-edge-type controls for supersonic flights may be obtained from ref. 21. However, since theoretical values are subject to errors because of flow separation, viscous effects, etc., experimental wind-tunnel hinge-moment data when obtained under conditions reasonably close to those actually experienced in flight should be obtained for design purposes. Most of the experimental data on hinge-moment characteristics of various practical designs are classified for security reasons.

10-6. AERODYNAMIC HEATING

Thermal loading or aerodynamic heating may constitute a major problem in the design of a high-speed missile. Hence, during the preliminary-design phase of the missile project, it is important to estimate the heat-transfer rate and temperature on the critical portions

(i.e., nose, leading edge of aerodynamic surfaces, etc.) of the missile. Aerodynamic heating results from the airflow about the surface of the missile: friction of the air along the surface of the missile and compression at and near the stagnation regions of the missile external components. In these processes, a portion of the kinetic energy of the air is converted into thermal energy within the boundary layer of the missile.

The temperature rise for bringing the air to rest ΔT is expressed as

$$\Delta T = \frac{\gamma - 1}{2} M_\infty^2 T_\infty \quad (10-22)$$

where γ = ratio of specific heats at constant pressure C_p to specific heat at constant volume C_v .

M_∞ = free-stream Mach number

T_∞ = free-stream temperature, ° Rankine

The final or stagnation temperature T_0 is

$$T_0 = T_\infty \left(1 + \frac{\gamma - 1}{2} M_\infty^2 \right) \quad (10-23)$$

Equation (10-23) is applicable for a compressible non-heat-conducting gas. Since there is a small amount of heat transfer within the boundary layer, the "recovery" temperature T_r differs from the stagnation temperature by the temperature-recovery factor r and is expressed as

$$T_r = T_\infty \left(1 + r \frac{\gamma - 1}{2} M_\infty^2 \right) \quad (10-24)$$

The temperature-recovery factor r can thus be expressed as

$$r = \frac{T_r - T_\infty}{T_0 - T_\infty} \quad (10-25)$$

The value of r varies from approximately 0.85 for laminar flow to approximately 0.88 for turbulent flow. Hence it can be seen that the recovery temperature is relatively independent of the type of flow except at very high Mach numbers. For an insulated wall (i.e., no heat transfer through the skin of the missile) the recovery temperature T_r is identical to the adiabatic wall temperature T_{aw} :

$$T_{aw} = T_r = T_\infty \left(1 + r \frac{\gamma - 1}{2} M_\infty^2 \right) \quad (10-26)$$

In most practical applications, heat transfer through the skin or wall of the missile occurs. The heat-transfer rate through the wall q_w is governed by the following classical relationship:

$$q_w = h(T_r - T_w) \quad (10-27)$$

where h = heat-transfer coefficient

T_w = wall temperature

It is more convenient to use a nondimensional coefficient called the Stanton number C_h , which is defined as

$$C_h = \frac{h}{\rho \mu C_p} \quad (10-28)$$

where ρ = fluid density

μ = coefficient of fluid viscosity

The Stanton number is related to the skin-friction coefficient C_f , as

$$C_h = \frac{1}{s} \frac{C_f}{2} \quad (10-29)$$

where s is the Reynolds analogy factor and has a value of approximately 0.8.

Hence the heat-transfer rate may be expressed as

$$\begin{aligned} q_w &= \frac{1}{s} \frac{C_f}{2} \rho \mu C_p (T_r - T_w) \\ &= \frac{1}{s} \frac{C_f}{2} \rho \mu C_p \left[T_\infty \left(1 + r \frac{\gamma - 1}{2} M^2 \right) - T_w \right] \end{aligned} \quad (10-30)$$

It is seen from Eq. (10-30) that the heat-transfer rate varies directly as the friction coefficient C_f . Since C_f for turbulent flow can be many times C_f for laminar flow, it is essential that laminar flow be maintained over as great a portion of the missile as possible.

In the calculation of aerodynamic heating of the missile, the following fundamental heat-balance equation is used:

$$\text{Heat input} = \text{heat stored} + \text{heat radiated} \quad (10-31)$$

where $\text{Heat stored} = (\text{weight})(\text{specific heat})(\text{temp. rise})$

$$= (W)(C)(T_1 - T_2) \quad (10-31a)$$

and

$$\text{Heat radiated} = \sigma A \epsilon T_w^4 \quad (10-31b)$$

The term σ in Eq. (10-31b) is the Stefan-Boltzmann constant and has a value of 0.48×10^{-12} Btu/(ft²)(sec)(°R)⁴. The term A is the surface

area being checked for heating effects. The term ϵ is the emissivity factor of the surface material, which depends upon the surface temperature, degree of surface roughness, etc. Since the temperature of a body exposed to transient heating conditions at any instant depends upon the previous thermal history of the body, a time-step solution of the heat-balance equation is required.

Many methods and procedures exist for the determination of aerodynamic heating of the missile. Some of these methods are limited to the determination of heat transfer to a specified location on the missile (i.e., stagnation point only), flight condition (i.e., hypersonic speeds only), etc. Hence an extensive study on the subject of heat transfer is required before the proper method or methods are selected for a particular design condition. References 22 through 44 constitute a partial list of the many reports written on this subject.

SYMBOLS

A	surface area being checked for heating effects
C	specific heat [see Eq. (10-31a)]
C_f	skin-friction coefficient
C_h	Stanton number
C_N	normal-force coefficient
C_n	local normal-force coefficient
C_p	specific heat at constant pressure, or pressure coefficient
C_v	specific heat at constant volume
F	scale factor as used in Eq. (10-19)
HM	hinge moment
$K_{B(C)}, K_{B(W)}, K_{B(T)}$	see Symbols in Chap. 5
$K_{C(B)}, K_{W(B)}, K_{T(B)}$	see Symbols in Chap. 5
L_N	nose length (see Fig. 10-4)
M	Mach number
N	normal force
N'	spanwise loading distribution
S	reference area
T	temperature
T_{aw}	adiabatic wall temperature
T_r	recovery temperature
T_w	wall temperature
T_0	stagnation pressure
T_∞	free-stream temperature

V	forward velocity
V_g	gust velocity
W	weight
a	a term in Eq. (10-15) and defined by Eq. (10-18e)
c	local chord
d	body diameter
h	heat-transfer coefficient
k	a term in Eqs. (10-13) and (10-14) and defined by Eq. (10-18b)
$k_{B(C)}, k_{B(T)}$	see Symbols in Chap. 5
$k_{C(B)}, k_{T(B)}$	see Symbols in Chap. 5
n	a term in Eq. (10-14) and defined by Eq. (10-18c)
p	static pressure
q	dynamic pressure
q_w	heat-transfer rate through the wall
r	radius of body, spanwise wing location, temperature-recovery factor
s	Reynolds analogy factor [see Eq. (10-29)]
t_1	a term in Eq. (10-14) and defined by Eq. (10-18d)
x, y	coordinates as shown in Fig. 10-8
$\bar{x}_\alpha, \bar{x}_\delta$	center of pressure due to α and δ , respectively
α	angle of attack
$\Delta\alpha_g$	incremental angle of attack due to gust velocity
β	$\sqrt{M^2 - 1}$ [see Eq. (10-18a)]
γ	specific heat ratio of air
δ	control-surface deflection
ϵ	downwash angle, emissivity factor
θ	circumferential angle (see Fig. 10-5)
Λ	leading-edge sweep angle
μ	Mach angle [see Eq. (3-35)], coefficient of fluid viscosity
ρ	air or fluid density
σ	Stefan-Boltzmann constant [see Eq. (10-31b)]

REFERENCES

1. Allen, H. J.: Pressure Distribution and Some Effects of Viscosity on Slender Inclined Bodies of Revolution, *NACA Tech. Note 2044*, 1950.
2. Allen, H. J.: Estimation of the Forces and Moments Acting on Inclined Bodies of Revolution of High Fineness Ratio, *NACA Research Mem. A9126*, 1949.

3. Von Kármán, T., and N. B. Moore: Resistance of Slender Bodies Moving with Supersonic Velocities with Special Reference to Projectiles, *Trans. ASME* vol. 54, no. 23, pp. 303-310, Dec. 15, 1932.
4. Van Dyke, M. D.: A Study of Second-order Supersonic-flow Theory, *NACA Rept.* 1081, 1952 (formerly *NACA Tech. Note* 2200).
5. Ehret, D. M., V. J. Rossow, and V. I. Stevens, Jr.: An Analysis of the Applicability of the Hypersonic Similarity Law to the Study of Flow about Bodies of Revolution at Zero Angle of Attack, *NACA Tech. Note* 2250, 1950.
6. Perkins, E. W., and D. M. Kuehn: Comparison of the Experimental and Theoretical Distribution of Lift on a Slender Inclined Body of Revolution at $M = 2$, *NACA Tech. Note* 3715, May, 1956.
7. Perkins, E. W., and L. H. Jorgensen: Comparison of Experimental and Theoretical Normal-force Distributions (Including Reynolds Number Effects) on an Ogive-cylinder Body at Mach Number 1.98, *NACA Tech. Note* 3716, May, 1956.
8. Perkins, E. W., F. E. Gowen, and L. H. Jorgensen: Aerodynamic Characteristics of the NACA RM-10 Research Missile in the Ames 1- by 3-foot Supersonic Wind Tunnel No. 2—Pressure and Force Measurements at Mach Numbers of 1.52 and 1.98, *NACA Research Mem.* A51G13, 1951.
9. Allen, H. J., and E. W. Perkins: Characteristics of Flow over Inclined Bodies of Revolution, *NACA Research Mem.* A50L07, 1951.
10. Rossow, V. J.: Applicability of the Hypersonic Similarity Rule to Pressure Distribution Which Include the Effects of Rotation for Bodies of Revolution at Zero Angle of Attack, *NACA Tech. Note* 2399, 1951 (extension of *NACA Tech. Note* 2250).
11. Bolton-Shaw, B. W., and H. K. Zienkiewicz: The Rapid, Accurate Prediction of Pressure on Non-lifting Ogival Heads of Arbitrary Shape at Supersonic Speeds, English Electric Company, Navigational Project Division, no. L.A.t. 034 (British), June 23, 1952.
12. Van Dyke, M. D.: Practical Calculation of Second-order Supersonic Flow Past Nonlifting Bodies of Revolution, *NACA Tech. Note* 2744, 1952.
13. Savin, R. C.: Application of the Generalized Shock-expansion Method to Inclined Bodies of Revolution Traveling at High Supersonic Airspeeds, *NACA Tech. Note* 3349, April, 1955.
14. Beskin, L.: Determination of Upwash around a Body of Revolution at Supersonic Velocities, CM-251, Applied Physics Laboratory, Johns Hopkins University, May 27, 1946.
15. Martin, J. C., and I. Jeffreys: Span Load Distributions Resulting from Angle of Attack, Rolling, and Pitching for Tapered Sweptback Wings with Streamwise Tips, Supersonic Leading and Trailing Edges, *NACA Tech. Note* 2643, July, 1952.
16. Hannah, M. E., and K. Margolis: Span Load Distributions Resulting from Constant Angle of Attack, Steady Rolling Velocity, Steady Pitching Velocity, and Constant Vertical Acceleration for Tapered Sweptback Wings with Streamwise Tips, Subsonic Leading Edges and Supersonic Trailing Edges, *NACA Tech. Note* 2831, December, 1952.
17. Margolis, Kenneth, Windors L. Sherman, and M. E. Hannah: Theoretical Calculation of the Pressure Distribution, Span Loading, and Rolling Moment Due to Sideslip at Supersonic Speeds for Thin Swept-back Tapered

Wings with Supersonic Trailing Edges and Wing Tips Parallel to the Axis of Wing Symmetry, *NACA Tech. Note* 2898, February, 1953.

18. Schrenk, O.: A Simple Approximation Method for Obtaining the Spanwise Lift Distribution, *NACA Tech. Mem.* 948, August, 1940.

19. DeYoung, J., and C. W. Harper: Theoretical Symmetric Span Loading at Subsonic Speeds for Wings Having Arbitrary Plan Form, *NACA Rept.* 921, 1948.

20. Czarnecki, K. R., and D. R. Lord: Load Distributions Associated with Controls at Supersonic Speeds, *NACA Research Mem.* L53D15a, May 29, 1953.

21. Goin, K. L.: Equations and Charts for the Rapid Estimation of Hingemoment and Effectiveness Parameters for Trailing-edge Controls Having Leading and Trailing-edges Swept Ahead of the Mach Lines, *NACA Rept.* 1041, 1951.

22. Van Driest, E. R.: The Problem of Aerodynamic Heating, IAS Preprint 645, June, 1956 (also in *Aero. Eng. Rev.*, vol. 15, no. 10, pp. 26-41, October, 1956).

23. Kemp, N. H., and F. R. Riddell: Heat Transfer to Satellite Vehicles Re-entering the Atmosphere, *Jet Propulsion*, vol. 27, pp. 132-137, February, 1957 (addendum in *Jet Propulsion*, vol. 27, no. 12, pp. 1256-1257, December, 1957).

24. Romig, M. H.: Stagnation Point Heat Transfer for Hypersonic Flow, *Jet Propulsion*, vol. 26, no. 12, pp. 1098-1101, December, 1956 (addendum in *Jet Propulsion*, vol. 27, no. 12, p. 1255, December, 1957).

25. Van Driest, E. R.: Turbulent Boundary Layer in Compressible Fluids, *J. Aeronaut. Sci.*, vol. 18, no. 3, March, 1951.

26. Van Driest, E. R.: Turbulent Boundary Layer on a Cone in Supersonic Flow at Zero Angle of Attack, *J. Aeronaut. Sci.*, vol. 19, no. 1, January, 1952.

27. Slote, L., and W. D. Murray: A Method of Predicting Skin, Compartment, and Equipment Temperatures for Aircraft, *WADC AD* 19722, July, 1953.

28. Seiff, A.: Examination of the Existing Data on the Heat Transfer of Turbulent Boundary Layers at Supersonic Speeds from the Point of View of Reynolds Analogy, *NACA Tech. Note* 3284, August, 1954.

29. Reshotko, E., and I. E. Beckwith: Compressible Laminary Boundary Layer over a Yawed Infinite Cylinder with Heat Transfer and Arbitrary Prandtl Number, *NACA Tech. Note* 3986, June, 1957.

30. Englert, G. W.: Estimation of Compressible Boundary-layer Growth over Insulated Surfaces with Pressure Gradient, *NACA Tech. Note* 4022, June, 1957.

31. Czarnecki, K. R., and A. R. Sinclair: A Note on the Effect of Heat Transfer on Peak Pressure Rise Associated with Separation of Turbulent Boundary Layer on a Body of Revolution (NACA RM-10) at a Mach Number of 1.61, *NACA Tech. Note* 3997, April, 1957.

32. Reshotko, E., and C. B. Cohen: Heat Transfer at the Forward Stagnation Point of Blunt Bodies, *NACA Tech. Note* 3513, July, 1955.

33. Brinich, P. F., and N. Sands: Effect of Bluntness on Transition for a Cone and a Hollow Cylinder at Mach 3.1, *NACA Tech. Note* 3979, May, 1957.

34. Stine, H. A., and K. Wanlass: Theoretical and Experimental Investigation of Aerodynamic-heating and Isothermal Heat-transfer Parameters on a

Hemispherical Nose with Laminar Boundary Layer at Supersonic Mach Number, *NACA Tech. Note 3344*, December, 1954.

35. Rubesin, M. W.: A Theoretical Study of the Effect of Upstream Transpiration Cooling on the Heat Transfer and Skin-friction Characteristics of a Compressible, Laminar Boundary Layer, *NACA Tech. Note 3969*, May, 1957.

36. Eber, G. R.: Recent Investigation of Temperature Recovery and Heat Transmission on Cones and Cylinders in Axial Flow in the N. O. L. Aeroballistics Wind Tunnel, *J. Aeronaut. Sci.*, vol. 19, no. 1, pp. 1-6, 14, January, 1952.

37. Von Kármán, T.: The Analogy between Fluid Friction and Heat Transfer, *Trans. ASME*, vol. 61, no. 11, November, 1939.

38. des Clers, B., and J. Sternberg: On Boundary-layer Temperature Recovery Factors, *J. Aeronaut. Sci.*, vol. 19, no. 9, pp. 645, 646, September, 1952.

39. Eckert, E. R. G.: "Introduction to the Transfer of Heat and Mass," McGraw-Hill Book Company, Inc., New York, 1950.

40. Kemp, N. H., P. H. Rose, and R. W. Detra: Laminar Heat Transfer Around Blunt Bodies in Dissociated Air, *J. Aero/Space Sci.*, vol. 26, no. 7, pp. 421-430, July, 1959.

41. Biot, M. A.: Further Developments of New Methods in Heat-flow Analysis, *J. Aero/Space Sci.*, vol. 26, no. 6, pp. 367-381, June, 1959.

42. Lees, L.: Laminar Heat Transfer over Blunt-nosed Bodies at Hypersonic Flight Speeds, *Jet Propulsion*, vol. 26, no. 4, p. 259, 1956.

43. Allen, H. J., and A. J. Eggers, Jr.: A Study of the Motion and Aerodynamic Heating of Missiles Entering the Earth's Atmosphere at High Supersonic Speeds, *NACA Tech. Note 4047*, October, 1957.

44. Allen, H. J.: Motion of a Ballistic Missile Angularly Misaligned with the Flight Path upon Entering the Atmosphere and its Effects upon Aerodynamic Heating, Aerodynamic Loads, and Miss Distance, *NACA Tech. Note 4048*, October, 1957.

CHAPTER 11

AERODYNAMIC LAUNCHING PROBLEMS

11-1. INTRODUCTION

The aerodynamic problem of launching missiles from ground launchers, shipboard, and particularly from high-speed parent aircraft is indeed a difficult and challenging one. Careful design practice must be exercised in order to assure that the missile realizes clean and safe separation as well as minimum deviation from the intended flight path. "Beam-riding" missiles have occasionally lost "beam lock-on" during their boost or launching phase as the result of excessive flight-path excursion, resulting in aborted flights. Hence detailed analyses must be made of the sources and magnitudes of both internal and external forces acting on the missile during its launching phase. Should these forces cause undesirable launching dispersion proper design modifications must be incorporated to assure a satisfactory launch. In the case of an air-launched missile, aircraft-missile compatibility must be realized. Hence the requirement of over-all system performance and accuracy as well as safety of launch must be satisfied. Thus the designer must consider carefully all the numerous factors which may cause undesirable and detrimental launching characteristics. It is the purpose of this chapter to point out and discuss some of the more important aspects of missile launching.

11-2. SAFETY OF PARENT AIRCRAFT—AIR LAUNCH

In addition to satisfying the requirement that the dispersion of the missile during launch must not exceed the limit dictated by guidance considerations, safety of launch must be assured to the parent aircraft and its crew. Unfortunately, in the majority of the cases, the airplane and missile designers are foreign to each other and often make undue design compromises when the over-all missile-aircraft weapon system is ready to be integrated. One of the chief reasons leading to the difficulties of integrating the missile to the parent aircraft or vice

versa is the fact that the air-launched missile is usually designed to be carried by many different aircraft which are either operational or fairly well finalized in design. Hence the missile engineer is left with the problem of "retrofitting" his missile to the parent aircraft, the design of which is "frozen."

The problem of safety of launch is particularly severe in the case of "retrofitting" the missile to a particular parent aircraft because of the following limitations imposed by the design of the parent aircraft: (1) extreme inboard or external store location, (2) restricted longitudinal center-of-gravity movement, (3) unduly long forebody for the missile to fly clear of, and (4) limited ground and wing clearance, etc. The above limitations can be alleviated to a great extent whenever the parent aircraft and missile are designed as an integrated system at their earliest design stages. In either case, however, detailed analysis must be conducted on the various factors which may contribute to the hazards of launching.

In many modern aircraft, pilots have reported and subsequently verified that bombs and external stores such as fuel tanks exhibited extremely erratic separation characteristics upon release or ejection. Bombs have been shown to pitch violently inside the bombbay prior to their eventual separation from the carrier aircraft while fuel tanks have been shown to travel from their wing-tip location inboard to hit the fuselage of the airplane during their release. Obviously such erratic release characteristics for a missile are totally unacceptable from the standpoint of safety to the parent aircraft, not to mention the strong possibility of a completely inaccurate and consequently ineffective round.

Although no detailed safety criteria are specified, they should consist of the following as a guide for the missile or airplane designer:

1. The missile should not strike the parent aircraft during boost or jettison.
2. The missile structure should not fail under any conditions of flight in the immediate vicinity of the parent aircraft.
3. The jet blast from the rocket of the missile should not adversely affect the parent-aircraft structures and its operating components such as air inlets and control surfaces.

1. Missile-aircraft Collision. Perhaps the two most important causes which may result in missile collision with the launch aircraft are (1) adverse aerodynamic forces on the missile induced by the flow field about the missile-pylon-wing combination and (2) control-system failure at launch, which causes the control surfaces to deflect

fully to their hard-over position in pitch, yaw, or roll. Other contributing factors are normal manufacturing malalignment of the control surfaces, thrust malalignment, missile center of gravity off center, and launch-aircraft maneuvers. In general, the latter effects are small relative to those mentioned previously.

Over the past several years, the NACA (now NASA) and private companies in the aircraft-missile industry have conducted extensive experimental and theoretical studies on the nature and magnitude of

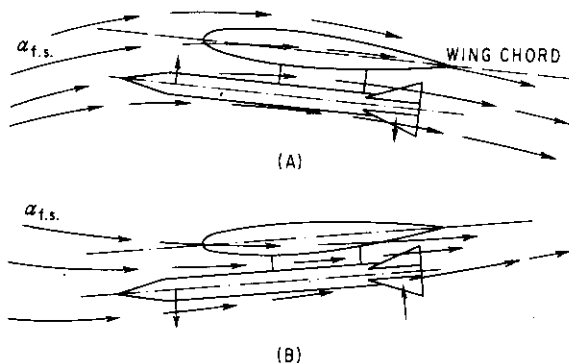


FIG. 11-1. Induced flow field in pitch of wing-pylon-missile combination. (A) Low-speed (high α) condition. (B) High-speed (low α) condition.

the effects of flow field induced by and on the missile-pylon-wing and missile-fuselage combinations. Numerous configurations have been investigated to provide the data to evaluate missile-launch dispersion characteristics. References 1 through 10 are but a partial list of unclassified reports on the subject of missile-aircraft flow interference. Many more reports that are available but classified should be consulted for a satisfactory solution to this launch problem.

A rather crude but informative representation of the nature of the flow field is shown in Figs. 11-1 and 11-2 for the sources of pitching, yawing, and rolling moments. As seen in Fig. 11-1, the flow field in pitch for a low-speed launch condition is typified by the flow about a wing at a relatively high angle of attack. In this attitude the missile is shown to be experiencing a positive angle of attack at the forebody section and a negative angle of attack at the aft section. Hence one would expect the missile to pitch upward upon launch. On the other hand, for the high-speed launch condition, the missile tends to pitch downward at launch. In addition to the pitching moments, adverse

yawing moments and side force may be of sufficient magnitude to cause the missile to veer into the parent aircraft at launch. The extremely long forebody on modern high-speed aircraft often presents a critical problem from the standpoint of missile-aircraft collision. Rolling

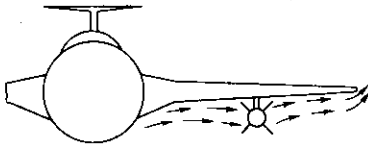


FIG. 11-2. Flow field induced by cross-flow phenomenon.

moments also exist even in a rather simple straight-forward installation (straight wing, say). As a result the missile has a tendency to roll into the pylon upon separation. In the case where the rear fin of the missile "slaps on" the side of the pylon no particular harmful effect (from the aircraft-safety standpoint) is expected. However, if the missile rolls sufficiently to cause the leading edge of the tail fins of the missile to hit the trailing edge of the pylon, the damage can be extremely serious.

Another very important aspect of the flow field is its effect on the aerodynamic hinge moments of the movable surfaces on the missile. This is particularly critical at high subsonic speeds and above since local shock waves may be present and can have a strong effect on the center-of-pressure location and hinge-moment characteristics. Careful analysis should include experimental wind-tunnel tests or flight testing with the full-scale missile by utilizing a "captive-flight-balance system" to measure these induced forces and moments to make certain that the resultant aerodynamic hinge moments are within the capability of the servo system in the missile. Improper design or failure to account for the actual aerodynamic hinge moments in the "captive flight" or launch attitude could cause the servo to be overpowered, with the result that the missile would be launched with its control surfaces fully deflected.

The most commonly used method for determining the induced loads and mutual interference effects of the airplane-missile combination is scaled-model wind-tunnel testing. Separate sting mountings for the airplane and missile are used to measure the loads on the missile and airplane as shown in Fig. 11-3. Using this technique, data on the

missile rolls sufficiently to cause the leading edge of the tail fins of the missile to hit the trailing edge of the pylon, the damage can be extremely serious.

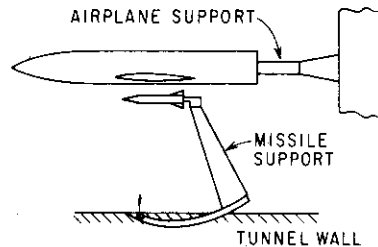


FIG. 11-3. Schema of test installation for measurement of airplane-missile mutual-interference effects.

effect of the missile on the parent aircraft may also be obtained in order to predict the performance degradation of the parent aircraft with the missile in the carried position. The effects of missile location in the immediate vicinity of the parent aircraft can also be determined by moving the complete missile-sting assembly relative to the airplane model.

Captive balance testing using a full-scale missile is also used to determine captive-flight loads on the missile as well as the effect of the missile on the launch aircraft. This particular technique has the advantage of obtaining full-scale-model test data. However, investigation of the various parameters such as spanwise and chordwise location and missile installation attitude is obviously extremely limited. Hence this test technique may be used to check the design installation based on scaled-model-test results obtained in the wind tunnel.

Control-system malfunction resulting from electrical- or hydraulic-system failure at launch may also cause the missile to be launched with its control surfaces deflected fully onto their physical stops. From the standpoint of safety of launch, this condition should be fully investigated. If results of calculations indicate the possibility of missile collision with the parent aircraft, proper design modification must be made. Such modification may consist of physically locking the control surfaces for a finite time after launch until the missile is sufficiently ahead of the aircraft.

The launch-dispersion characteristics in yaw may be determined by manual computation for one or two most adverse launch conditions. However, for detailed studies of the effects of individual parameters, such as missile stability margin and thrust malalignments, the computation procedure should be mechanized on the automatic computing machine. The basic equations of motion (in yaw) may be written as

$$\Sigma F_x = \frac{W}{g} \ddot{X} \quad (11-1)$$

$$\Sigma F_y = \frac{W}{g} \ddot{Y} \quad (11-2)$$

$$\Sigma M_z = I\ddot{\theta} \quad (11-3)$$

From Fig. 11-4, the right-hand side of Eqs. (11-1) and (11-2) may be expressed as

$$\Sigma F_x = F_A \cos \theta - F_N \sin \theta \quad (11-4)$$

and

$$\Sigma F_y = F_A \sin \theta + F_N \cos \theta \quad (11-5)$$

where

$$F_A = T - C_A q S \quad (11-6)$$

$$F_N = C_N q S \quad (11-7)$$

The summation of moments in yaw is

$$\Sigma M_z = M_\alpha \alpha + M_\delta \delta + M_{\dot{\theta}} \dot{\theta} + M_T + M_M + M_{\text{flow field}} \quad (11-8)$$

where M_T = moment due to thrust malalignment

M_M = moment due to aerodynamic-surface malalignment

The flow-field effect should be determined for several points along the missile trajectory if a reasonably accurate answer is to be obtained.

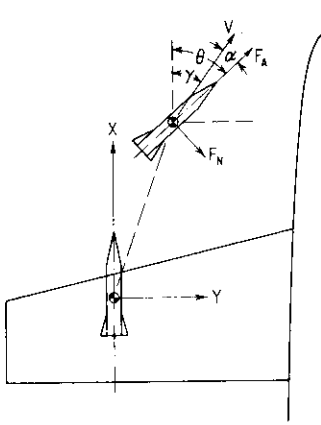


FIG. 11-4. Force diagram for missile-launch aircraft-collision study.

The values of C_A and C_N in Eqs. (11-6) and (11-7) should include the flow-field effect and can be determined from either wind-tunnel tests or captive-balance-flight-test results. For preliminary analysis, it is sufficient to assume a constant forward speed over the relatively short time interval to be studied. Using the iteration procedures similar to those described in Chap. 4, the above equations can be solved to determine the missile launch-dispersion characteristics.

2. Missile Structural Failure.

Another important consideration for parent-aircraft safety is the structural integrity of the missile during its captive flight and free flight in the immediate vicinity of the launch aircraft. The loads imposed by the flow-field effects must be carefully determined for a particular installation and speed condition in accordance with specification requirements. The missile airframe should then be designed to these captive-flight loads, which may in some cases be critical-design loads. The missile should also be designed to withstand the critical-flight loads under both normal and adverse flight conditions. Failure of the missile structure in flight in the vicinity of the launch aircraft is extremely hazardous and must be avoided by proper design.

11-3. LAUNCH BOUNDARIES—AIR LAUNCH

In addition to the problems of missile collision with the parent aircraft and missile structural break-up in front of the launch aircraft just discussed, additional consideration must be given to the safety of the launch aircraft. This takes the form of launch-aircraft boundaries

which would restrict the aircraft's "zone of operation" and hence provide a measure of safety against ground fire, blast effects from the missile and its warhead, etc. These launch boundaries are particularly meaningful for an air-to-surface missile weapon system which requires that the parent aircraft fly essentially the same path as the missile. Such a system may be a line-of-sight command guidance or a particular type of beam-rider system.

1. Launch-aircraft Trajectory. Figure 11-5 shows the pertinent parameters governing the flight path of the parent aircraft following missile launching. It is apparent that, from the kinematic standpoint, aircraft speed, maneuvering capability, missile flight time, and terrain clearance are the major governing factors in the determination of the launch boundaries. The launch boundaries may be readily determined by the following procedure.

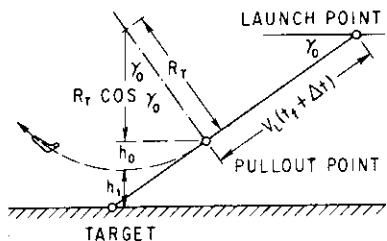


FIG. 11-5. Kinematics of launch boundary.

First, the kinematic or flight trajectory of the launch aircraft must be determined. The turn radius R_T in pitch may be calculated as

$$R_T = \frac{V_L^2}{g[n - (1 + \cos \gamma_0)/2]} \quad (11-9)$$

where V_L = launch velocity, fps, assumed to be constant throughout entire airplane trajectory

n = load-factor capability of airplane

γ_0 = initial launch angle which airplane and missile follow

The altitude required to turn from γ_0 to level attitude, designated as h_0 in Fig. 11-5, is shown to be

$$h_0 = R_T - R_T \cos \gamma_0 = R_T(1 - \cos \gamma_0) \quad (11-10)$$

Hence the distance S_0 shown in Fig. 11-5 may be determined as a function of h_0 and the terrain-clearance altitude h_1 , as follows:

$$S_0 = \frac{h_0 + h_1}{\sin \gamma_0} \quad (11-11)$$

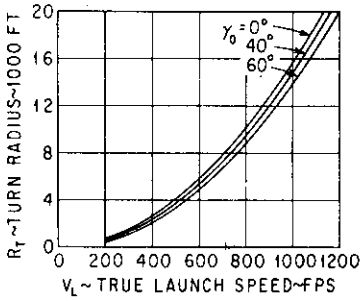


FIG. 11-6. R_T vs. V_L for various γ_0 's ($n = 3$).

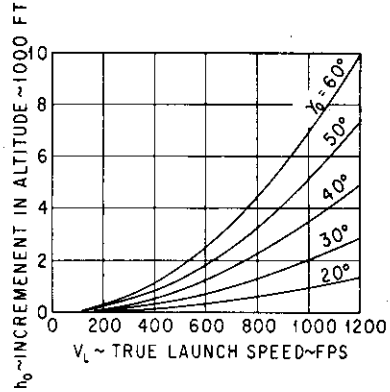


FIG. 11-7. h_0 vs. V_L for various γ_0 's ($n = 3$).

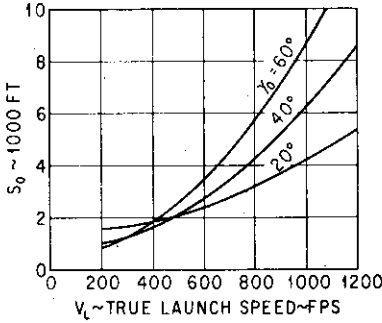


FIG. 11-8. S_0 vs. V_L for various γ_0 's ($n = 3, h_1 = 500$ ft).

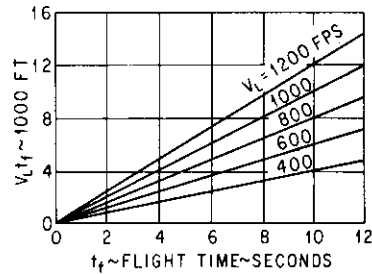


FIG. 11-9. $V_L t_f$ vs. t_f .

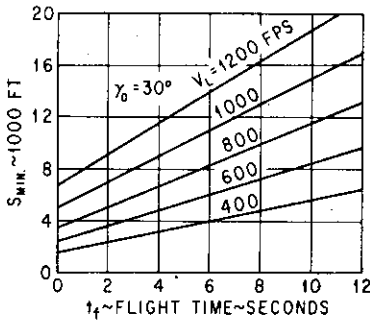


FIG. 11-10. S_{min} vs. t_f ($\gamma_0 = 30^\circ, n = 3, h_1 = 500$ ft).

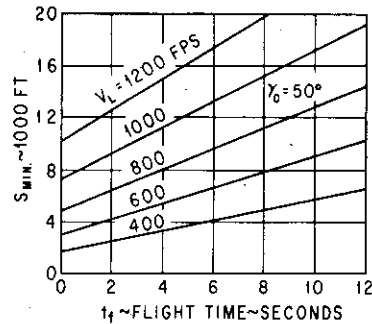


FIG. 11-11. S_{min} vs. t_f ($\gamma_0 = 50^\circ, n = 3, h_1 = 500$ ft).

The value of h_1 may also represent the altitude clearance required from the standpoint of enemy ground fire, blast effect from the warhead of the missile, etc. Thus the trajectory of the launch aircraft written in terms of S_{\min} may be summarized as

$$S_{\min} = S_0 + V_L(t_f + \Delta t) \quad (11-12)$$

$$S_{\min} = \frac{h_0 + h_1}{\sin \gamma_0} + V_L(t_f + \Delta t) \quad (11-12a)$$

$$S_{\min} = \frac{R_T(1 - \cos \gamma_0) + h_1}{\sin \gamma_0} + V_L(t_f + \Delta t) \quad (11-12b)$$

where t_f = flight time of missile

Δt = time lag from missile impact to commencement of aircraft-pull-out maneuver

Assuming a typical aircraft load-factor capability of 3 g's and a terrain-clearance requirement of 500 ft, values of the pertinent trajectory parameters R_T , h_0 , S_0 , and $V_L t_f$ have been calculated from Eqs. (11-9) through (11-11) and presented in Figs. 11-6 through 11-9. The values of S_{\min} for two typical launch angles (30 and 50°) are shown in Figs. 11-10 and 11-11 for a range of launch speeds.

2. Missile Trajectory. Next, missile trajectory must be calculated before the launch boundaries of the parent aircraft can be determined. This may be done by calculating the missile trajectory and flight time for three different slant ranges S_L at a given initial launch angle and calculating speed by the methods outlined in Chap. 4. The resultant trajectory data may then be plotted as missile slant range vs. missile flight time $t_{f(m)}$, as shown in Fig. 11-12.

3. Launch-boundary Determination. The actual launch boundary of the parent aircraft may be determined by matching the trajectory data of the parent aircraft and missile previously described. This may be done readily by superimposing the trajectory information of the parent aircraft in Fig. 11-12 in terms of S_{\min} as a function of $(t_f + \Delta t)$ from Eq. (11-12b). The intersection of the two curves establishes

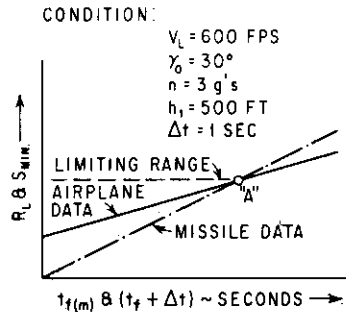


FIG. 11-12. Determination of launch boundary.

the limiting range for the given condition of launch speed and dive angle. This range is defined as the minimum range from which the parent aircraft can launch the missile, follow the missile toward the target, pull out at (or very shortly after) missile impact, and clear the ground by the desired height h_1 . Limiting range for other launch conditions can also be determined by the methods just described. Typical launch boundaries for two launch speeds are shown in Fig. 11-13.

From the standpoint of guidance accuracy, the missile must also be designed to fly within a certain boundary during launch. This boundary represents the maximum launch dispersion permissible

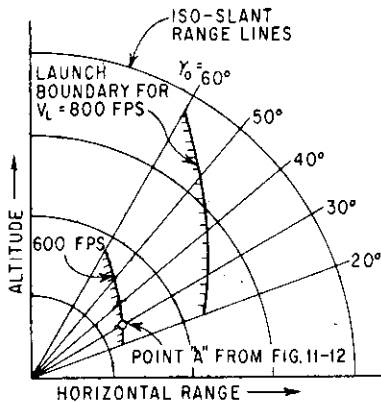


FIG. 11-13. Typical launch boundaries.

before the degradation to the delivery accuracy of the missile becomes unacceptable. As previously mentioned, the beam-riding missile must stay within the beam width of the guidance system in order to achieve "lock-on" for the remainder of its flight trajectory. For command control (particularly in the case of visual line-of-sight command), the missile must not disperse out of the pilot's normal field of view or too far off the normal intended flight path for the missile to return within the flight duration of the missile. Quite frequently, finite-length rail launchers are used

to "guide" the missile through the adverse-flow-field region in order to minimize missile dispersion at launch. These launching rails are mostly used in cases where the parent aircraft are "retrofitted" for missile launching. In cases where the parent aircraft and missile are designed initially as an integrated weapon system, the requirements for finite length rail launchers are minimized.

11-4. CONSIDERATION TO PARENT-AIRCRAFT PERFORMANCE

Consideration should be given by both the missile and aircraft designers to minimizing the performance degradation of the parent aircraft with external missile installation. Since selection of the spanwise and chordwise locations is generally limited by wing-bending and

aircraft center-of-gravity considerations, the designer must exercise extreme care in selecting the most favorable installation within this limited range. The final selected installation should represent the best compromise from the standpoint of the effect of the launch aircraft on the missile and the effect of the missile installation on the aircraft. The importance of the latter effect is readily apparent when one considers the fact that severe performance degradation may be realized with an improper missile installation. The resultant loss in range and in high-speed capability of the launch aircraft with its store of externally carried missiles is obviously undesirable from a tactical standpoint.

The problem of designing a missile-aircraft system with the least detrimental mutual effect is a challenging one that requires additional research and experimental work. Much experimental work has already been done on the various types of missiles or external-store installations. Measurements of loads on the missile as well as on the parent aircraft have been made in the wind tunnel, as previously mentioned. In the calculation of the performance degradation of the parent aircraft, the two most important pieces of information required are (1) basic performance curves of the parent aircraft and (2) a good correlation of installation drag of the missile. The former information consists basically of the thrust and drag variation with speed (see Fig. 4-8) and other engine data such as fuel-flow data. The latter may be obtained only after extensive study of the flow-field problem has been conducted or data from experimental tests of the configuration are available. It is emphasized here that item 1 is extremely important in that one must know exactly in what region of the drag curve the airplane is operating before any reasonable (let alone accurate) estimates of the performance degradation can be made. Hence it is important that the airplane and missile engineers work closely in this area to assure aircraft-missile compatibility. Once the above required data are made available, the performance degradation of the parent aircraft can be determined by the methods outlined in Chap. 4.

It should be remembered that, even with a well-designed installation, the penalty involved in externally carried missiles can be very high. Often a fairly respectable high-supersonic fighter becomes merely another high-subsonic aircraft when carrying several missiles externally. The present trend is toward internal stowage. Consequently much work is now in progress to study the aerodynamics of very-low-aspect-ratio wings for future design considerations, for both internal- and external-stowage considerations.

11-5. GROUND LAUNCH

The problem of launching missiles from the ground may be divided broadly into two general categories: (1) effects of the launching phase on the missile and (2) effects of the missile on the launcher and surrounding areas. The former effects are studied from the standpoint of missile-guidance and missile-component operation, while the latter effects are concerned primarily with the safety of the launching crew and surrounding areas. The latter problem is the topic of discussion in Sec. 11-6. This section is primarily concerned with the effects of the launching environment on the missile and its operation.

From the standpoint of missile guidance, several potential sources of detrimental effects causing excessive missile dispersion at launch are present. These include launcher deflection, missile tip-off from the launcher, thrust and fin malalignments, and atmospheric disturbances such as tail wind, cross wind, and gusts. Each of these factors affecting missile launch dispersion is discussed below.

1. Launcher Deflection. One of the most common factors present, particularly with mobile launchers, is the launcher deflection which results from ignition shock and sudden high thrust build-up from the booster. This motion can have a detrimental effect on the missile flight in that the initial heading of the booster configuration is different from that set previously. The missile will therefore fly a new flight path as the result of this pitching rate just as the missile leaves the launcher. This problem can be solved by (1) designing a stiffer launcher, (2) accounting for this motion in setting the launcher, or (3) a combination of both. For long-range ballistic missiles, which are generally launched vertically from rugged launching pads, this problem is virtually nonexistent.

2. Tip-off. Another common factor arises if the supporting shoes on the missile do not leave the supporting rail or rails simultaneously. Such a case may be one in which the two shoes (one forward and one aft) ride on the same rail. When this happens, the missile will tilt downward under the force of gravity and cause the missile to fly a new flight path. With simultaneous shoe release, the missile would have a simple translational instead of combined translational and rotational motion immediately upon leaving the launcher. This translational motion is not so detrimental to the dispersion as the rotational motion.

3. Thrust and Fin Malalignment. Turning moment due to thrust and aerodynamic surface malalignments is another important cause of missile dispersion during launch. The dispersion resulting

from this source can be very serious for missiles flying on "open loop" (i.e., without guidance or control) during their early phase of launch. In this case, a relatively large static stability margin (see Sec. 5-3 or 5-7) is required to minimize the dispersion due to these malalignments. This may be realized by incorporating relatively large tail surfaces on the missile (or large fins at the aft section of external droppable boosters). It will be shown in Chap. 12 that excessive static stability margin may prove to be undesirable when the missile is launched in a cross wind. Another method of minimizing missile dispersion at launch due to thrust and fin malalignment is spinning the missile immediately off the launcher. This technique is commonly used on uncontrolled and unguided ballistic missiles designed for relatively short ranges (i.e., less than 50 miles). For missiles which are controlled from the instant of launch, thrust and fin malalignment effects are of secondary importance.

Intentional thrust misalignment is used on certain types of cruise missile to counteract the effect of gravity during boost. In this case, the thrust vector is aligned below the center of gravity of the missile-booster combination. If the underalignment is too great, the missile may attain a large angle of attack, possibly resulting in stalling the missile at the end of its boost phase. On the other hand, insufficient underalignment may result in an angle of attack which is too low to sustain missile weight, causing an undesirable loss in flying altitude before the missile can attain sufficient speed under its own power.

4. Wind. Since it is tactically impractical always to launch into the wind, one must contend with the problem of wind blowing from any direction. Depending upon the application, sometimes the tail wind and sometimes the side wind may result in the critical design point. One of the main points to remember is that the static stability of the missile should not be so large that the configuration weathercocks into the relative wind, resulting in flight-path dispersion under conditions of uncontrolled flight. For missiles which are being controlled from the instant of launch, sufficient aerodynamic control effectiveness must be provided to maintain the missile on the desired flight path during launch.

Special consideration should be given to the effect of wind on long-range ballistic missiles, which lift off vertically from their launching pads. Strong cross winds could cause sufficient force to topple the missile over its base unless some tie-down provisions are made. In addition, loads induced by vortex effects at or near the tip of the missile may be sufficiently critical to cause structural failure of the missile on

the launch pad. These ground wind-induced loads are particularly critical for a missile with large length-to-diameter ratio and its attendant low structural strength and natural cantilever mode frequencies. The latter is conducive to a condition of resonance with the wind-induced load frequency. Modification of the nose geometry may be necessary to alleviate or alter the nature of the loads induced by the forebody vortices. Detail analysis including wind-tunnel tests on structural or dynamically similar models is required to determine the severity of this wind-induced loading problem for each missile design.

11-6. RANGE SAFETY

The advent of atomic- and nuclear-warhead-carrying missiles poses an extremely serious problem of safety not only to the large cities and their populations in the case of area-defense missiles but also to friendly troops and installations for the front-line tactical missiles. For the very-short-range tactical ballistic missiles which fly essentially a zero-lift trajectory, the problem of safety is not particularly severe since the missile is aimed and should fly into the general direction of the target. However, proper warhead arming and fusing must be provided to prevent premature warhead detonation at or near the launch site. For all other types of missiles which generally fly a prescribed lifting trajectory (including the long-range ballistic missiles), the flight path and resultant impact point can be extremely erratic if guidance- and control system failures occur. Hence reliability of the components as well as a proper arming system are prime requisites in any missile weapon system.

Since it is practically impossible to attain 100 per cent reliability for the over-all missile system, the problem of range safety must be analyzed from a realistic standpoint. For example, a multiple compound failure of components, which may be an extremely remote possibility, should not be used in the determination of the maximum missile impact area. On the other hand, simple failure or realizable compound failure of certain components should be taken into consideration to determine the severity of the range safety problem and consequently the requirement for a destructive system in the missile. Perhaps one of the most common failures is one which results in fully deflected controls causing the missile to turn in azimuth, or backward toward the launching area. The maximum area surrounding the launch site within which the missile can impact (when a component malfunctions) should be calculated to determine the need of the destructive system.

11-7. SHIPBOARD AND UNDERWATER LAUNCHES

Two very important design aspects in designing missiles for launching from ships or submarines are (1) space limitation and (2) motions of the ship during both check-out and launching. In addition to these, protection to both the ship and personnel from rocket-motor blast effects must be provided. For a particular type of missile configuration (airplane type where large wings are used to maintain sufficiently high lift-to-drag ratio L/D for long-range flights) extreme care must be exercised to assure a successful launch. The motions (pitch in particular) of the ship or submarine must be taken into account (if the launching platform is not stabilized) in order to determine the exact attitude of the missile at the end of the boost phase. This is particularly critical, since most missiles which fall into this category generally fly close to their maximum C_L . A slight change in attitude as the result of ship motions could mean an aborted flight.

Experience and test results on launching ballistic missiles from underwater are presently extremely limited. One of the main problems associated with underwater launch is to assure that the missile emerges from the water at an attitude compatible with the capabilities of the guidance and control system of the missile. In addition, aerodynamic stability and control must be provided in order to steer the missile back to the desired flight path. Extensive systematic tests must be made with dynamically similar models to determine such obvious effects as launch speed, attitude, and depth of the launching submarine on the attitude of the missile when it emerges from the surface of the water. The effect of sea state (roughness of the sea) should also be studied since it may be a major factor in determining the trajectory of the emerging missile. Rocket-motor ignition for an underwater-launched ballistic missile occurs when the missile has attained sufficient clearance from the surface of water to assure that the rocket motor experiences no adverse back pressure such as would be the case if the rocket motor were ignited while in the water. Ignition of the rocket motor in this mode of launch may be achieved effectively with a timer.

SYMBOLS

C_A	axial-force coefficient
C_L	lift coefficient
C_N	normal-force coefficient

F	force
M	moment
M_M	moment due to aerodynamic surface malalignment
M_T	moment due to thrust
R_T	turn radius
S	reference area
S_L	slant range
S_{\min}	minimum slant range for launch boundary
S_0	distance used in launch-boundary determination
T	thrust
V_L	launch velocity
W	weight
X	distance along X axis shown in Fig. 11-4
Y	distance along Y axis shown in Fig. 11-4
h_0	altitude required to turn
h_1	terrain-clearance altitude
n	load factor
q	dynamic pressure
$t_f, t_{f(m)}$	missile flight time
Δt	time lag between missile impact and commencement of aircraft pull-out maneuver
α	angle of attack
γ_0	initial launch angle
θ	missile attitude

Subscripts

A	axial direction
N	normal direction
fs	free stream
x, y, z	about the X, Y, Z axis system

REFERENCES

1. Alford, W. J., Jr., and H. N. Silver: Investigation at High Subsonic Speeds of Finned and Unfinned Bodies Mounted at Various Locations from the Wings of Unswept- and Swept-wing Fuselage Models, Including Measurements of Body Loads, *NACA Research Mem.* L54B18, Apr. 1, 1954.
2. Margolis, K., F. S. Malvestuto, Jr., and P. J. Maxie, Jr.: Theoretical Calculations of Supersonic Wave Drag at Zero Lift for a Particular Store Arrangement, *NACA Tech. Note* 4120, June, 1958.
3. O'Bryan, T. C.: Flight Measurement of Aerodynamic Loads and Moments on an External Store Mounted under the Wing of a Swept-wing Fighter-type Airplane, *NACA Research Mem.* L53G22, Nov. 25, 1953.

4. Silvers, H. N., and K. P. Spreeman: Wind-tunnel Investigation of a Wing-fuselage Combination with External Stores, *NACA Research Mem.* L7K20, July 9, 1948.
5. Silvers, H. N., and T. C. O'Brien: Some Notes on the Aerodynamic Loads Associated with External-store Installations, *NACA Research Mem.* L53E06A, June 22, 1953.
6. Silvers, H. N., T. J. King, Jr., and W. J. Alford, Jr.: Wind-tunnel Investigation at High Subsonic Speeds of the Effects of Wing-mounted External Stores on the Loading and Aerodynamic Characteristics in Pitch of a 45° Sweptback Wing Combined with a Fuselage, *NACA Research Mem.* L54A21, Mar. 23, 1954.
7. Spreeman, K. P., and W. J. Alford, Jr.: Investigation of the Effects of Geometric Changes in an Underwing Pylon-suspended External-store Installation on the Aerodynamic Characteristics of a 45° Sweptback Wing at High Subsonic Speeds, *NACA Research Mem.* L50L12, Mar. 5, 1951.
8. Alford, W. J., Jr., N. H. Silvers and T. J. King, Jr.: Preliminary Low-speed Wind Tunnel Investigation of Some Aspects of the Aerodynamic Problems Associated with Missiles Carried Externally in Positions Near Aircraft Wings, *NACA Research Mem.* L54J20, December, 1954.
9. Alford, W. J., Jr.: Theoretical and Experimental Investigation of the Subsonic Flow Fields beneath Swept and Unswept Wings with Tables of Vortex-induced Velocities, *NACA Rept.* 1327, 1957 (supersedes *Tech. Note* 3738).
10. Alford, W. J., Jr., H. N. Silvers, and T. J. King, Jr.: Experimental Aerodynamic Forces and Moments at Low Speed of a Missile Model during Simulated Launching from the Midsemispan Location of a 45° Sweptback Wing-fuselage Combination, *NACA Research Mem.* L54K11a, Feb. 4, 1955.

CHAPTER 12

FREE-FLIGHT DISPERSIONS

12-1. INTRODUCTION

In addition to the range safety considerations mentioned in Chap. 11, the dispersion characteristics of the missile during free flight are of considerable importance from the standpoint of delivery accuracy of the missile weapon system. In the case of the free-flight (uncontrolled) short-range ballistic missile, the total dispersion results primarily from the free-flight portion of its trajectory (the other causes are launcher-aiming error, target-location error, etc.). In the case of a reentry body of a long-range ballistic missile, the dispersion resulting from its free-flight or terminal phase must be kept low in order to minimize the requirements for an extremely accurate and expensive guidance system to steer the missile (and its reentry body) to the prescribed point in space prior to separation of the reentry body and its warhead. Even in cases where terminal guidance is employed, the missile may fly a limited uncontrolled or unguided trajectory just prior to impact. Such occurrences may take place as a result of loss of guidance due to component malfunction, ground clutter, enemy countermeasures, etc. Hence the dispersion characteristics of the missile during free flight must be carefully analyzed before the effectiveness of the missile weapon system can be accurately determined.

The following sections in this chapter deal with the problems of dispersion of short-range free ballistics during launch or boosting phase. The problem of drift (dispersion) due to cross wind is treated in detail to show the pronounced effect of the external-configuration design. In addition, the dispersion-sensitivity factors for vacuum-flight conditions simulating very-high-altitude reentry are discussed. Finally, reentry body-design considerations are discussed from the standpoint of minimizing free-flight dispersion as well as other pertinent design considerations.

12-2. BOOST PHASE

The primary sources of dispersion during the launch or boost phase of flight for a free-flight ballistic missile consist of the following: (1) launcher dynamics (i.e., launcher deflection, tip-off effects, etc.), (2) launcher setting or aiming error, (3) variation in rocket-motor performance, (4) thrust and fin malalignments, and (5) cross-wind effects. Each of these effects will be treated in the following sections.

1. Launcher Dynamics. As discussed in Sec. 11-5, the launcher may deflect under the influence of rocket-motor ignition shock and sudden thrust build-up. Since the launcher is generally considered by the dynamics engineers as a complex structural system, particularly one which is integral with a mobile vehicle, the exact nature and magnitude of the launcher deflection are extremely difficult to calculate. Hence experimental test data must be obtained by high-speed-camera coverage of several actual missile launchings to determine the amount of the launch deflection under operating conditions. This information can then be fed back into the analysis of the missile delivery accuracy. Should the deflection prove to be intolerable, the launcher must be modified or "beefed up" to reduce the magnitude of the deflection. Since finite-length rail launchers are commonly used on unguided free-flight missiles and rockets, missile tip-off off the launcher may occur if the front shoe leaves the rail prior to the aft shoe. The consequent rotation under the force of gravity is undesirable and may be eliminated by designing equal launch rails with simultaneous fore- and aft-shoe releases.

2. Launcher Setting. Since it is physically impossible to set the launcher precisely at the desired angle, error in launcher setting is always present. The severity of the error in launcher setting increases at launch angles below and above the launch angle for maximum range. This is readily apparent from Fig. 12-1, which shows the range variation with launch attitude. For most short-range (i.e., say, less than 30 miles) applications, the optimum launch attitude γ_{opt} is closer to 50° than to 45° obtained from drag-free consideration. For somewhat greater range applications where the ratio of total rocket-motor

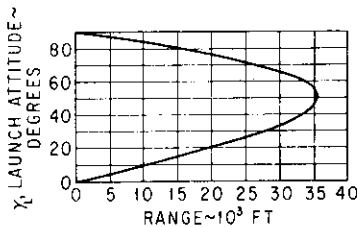


FIG. 12-1. Typical variation of launch attitude with range.

impulse to burnout weight is in excess of about 100, the angle for maximum range increases from 50 to approximately 65°, as shown in Fig. 12-2. In either case, however, the (down-range) dispersion sensitivity due to launcher-setting

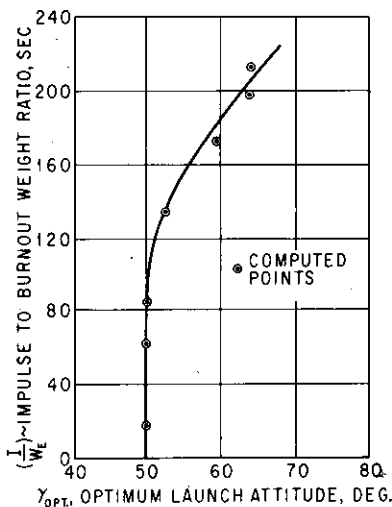


FIG. 12-2. Effect of ratio I/W_E on γ_{opt} .

error, defined as $\partial X/\partial \gamma_L$, is zero at γ_L for maximum range and increases (negatively) above and below this optimum angle, as shown in Fig. 12-3. The down-range dispersion ΔX_γ due to launcher-setting is thus

$$\Delta X_\gamma = \frac{\partial X}{\partial \gamma_L} \Delta \gamma_p \quad (12-1)$$

where $\Delta \gamma_p$ is the error in launcher setting in pitch. The azimuth dispersion $\Delta \gamma_v$ (due to azimuth launch-setting error) is simply

$$\Delta Y_\gamma = X \Delta \gamma_v \quad (12-2)$$

where X is total range and $\Delta \gamma_v$ is the error in launcher setting in the azimuth plane.

3. Variation in Rocket-motor Performance. Because of the tolerances in rocket-motor design, propellant properties, manufacturing, etc., the total impulse of the rocket motor may vary over a range of a fraction of a per cent to several per cent depending on the operating environment. Variation of rocket-motor performance due to temperature variation in the propellant (particularly in the case of most solid-propellant rocket motors) may be partially accounted for by measuring the temperature inside the rocket motor prior to launch. The uncertainty in temperature measurement constitutes a source of dispersion. Perhaps the easiest method of determining this dispersion is to (1) first calculate the effect on range due to variation in total

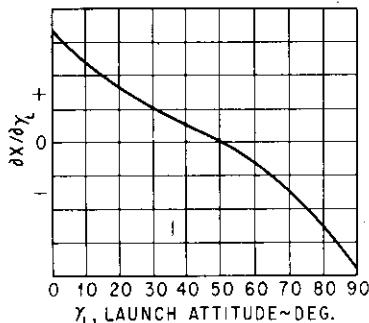


FIG. 12-3. Typical variation of range-sensitivity factor with range.

rocket-motor impulse I , (2) determine the range-sensitivity factor $\partial X/\partial I$, and (3) evaluate the effect of temperature on total impulse. The latter is generally furnished by the rocket-motor manufacturer. With the above data, the range dispersion due to impulse variation ΔX_I may be calculated as follows:

$$\Delta X_I = \frac{\partial X}{\partial I} \Delta I \quad (12-3)$$

where ΔI is the impulse variation. Equation (12-3) may also be written in terms of propellant-temperature error as

$$X_T = \frac{\partial X}{\partial I} \frac{\partial I}{\partial T} \Delta T \quad (12-4)$$

where $\partial I/\partial T$ is determined from the rocket-motor basic performance data shown in Fig. 12-4. In addition to the effect of temperature variation, the rocket-motor impulse may vary from one motor to the next for a given propellant-temperature condition. The range dispersion due to this basic inherent tolerance may also be calculated by Eq. (12-3) above.

4. Thrust and Fin Malalignment. Perhaps the most difficult parameter to determine is the malalignment of the thrust vector and/or aerodynamic surfaces. Results from static firings from many rocket motors must be obtained in order to evaluate the magnitude and nature of the thrust malalignment. In addition, numerous measurements must be made on the aerodynamic fins to get a representative statistical average of the fin malalignments. Since the direction of these malalignments is generally random in nature, the dispersion resulting from these malalignments is also random. Since no method of compensating the effects of thrust or fin malalignments is available, the designer must resort to methods of minimizing the dispersion due to these effects. One obvious method is to hold the tolerances on the rocket-motor and fin designs to an absolute minimum. However, such design practice is generally extremely costly and hence is not adhered to. Another method involves designing a missile with very large static stability margin for the launch condition. This may be realized by either locating the center of gravity relatively far forward

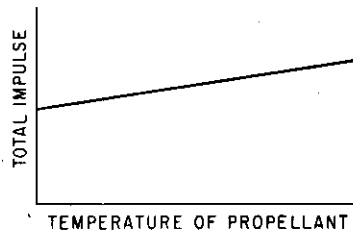


FIG. 12-4. Effect of propellant temperature on total impulse.

of the center of pressure or putting large stabilizing fins at the aft end of the missile. While the missile with this large static stability margin is more resilient to any thrust or fin malalignment effects, it is also more conducive to dispersion due to cross-wind effects since its weather-cocking tendency is greatly increased, as discussed in a subsequent section.

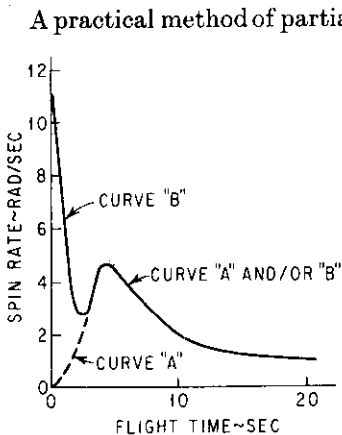


FIG. 12-5. Spin rate vs. time.

A practical method of partially nullifying the effects of thrust and fin malalignments is by imparting a spin to the missile at the instant of launch and throughout its boost phase. This initial spin may be produced either by spin-jet rockets mounted on the missile or by using helical-rail launchers. Spin rate or rolling velocity for the remainder of the powered (or unpowered) flight may be obtained by canting the aerodynamic stabilizing fins. The effectiveness of the initial spin on reducing the dispersion due to thrust and fin malalignments is readily apparent from the following sample calculations:

Example: $\gamma_L = 20^\circ$, $X = 13,500$ yd.

- a. Lateral-thrust malalignment = $\frac{1}{8}$ in. from center of gravity
- b. Angular-thrust malalignment = 0.00176 radian
- c. Fin malalignment = $\frac{1}{2}^\circ$ (in pitch)
- d. Fin intentionally canted to produce spin rate as shown by curve A in Fig. 12-5.

The range and azimuth dispersions Δx and Δy for the missile launched without initial spin (curve A in Fig. 12-5) are 1,300 and 125 yd, respectively. The resultant dispersion is thus $[(1,300)^2 + (125)^2]^{1/2} = 1,305$ yd. However, by imparting an initial spin rate of 11 radians/sec through the use of a helical-rail launcher (shown by curve B in Fig. 12-5), the corresponding dispersions are reduced to 425 and 185 yd, respectively. The resultant dispersion is hence reduced to 463 yd, corresponding to a reduction of approximately 65 per cent.

5. Surface Winds. In launching free-flight ballistic rockets, the magnitude and direction of the surface winds as well as winds aloft (the latter are generally called ballistic winds) must be taken into account. This is done by properly canting the launcher in elevation or in the azimuth plane depending on the presence of either a head or tail wind

or a cross wind. Since it is impractical to obtain an accurate wind measurement at or near the launch site, the inaccuracy in such measurements results in an incomplete compensation for the presence of surface winds; hence dispersion due to surface-wind effects is realized.

From the standpoint of dispersion due to surface-wind effects, it is desirable to design the missile with zero (or even a slightly negative) stability margin (i.e., neutral stability). A highly statically stable missile is undesirable since it has a very strong tendency to weather-cock into the relative wind and hence is more conducive to dispersion due to surface winds. References 1 to 5 are recommended to the readers for the mathematical and quantitative treatments of the general effects of wind and malalignments, as well as a discussion on the optimization of these two effects on dispersion.

12-3. POWER-OFF FLIGHT

During the power-off trajectory of a free-flight ballistic missile, dispersions may be caused by several factors which are discussed below.

1. Variation in Missile Characteristics. Since it is generally impractical to maintain the exact missile characteristics on all missiles coming off the assembly line, the range of each missile will vary somewhat from the nominal range calculated for an "average" or "datum" missile configuration. Hence this variation may be considered as a dispersion over the nominal condition. Since the weight from one missile to another may vary from a few to many pounds, the range variation or dispersion may be readily calculated by getting a statistical average of this weight variation by the following relationship:

$$\Delta X_w = \frac{\partial X}{\partial W} \Delta W \quad (12-5)$$

where ΔX_w = range dispersion due to weight variation

$\partial X/\partial W$ = range-sensitivity factor due to weight variation

ΔW = statistical average weight variation

Because of aerodynamic smoothness tolerances as well as rough-handling effects in the field, the drag of the missile may also vary from one missile to the next. This variation in drag characteristic may be significant for the relatively long range flight conditions (i.e., near γ_{opt} launch attitudes). This factor is rather difficult to assess. Hence

intelligent guesses must be made; they should be based on past experience or data on this subject. Consequently the dispersion resulting from this factor may be conveniently calculated as follows:

$$\Delta X_D = \frac{\partial X}{\partial C_D} \Delta C_D \quad (12-6)$$

where ΔX_D = range dispersion due to C_D variation

$\partial X/\partial C_D$ = range-sensitivity factor due to C_D

ΔC_D = variation in drag coefficient

2. Variation in Atmospheric Density. During its power-off free-flight phase, the missile trajectory is primarily a function of its drag and mass characteristics (assuming still-air condition). Since the drag of the missile is the product of $C_D \frac{1}{2} \rho V^2$, the density of the atmosphere must be known or assumed. Meteorological data taken prior to launch may be subject to (1) error due to inaccuracy in the basic instrumentation and (2) changes in atmospheric condition between the time the data were recorded and the time of launch. Hence the error in the determination of atmospheric density results in a range dispersion which may be calculated as

$$\Delta X_\rho = \frac{\partial X}{\partial (\% \rho)} \Delta (\% \rho) \quad (12-7)$$

where ΔX_ρ = range dispersion due to density variation

$\partial X/\partial (\% \rho)$ = range sensitivity due to density variation (generally expressed as per cent density error)

$\Delta (\% \rho)$ = per cent density error

3. Drift Due to Cross Wind. The problem of evaluating the missile dynamic response in the presence of cross winds during its power-off (ballistic) flight trajectory may be conveniently divided into two phases. A qualitative analysis will be presented first to clarify the nature of its response characteristics. Then an analytical method will be derived in order to evaluate this cross-wind effect quantitatively.

a. Qualitative Analysis. The mechanics of missile response (or drift) due to cross winds may be conveniently illustrated by means of Fig. 12-6. A constant forward velocity is assumed for the moment. Figure 12-6A shows the plan view of the normal attitude of the missile during its power-off flight. As it encounters a cross wind, shown in Fig. 12-6B, it weathercocks into the relative wind as shown in Fig. 12-6C. The rapidity with which the missile weathercocks of course depends on the static stability margin of the missile in this flight condition (positive static stability margin is assumed throughout this

analysis, i.e., the missile is statically stable at all times during its trajectory). It is seen from Fig. 12-6C that, at this instant, the missile will be accelerated in the azimuth direction by the drag component $D_0 \sin \beta_0$. Thus it is clear that, as time elapses, the missile drift rate \dot{y}_D develops, as indicated in Fig. 12-6D, and consequently reduces β . For a reasonably long flight trajectory, a steady-state condition will be attained wherein the missile will be drifting at the velocity of the cross wind, as shown in Fig. 12-6E. Obviously, in this steady-state condition, the missile will experience no unbalance of forces in the azimuth direction and hence no acceleration in that direction. The above simplified qualitative analysis may be summarized in terms of acceleration \ddot{y}_D and drift rate \dot{y}_D with a time history as presented in Fig. 12-7. The corresponding "instants" of conditions described above are included in Fig. 12-7 for clarification.

As the result of the above discussion, it is clear that a single-body-mounted lateral accelerometer will not sense acceleration in the azimuth direction since the only external driving force in the azimuth direction is the aerodynamic drag (component) which lies in the insensitive axis of this accelerometer.

Hence a single accelerometer mounted rigidly within the missile airframe cannot be employed as a device to detect or compensate for cross-wind effects.

b. Quantitative Analysis. The above section presented the qualitative behavior of the missile flying in the cross-wind condition. A quantitative evaluation of the missile response is presented below for calculating the drift dispersion due to cross winds.

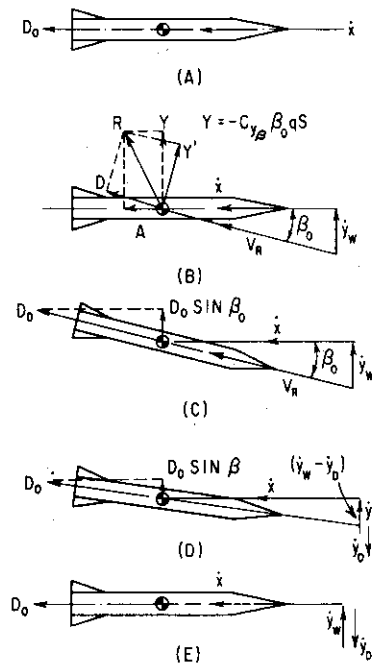


FIG. 12-6. Mechanics of drift due to cross wind. (A) Undisturbed-flight condition. (B) Instant of cross-wind occurrence. (C) Missile has weathercocked into resultant velocity V_R . (D) Shortly after occurrence of cross wind. (E) Steady-state condition (i.e., missile drifting with velocity of cross wind $Y_D = Y_W$).

In the development of the method for calculating drift due to cross winds, it is convenient to assume that the missile has already weather-cocked and commenced to drift, as shown in Fig. 12-6*D*. From Fig.

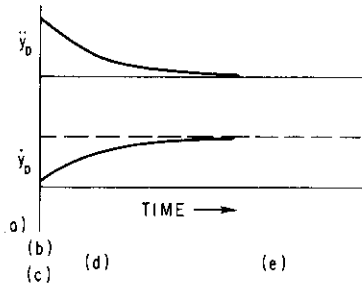


FIG. 12-7. Summary of missile dynamic response to cross wind.

12-6*D*, the acceleration of the missile in the azimuth direction \ddot{y}_D may be written as

$$F_Y = m\ddot{y}_D = D_0 \sin \beta \quad (12-8)$$

Since $D_0 = C_{D_0} \frac{1}{2} \rho V^2 S$, Eq. (12-8) becomes

$$\ddot{y}_D = \frac{C_{D_0} \frac{1}{2} \rho V^2 S \sin \beta}{2m} \quad (12-9)$$

$$\text{But } \beta = \sin^{-1} \frac{\dot{y}_W - \dot{y}_D}{V_R} \quad (12-10)$$

where \dot{y}_D is the drift rate of the missile and V_R the resultant velocity defined as

$$V_R = \sqrt{\dot{x}^2 + (\dot{y}_W - \dot{y}_D)^2} = \sqrt{\dot{x}^2 + \dot{y}_W^2 + \dot{y}_D^2 - 2\dot{y}_W \dot{y}_D} \quad (12-11)$$

For most applications, β is small and may be written as

$$\beta \cong \frac{(\dot{y}_W - \dot{y}_D)}{V_R} \quad (12-12)$$

Hence Eq. (12-9) may be expressed as

$$\ddot{y}_D = \frac{C_{D_0} \rho S V_R (\dot{y}_W - \dot{y}_D)}{2m} \quad (12-13)$$

Since $V_R \cong \dot{x}$, the forward speed of the missile, Eq. (12-13) becomes

$$\ddot{y}_D = \frac{C_{D_0} \rho S \dot{x} (\dot{y}_W - \dot{y}_D)}{2m} \quad (12-14)$$

Integrating \ddot{y}_D from the limits of $(\dot{y}_D)_0$ to \dot{y}_D ,

$$\int_{(\dot{y}_D)_0}^{\dot{y}_D} \frac{d\dot{y}_D}{\dot{y}_W - \dot{y}_D} = \frac{S}{2m} \int_0^t (C_{D_0} \rho \dot{x}) dt \quad (12-15)$$

we get

$$-\ln (\dot{y}_W - \dot{y}_D) - \ln [\dot{y}_W - (\dot{y}_D)_0] = \frac{S}{2m} \int_0^t (C_{D_0} \rho \dot{x}) dt \quad (12-16)$$

or

$$\ln \left[\frac{\dot{y}_W - (\dot{y}_D)_0}{\dot{y}_W - \dot{y}_D} \right] = \frac{S}{2m} \int_0^t (C_{D_0} \rho \dot{x}) dt \quad (12-17)$$

OR

$$\frac{\dot{y}_W - (\dot{y}_D)_0}{\dot{y}_W - \dot{y}_D} = \frac{S}{e^{2m}} \int_0^t (C_{D_0} \rho \dot{x}) dt \tag{12-18}$$

In order to evaluate the missile drift rate \dot{y}_D , the values of $\int_0^t (C_{D_0} \rho \dot{x}) dt$ and $(\dot{y}_D)_0$ must be determined first. In most cases, however, ideal-trajectory data (standard atmospheric trajectories with no wind or malalignments) are available since these are basic data with which the designer commences his design and analyses. Hence plots of $(C_{D_0} \rho \dot{x})$ vs. time, such as shown in Fig. 12-8, can be readily made for most of

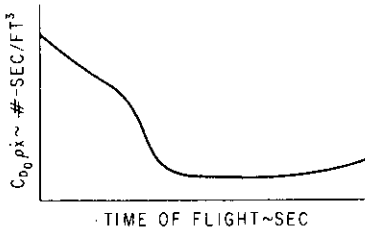


FIG. 12-8. Variation of $C_{D_0} \rho \dot{x}$ with time.

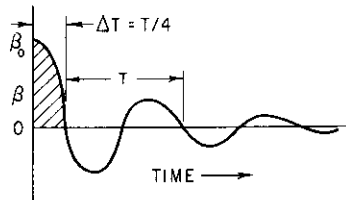


FIG. 12-9. Initial transient response of a typical statically stable missile.

the flight conditions for which the drift dispersions are desired. By simple graphical integration of the $(C_{D_0} \rho \dot{x})$ vs. time curve (Fig. 12-8), the value of $[\dot{y}_W - (\dot{y}_D)_0] / (\dot{y}_W - \dot{y}_D)$ may be calculated vs. flight time of the missile.

The only remaining term that needs to be determined in order to calculate the missile drift rate \dot{y}_D is $(\dot{y}_D)_0$. The term $(\dot{y}_D)_0$ represents the initial drift rate of the missile from initial missile transient due to cross wind. Schematically, the initial transient-response characteristics of a typical stable missile are shown in Fig. 12-9. Again, for a statically stable missile with a reasonably high degree of damping, the value of $(\dot{y}_D)_0$ may be approximated by the first quarter cycle of the initial transient response as shown in Fig. 12-9. During this small time interval Δt the Mach number, q , and density can be assumed to be constant. Hence the impulse due to this initial transient (from Fig. 12-6B) is

$$Y \Delta t = m \Delta \dot{y}_D = C_{Y_\beta} \beta_0^{1/2} \rho V_R^2 S \Delta t \tag{12-19}$$

Since

$$\beta_0 \cong \frac{\dot{y}_W}{V_R}$$

Eq. (12-19) becomes

$$m \Delta \dot{y}_D = C_{Y\beta} \dot{y}_W \frac{1}{2} \rho V_R^2 S \frac{2}{\pi} \frac{T}{4} = m (\dot{y}_D)_0 \quad (12-20)$$

where $2/\pi$ is the ratio of the area under a cosine curve to that for a constant β_0 over the time interval Δt (or $T/4$). The period T shown in Fig. 12-9 is related to the yawing-moment derivative $C_{n\beta}$, as

$$T = 2\pi \sqrt{\frac{I_z}{C_{n\beta} q S d}} \quad (12-21)$$

Hence the value of $(\dot{y}_D)_0$ may be expressed as

$$(\dot{y}_D)_0 = \frac{C_{Y\beta} \dot{y}_W \dot{x} \rho S}{2m} \sqrt{\frac{I_z}{C_{n\beta} q S d}} \quad (12-22)$$

Therefore, once the initial conditions in which the cross wind is assumed to occur are known, the value of $(\dot{y}_D)_0$ can be readily calculated by Eq. (12-22). Consequently the drift rate of the missile \dot{y}_D ,

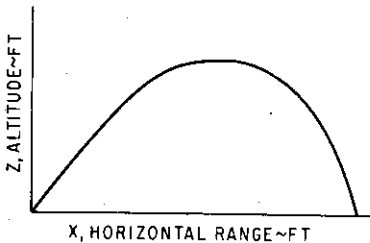


FIG. 12-10. Ideal trajectory (no wind).

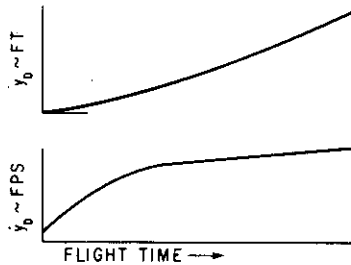


FIG. 12-11. Variation of \dot{y}_D and y_D with time.

may be readily calculated from Eq. (12-18) for the entire trajectory for any cross-wind conditions. The drift dispersion y_D is merely the integral of the \dot{y}_D vs. time curve previously calculated.

A sample calculation is presented in Table 12-1 for clarification, as well as to facilitate future application of the method developed here. The sample presented assumes a cross wind of constant magnitude throughout the entire altitude range of the missile trajectory shown in Fig. 12-10. For cross winds which vary with altitude, Eq. (12-18) is still applicable if incremental altitudes and the average cross-wind for these altitude intervals are used. The drift rate and drift dispersion due to a constant cross wind of 20 fps (occurring at 4 sec after launch) for this sample problem are shown in Fig. 12-11.

4. Determination of Over-all Free-flight Dispersion. In general, the dispersion of a free-flight ballistic missile is of the elliptical pattern. The elliptical probable error is the probability that 50 per cent of all missiles fired will fall within an ellipse defined by

$$\frac{x^2}{\sigma_x^2} + \frac{y^2}{\sigma_y^2} = 1.386 \quad (12-23)$$

where σ_x and σ_y are the standard deviations of error in the x and y direction and may be expressed as

$$\sigma_x = \sqrt{\sigma_{x_1}^2 + \sigma_{x_2}^2 + \sigma_{x_3}^2 + \dots} \quad (12-24)$$

$$\sigma_y = \sqrt{\sigma_{y_1}^2 + \sigma_{y_2}^2 + \sigma_{y_3}^2 + \dots} \quad (12-25)$$

where σ_{x_1} , σ_{y_1} , etc., are the standard deviations of error in the x and y direction caused by launcher setting, wind, malalignment effects, etc. When the values of σ_x and σ_y are approximately equal, the error between the elliptical probable error and the circular probable error in defining the area in which 50 per cent of the missiles will fall is negligible. The circular probable error (CEP) is defined as

$$\text{CEP} = 1.18\sqrt{\sigma_x\sigma_y} \quad (12-26)$$

12-4. DISPERSION-SENSITIVITY FACTORS IN VACUUM

Heretofore discussion has been focused on the free-flight dispersion characteristics associated with atmospheric trajectories. This presupposes that trajectory data are available in order to assess these dispersion characteristics. However, for some cases where no trajectory data are available, it is desirable to estimate the order of magnitude of the dispersions resulting from errors in several of the missile trajectory parameters. In addition, it is important to determine the relative importance of these trajectory parameters in order that proper emphasis may be placed on the more important components of the missile system during its early preliminary-design phase. In the following paragraphs, the dispersion-sensitivity factors in vacuum condition are derived and are based on (1) a flat earth, rectilinear coordinate system and (2) a spherical earth, nonrectilinear coordinate system.

TABLE 12-1. SAMPLE CALCULATION ON MISSILE DISPERSION DUE TO CROSS WIND DURING POWER-OFF FLIGHT

Given:	$m = 11.54$ slugs	$\dot{x} = 1,770$ fps	$d = 1.0$ ft
	$C_{T\beta} = -0.283$ per deg	$\rho = 0.0022$ slug/ft ³	$I_z = 60$ slug/ft ²
	$C_{n\beta} = 0.549$ per deg	$S = 0.786$ ft ²	$\dot{y}_W = 20$ fps at $t = 4$ sec after launch
	$q = 3,468$ psf		

Using Eq. (12-22),

$$\begin{aligned}
 (\dot{y}_D)_b &= \frac{(0.283 \times 57.3)(20)(1,770)(0.0022)(0.786)}{2(11.54)} \sqrt{\frac{60}{(0.549)(57.3)(3,468)(0.786)(1)}} \\
 &= 1.13 \text{ fps}
 \end{aligned}$$

NO WIND—Ideal-Trajectory Data

1	2	3	4	5	6	7	8	9	10	11	12	13	14	15
t sec	ρ	\dot{x}	C_{D_0}	$C_{D_0} \rho \dot{x}^2$	t	$(C_{D_0} \rho \dot{x}^2)_{av}$	$\int_0^t C_{D_0} \rho \dot{x}^2 dt$	$\Sigma(s)$	$\frac{s}{2m}$	$\ln \left\{ \frac{\dot{y}_w - (\dot{y}_D)_0}{\dot{y}_w - \dot{y}_D} \right\}$	$\dot{y}_w - \dot{y}_D$	\dot{y}_D	Δy_D	Σy_D ft
4.00	0.00220	1,777	0.4225	1.650	4	1.46	0	0	0	1.0	18.87	1.13	0	0
5.02	0.00215	1,664	0.4354	1.556	8	1.22	5.84	5.84	0.1985	1.220	15.45	4.55	11.36	11.36
6.62	0.00206	1,511	0.4552	1.416	12	0.74	4.88	10.72	0.3645	1.440	13.10	6.90	22.90	34.26
8.98	0.00197	1,323	0.4914	1.289	16	0.37	2.96	13.68	0.4650	1.594	11.82	8.18	30.16	64.42
10.33	0.00192	1,232	0.5036	1.190	20	0.24	1.48	15.16	0.5150	1.675	11.25	8.75	33.86	98.28
11.13	0.00190	1,183	0.5097	1.142	24	0.24	0.96	16.12	0.5485	1.730	10.90	9.10	35.70	133.98
11.93	0.00188	1,138	0.5137	1.096	28	0.245	0.96	17.08	0.5800	1.786	10.57	9.43	37.06	171.04
12.77	0.00186	1,095	0.4905	0.996	32	0.25	0.98	18.06	0.6140	1.850	10.20	9.80	38.46	209.50
13.65	0.00184	1,055	0.4297	0.830	36	0.26	1.00	19.06	0.6480	1.912	9.86	10.14	39.88	249.38
14.53	0.00182	1,023	0.3397	0.632	40	0.29	1.04	20.10	0.6840	1.983	9.51	10.49	41.26	290.64
15.49	0.00181	996	0.2429	0.438	44	0.33	1.16	21.26	0.7240	2.063	9.13	10.87	42.72	333.36
16.41	0.00179	977	0.1731	0.303	48	0.39	1.32	22.58	0.7680	2.158	8.74	11.26	44.26	377.62
17.47	0.00178	959	0.1542	0.263	50.4*		0.94	23.52	0.7990	2.225	8.48	11.52	47.35	404.97
20.83	0.00175	914	0.1550	0.247										
24.67	0.00174	881	0.1556	0.239										
30.59	0.00178	864	0.1560	0.240										
34.79	0.00184	876	0.1558	0.252										
38.51	0.00193	899	0.1555	0.269										
42.87	0.00206	937	0.1549	0.299										
46.87	0.00222	978	0.1543	0.335										
49.79	0.00235	1,009	0.1727	0.409										

Notes: Total drift dispersion $y_D = 404.97$ ft at end of flight. Columns 1 through 5 from digital computation. Columns 6 through 7 from fared curve (i.e., Fig. 12-8). Column 8 = column 7 $\times \Delta t$. Column 11: see Eq. (12-17).

* End of flight.

1. Flat Earth, Rectilinear Coordinate System. For relatively short range flights whereby a flat earth, rectilinear coordinate system may be assumed, the equations of motion of a point mass in a vacuum are readily expressed from Fig. 12-12.

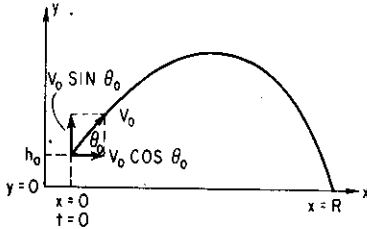


FIG. 12-12. Definition of terms for sensitivity-factor determination (flat earth).

$$\dot{x} = V_0 \cos \theta_0 \quad (12-27)$$

$$\dot{y} = V_0 \sin \theta_0 - gt \quad (12-28)$$

Integrating Eqs. (12-27) and (12-28), we get

$$x = V_0 \cos \theta_0 t + C_1 \quad (12-29)$$

$$y = V_0 \sin \theta_0 t - \frac{gt^2}{2} + C_2 \quad (12-30)$$

From the boundary conditions,

$$t = 0, y = h_0 \quad \text{then } C_2 = h_0$$

$$t = 0, x = 0 \quad \text{then } C_1 = 0$$

Substituting the values of C_1 and C_2 and Eq. (12-29) into (12-30), we get

$$y = x \tan \theta_0 - \frac{gx^2}{2V_0^2 \cos^2 \theta_0} + h_0 \quad (12-31)$$

Since $x = R$ at $y = 0$, Eq. (12-31) becomes

$$0 = R \tan \theta_0 - \frac{gR^2}{2V_0^2 \cos^2 \theta_0} + h_0 \quad (12-32)$$

$$R^2 - \frac{(2V_0^2 \sin \theta_0 \cos \theta_0)R}{g} - \frac{2V_0^2 h_0 \cos^2 \theta_0}{g} = 0 \quad (12-33)$$

hence
$$R = \frac{V_0^2 \sin 2\theta_0}{2g} \pm \frac{V_0 \cos \theta_0 \sqrt{V_0^2 \sin^2 \theta_0 + 2gh_0}}{g} \quad (12-34)$$

Since R is positive for $\theta_0 = 0^\circ$ (i.e., $R = V_0 \sqrt{2h_0/g}$), the negative sign in the second term of Eq. (12-34) may be neglected. Thus Eq. (12-34) becomes

$$R = \frac{V_0^2 \sin 2\theta_0}{2g} + \frac{V_0 \cos \theta_0 \sqrt{V_0^2 \sin^2 \theta_0 + 2gh_0}}{g} \quad (12-35)$$

The dispersion-sensitivity factors due to errors in velocity, altitude, and missile attitude at missile cutoff, $\partial R/\partial V_0$, $\partial R/\partial h_0$, and $\partial R/\partial \theta_0$, respectively, may be obtained by taking the partial derivative of R with respect to V_0 , h_0 , and θ_0 in Eq. (12-35). These dispersion-sensitivity factors are

$$\frac{\partial R}{\partial V_0} = \frac{V_0 \sin 2\theta_0}{g} + \frac{2 \cos \theta_0 (V_0^2 \sin^2 \theta_0 + gh_0)}{g\sqrt{V_0^2 \sin^2 \theta_0 + 2gh_0}} \quad (12-36)$$

$$\frac{\partial R}{\partial h_0} = \frac{V_0 \cos \theta_0}{\sqrt{V_0^2 \sin^2 \theta_0 + 2gh_0}} \quad (12-37)$$

and

$$\frac{\partial R}{\partial \theta_0} = \frac{V_0^2 \cos 2\theta_0}{g} \left(1 + \frac{V_0 \sin \theta_0}{\sqrt{V_0^2 \sin^2 \theta_0 + 2gh_0}} \right) - \frac{2h_0 V_0 \sin \theta_0}{\sqrt{V_0^2 \sin^2 \theta_0 + 2gh_0}} \quad (12-38)$$

For $\theta_0 = 0^\circ$ (i.e., free flight commencing at the apogee) condition, the above expressions can be simplified as

$$R = V_0 \sqrt{\frac{2h_0}{g}} \quad (12-39)$$

$$\frac{\partial R}{\partial V_0} = \sqrt{\frac{2h_0}{g}} \quad (12-40)$$

$$\frac{\partial R}{\partial h_0} = \frac{V_0}{\sqrt{2gh_0}} \quad (12-41)$$

$$\frac{\partial R}{\partial \theta_0} = \frac{V_0^2}{g} \quad (12-42)$$

Although the above expressions are applicable only for the vacuum (drag-free) flight condition, they are useful in that the order of magnitude of the dispersions as well as the relative importance of the various trajectory parameters (i.e., V_0 , h_0 , and θ_0) may be readily determined. The range and sensitivity factors for two actual flight conditions using the drag of a typical missile configuration have been computed and

compared with the values derived from Eqs. (12-39) through (12-42) below.

$V_0 = 1,000$ fps, $h_0 = 5,000$ ft	$V_0 = 1,000$ fps, $h_0 = 10,000$ ft
$R = 16,500$ ft (actual condition)	$R = 23,000$ ft (actual)
$= 17,700$ ft (vacuum condition)	$= 25,000$ ft (vacuum)
$\frac{\partial R}{\partial h_0} = 1.60$ ft/ft (actual)	$= 1.10$ ft/ft (actual)
$\frac{\partial R}{\partial h_0} = 1.77$ ft/ft (vacuum)	$= 1.25$ ft/ft (vacuum)
$\frac{\partial R}{\partial V_0} = 13.0$ ft/fps (actual)	$= 17.8$ ft/fps (actual)
$\frac{\partial R}{\partial V_0} = 17.7$ ft/fps (vacuum)	$= 25.0$ ft/fps (vacuum)
$\frac{\partial R}{\partial \theta_0} = 26.4$ ft/mil (actual)	$= 25.4$ ft/mil (actual)
$\frac{\partial R}{\partial \theta_0} = 31.0$ ft/mil (vacuum)	$= 31.0$ ft/mil (vacuum)

2. Spherical Earth, Nonrectilinear Coordinate System.

For long-range ballistic flight trajectories such as those of the ICBM's, the dispersion-sensitivity factors for a vacuum (drag-free) flight condition may be readily determined from the simplified expression for the range⁶ [Eq. (4-43)] shown below.

$$R = 2r_0 \tan^{-1} \frac{\sin \theta_f \cos \theta_f}{1/\bar{V}_f^2 - \cos^2 \theta_f} \quad (12-43)$$

where $\bar{V}_f = V_f/V_s =$ ratio of cutoff velocity to satellite velocity

$\theta_f =$ angle of incidence as shown in Fig. 4-16

Substituting V_f/V_s for \bar{V}_f and deleting the subscript f in θ , Eq. (12-43) becomes

$$R = 2r_0 \tan^{-1} \frac{\sin \theta \cos \theta}{(V_s/V)^2 - \cos^2 \theta} \quad (12-44)$$

Taking the partial derivative of R with respect to V and θ , the dispersion-sensitivity factors become

$$\frac{\partial R}{\partial V} = 4r_0 \frac{\sin \theta \cos \theta (V_s^2/V^3)}{\left\{ 1 + \left[\frac{\sin \theta \cos \theta}{(V_s/V)^2 - \cos^2 \theta} \right]^2 \right\} \left[\left(\frac{V_s}{V} \right)^2 - \cos^2 \theta \right]^2} \quad (12-45)$$

and

$$\frac{\partial R}{\partial \theta} = \frac{2r_0}{\left\{ 1 + \left[\frac{\sin \theta \cos \theta}{(V_s/V)^2 - \cos^2 \theta} \right]^2 \right\}} \left\{ \frac{(\cos^2 \theta - \sin^2 \theta)}{\left[\left(\frac{V_s}{V} \right)^2 - \cos^2 \theta \right]} - \frac{2 \sin^2 \theta \cos^2 \theta}{\left[\left(\frac{V_s}{V} \right)^2 - \cos^2 \theta \right]^2} \right\} \quad (12-46)$$

The values of the above sensitivity factors have been computed for


the optimum cutoff attitude (see Fig. 4-14b) for ranges of 2,000- and 4,000-nautical-mile ballistic-missile flight conditions. These values are shown below to indicate the order of magnitude of these sensitivity factors.

$R = 2,000$ nautical miles	$R = 4,000$ nautical miles
$\theta = 37^\circ$	$\theta = 28.5^\circ$
$V = 17,300$ fps	$V = 21,700$ fps
$V_s = 25,900$ fps	$V_s = 25,900$ fps
$h_0 = 0$ ft	$h_0 = 0$ ft
$r_0 = 20.9 \times 10^6$ ft	$r_0 = 20.9 \times 10^6$ ft
$\frac{\partial R}{\partial V} = 1,558$ ft/fps	$\frac{\partial R}{\partial V} = 3,293$ ft/fps
$\frac{\partial R}{\partial \theta} = -2,990$ ft/mil	$\frac{\partial R}{\partial \theta} = -2,470$ ft/mil

12-5. REENTRY-BODY DESIGN CONSIDERATIONS

One of the most important subsystems of a long-range ballistic-missile system is the reentry body. In view of the order of magnitude of the dispersion-sensitivity factors due to errors in cutoff velocity and missile attitude, $\partial R/\partial V$ and $\partial R/\partial \theta$ discussed in the previous section, it is of paramount importance that the reentry-body configuration must be designed which will result in the lowest possible free-flight dispersion. On the other hand, it must also be optimized from other design considerations, i.e., aerodynamic heating, minimum structural weight, reliability, etc.

In general, it is desirable to avoid the use of a guidance system in the reentry body in order to minimize the cost of the missile as well as to improve the reliability of the reentry-body subsystem. Hence, the reentry-body configuration must be carefully designed in order that its free-flight dispersion resulting from atmospheric disturbances, i.e., wind shears, cross winds, etc., is within the specification limits. From the discussion in Sec. 12-3, it is apparent that a low-drag configuration is desirable from the standpoint of minimum free-flight drift dispersion due to cross winds. Specifically, it is desirable to make the value of $C_D S/m$, commonly known as the "ballistic factor," as low as possible to achieve low free-flight dispersion due to wind effects. A low value of ballistic factor has the added advantage that the impact Mach number for a given flight range is greater; hence the vulnerability to enemy countermeasures is reduced. In addition, a reentry-body configuration with a low ballistic factor minimizes the separation problem since



the force required to separate the reentry body from its last-stage booster is decreased or may be completely eliminated. In the latter case, separation is achieved by the force of gravity simply by releasing a clamp which holds the structures of the two bodies together during their exit flight.

While a low drag or ballistic factor is desirable from the standpoints of free-flight dispersion, vulnerability, etc., the problems associated with aerodynamic heating become more severe. Hence a severe weight penalty may be imposed by the added material required to protect the reentry body during its terminal flight. At the present, the two most feasible techniques used in combating this heating problem are (1) the heat-sink method and (2) ablation. The former method involves using a material which absorbs most of the heat generated while the latter method involves using a material which melts or ablates off during reentry. Other methods such as cooling the surface by a liquid, alteration of the flow over the body by protruding spikes, or magnetohydrodynamic are being investigated for possible future applications. The selection of the best method can be made only after a thorough analysis of the magnitude and rate of heat transfer, the cost and availability of materials, etc.

In addition to the problems associated with the dispersion and aerodynamic heating, consideration must be given to the dynamic-response characteristics of the reentry body during its critical terminal flight. In general, a reentry body without a control or guidance system must be statically and dynamically stable. Static stability is required in order to prevent the reentry body from tumbling during its entire terminal flight. Adequate damping is desirable since it reduces the induced drag and hence its dispersion during its flight in the sensible atmosphere. In addition, good damping characteristics decrease the severity of the aerodynamic loading and heating during reentry. Spinning the reentry body prior to its terminal flight into the atmosphere may be used to obtain stability and to nullify the detrimental effects of aerodynamic out of trim. Readers are referred to the partial list of reports (refs. 7 through 18) for detailed treatments of many of the important aspects of reentry-body design.

SYMBOLS

C_D	drag coefficient
C_n	yawing-moment coefficient
C_v	side force

C_1, C_2	constants of integration
D	drag
D_0	drag at zero lift or normal force
F	force
I	rocket-motor impulse
I_x, I_z	moment of inertia about the X and Z axis
R	range of the missile
S	reference area
T	period of oscillation
V	forward velocity
V_f	cutoff velocity
\bar{V}_f	ratio of V_f to V_s
V_R	resultant forward velocity
V_s	satellite velocity
W	weight of missile
W_E	burnout weight of missile
X	range of missile
Y	side force
Z	altitude
d	body diameter
h	altitude
m	mass
$C_D S/m$	"ballistic factor"
q	dynamic pressure
r_0	radius of earth
t	(flight) time
x	down-range (in X direction)
y	distance in the azimuth direction
\dot{y}_D	drift rate
\dot{y}_W	wind velocity
β	angle of sideslip
γ_L	launch attitude
ρ	air density
θ_f	angle of incidence as shown in Fig. 4-16
σ_x, σ_y	standard deviations of error in the x and y direction

Subscripts

D	drift
p	pitch setting
y	azimuth setting
0	initial condition

REFERENCES

1. Rosser, J. B., R. R. Newton, and G. L. Gross: "Mathematical Theory of Rocket Flight," McGraw-Hill Book Company, Inc., New York, 1947.
2. Davis, L., Jr., J. W. Follin, Jr., and L. Blitzer: "The Exterior Ballistics of Rockets," D. Van Nostrand Company, Inc., Princeton, N.J., 1958.
3. Hunter, M. W., A. Shef, and D. V. Black: Some Recent Aerodynamic Techniques in Design of Fin-stabilized Free-flight Missiles for Minimum Dispersion, *J. Aeronaut. Sci.*, vol. 23, no. 6, pp. 571-577, June, 1956.
4. Oswald, T. W.: Dynamic Behavior during Accelerated Flight with Particular Application to Missile Launching, *J. Aeronaut. Sci.*, vol. 23, no. 6, pp. 781-791, August, 1956.
5. Whitehurst, J. W.: "Some Aspects of Missile Launch Dispersion," The Catholic University of America 1959 First Award Papers, IAS Regional Student Conferences, 6th annual ed., The Minta Martin Aeronautical Student Fund.
6. Eggers, A. J., H. J. Allen, and S. E. Niece: A Comparative Analysis of the Performance of Long-range Hypervelocity Vehicles, *NACA Tech. Note* 4046, October, 1957.
7. Allen, H. J., and A. J. Eggers, Jr.: A Study of the Motion and Aerodynamic Heating of Missiles Entering the Earth's Atmosphere at High Supersonic Speeds, *NACA Tech. Note* 4047, October, 1957.
8. Allen, H. J.: Motion of a Ballistic Missile Angularly Misaligned with the Flight Path upon Entering the Atmosphere and Its Effects upon Aerodynamic Heating, Aerodynamic Loads, and Miss Distance, *NACA Tech. Note* 4048, October, 1957.
9. Tobak, M., and W. R. Wehrend: Stability Derivatives of Cones at Supersonic Speeds, *NACA Tech. Note* 3788, September, 1956.
10. Nelson, R. L.: The Motions of Rolling Symmetrical Missiles Referred to a Body-axis System, *NACA Tech. Note* 3737, November, 1956.
11. Charters, A. C.: The Linearized Equations of Motion Underlying the Dynamic Stability of Aircraft, Spinning Projectiles, and Symmetrical Missiles, *NACA Tech. Note* 3350, January, 1955.
12. Philips, W. H.: Effect of Steady Rolling on Longitudinal and Directional Stability, *NACA Tech. Note* 1627, June, 1958.
13. Bolz, R. E.: Dynamic Stability of a Missile in Rolling Flight, *J. Aeronaut. Sci.*, vol. 19, no. 6, pp. 395-403, June, 1952.
14. Laitone, E. V.: Dynamic Longitudinal Stability Equations for the Re-entry Ballistic Missile, *J. Aeronaut. Sci.*, vol. 26, no. 2, pp. 94-98, February, 1959.
15. Bogdonoff, S. M., and I. E. Vas: Preliminary Investigations of Spiked Bodies at Hypersonic Speeds, *J. Aeronaut. Sci.*, vol. 26, no. 2, pp. 65-74, February, 1959.
16. Allen, H. J.: Hypersonic Flight and the Re-entry Problem (Twenty-first Wright Brothers Lecture), *J. Aeronaut. Sci.*, vol. 25, no. 4, pp. 217-227, April, 1958.
17. Singer, S. F., and R. C. Wentworth: A Method for Calculating Impact Points of Ballistic Rockets, *Jet Propulsion*, vol. 27, no. 4, pp. 407-409, April, 1957.
18. Robertson, R. E.: Impact Points of Ballistic Rockets, *Jet Propulsion*, vol. 27, no. 12, p. 1256, December, 1957.

CHAPTER 13

POWER-PLANT-DESIGN CONSIDERATIONS

13-1. INTRODUCTION

Heretofore the discussion on missile configuration design has been focused primarily from the aerodynamic standpoint. Since the power plant constitutes a major component of the over-all configuration of the missile, it is well to discuss some of its more important design aspects and how it affects the configuration of the missile. The type of power plant selected is primarily dictated by the type of mission the missile is designed to accomplish. The selected power plant may be one of the many which will be described in a later section. Its installation must then be optimized from the standpoint of the over-all efficiency of the external configuration. It may be installed as an integral part of the main body of the missile, as in the case of a solid-propellant or pre-packaged-liquid rocket motor, or it may be pylon-mounted, particularly in the case of air-breathing power plants. For certain missions, it may be advantageous to use a combination of an integral rocket or pylon-mounted power plant and an external droppable booster. The optimum installation can be made only after a thorough analysis of the problems involved has been made.

13-2. TYPES OF POWER PLANT

There are a great variety of propulsive devices ranging from the time-tested, reliable reciprocating engine to the more recently developed air turbo rocket. Each of these power plants has its advantages and disadvantages as well as limitations regarding its applications. Categorically speaking, it can be said that all air-breathing engines are limited to operation in the lower atmosphere whereas rocket engines, which carry their own oxidizer, may be used at all altitudes. Thus, for altitudes below approximately 20 miles, both rockets and air-breathing engines may be used whereas, above this altitude, only rockets may be

considered. From the standpoint of efficient operation, the velocity ranges are considered for the following types of power plant:

<i>Mach No. range</i>	<i>Propulsion system</i>
0 to 0.7	Piston engine and propeller
0.5 to 0.8	Turboprop
0.7 to 2.5	Turbojet
2.0 and 4.0	Ram jet, air turbo rocket, rocket
4.0 and up	Rocket

1. Reciprocating Engine. The four-stroke-cycle spark-ignition engine is probably the simplest in principle of all prime movers.

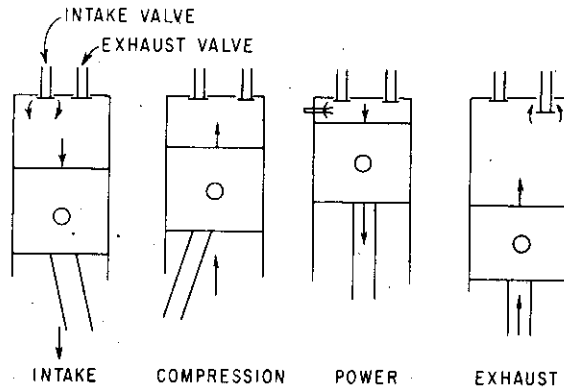


FIG. 13-1. Four-stroke-cycle reciprocating engine.

As shown in Fig. 13-1, a piston reciprocating in a cylinder draws a mixture of fuel and air in through the intake valve during its downward stroke and compresses the mixture on its subsequent upward stroke.

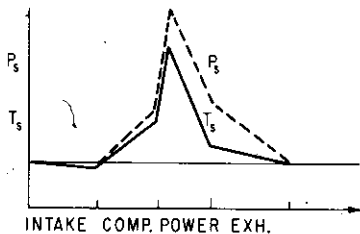


FIG. 13-2. Pressure and temperature as function of stroke—four-cycle reciprocating engine.

the exhaust stroke. Figure 13-2 shows the pressure and temperature characteristics of the fuel-air mixture as a function of piston travel.

An electric spark then occurs, which ignites the gas mixture, releasing chemical energy in the form of heat, which in turn causes a substantial increase in pressure. This increased pressure forces the piston downward, delivering mechanical power to the crankshaft. When the piston reaches the bottom of the cylinder, the exhaust valve opens to allow the burned gases to push out on

The reciprocating engine has the advantage of very low specific fuel consumption and relatively high static power. These favorable characteristics make this type of engine far superior to any other type of engine for relatively low speed and low altitude operation.

2. Turbojet. The major components of a turbojet engine are the compressor, combustion chamber, and the turbine to drive the compressor as shown schematically in Fig. 13-3. Atmospheric air enters the diffuser, where it is partially compressed to reduce its velocity. As it passes through the compressor, its pressure is raised to several times

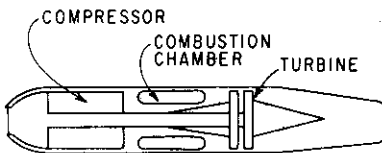


FIG. 13-3. Schema of a turbojet.

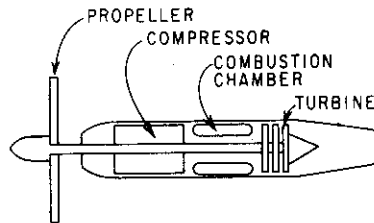


FIG. 13-4. Schema of a turboprop.

its original value. The temperature also increases appreciably. Between the compressor outlet and the combustion chamber, the air undergoes a slight diffusion. In the combustion chamber, heat is added to raise the energy level of the gases. Although the process of combustion is essentially a constant-pressure process, a slight pressure loss occurs because of friction and momentum changes. From the combustion chamber, the hot gases are expanded through the turbine, which extracts just enough energy to drive the compressor and to overcome bearing friction. The gases then flow through the exhaust nozzle to increase the kinetic energy and obtain thrust.

3. Turboprop. This engine is practically identical to the turbojet. The differences are primarily due to the manner in which the generated power is used. Where the principal function of the turbojet is to produce thrust in the form of an exhaust jet, the turboprop uses most of the energy of the gases to drive a propeller, as shown in Fig. 13-4.

4. Air Turbo Rocket. This type of engine, which combines the essential features of both the turbojet and rocket, is in the development stage. A gas generator, using ethylene oxide as a monopropellant, produces gas which exhausts through a turbine, which in turn drives a single-stage axial-flow compressor as shown in Fig. 13-5. JP-4 fuel is

introduced and burned downstream in what is essentially an afterburner. Thrust is obtained from both the JP-4 air mixture and the gases from the ethylene oxide reaction. This engine would have the advantage of being capable of operating at very high Mach numbers (up to 4.0) and yet producing a high thrust at static sea-level condition. The chief disadvantages are (1) very high fuel consumption and (2) high vapor pressure.

5. Ram Jet. The most important feature of a ram-jet engine is that it has no moving parts in the engine proper. For this reason, it

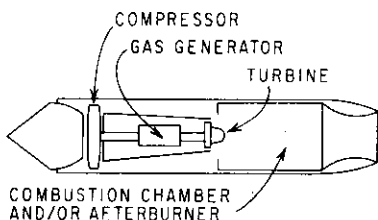


FIG. 13-5. Schema of an air turbo-rocket.

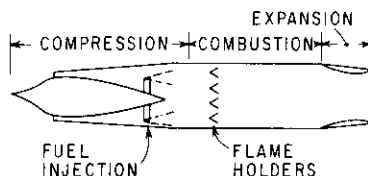


FIG. 13-6. Schema of a ramjet.

is simple, easily fabricated, and relatively inexpensive. The basic components, as shown schematically in Fig. 13-6, are an inlet, a combustion chamber, and a nozzle. The operating cycle is basically similar to other jet engines, i.e., compression, burning, and expansion. Entering air is diffused as it flows to the burner section. Fuel is injected and burned. The hot gases are then expelled at high velocity through the nozzle to develop thrust. This type of engine is a continuing burning device operating with a continuous flow of air. Hence a ram-jet-powered vehicle must have an initial velocity before the ram jet can operate. Since the compression ratio and hence power output increase with speed, the ram jet is generally used only for flights at relatively high supersonic speeds.

6. Rocket. The rocket is technically a jet engine. It differs from the air-breathing type in that it does not depend upon the atmospheric air as an oxidizing agent. Both the fuel or propellant(s) and the oxidizing agent are carried within the rocket motor. The propelling action is derived from the generation of large quantities of gases by the chemical reaction of propellants within the combustion chamber. These gases are expelled with supersonic velocity.

For sustained or intermittent operation over relatively long periods of time, the liquid-propellant rocket is generally used. The duration

depends primarily on the quantity of fuel available. The operating pressures are lower than those employed by the solid-propellant units (300 to 750 psi as compared with 1,500 to 3,000 psi). Because of their reliability and handling characteristics, etc., the solid-propellant units are becoming more "popular" in filling the bill that has normally been filled by the liquid-propellant rockets. Design considerations for both liquid- and solid-propellant rockets will be presented in a later section of this chapter.

13-3. FUNDAMENTALS OF ROCKET ENGINES

1. Principles of Rocket Propulsion. Rocket propulsion is one form of jet propulsion which involves forward thrust or motion due to rearward ejection of high-velocity gases or fluid jet. The principle of jet propulsion is based on Newton's third law of motion, which states that for every action there is an equal and opposite reaction. In a rocket engine, the force of the momentum of the rearward ejection of hot gases imparts a reverse or forward thrust to the engine.

2. General Equations. In the quantitative analysis of the performance of a rocket engine, it is generally assumed that the chemical reactions in the combustion chamber are in the state of thermochemical equilibrium. This assumption appears to be quite valid except where high-energy fuels are considered. For the latter type of fuel, the exact nature of their thermochemical reactions has not been completely determined. Because of the strong possibility of ionization and recombination in the products of combustion in the nozzle and downstream of the nozzle, an exact determination of the performance of a rocket motor using these high-energy fuels cannot be easily made by theoretical analysis. Hence experimental means involving static firings, etc., must be employed. Another important assumption made is that the flow within the rocket engine is isentropic. This assumption is generally valid as long as the nozzle is designed so that the gases undergo a full or underexpansion at the exit of the nozzle. A condition of full expansion is one in which the gases have been expanded from a high pressure from the combustion chamber to a pressure at the nozzle exit equal to the ambient. A condition of underexpansion is one in which the exit pressure of the gases is higher than the ambient pressure. The assumption of isentropic flow for a condition of overexpansion (exit pressure less than ambient pressure) may be completely unjustifiable, particularly when the ambient pressure is very much greater than the exit pressure of the gases because of flow separation

and shock formation within the nozzle. However, with careful design practices, the above assumptions may be used in the quantitative prediction of the performance of the rocket engine.

The thrust of a rocket engine is the resultant pressure of forces acting upon its outer and inner surfaces and may be expressed as

$$T = \int_{A_o} p_o dA_x + \int_{A_i} p_i dA_x \quad (13-1)$$

where T = thrust

p_o = outside or ambient pressure

p_i = inside pressure

A_x = axial or x component of wall of rocket engine

From Fig. 13-7, the value of the first integral is

$$\int_{A_o} p_o dA_x = -p_o A_e \quad (13-2)$$

where A_e is the exit area of the nozzle. From the momentum theorem, which states that the integral of all the pressure forces acting on a mathematical closed surface is equal to the momentum flux through the surface, the second integral may be written as

$$\int_i p dA_x - \int_e p_e dA_x = M_x \quad (13-3)$$

where p_e = pressure at the nozzle exit

M_x = momentum flux in the axial direction and may be written as

$$\int_e \rho V_x^2 dA_x$$

Hence Eq. (13-1) becomes

$$T = \int_e \rho V_x^2 dA_x + \int_e p_e dA_x - p_o A_e \quad (13-4)$$

Since

$$\int_e \rho V_x^2 dA_x = \frac{W_p}{g} V_j \quad (13-5)$$

and

$$\int_e p_e dA_x = p_e A_e \quad (13-6)$$

Equation (13-4) becomes

$$T = \frac{W_p V_j}{g} + (p_e - p_o) A_e \quad (13-7)$$

where W_p = propellant-weight flow rate

V_j = exit velocity of exhaust gas

In the above derivation it was assumed that the exit velocity is parallel to the direction of the thrust. For nozzles with a large divergence angle α as shown in Fig. 13-8, a divergence coefficient λ must be applied. The value of λ is defined as^{1,*}

$$\lambda = \frac{1 - \cos 2\alpha}{4(1 - \cos \alpha)} = \frac{1}{2} + \frac{1}{2} \cos \alpha \quad (13-8)$$

and is plotted in Fig. 13-8. Hence Eq. (13-7) becomes

$$T = \lambda \frac{\dot{W}_p V_j}{g} + (p_e - p_o)A_e \quad (13-9)$$

From Eq. (13-9), it is seen that for a fully expanded (or design) condition the term $(p_e - p_o)$ is equal to zero. For underexpansion, the

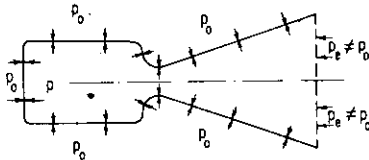


FIG. 13-7. Pressure forces.

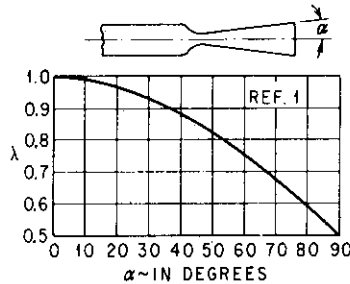


FIG. 13-8. Divergent coefficient vs. divergence angle.

value of thrust is increased by the amount $(p_e - p_o)A_e$. Thus, for operation at altitudes above the design altitude, the nozzle and hence the rocket engine becomes more efficient. Conversely, below design altitudes, the rocket engine is less efficient.

The thrust coefficient is often used as a measure of performance of the nozzle or the expansion process in the nozzle and is used as follows:

$$T = C_T p_c A_t \quad (13-10)$$

where C_T = thrust coefficient

p_c = chamber pressure

A_t = throat area of nozzle

* Superscript numbers indicate references listed at the end of the chapter.

From relationships derived for isentropic flow through a converging-diverging (DeLaval-type) nozzle, the thrust coefficient may also be expressed as

$$C_T = \sqrt{\frac{2\gamma^2}{\gamma-1} \left(\frac{2}{\gamma+1}\right)^{(\gamma+1)/\gamma(-1)} \left[1 - \left(\frac{p_e}{p_c}\right)^{(\gamma-1)/\gamma}\right]} + \frac{p_e - p_o}{p_c} \frac{A_e}{A_t} \quad (13-11)$$

The values of C_T for condition of full expansion ($p_e = p_o$) for various values of γ and p_c/p_e have been calculated and are presented in Fig. 13-9.

Another useful expression involves the area ratio (defined as ratio of throat area to exit area of the nozzle) required for complete or full

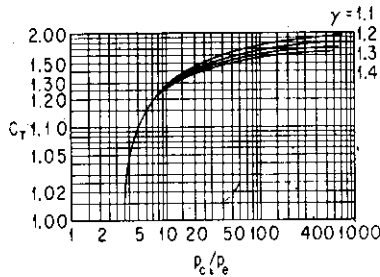


FIG. 13-9. Thrust coefficient vs. p_c/p_e for various γ 's—full-expansion condition.

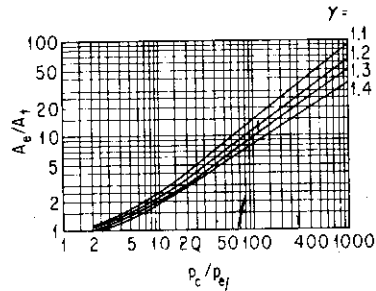


FIG. 13-10. Variation of A_e/A_t with p_c/p_e for various γ 's—full-expansion condition.

expansion. This ratio may be expressed as a function of γ and p_e/p_c as follows:

$$\frac{A_t}{A_e} = \left(\frac{\gamma+1}{2}\right)^{1/(\gamma-1)} \left(\frac{p_e}{p_c}\right)^{1/\gamma} \sqrt{\frac{\gamma+1}{\gamma-1} \left[1 - \left(\frac{p_e}{p_c}\right)^{(\gamma-1)/\gamma}\right]} \quad (13-12)$$

Values of A_t/A_e for various values of γ and p_c/p_e are shown in Fig. 13-10

Other equations and definitions which are useful in rocket-motor performance analysis are (1) fuel specific impulse, (2) over-all specific impulse, (3) total impulse, and (4) characteristic velocity. The fuel specific impulse I_{sp} is defined as the ratio of total impulse to fuel weight and may be expressed as

$$I_{sp} = \frac{\int_0^{t_b} T dt}{W_p} = \frac{I}{W_p} \quad \text{sec} \quad (13-13)$$

where t_b = total burning time of rocket motor

It may also be expressed as

$$I_{sp} = \frac{T}{\dot{W}_p} \quad \text{sec} \quad (13-13a)$$

The over-all specific impulse I_o is defined as the ratio of total impulse to total motor weight and is expressed as

$$I_o = \frac{\int_0^{t_b} T dt}{W_m} \quad \text{sec} \quad (13-14)$$

where W_m = total rocket-motor weight (propellant plus inert weights)
The total impulse I is defined as the integral of the thrust vs. burning-time curve and is expressed as

$$I = \int_0^{t_b} T dt \quad \text{lb-sec} \quad (13-15)$$

The characteristic velocity C^* is a measure of the efficiency of the propellant of the rocket motor and is defined as

$$C^* = \frac{V_j}{C_T} = \frac{g p_c A_t}{\dot{W}_p} \quad (13-16)$$

13-4. ROCKET-MOTOR-DESIGN CONSIDERATIONS

The selection of either a liquid- or solid-propellant rocket motor is perhaps one of the most complex problems a designer must solve before an optimum missile configuration and weapon system can be realized. Each type has its advantages and disadvantages which the designer must consider in detail before a compromise can be made. The following sections are devoted to a discussion of some of the various design aspects associated with each type in order to provide a fuller appreciation of the problems involved.

1. Liquid-propellant Rocket Motor. Until recently, liquid propellant rockets have been used exclusively to propel such vehicles as ballistic missiles, high-altitude-research vehicles, and ICBM's. The employment of liquid rockets was long undisputed because:

a. It was the only type of propulsion system far along in its development that could ensure, with some degree of reliability, long duration of sustained or intermittent operation.

b. It can provide thrust-vector control with relative ease by gimbaling of the thrust chamber.

However, with the advent of solid-propellant rocketry in recent years, parts of the above which used to be characteristic of liquid rockets have been largely nullified. The details of solid rockets are discussed in subsequent paragraphs.

A liquid-propellant rocket system generally consists of the following:

- a. One or more tanks to store the propellants—depending on the type of propellants used (monopropellants or bipropellants)
- b. A feed mechanism for forcing the liquids into the thrust chamber
- c. A power source to furnish the energy required by the feed mechanism

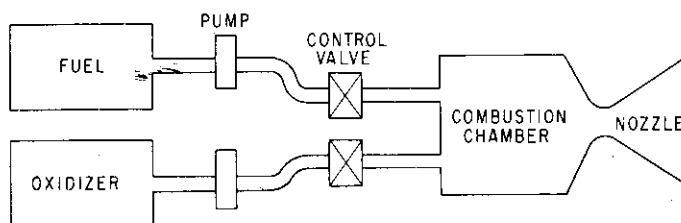


FIG. 13-11. Schema of a liquid-propellant rocket motor.

- d. A control device for regulating the propellant flow rates
- e. A chamber for combustion
- f. An expansion nozzle

A typical liquid system is schematically shown in Fig. 13-11.

One of the most attractive features of a liquid-propellant rocket motor is that the motor may be throttled, stopped, and restarted during missile flight. Hence it is relatively simple to program the thrust desired for a given mission. In addition, the specific impulse of liquid propellant is generally higher than that of a solid propellant. Gimballed nozzles and thrust chambers are practical on this type of motor for thrust-vector control. Another attribute of a liquid-propellant rocket motor is that regenerative cooling of the nozzle using its own fuel supply is feasible and practical. Liquid-propellant rocket motors also offer good (range) growth potential by increasing the volume of the fuel tanks.

Because of the more complex nature of a liquid-propellant rocket-motor system, it is inherently less reliable and generally more costly. Despite the higher values of fuel specific impulse, the additional weight due to auxiliary devices such as pumps, valves, and fuel lines may result in an over-all specific impulse equal to or less than that realized on

a solid-propellant rocket motor. Sloshing of the liquid fuel may create a dynamic problem unless suitable baffles or pressurization are provided. Finally, the fuel-handling problems including the toxic effects on personnel and the long count-down to get the missile to firing status may be highly undesirable for most missile weapon systems. This undesirable feature is presently ameliorated through the development of "prepackaged" liquid-propellant rocket motors² which eliminate the long count-down and can be stored in the "ready" state.

Presently, "prepackaged" liquid-propellant rocket motors have been restricted to total impulses in the neighborhood of 50,000 lb-sec and below. Additional development is necessary to prove their design feasibility for the higher total impulse required for long-range ballistic missiles. The "prepackaged" liquid-propellant rocket motor is relatively simple since it requires no pumps, valves, etc., which are required for other liquid-propellant units. A solid-charge propellant gas generator within the motor provides the pressurization which forces the liquid propellant into the combustion chamber.

2. Solid-propellant Rocket Motor. A typical solid-propellant rocket motor is schematically shown in Fig. 13-12. The principal components of this type of motor are:

- a. Propellant grain
- b. Chamber
- c. Nozzle
- d. Igniter

The grain configuration of internal burning varies greatly and is governed by the desired thrust-time history. In general, regressive burning (thrust decreases with time) is desired to keep the axial g of a missile to a minimum. However, many other factors are involved in the final selection of the thrust-time history or grain configuration. Some typical grain configurations used are shown in Fig. 13-13 for various thrust-time histories.

Solid propellants are composed of solid mixtures of an oxidizer and a combustible fuel. Presently, there are two general types of propellants: double-base and composite. Double-base propellants consist essentially of nitrocellulose colloided with nitroglycerin. The composite propellants consist principally of crystalline oxidizer (an inorganic salt such as potassium perchlorate, ammonium perchlorate, or ammonium nitrate) and a polymeric binder such as synthetic rubber,

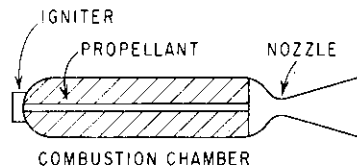


FIG. 13-12. Schema of a solid-propellant rocket motor.

plastic, or polystyrene. These propellants may be either mechanically extruded or cast into the proper grain geometry such as those shown in Fig. 13-13.

The art of designing solid-propellant units has been significantly advanced over the past decade, so that this type of rocket motor is now highly competitive with liquid-propellant units. Development in solid propellants together with technological advances in high-strength materials result in the attainment of very high values of fuel specific

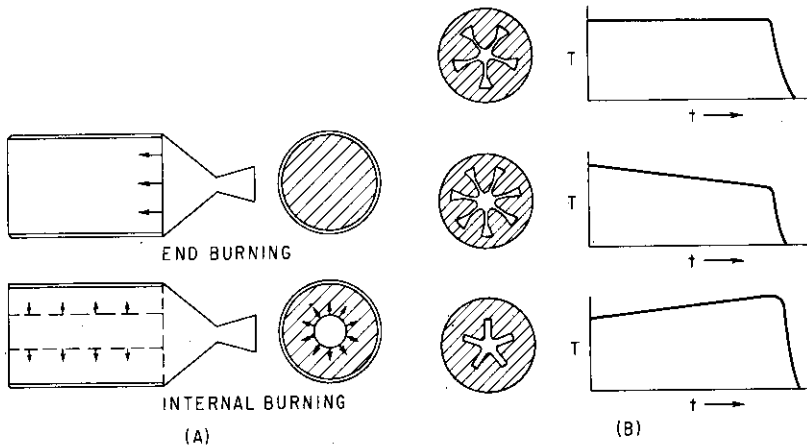


FIG. 13-13. Propellant grain configurations. (A) End- and internal-burning motors. (B) Various thrust histories.

impulse and motor mass fraction or over-all specific impulse. Furthermore, with the inherent simplicity due to the elimination of moving parts such as pumps and valves, solid-propellant rocket motors have been considered and used on practically all types of missiles. Logistics is another consideration which favors this type of rocket motor very heavily.

Recent development has indicated that thrust termination can be effected by nozzle blow-out or by blowing out ports in the forward section of the combustion chamber. By this means the chamber pressure can be reduced below that required for sustained burning and hence terminate the thrust. Careful design must be made in order that random reignition does not occur once burning is stopped. The accomplishment of thrust termination and vector control (jet vanes and jetavators) paves the way for application of this type of motor to ballistic missiles which require thrust cutoff for different range

missions. It has been shown (see Sec. 12-4) that an error in the burnout velocity has a large detrimental effect on the accuracy of the ballistic missile. Hence it is important that thrust termination of the propellant unit be accurately accomplished and with a good degree of repeatability from one motor to another.

Several undesirable features are present in the solid-propellant rocket motors. One of the most outstanding of these is that the unit cannot be throttled or restarted once it has been shut off. Another undesirable feature is that for certain types of solid propellants the temperature sensitivity may be very high. Since most missile weapon systems are designed to operate over a wide range of temperature conditions (usually from -65 to $+160^{\circ}\text{F}$), the propellant must withstand the stresses imposed by temperature changes without cracking. In addition, the rocket motor must ignite and fire successfully within these temperature limits. High temperature sensitivity leads to unduly high chamber pressure at elevated propellant-grain temperatures and hence results in heavier motor casing. In general, the low-temperature conditions result in the most critical operating condition wherein the propellant grain may crack and cause erratic burning or explosion. Consequently heating blankets are frequently used on units using propellants with undesirably high temperature sensitivity.

Another poor feature in the use of solid-propellant rocket motors is that they generally incur a relatively large shift in missile center-of-gravity location between the launch and burnout condition. This may be undesirable for those missiles which require high maneuverability after motor burnout. One such example may be a short-range air-to-air missile which uses a solid-propellant unit to accelerate to speed and then coasts the remainder of the way toward the target. Since a forward center-of-gravity movement increases the static stability margin of the missile, the maneuverability of the missile is decreased (see Sec. 6-4). The large center-of-gravity shift between launch and burnout condition may be minimized to some extent by locating the main part of the rocket motor as close to the missile center of gravity as possible. In such an arrangement, a blast tube connecting the main combustion chamber and nozzle is required and incurs both a weight penalty and loss in motor efficiency. In many cases, it may be necessary to attach the propulsion unit at the aft end of the missile. In these cases, the large center-of-gravity shift may dictate a configuration which is statically unstable at launch in order that sufficient maneuverability can be obtained for the burnout center-of-gravity condition.

In preliminary design, it is often desirable to lay out the approximate dimensions of the rocket motor in order to determine the over-all dimensions of the complete missile configuration. The pertinent data involved are the value of total impulse and thrust level required for the missile system.

a. *Determination of Propellant weight.* The propellant weight is determined by Eq. (13-13) or

$$W_p = \frac{I}{I_{sp}} \quad (13-13b)$$

The value of fuel specific impulse depends upon the type of solid propellant selected. The propellant chosen must be compatible with the following requirements: (1) desired value of I_{sp} , (2) burning rate, (3) temperature sensitivity, (4) operating pressure, and (5) cost and availability (see Table 13-1).

b. *Determination of Propellant Length.* For an end-burning (cigarette-type) grain design (see Fig. 13-13a), the length of the propellant may be calculated as follows:

$$l_e = \frac{4W_p}{\pi d^2 \rho} \quad (13-17)$$

where l_e = length of propellant for end-burning grain design

d = diameter of propellant (may be assumed to be diameter of missile if rocket motor is integral part of missile)

ρ = density of propellant (approximately 0.06 lb/cu in. for most propellants)

The volumetric loading, defined as the ratio of propellant volume to total combustion-chamber volume for this end-burning grain design, is one. For an internal-burning grain design such as that shown in Fig. 13-13a, the volumetric loading is less than unity. The exact value is a function of many variables, including chamber pressure, type of propellant, and velocity of gas flow past the propellant surface. For preliminary analysis the value of 0.85 appears to be reasonable. Hence the length of the propellant for the internal-burning grain design may be approximated as

$$l_i = \frac{l_e}{0.85} \quad (13-17a)$$

where l_i = length of propellant for an internal-burning grain design

The variation of propellant length with propellant weight for various missile diameters is shown in Fig. 13-14.

c. *Determination of Nozzle Length.* The length of the nozzle is a function of several variables including thrust level, chamber pressure, and design operating altitude (or expansion ratio). As a first crude approximation, the length of the nozzle may be assumed to be between 30 and 35 per cent of the propellant length. For a more accurate

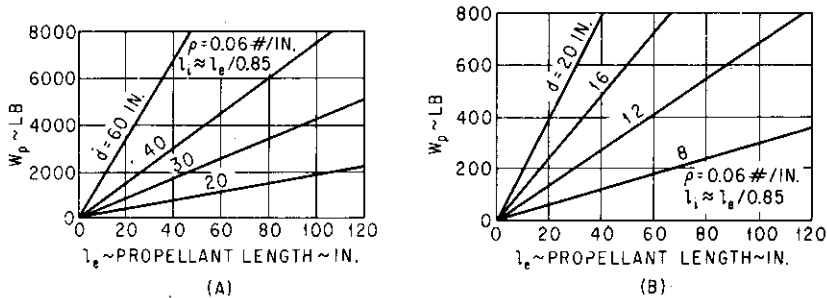


FIG. 13-14. Variation of propellant length with propellant weight. (A) Large motors. (B) Small motors.

approximation, the length of the nozzle may be determined analytically. To determine the nozzle length analytically, certain assumptions must be made. These are:

1. Chamber pressure p_c
2. Specific-heat ratio of the propellant γ
3. Exit pressure of the nozzle p_e
4. Half convergence angle β
5. Half divergence angle α

If the type of propellant is not specified in the preliminary design study, a low operating pressure should be chosen in order to minimize the weight of the thrust chamber. On the other hand, if too low a pressure is assumed, the fuel specific impulse may be unduly compromised. For motor casings which must carry large external loadings (such as those from aerodynamic wing or tail surfaces) the thickness of these motor casings will be governed by the external loading conditions. In such cases a high chamber pressure should be used in order to realize higher values of fuel specific impulse. The specific-heat ratio γ varies from propellant to propellant depending upon composition. However, the value of γ varies from 1.10 to 1.25 for most propellants. For optimum efficiency, the nozzle exit pressure p_e is assumed to be equal to the ambient pressure p_o at the design altitude.

LIQUID

Fuel	Oxidizer	Best oxidizer fuel mixture ratio (by weight)	Theoretical combustion temperature deg. F	Ratio of specific heats	Average molecular weight of combustion products	Bulk density at 80° F propellant combination temperature g/cm ³	Specific impulse at 400 psia (sea-level expansion, sec)
Ammonia	Chlorine trifluoride	3	4980	1.32	22	1.26	238
Ammonia	Fluorine	3	7270	1.33	19	1.16	300
Ammonia	Fluorine (50%) and nitrogen trifluoride (50%)	2.8	6540	1.32	19	1.15	290
Ammonia	ON 7030 ⁵	2.1	4900	1.23	21	1.03	
Ammonia	Oxygen	1.3	4940	1.23	19	0.88	255
Ammonia	RFNA (22% NO ₂)	2.15	4220	1.24	21	1.12	230
Butyl mercaptan	Nitric acid (95%)	4	4780	1.22	27	1.28	220
Diborane	Fluorine	5	7880	1.3	21	1.07	270
Diethylenetriamine	Oxygen	1.5	6500	1.24	21	1.06	245
Diethylenetriamine and hydrazine	Oxygen	2.5	6000	1.22	22		245
Diethylenetriamine (80%) and methylamine (20%)	RFNA (22% NO ₂)	3	5250	1.23	24	1.33	240
Ethyl alcohol (92.5%, obsolescent)	Oxygen	1.5	5400	1.21	23	0.98	232
Ethyl alcohol (75%) and water (obsolescent)	Oxygen	1.3	5150	1.22	23	0.99	225
Ethylene diamine	Oxygen	1.4	6000	1.23	19	1.04	250
Ethylene oxide	ON 7030 ⁵	2	5730	1.24	24	1.14	
Ethylene oxide	Oxygen	1.1	5750	1.24	22	0.99	215
Hydrazine (anhydrous)	Chlorine trifluoride	2.5	6000	1.33	23	1.46	255
Hydrazine (anhydrous)	Fluorine	2	7740	1.33	19	1.3	290
Hydrazine (anhydrous)	H ₂ O ₂ (90%)	1.5	4170	1.25	18	1.2	245
Hydrazine (anhydrous)	H ₂ O ₂ (99.6%)	1.7	4690	1.22	19	1.24	255
Hydrazine (anhydrous)	Nitrogen tetroxide	1.1	4950	1.26	19	1.2	250
Hydrazine (anhydrous)	Oxygen	0.75	5370	1.25	18	1.06	265
Hydrazine (anhydrous)	Oxygen difluoride	1.1	6380	1.28	18	1.28	280
Hydrazine (anhydrous)	RFNA (15% NO ₂)	1.3	4980	1.25	20	1.26	247
Hydrazine (anhydrous)	Tetrahydrofuran	1.4	5250	1.27	20	1.29	228
Hydrogen (max 1 sp)	Fluorine	0.42 ⁷	8100	1.31	10	0.46	380
		3.8	4600	1.30	7.8	0.27	390
Hydrogen (max 1 sp) ⁸	Oxygen	8 ⁷	5870	1.22	16	0.43	360
		3.5	4500	1.26	9	0.26	348
JP-4	Fluorine	2.9	7100	1.22	24	1.19	275
JP-4	H ₂ O ₂ (99.6%)	6.5	4830	1.2	22	1.28	238
JP-4 (C/H = 6.85)	Oxygen	2.2	5880	1.24	22	0.9 ⁹	240
JP-4 (C/H = 6)	Oxygen	2.3	5770	1.24	22	0.98	247
JP-4	Oxygen (70%) and ozone (30%)	2.3	5950	1.24	22	1.04	252
JP-4	Oxygen (30%) and ozone (70%)	2.3	6180	1.25	21	1.08	257
JP-4	(zone)	2.4	6380	1.25	21	1.14	260
JP-4	RFNA (22% NO ₂)	4.1	5150	1.23	25	1.3	228
Kerosene	H ₂ O ₂ (54%), ammonium nitrate (40%), and H ₂ O (6%)	9	4270	1.21	22	1.34	228
Kerosene	Oxygen	2.2-2.5	5200	1.24	22	0.99	240
Methyl acetylene	Oxygen	2	6180	1.27	22	0.93	237
Methylamine	Oxygen	1.6	5460	1.22	20	0.91	248

* Reproduced by permission from Conover-Mast Publications, Inc., © April, 1959.

ROCKET PROPELLANTS

PROPELLANTS

Cost per lb		Ideal use	Handling hazard ¹		Coolant qualities		Best container material ²		Storability ³	
Fuel	Oxidizer		Fuel	Oxidizer	Fuel	Oxidizer	Fuel	Oxidizer	Fuel	Oxidizer
\$0.04	\$3.50	Small, high-performance research rockets Superperformance vehicle Superperformance vehicle	Some	Dangerous	Fair to poor	Unknown	All	Mild S, SS 347	Fair to poor	Fair to poor
0.04	6.00 ⁴		Some	Dangerous	Fair to poor	Very poor	All	Al, SS 347	Fair to poor	Fair to poor
0.04			Some	Dangerous	Fair to poor	Unknown	All	Al, SS 347	Fair to poor	Fair to poor
0.04			Some		Fair to poor		All		Fair to poor	
0.04	0.05		Rocket aircraft, small missile	Some	Some	Fair to poor		All	Al, mild S, SS 347	Fair to poor
0.04	0.11	IRBM, rocket aircraft	Some	Dangerous	Fair to poor	Good	All	Al, SS 347	Fair to poor	Good
\$0.20	\$0.10		Some	Dangerous	Unknown	Good	SS 347	Al, SS 347	Good	Good
	\$6.00 ⁴	Long-range medium-size rocket Large nonproduction missile Short-range liquid rockets Gas generator	Dangerous		Fair to poor	Very poor	All	Al, SS 347	Good	Fair to poor
0.18	0.05		None	Some	Good	Very poor ⁵	All	Al, mild S, SS 347	Good	Fair to poor
0.18	0.11		None	Some	Good	Very poor	All	Al, mild S	Good	Fair to poor
		Gas generator	None	Dangerous	Good	Good	All	Al, SS 347	Good	Good
\$0.15	\$0.05	Rocket aircraft, general-purpose High-altitude rocket (Viking) Superperformance vehicle	None	Some	Good	Very poor ⁵	All	Al, mild S, SS 347	Good	Fair to poor
0.12	0.05		None	Some	Good		All	Al, mild S, SS 347	Good	Fair to poor
0.25	0.05		Unknown	Some	Good	Very poor	All	Al, mild S, SS 347	Good	Fair to poor
0.20			Some		Good		All		Fair to poor	
0.20	0.05		Auxiliary power generators	Some	Some	Good	Very poor ⁵	All	Al, mild S, SS 347	Good
\$2.00	\$0.50	High-performance vehicle Superperformance vehicle (satellite) Rocket aircraft Rocket aircraft Small vehicle (A-A) Small vehicle (A-A) Small vehicle (A-A) Air-ground rockets Rocket aircraft Superperformance vehicle (space flight) Superperformance vehicle (space flight) Superperformance vehicles Superperformance vehicles	Some	Dangerous	Good	Unknown	All	Mild S, SS 347	Good	Fair to poor
2.00	6.00 ⁴		Some	Dangerous	Good	Very poor	All	Al, mild S, SS 347	Good	Fair to poor
2.00	0.55		Some	Some	Good	Good	All	Al, SS 347	Good	Good
2.00	1.20		Some	Some	Good	Good	All	Al, SS 347	Good	Fair to poor
2.00	0.08		Some	Dangerous	Good	Unknown	All	SS 347	Good	Fair to poor
2.20	0.05		Some	Some	Good	Very poor ⁵	All	Al, mild S, SS 347	Good	Fair to poor
2.00			Some	Dangerous	Good	Unknown	All	Al, mild S, SS 347	Good	Fair to poor
2.00	0.10		Some	Dangerous	Good	Good	All	Al, SS 347	Good	Good
2.20	0.30		Some	Some	Good	Good	All	all	Good	Good
7.00	6.00		Dangerous	Dangerous	Good	Very poor	All	Al, SS 347	Fair to poor	Fair to poor
7.00	6.00		Dangerous	Dangerous	Good	Very poor	Al, mild S, SS 347	Al, SS 347	Fair to poor	Fair to poor
7.00	0.05		Dangerous	Some	Good	Very poor	Al, mild S, SS 347	Al, mild S, SS 347	Fair to poor	Fair to poor
7.00	0.05		Dangerous	Some	Good	Very poor	Al, mild S, SS 347	Al, mild S, SS 347	Fair to poor	Fair to poor
\$0.015	\$0.00 ⁴	Superperformance vehicle	None	Dangerous	Good	Very poor	All	Al, SS 347	Good	Fair to poor
0.015	1.20	Gas generator	Some	Some	Good	Good	All	Al, SS 347	Good	Fair to poor
0.015	0.05	IRBM	None	Some	Good	Very poor ⁵	All	Al, mild S, SS 347	Good	Fair to poor
0.015	0.05	IRBM	None	Some	Good	Very poor ⁵	All	Al, mild S, SS 347	Good	Fair to poor
0.015		Superperformance vehicle	None	Some	Good	Very poor	All	Al, SS 347	Good	Fair to poor
0.015		Superperformance vehicle	None	Dangerous	Good	Very poor	All	Al, SS 347	Good	Fair to poor
0.015		Superperformance vehicle	None	Dangerous	Good	Very poor	All	Al, SS 347	Good	Fair to poor
0.015	0.11	Small missile (A-A)		Dangerous	Good	Good	All	Al, SS 347	Good	Good
\$0.015	\$0.75	Rocket aircraft	None	Some	Good	Good	All	All	Good	Good
0.013	0.05	IRBM, ICBM	None	Some	Good	Very poor	All	Al, SS 347	Good	Fair to poor
\$0.17	\$0.05	Liquid JATO	Some	Some	Unknown	Very poor	Al, mild S, SS 347	Al, mild S, SS 347	Fair to poor	Fair to poor
0.35	0.05	Gas generator	None	Some	Unknown	Very poor	All	Al, mild S, SS 347	Good	Fair to poor

LIQUID							
Fuel	Oxidizer	Best oxidizer fuel mixture ratio (by weight)	Theoretical combustion temperature deg. F	Ratio of specific heats	Average molecular weight of combustion products	Bulk density at 80° F propellant combination temperature g/cm ³	Specific impulse at 400 psia (sea level expansion, sec)
n-Octane	Oxygen	2.4	5790	1.23	22	0.96	250
n-Octane	Oxygen difluoride	3.8	7340	1.33	20	1.22	Unknown
n-Octane	RFNA (6.5% NO ₂)	4.5	5100	1.24	24	1.26	226
Nitroethane	Oxygen	0.65	5570	1.23	23	1.09	215
Nitropropane	Oxygen	0.9	5620	1.23	23	1.06	210
Polyethylene	RFNA (22% NO ₂)	4.5	5320	1.22	25	1.4	Unknown
Propylene oxide	Oxygen	1.6	5900	1.23	23	1	230
Propylene oxide (69.5% and ethylene oxide (30.5%))	Oxygen	1.5	5900	1.23	23	1	Unknown
Triethylamine (63%) and orthotolidine (37%) ⁹	ON 7030 ⁸	3.7	5800	1.24	25	1.19	
Triethyl-trithiophosphate ⁹	ON 7030 ⁸	2.5	6000	1.23	30	1.28	
Triethyl-trithiophosphate ⁹	RFNA (22% NO ₂)	3	5520	1.21	30	1.43	230
Turpentine ⁹	Nitric acid	4.4	4050	1.22	25	1.32	244
Turpentine ⁹	Oxygen	2.4	5880	1.23	22	1.04	240
Turpentine ⁹	RFNA (22% NO ₂)	4.2	5400	1.22	26	1.36	241
Unsymmetrical dimethyl hydrazine	Oxygen	1.4	5650	1.24	20	0.96	249
Unsymmetrical dimethyl hydrazine	RFNA (22% NO ₂) ¹⁰	2.6	5200	1.23	22	1.23	241
Unsymmetrical dimethyl hydrazine	WFNA ¹¹	2.7	5100	1.23	22	1.22	240

SOLID

Fuel and oxidizer ¹²	Type	Pressure range, psi	Low-pressure limit, psi	Specific impulse at 300 psi, sec	Burning-rate exponent	Burning rate, ips	Ignition sensitivity
Amino ethanes ¹³	Composite	300-2000	80	200		0.3-0.6	Medium
Ballistite ¹³	Double-base	1000-3000	200	200	0.85		Low
Black powder ¹³	Composite	100-1000	15	70	0.5-0.8	0.1-0.5	Low
Buna and sulfo rubbers ¹³	Composite	100-800	30	210		0.4	Very low
Cordite ¹³	Double-base	1000-3000	300	180	0.77		Low
GALCIT 161 ¹³	Composite	1300-3700	700	190	0.75	1.4-1.5	High
Hydrogen peroxide and polyethylene	Liquid-solid	100-300	75	160			Very low
Lox-rubber	Liquid-solid	100-500	15	225			
NDRC EJA ¹³	Composite	600-1000		180	0.45	0.2-1	Low
Polymethane ¹³	Composite	500-2000		215			Low
WASAG DEGN	Homogeneous	700-4000	700	180	0.73	0.2-0.8	Medium
Polyurethane ¹⁴	Composite						Low

¹ "Some" hazard means slightly toxic and corrosive;

"dangerous" hazard means toxic, corrosive, and explosive;

² "Al" means aluminum alloys; "all", all normal metals and plastics; "mild S", mild steels; "SS", stainless steels.

³ "Good" storability means liquid can be stored in ordinary vessels or tanks over long periods and at many temperatures without decomposition or change of state.

⁴ Liquid.

⁵ Nitrogen tetroxide (70 per cent) and nitric oxide (30 per cent).

⁶ Except at high coolant pressure.

⁷ Mixture ratio yielding the highest loading density, or mass ratio.

⁸ The combination of hydrogen and oxygen is rapidly becoming a favorite and will be widely used in the future. The hydrogen is used as the engine coolant.

⁹ Little used; mostly of academic interest.

¹⁰ Hydrogen fluoride is often added to reduce the corrosive effect of nitric acid.

¹¹ A little worse than RFNA.

¹² Ammonium nitrate, ammonium perchlorate, and potassium nitrate are oxidizers used with such fuels as Thiokol and the sulfo rubbers.

¹³ Various light metal powders are added to some of the composite and double-base propellants to increase the specific impulse.

¹⁴ A favorite for long-range vehicles.

ROCKET PROPELLANTS (Continued)

PROPELLANTS

Cost per lb		Ideal use	Handling hazard ¹		Coolant qualities		Best container material ²		Storability ³	
Fuel	Oxidizer		Fuel	Oxidizer	Fuel	Oxidizer	Fuel	Oxidizer	Fuel	Oxidizer
\$0.07	\$0.05	Precision rocket chamber	None	Some	Good	Very poor	All	Al, mild S, SS 347	Good	Fair to poor
0.07			None	Dangerous	Good	Unknown	All	Al, SS 347	Good	Fair to poor
0.07		0.08	Precision research rocket testing	None	Dangerous	Good	Good	All	Al, SS 347	Good
1.00	0.05	Auxiliary power pack	Dangerous	Some	Unknown	Very poor	All	Al, mild S, SS 347	Fair to poor	Fair to poor
	0.05		Dangerous	Some	Unknown	Very poor	All	Al, mild S, SS 347	Fair to poor	Fair to poor
\$0.10	\$0.11		None	Dangerous	Unknown	Good	All	Al, SS 347	Fair to poor	Good
	0.05		Some	Some	Unknown	Very poor	All	Al, mild S, SS 347	Fair to poor	Fair to poor
\$1.50		Starting liquid for large engines Small storable rockets Gas generator, auxiliary power unit	None		Good		All		Good	
3.80			Some		Unknown		Mild S, SS 347		Good	
3.80	\$0.11		Some	Dangerous	Unknown	Good	Mild S, SS 347	Al, SS 347	Good	Good
0.11	0.12		None	Dangerous	Fair to poor	Good	All	Al, SS 347	Good	Good
0.10	0.05		None	Some	Fair to poor	Very poor	All	Al, mild S, SS 347	Good	Fair to poor
0.10	0.11		None	Dangerous	Fair to poor	Good	All	Al, SS 347	Good	Good
\$1.50	\$0.05		ICBM, IRBM	Some	Some	Good	Very poor ⁴	All	Al, mild S, SS 347	Good
1.50	0.11	Rocket aircraft, small missiles	Some	Dangerous	Good	Good	All	Al, SS 347	Good	Good
1.50	0.15		Some	Dangerous	Good	Good	All	Al, SS 347 and 410	Good	Good

PROPELLANTS

Pressure sensitivity to temperature, %/°F	Weight, lb/cu ft	Storability	Ideal use	Cost per lb	Hygroscopicity	Exhaust
0.5-1.3	90 (approx) 75-105 75-130 70 (approx)	Good Fair Good Medium	Very large booster Small ordnance Igniters Medium-size high-performance units (when case-banded) Ordnance JATO Start-stop or throttling solids	\$5-\$10 0.60-1.00	Negligible Low Low Low	High flash, black smoke Gray smoke
0.7 0.23	110	Fair Very good Very good (for polyethylene)	JATO Super boosters High-performance boosters	0.75-1.00	Negligible Negligible	High flash, black smoke White smoke Almost invisible
0.2-0.3		Good Good Good Very good	JATO Super boosters High-performance boosters High-performance boosters	2.00-5.00	Very low Low Low	Smokeless Gray smoke High flash, black smoke

Additives

	Application	Remarks
Ammonium nitrate	Depresses freezing point of nitric acid	Difficult to mix with acid in small amounts
Hydrogen fluoride	Inhibits corrosive effect of RFNA and WFNA	Action not well understood; believed to react with Al in tanks and chamber
Aluminum	Increases specific impulse or combustion temperature of solid propellants	Affects exhaust products; coats exhaust nozzle
Silicon monoxide	With hydrocarbon fuels (in very small amounts)	Deposits out a protective film on thrust chamber wall; may reduce burn-through
Diboranes and boron hydrides	With kerosene and JP fuels for turbojets; not yet ready for rockets	Raises combustion temperature (and so impulse) considerably; usually added in afterburner

Monopropellants

	Specific impulse at 300 psia, sec	Application	Remarks
Hydrogen peroxide (95-98%)	150	Gas generator for pumps; auxiliary for rocket-vehicle control	Difficult handling; needs pure Al or SS 347; clean
Nitro-methane	180	Small, simple ordnance rockets	Dangerous handling (can detonate unexpectedly)
Hydrazine	195-220 (?)	Gas generator; small rocket	Difficult handling; poisonous fumes; can break up at high temperature
Methyl acetylene	160	Gas generator; small rocket	Safe handling; dangerous and very smoky exhaust fumes

With the assumptions on the operating pressure, propellant specific-heat ratio, and exit pressure made, the thrust coefficient C_T can be calculated by Eq. (13-11). Hence

$$C_T = \sqrt{\frac{2\gamma^2}{\gamma-1} \left(\frac{2}{\gamma+1}\right)^{(\gamma+1)/\gamma-1} \left[1 - \left(\frac{p_e}{p_c}\right)^{(\gamma-1)/\gamma}\right]} \quad (13-18)$$

With C_T known, the nozzle throat area A_t can be readily determined from Eq. (13-10). In actual practice, Eq. (13-10), which is applicable for an ideal condition, must be modified by the nozzle divergence

coefficient λ [Eq. (13-8)], nozzle discharge coefficient C_d , and nozzle velocity coefficient φ . For a well-designed nozzle, the value of C_d and φ approaches unity. Hence

$$A_t = \frac{T}{C_T p_c C_d \varphi} \quad (13-19)$$

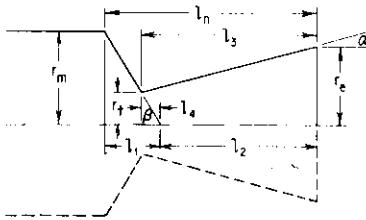


FIG. 13-15. Nozzle geometry.

Since it is assumed that the nozzle will be designed for full expansion (i.e., $p_e = p_o$), the nozzle exit area A_e may be determined from Eq. (13-12) or Fig. 13-10. Finally, the length of the nozzle may be calculated by assuming the value of the half convergence and divergence angle. From Fig. 13-15, the length of the nozzle l_n can be derived as follows:

$$l_n = l_1 + l_2 \quad (13-20)$$

where

$$l_1 = r_m \cot \beta \quad (13-20a)$$

$$l_2 = l_3 - l_4 \\ = (r_e - r_t) \cot \alpha - r_t \cot \beta \quad (13-20b)$$

Hence

$$l_n = (r_m - r_t) \cot \beta + (r_e - r_t) \cot \alpha \quad (13-20c)$$

d. Determination of Rocket-motor Weight. Without going into a detailed stress analysis of the combustion chamber and nozzle, the weight of the total (loaded) rocket motor may be estimated by assuming a value for either the over-all specific impulse I_o or rocket-motor mass ratio ζ . The latter is defined as

$$\zeta = \frac{W_p}{W_m} \quad (13-21)$$

From Eqs. (13-13), (13-14), and (13-15), Eq. (13-21) may be written as

$$\zeta = \frac{I_o}{I_{sp}} \quad (13-21a)$$

The value of ζ varies from approximately 0.75 for small motors with high operating pressure (i.e., 1,000 psi and above) and large external loads to 0.90 for the larger units used on long-range ballistic missiles. For the latter applications, the operating pressure is generally relatively low (i.e., between 300 to 600 psi). Furthermore, because of the near zero lift trajectory (i.e., gravity turn), the aerodynamic loading for long-range ballistic missiles is kept to a minimum. Hence, with the assumed value of ζ , the total rocket-motor weight may be determined from Eq. (13-21).

SYMBOLS

A_e	exit area of nozzle
A_t	throat area of nozzle
A_x	axial or x component of the wall area of the nozzle
C^*	characteristic velocity
C_d	nozzle discharge coefficient
C_T	thrust coefficient
I	rocket-motor impulse
I_o	over-all specific impulse
I_{sp}	fuel specific impulse
M_x	momentum flux in the axial direction
P_s	stagnation pressure
T	thrust
T_s	stagnation temperature
V_j	exit velocity of the exhaust gas
W_m	total rocket-motor weight
W_p	weight of propellant
l_e	length of propellant for an end-burning grain design
l_i	length of propellant for an internal-burning grain design
l_n	nozzle length
l_1, l_2, l_3, l_4	nozzle dimensions (see Fig. 13-15)
p	pressure forces
p_c	chamber pressure
p_i	pressure forces acting upon the inner surfaces of the rocket
p_o	pressure forces acting upon the outer surfaces of the rocket
r_m	radius of rocket motor
r_t	radius of nozzle throat
α	half divergence angle of nozzle
β	half convergence angle of nozzle
γ	specific-heat ratio of propellant

ζ	rocket-motor mass ratio
λ	divergence coefficient
ρ	propellant density
φ	nozzle velocity coefficient

REFERENCES

1. Malina, F. J.: Characteristics of Rocket Motor Unit Based on Theory of Perfect Gases, *J. Franklin Inst.*, vol. 230, no. 4, October, 1940.
2. Kaprielyan, S. P., and J. P. Kushnerick: Liquid-prepack Engines, *Aircraft and Missiles*, vol. 2, no. 11, pp. 6-10, November, 1959.
3. Wimpres, R. N.: "Internal Ballistics of Solid Fuel Rockets," McGraw-Hill Book Company, Inc., New York, 1950.
4. Bonney, A. E., M. J. Zucrow, and C. W. Besserer: "Aerodynamics Propulsion—Structures and Design Practice," D. Van Nostrand Company, Inc., Princeton, N.J., 1956.
5. Sutton, G. P.: "Rocket Propulsion Elements," John Wiley & Sons, Inc., New York, 1956.
6. Zucrow, M. J.: "Principles of Jet Propulsion and Gas Turbines," John Wiley & Sons, Inc., New York, 1948.
7. Geckler, R. D., and R. E. Davis: Modern Developments in Solid-propellant Rocket Engineering, *Aeronaut. Eng. Rev.*, vol. 16, no. 8, August, 1957.
8. Marsel, C. J.: Rocket Propulsion, *Astronautics*, vol. 4, no. 4 (pt. 2 of 2 parts), pp. 7-11, April, 1959.
9. Warren, F. A.: "Rocket Propellants," Reinhold Publishing Corporation, New York, 1958.
10. Geckler, R. D.: "The Mechanism of Combustion of Solid Propellants," p. 289, Selected Combustion Problems, AGARD, 1954.
11. Vandenkerekhove, J. A.: Recent Advances in Solid Propellant Grain Design, *ARS J.*, vol. 29, no. 7, pp. 483-491, July, 1959.
12. Shafer, J. I.: "Solid Rocket Propulsion," John Wiley & Sons, Inc., New York, 1959.
13. Newman, R. S.: The Dual-thrust Solid Propellant Rocket Engine, *Astronautics*, vol. 3, no. 3, March, 1958.
14. Stone, M. W.: A Practical Mathematical Approach to Grain Design, *Jet Propulsion*, vol. 28, no. 4, pp. 236-244, April, 1958.
15. Mayer, E.: Vaporization Rate Limited Combustion in Bipropellant Rocket Motors, *ARS J.*, vol. 29, no. 7, pp. 505-513, July, 1959.
16. Gerstein, Melvin: Correlation and Prediction of Flame Properties with Special Reference to Liquid Hydrazine, *ARS J.*, vol. 29, no. 7, pp. 514-516, July, 1959.
17. Dugger, G. L.: Recent Advances in Ramjet Combustion, *ARS J.*, vol. 29, no. 11, pp. 819-827, November, 1959.

CHAPTER 14

STRUCTURAL-DESIGN CONSIDERATIONS

14-1. INTRODUCTION

In most preliminary missile configuration designs, detailed structural-design analysis is not made. This arises primarily from the fact that the exact magnitude of the air loads and inertia loads is not available. However, the designer should bear in mind that a simple efficient external configuration can also lead to a more efficient and lighter structural configuration. In addition, the designer should be aware of the fact that structural weight can have a pronounced and detrimental effect on the performance of the missile system. For example, in the case of a long-range ballistic missile, each additional pound of "excess" inert weight requires an addition of as much as 100 lb of propellant weight to achieve a given design range. Or, as another aspect of this, an increase of 1 lb of inert weight decreases the range of the missile by several miles. Hence proper emphasis must be placed on the structural design aspects during the early design phase of a given missile weapon system. With proper structural design practices, the resultant missile configuration and hence the over-all missile weapon system will be lighter in weight, easier to manufacture, and hence generally lower in per unit cost.

The primary function of the structural-design engineer is manifold: (1) to provide structural adequacy of the missile airframe under its operating environment, (2) to investigate the most suitable materials to meet the loadings and their associated operating environmental conditions in the missile weapon system, and (3) to analyze and select the most optimum type of construction for the type of configuration from the standpoint of ease of manufacturing, cost per unit, and interchangeability of parts, which is a stringent requirement for certain missile systems. The purpose of this chapter is to present some of the more important structural-design considerations involved in the design of missile configurations.

14-2. FUNDAMENTAL STRUCTURAL CONCEPTS

Before a detailed discussion on design loads and structural analysis is presented, a brief summary of some of the fundamental structural concepts is given in the subsequent paragraphs.

1. Dynamic Equilibrium. Newton's third law of motion states that for every action there is an equal and opposite reaction. In the case of a body of a missile which is accelerated in the direction of an external load or force, the reaction in the opposite direction consists of the inertia force of the body. The application of the inertia forces to oppose the external resultant force is known as D'Alembert's principle. This principle states that "the impressed forces acting on any body are in dynamic equilibrium with the inertial forces of the particles of the body." Since a body must be placed in equilibrium before the internal shears and bending moments can be determined, it follows that accelerating bodies must be placed in equilibrium by applying the necessary inertia forces in accordance with D'Alembert's principle. The following paragraphs outline the procedure for determining the magnitude of the forces. Note that the inertia-load factors always act in a direction opposite to that of the acceleration which produces them.

2. Linear Acceleration Due to Translation. When the missile is flying in its trimmed condition (i.e., condition *B* as described in Sec. 10-2, Fig. 10-2), it experiences a linear acceleration as the result of pure translational motion. The magnitude of the force normal to the missile longitudinal axis is determined by

$$F = N = C_{N_{TR}} q S_{\pi} \quad (14-1)$$

where $C_{N_{TR}}$ is the trimmed normal-force coefficient as defined in Sec. 5-5 (Fig. 5-6). In dealing with the inertia of a missile, it is more convenient to express the magnitude of the forces (those due to external aerodynamic loading and inertia loading) in terms of gravitational units rather than in terms of mass and acceleration. Hence, from Newton's equation, $F = ma$ or $(W/g)a$, the magnitude of F is expressed as

$$F = nW \quad (14-1a)$$

where n is equal to a/g and is the load factor expressed in g 's, and F is the force expressed in gravitational units. For example, a force of 1,000 lb acting on a 500-lb missile results in a magnitude of F of 2 g 's.

3. Linear Component of Angular Acceleration. In addition to the linear acceleration due to pure translational motion, the missile experiences an angular acceleration as the result of any unbalanced external aerodynamic loads. These angular accelerations may be considered as transient conditions such as those discussed in Chap. 10 (i.e., condition *A*, *C*, *D*, and *E* described in Sec. 10-2). The magnitude of these angular accelerations may be determined as

$$\ddot{\theta} = \frac{M}{I} \quad (14-2)$$

where $\ddot{\theta}$ = angular acceleration, radians/sec

M = external rotational moment due to external unbalanced forces, ft-lb

I = moment of inertia of the missile, slug-ft²

The magnitude of the moment may be determined from the aerodynamic derivatives or plots of moment coefficient vs. angle of attack for various control-surface deflections (i.e., Figs. 10-2 and 10-3). Hence

$$M = (C_{m_\alpha} \alpha + C_{m_\delta} \delta) q S_\pi d \quad (14-3)$$

or
$$M = C_m q S_\pi d \quad (14-3a)$$

The magnitude of the moment of inertia of the missile may be calculated by summing the moment of inertia of the various component parts about their respective centers of gravity and then transferring to the missile center-of-gravity location. Mathematically, it can be expressed as

$$I = \Sigma \left(I_0 + \frac{W}{g} x^2 \right) \quad (14-4)$$

where I_0 = moment of inertia of a given mass about its own center of gravity

x = distance from missile center of gravity to any mass W/g

The linear component of angular acceleration Δn is expressed as

$$\Delta n = \frac{\ddot{\theta} l}{g} \quad (14-5)$$

where l is any distance from the center of gravity of the missile (positive when measured forward of the center of gravity). From Eq. (14-5) it is apparent that the incremental load factor due to angular acceleration varies linearly with distance from the missile center of gravity as

illustrated in Fig. 14-1. Hence the total linear acceleration of the missile is the sum of the linear acceleration due to pure translation and the linear component due to angular acceleration and can be expressed as

$$(n_z)_{total} = \frac{F}{W} \pm \frac{\ddot{\theta}l}{g} \quad (14-6)$$

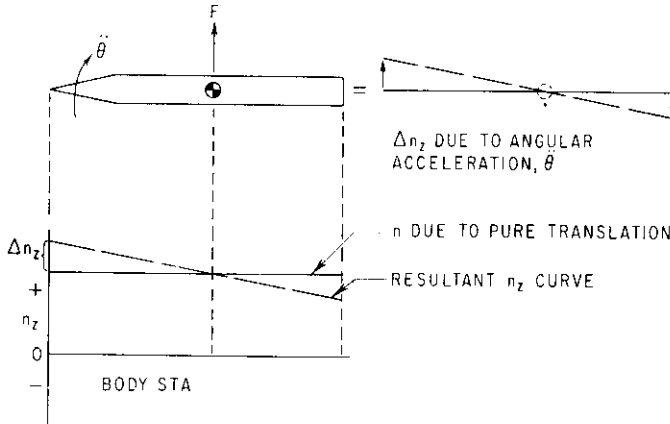


FIG. 14-1. Linear components of acceleration.

4. Missile-loading Concept. In order to facilitate the determination of critical structural-loading conditions on the body of the missile, the simple beam analogy is used. In this technique, the body of the missile is replaced by a simple beam supported at the center-of-gravity location of the missile as shown in Fig. 14-2. The external load distribution on the body is next superimposed on the beam. For simplicity, the wing and tail loadings are replaced by concentrated loads at their respective centers of pressure. For the purpose of illustration (see Fig. 14-2), the missile is assumed to be in trimmed level flight ($1g$) condition. Hence the summation of moments about the center of gravity or beam support due to the external loads acting on the missile is equal to zero. Since there is no unbalanced external moment, the missile undergoes no angular acceleration. Hence the resultant force is acting at the missile center of gravity against the acceleration of gravity. It is also assumed that the internal body weight distribution takes the simple form shown in Fig. 14-2.

With both external and internal loadings known, the missile is placed in dynamic equilibrium by opposing the external upward-acting

force (of lg) by lg of missile dead weight or inertia force acting downward. A shear diagram is then constructed by simply summing the external and inertia loads on the missile starting from the nose aft and from the aft end of the missile forward to the missile center of gravity as shown in Fig. 14-2. Finally, the moment diagram is made by taking the summation of the moment of the shear forces about the missile

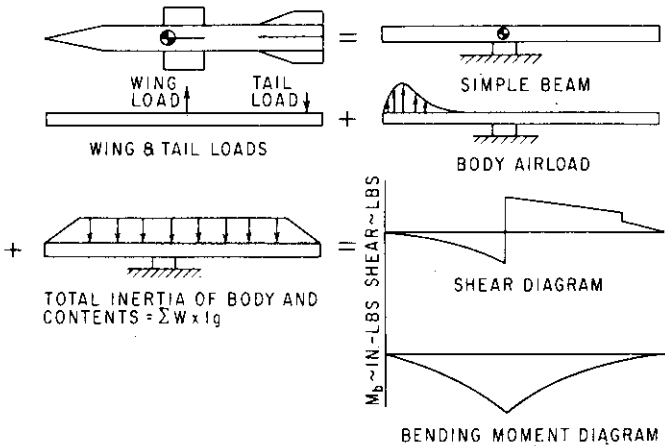


FIG. 14-2. Missile-loading concept.

center of gravity. Mathematically, the shear and moment may be expressed as

$$S = \int w dx \quad \text{and} \quad M_b = \int S dx = \int \int w dx dx$$

where S = shear force

M_b = bending moment

w = running load as illustrated in Fig. 14-3

x = any station along beam or body of missile

From the moment diagram, the change in bending moment between any two stations may be readily determined.

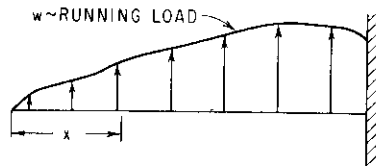


FIG. 14-3. General loading for the determination of shear and moment diagrams.

14-3. DESIGN LOADS

There are many types of external and internal loads imposed on the

missile structures and components. In general, these loads may be divided into two classes: flight loads and ground loads. In practical design, critical structural-design conditions arise from both classes of load. Hence the designer must consider these loadings with equal care.

1. Flight Loads. The flight loads may be subdivided into two categories: free-flight loads and captive-flight loads. Free-flight loads arise primarily from aerodynamic and thermal forces and internal pressure forces such as those present in a rocket motor or propulsion system. Captive-flight loads arise primarily from the aerodynamic loads induced on the missile during its carried condition by the parent aircraft. The missile structure must be adequate to withstand the most critical loadings imposed during flight on each component of the missile. The air loads on the missile for various conditions of flight may be determined by the methods outlined in Chap. 10. These air loads when combined with the missile inertia forces result in the net structural loads on the missile as discussed in Sec. 14-2.

2. Ground Loads. The basic ground loads consist of those which the missile experiences during transportation and preparation for launching. Many data have been gathered over the past several years on the environmental conditions of all modes of transportation.^{1,2*} These environmental loads, which are generally expressed in terms of amplitude and frequency (i.e., 30 *g*'s at 150 cps), may have a detrimental effect on the missile, particularly on its internal electronic components. Hence proper design such as shock mounting must be incorporated to minimize the effects of these environmental loads. In addition, proper design must be incorporated in missile shipping containers to withstand the loads encountered during transportation and ground handling.

The ground-handling loads must also be carefully analyzed to assure that the structural design of the missile and the ground-support equipment (i.e., missile launcher, erector, etc.) are satisfactory. The magnitude of these loads can be determined only after the complete concept and details of the ground-support system have been established.

3. Factors of Safety. Factors of safety are applied to the limit or actual flight or ground-handling loads to assure that all stresses are below the ultimate or yield strength of the material from which the missile structural components are fabricated. This procedure prevents the structure from attaining any appreciable permanent deformation

* Superscript numbers indicate references listed at the end of the chapter.

under the actual load and from failing at ultimate load. The magnitude of the factor of safety to be used in the design of each missile component must be carefully selected to preclude undue weight penalties in the missile. As previously noted, each pound of "excess" inert or structural weight added may have a large detrimental effect on the performance of the missile. On the other hand, the structural design should be realistic and adequate to satisfy the over-all mission requirements of the weapon system.

The factors of safety which are currently considered in the structural design of missiles are:

a. $1.5 \times$ limit (actual) stress for design conditions which involve a safety hazard to personnel, for example, a missile-launching condition in which failure of a structural component could endanger the lives of the handling personnel

b. $1.25 \times$ limit stress (actual) for design conditions which do not involve hazard to personnel, for example, a terminal dive on target

c. $1 \times$ limit stress for all other design conditions

Margins of Safety. The margin of safety is defined as a ratio of the excess strength to the required strength and is expressed as

$$\text{Margin of safety MS} = \frac{\sigma_{\text{allowable}}}{\sigma} - 1 \quad (14-7)$$

where $\sigma_{\text{allowable}}$ = ultimate or yield strength of material, psi (physical property of material)

σ = stress in member

Two values of margin of safety are generally computed for each missile structural component analyzed. These are based on the yield strength and ultimate strength of the material. Hence

$$\text{MS}_{\text{yield}} = \frac{\sigma_{\text{allowable yield}}}{\sigma_{\text{limit or actual}} \times \text{factor of safety (generally = 1)}} - 1 \quad (14-8)$$

$$\text{MS}_{\text{ultimate}} = \frac{\sigma_{\text{allowable ultimate}}}{\sigma_{\text{limit or actual}} \times \text{factor of safety (1.25 or 1.50)}} - 1 \quad (14-9)$$

The margin of safety should never be negative but should be zero or a small positive value. The margin of safety for each member should be clearly indicated in the stress analysis. If it is later desired to increase

the load on any member or to decrease the size of the member, the margin of safety gives an immediate indication of the permissible load increase.

14-4. OVER-ALL STRUCTURAL ANALYSIS

In the structural-load analysis, the net load or shear force the structure has to support is of primary interest. This net load is the difference between the external loads and the inertia loads for a given missile flight condition. Theoretically, if the inertia load distribution is exactly equal and opposite to the external load distribution (i.e., zero net force along the entire missile), the shear forces and bending moments are nonexistent. Hence, for this idealized condition, the structural weight of the missile approaches the theoretical minimum value from the standpoint of loads. Therefore, it is apparent that the configuration design engineer should carefully consider the general internal component weight distribution in an effort to minimize the magnitude of this net force. The critical design condition for a given portion of the structure is defined as that which results in a maximum net load or shear force on that portion of the structure.

After the critical structural-design conditions are determined, the structural components of the missile are analyzed. For simple structural members, the classic equation for beam bending may be used to determine the stresses produced by the design bending moments such as those shown in Fig. 14-2.

$$\sigma = \frac{M_b c}{I_a} \quad (14-10)$$

where σ = tensile or compressive stress, psi

M_b = applied bending moment, in.-lb

c = distance from neutral axis to element in which stress is to be determined, in.

I_a = area moment of inertia of cross section of structural member, in.⁴

In the case of circular, unstiffened, thin-walled cylinders (monocoque construction) which are frequently used for small missile bodies, Eq. (14-10) becomes

$$\sigma_{\max} = \frac{M_b r}{\pi r^3 t} = \frac{M_b}{\pi r^2 t} \quad (14-11)$$

where r = radius of tube

t = wall thickness of cylinder

For a solid rectangular cross section which is similar to the airfoil section of a small missile (see Fig. 14-4a), Eq. (14-10) becomes

$$\sigma_{\max} = \frac{M_b(t_1/2)}{(bt_1^3/12)} = \frac{6M_b}{bt_1^2} \quad (14-12)$$

where b = chord of section

t_1 = thickness of section

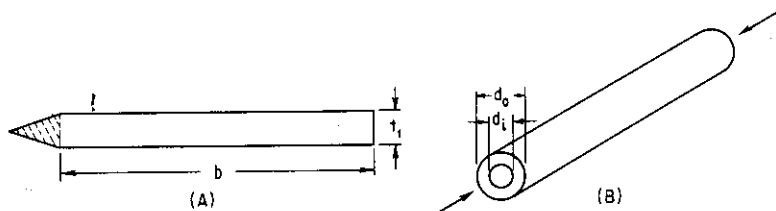


FIG. 14-4. Notations for structural analysis. (A) Airfoil cross section. (B) Circular cylinder.

The axial stress of a structural member which is axially loaded may be calculated by the following simple equation:

$$\sigma_{\text{axial}} = \frac{P}{A} \quad (14-13)$$

where P = magnitude of the axial load, lb

A = effective cross-sectional area of structural member in plane normal to direction of applied load, in.²

For a cylinder subjected to a compressive load P (see Fig. 14-4b), the axial stress is

$$\sigma_{\text{axial}} = \frac{P}{A} = \frac{4P}{\pi(d_o^2 - d_i^2)} \quad (14-14)$$

where d_o = outside diameter of cylinder, in.

d_i = inside diameter of cylinder, in.

The critical axial-loading condition generally occurs during the boost phase wherein the missile is subjected to high acceleration in the axial direction. For example, if a $10g$ axial acceleration is imposed on the missile, this force is opposed or reacted by a $10g$ inertia load acting

on each weight increment of the missile. The dead-weight distribution of the missile produces a corresponding axial-load distribution along the body axis of the missile as shown in Fig. 14-5. The axial stresses produced by this loading are then combined with the previously determined bending stresses to obtain the total stresses for the given design condition. Hence

$$\sigma_{\text{total}} = \sigma_{\text{bending}} \pm \sigma_{\text{axial}} = \frac{M_b c}{I_a} \pm \frac{P}{A} \quad (14-15)$$

The above simplified analysis is applicable for relatively simple structural members such as those previously described. However, in

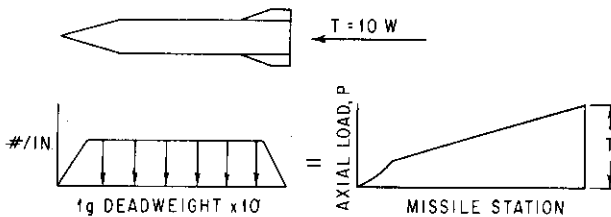


FIG. 14-5. Axial-load distribution.

most missile designs, particularly those associated with the larger missiles, many complex structural configurations are encountered. For these designs, much more elaborated analysis must be conducted. In cases where the most involved analysis is inadequate to predict accurately the stress on the structure, a relatively large factor of safety should be incorporated until results of static tests become available.

14-5. MATERIAL

The materials in general usage for the construction of missiles are aluminum, steel, magnesium, and titanium. Because of the high temperatures encountered by missiles flying at high supersonic and hypersonic speeds, other types of materials are coming into more common usage. These include molybdenum, beryllium, plastic, and graphite compounds. Since the designer has a wide variety of choice of these basic metals and many of their alloys, he must conduct a thorough analysis of their many advantages and disadvantages before he can select the best for his particular design. The following factors are

some of the most important of those which required careful consideration:

1. Material strength and density
2. Structural temperature expected in operation
3. Stiffness or deformation requirements
4. Corrosion resistance
5. Availability of materials
6. Fabrication limitations
7. Cost, both basic material and manufactured cost

For detailed discussion and data on material properties, the reader should consult any of the published literature on this subject (i.e., refs. 6, 10, and 12).

14-6. WEIGHT AND COST

In general, missile structural design permits more latitude in the selection of economic manufacturing processes and materials than manned aircraft. This is due primarily to the human-safety considerations involved in aircraft design. Adequate strength with minimum structural weight is generally the designer's aim for manned aircraft and cruise-type missiles. In short-range missiles, however, the unit cost vs. structural weight trade-off for each component must be closely examined. Structural weight can become less significant than manufactured cost of the component. However, for long-range ballistic missiles, it is mandatory to keep the structural weight as low as permissible without incurring unduly high cost for the material or its fabrication. Therefore, the designer should become more fully aware of the weight and cost interrelationship, particularly during the early design stages, in order to arrive at a more optimum design.

14-7. TYPES OF CONSTRUCTION

1. Body. The body of the missile can be constructed as a monocoque or semimonocoque structure. The monocoque structure consists of an unstiffened shell with very few transverse frames. This type of structure is relatively simple to manufacture with a minimum of detail parts and few manufacturing operations. This type of construction is used on ballistic missiles as well as for small missiles (up to approximately 24 in. outside diameter). The semimonocoque structure consists of a shell which is stiffened longitudinally by stringers and

transversely by bulkheads. This type of construction, which is generally used in the fabrication of manned aircraft, is also used in the construction of large ballistic missiles as well as cruise missiles. A large number of detail parts and assembly operations are required to produce this type of structure.

2. Aerodynamic Surfaces. Aerodynamic surfaces can be fabricated by a variety of methods. Small thin surfaces can feature solid, hollow-cast, or built-up honeycomb cross sections, depending perhaps upon the most economic means of fabrication. As the surfaces get larger and thicker, the use of solid sections becomes prohibitive from a weight standpoint and honeycomb or hollow-cast sections become more attractive. Casting materials have generally featured low material allowable strengths with the associated weight penalty but castings can be cheap in quantity production and require few final machining operations. Recent modifications to casting alloys have considerably improved their strength properties. Honeycomb construction permits the use of higher material allowables but obviously involves a multiplicity of detail parts (core, inserts, edge members, attachment fittings) and assembly operations. Again, the designer must carefully analyze the many factors involved including cost, weight, strength, etc., before he can select the optimum type of construction. An improper selection in the early stage of the missile design may require costly as well as time-consuming tooling and fabrication modifications for the final production design. However, the designer must also consider these changes in the event of subsequent technological advances. If proper foresight is used in selecting the type of construction during the early design stage, subsequent changes and modifications dictated by technological advances and other missile design requirements will be minimized.

SYMBOLS

A	effective cross-sectional area
C_m	moment coefficient
$C_{N_{TR}}$	trim normal-force coefficient
F	(normal) force
I	moment of inertia
I_a	area moment of inertia
I_0	moment of inertia of a given mass about its own center of gravity
M	moment

M_b	applied bending moment
MS	margin of safety
N	normal force
P	compressive or axial load
S	shear force
S_π	body frontal (reference) area
W	weight
c	distance from the neutral axis to the element in which the stress is to be determined
d	body diameter
d_i	inside diameter of the cylinder
d_o	outside diameter of the cylinder
l	distance from missile center of gravity
n	load factor
n_z	linear acceleration (in the normal direction)
q	dynamic pressure
r	radius of the tube (or cylinder)
t	wall thickness of the cylinder
t_1	thickness of the section
w	running load
x	any station along the beam or body of the missile
$\ddot{\theta}$	angular acceleration
σ	stress in member

REFERENCES

1. Firmage, D. A.: "Transportation Shock and Vibration Studies," University of Florida Engineering and Industrial Experiment Station, Proj. 8-91-06-002, Engineer Research and Development Laboratories, Fort Belvoir, Virginia, February, 1952.
2. The Applicability of Existing Truck and Rail Shock and Vibration Data to Freight Shipment Criteria, Vitro Corporation of America, Silver Springs Laboratory, *Tech. Rept.* 58, March, 1954.
3. "Climatic Extremes for Military Equipment," Military Standard Specification 210, 1953.
4. Environmental Criteria for Guided Missile Systems, *USAF Spec. Bull.* 106, February, 1954.
5. "Missiles, Guided; Design and Construction, General Specification for," MIL-M-8555.
6. "Strength of Metal Aircraft Elements," ANC-5, Government Printing Office, Washington, D.C., March, 1955.
7. Peery, D. J.: "Aircraft Structures," McGraw-Hill Book Company, Inc., New York, 1950.

8. Timoshenko, S. P., and D. H. Young: "Theory of Structures," McGraw-Hill Book Company, Inc., New York, 1945.
9. Wang, C. T.: "Applied Elasticity," McGraw-Hill Book Company, Inc., New York, 1953.
10. Bonney, E. A., M. J. Zucrow, and C. W. Besserer: "Aerodynamics, Propulsion, Structures, and Design Practice," D. Van Nostrand Company, Inc., Princeton, N.J., 1956.
11. Niles, A. S., and J. S. Newell: "Airplane Structures," vols. I and II, John Wiley & Sons, Inc., New York, 1943.
12. *Aircraft and Missiles*, vol. 2, no. 11, November, 1959.
13. Bruhn, E. F.: "Analysis and Design of Aircraft Structures," Tri-State Offset Co., Cincinnati, Ohio, 1950.

APPENDIX A

DETERMINATION OF RADIUS AND VOLUME OF TANGENT OGIVES

A-1. RADIUS

From Fig. A-1, the radius of the ogive is derived as follows:

$$R = \frac{d}{2} + R \cos \theta \quad (\text{A-1})$$

Since $l = R \sin \theta$ and $\sin \theta = \sqrt{1 - \cos^2 \theta}$ we get

$$\frac{l}{R} = \sqrt{1 - \cos^2 \theta} \quad (\text{A-2})$$

or

$$\cos \theta = \sqrt{1 - \frac{l^2}{R^2}} \quad (\text{A-3})$$

Substituting Eq. (A-3) into (A-1), we get

$$R = \frac{d}{2} + R \sqrt{1 - \frac{l^2}{R^2}} \quad (\text{A-4})$$

Rearranging Eq. (A-4), we get

$$1 - \frac{d}{2R} = \sqrt{1 - \frac{l^2}{R^2}} \quad (\text{A-5})$$

Squaring both sides of Eq. (A-5) and rearranging terms, we get

$$R = \frac{d}{4} + \frac{l^2}{d} \quad (\text{A-6})$$

The length-to-diameter ratio of the tangent ogive l/d may be

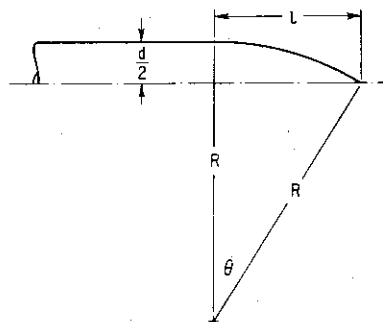


FIG. A-1. Radius of tangent ogive.

expressed in terms of the ogive caliber R/d as follows: Dividing Eq. (A-6) by d and rearranging, we get

$$\frac{l^2}{d^2} = \frac{R}{d} - \frac{1}{4} \quad (\text{A-7})$$

or
$$\frac{l}{d} = \sqrt{\frac{R}{d} - 0.25} = \sqrt{C - 0.25} \quad (\text{A-8})$$

where C is the caliber of the ogive.

A-2. VOLUME

From Fig. A-2A, the following relationship is obtained:

$$x = x_1 \quad (\text{A-9})$$

and
$$y_1 = \left(R - \frac{d}{2}\right) + y = a + y \quad (\text{A-9a})$$

where $a = R - \frac{d}{2}$

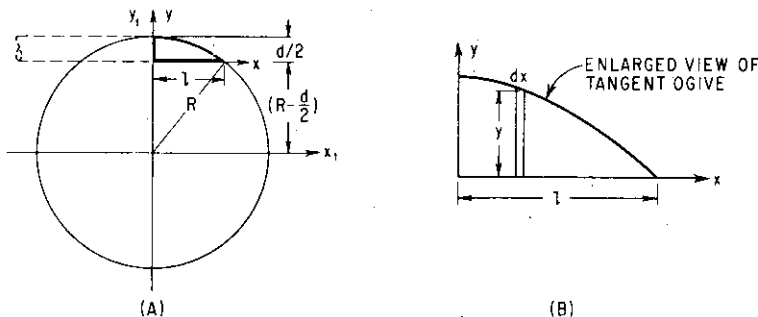


FIG. A-2. Volume of tangent ogive.

From the equation of a circle, we can write

$$x_1^2 + y_1^2 = R^2 \quad (\text{A-10})$$

or
$$x^2 + (a + y)^2 = R^2 \quad (\text{A-10a})$$

Hence
$$y = \sqrt{R^2 - x^2} - a \quad (\text{A-11})$$

or
$$y^2 = R^2 - x^2 - 2a\sqrt{R^2 - x^2} + a^2 \quad (\text{A-12})$$

From Fig. A-2B, the volume of the tangent ogive V may be expressed as

$$V = \pi \int_0^l y^2 dx \quad (\text{A-13})$$

Substituting Eq. (A-12) in Eq. (A-13), we get

$$V = \pi \int_0^l [R^2 + a^2 - x^2 - 2a\sqrt{R^2 - x^2}] dx \quad (\text{A-14})$$

$$\text{or } V = \pi \left[\int_0^l (R^2 + a^2) dx - \int_0^l x^2 dx - \int_0^l (2a\sqrt{R^2 - x^2}) dx \right] \quad (\text{A-15})$$

Integrating Eq. (A-15), we get

$$V = \pi \left((R^2 + a^2) \left[x \right]_{x=0}^{x=l} - \left[\frac{x^3}{3} \right]_{x=0}^{x=l} - 2a \left[\frac{x}{2} \sqrt{R^2 - x^2} + \frac{R^2}{2} \sin x \sqrt{\frac{1}{R^2}} \right]_{x=0}^{x=l} \right) \quad (\text{A-16})$$

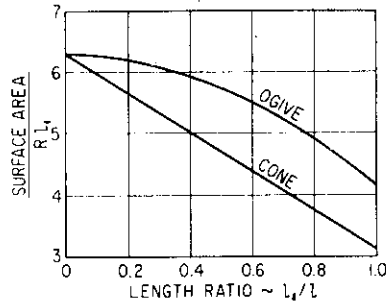
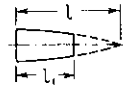
Hence

$$V = \pi \left[(R^2 + a^2)l - \frac{l^3}{3} - a l \sqrt{R^2 - l^2} - a R^2 \sin^{-1} \frac{l}{R} \right] \quad (\text{A-17})$$

Substituting $a = R - (d/2)$ in Eq. (A-17), we get

$$V = \pi \left[l \left(R^2 + R^2 - Rd - \frac{d^2}{4} \right) - \frac{l^3}{3} - \left(R - \frac{d}{2} \right) l \sqrt{R^2 - l^2} - \left(R - \frac{d}{2} \right) R^2 \sin^{-1} \frac{l}{R} \right] \quad (\text{A-18})$$

$$\text{or } V = \pi \left[l \left(2R^2 - Rd + \frac{d^2}{4} \right) - \frac{l^3}{3} - \left(R - \frac{d}{2} \right) l \sqrt{R^2 - l^2} - \left(R - \frac{d}{2} \right) R^2 \sin^{-1} \frac{l}{R} \right] \quad (\text{A-18a})$$



A-3. SURFACE AREA

In the determination of skin-friction drag coefficient, the surface (wetted) area of the aerodynamic component must be known [see Sec. 4-2, Eq. (4-7)]. Figure A-3 is a plot of the surface area of tangent ogive and truncated conical bodies of revolution.

FIG. A-3. Surface area of tangent ogive and truncated conical bodies of revolution.

APPENDIX B

EXPRESSIONS AND COORDINATES OF DIFFERENT NOSE SHAPES*

B-1. POWER SERIES

$$r = x^n \quad \text{for } (0 \leq x \leq 1) \quad (\text{B-1})$$

where $n = 1$ for a cone

$n = 1/2$ for a parabola with vertex at $x = 0$

B-2. PARABOLIC SERIES

$$r = \frac{-2x - Kx^2}{2 - K} \quad (\text{B-2})$$

where $K = 0$ for a cone

$K = 1$ for a parabolic nose

$K = 0.75$ for a "3/4 power" parabolic series

$K = 0.50$ for a "1/2 power" parabolic series

B-3. HAACK SERIES

$$r = \frac{1}{\sqrt{\pi}} \sqrt{\varphi - \frac{1}{2} \sin 2\varphi C \sin 3\varphi} \quad (\text{B-3})$$

where $\varphi = \cos^{-1}(1 - 2x)$

$C = 0$ for the Von Kármán nose shape (also known as the *L-D* Haack nose)

$C = 1/3$ for the *L-V* Haack nose

The letters *L-D* and *L-V* refer to the boundary conditions for which the drag was minimized. The *L-D* signifies given length and diameter and *L-V* length and volume. Profiles of these nose shapes are shown

* *NACA Research Mem.* L53K17.

APPENDIX C

OPTIMUM WING STUDY

As stated in Sec. 3-15, maximum L/D is obtained when the induced drag is equal to the drag at zero lift, i.e., $C_{D_i} = C_{D_0}$ or $C_D = 2C_{D_0}$. The proof of this statement is given below. In addition, the expressions for the value of C_L at $(L/D)_{\max}$ and $(L/D)_{\max}$ are derived as a function of C_{D_0} and the induced drag factor dC_{D_i}/dC_L^2 .

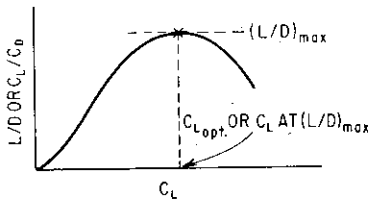


FIG. C-1. Optimum wing study.

C-1. C_D at $(L/D)_{\max}$

From the basic definition of lift and drag, we get

$$\frac{L}{D} = \frac{C_L q S}{C_D q S} = \frac{C_L}{C_D} \quad (\text{C-1})$$

Since $C_D = C_{D_0} + C_{D_i} = C_{D_0} + (dC_{D_i}/dC_L^2) C_L^2$, Eq. (C-1) becomes

$$\frac{C_L}{C_D} = \frac{C_L}{C_{D_0} + KC_L^2} \quad (\text{C-2})$$

where $K = dC_{D_i}/dC_L^2$

From Fig. C-1, it is apparent that $(L/D)_{\max}$ is obtained when

$$\frac{d(C_L/C_D)}{dC_L} = 0 \quad (\text{C-3})$$

Hence
$$\frac{d(C_L/C_D)}{dC_L} = \frac{d[C_L/(C_{D_0} + KC_L^2)]}{dC_L}$$

$$= \frac{(C_{D_0} + KC_L^2)(1) - C_L(0 + 2KC_L)}{(C_{D_0} + KC_L^2)^2} = 0 \quad (\text{C-4})$$

or

$$C_{D_0} - KC_L^2 = 0 \quad (\text{C-5})$$

From Eq. (C-5), it is seen that

$$C_{D_0} = KC_L^2 = C_{D_t} \quad (\text{C-6})$$

or
$$C_D = C_{D_0} + C_{D_t} = 2C_{D_0} \quad (\text{C-7})$$

Hence
$$C_D \text{ at } (L/D)_{\max} = 2C_{D_0} \quad (\text{C-8})$$

C-2. C_L at $(L/D)_{\max}$ or $C_{L_{\text{opt}}}$

From Eq. (C-6), we get

$$C_L = \sqrt{\frac{C_{D_0}}{K}} = \sqrt{\frac{C_{D_0}}{dC_{D_t}/dC_L^2}} \quad (\text{C-9})$$

Hence
$$C_L \text{ at } (L/D)_{\max} = \sqrt{\frac{C_{D_0}}{dC_{D_t}/dC_L^2}} \quad (\text{C-10})$$

C-3. $(L/D)_{\max}$

The value of $(L/D)_{\max}$ is determined by taking the ratio of C_L and C_D at $(L/D)_{\max}$ as shown in Fig. C-1. Hence, from Eqs. (C-10) and (C-8), we get

$$\left(\frac{L}{D}\right)_{\max} = \frac{C_L \text{ at } (L/D)_{\max}}{C_D \text{ at } (L/D)_{\max}} = \sqrt{\frac{C_{D_0}/K}{2C_{D_0}}} \quad (\text{C-11})$$

or
$$\left(\frac{L}{D}\right)_{\max} = \frac{1}{2} \sqrt{\frac{1}{(dC_{D_t}/dC_L^2)C_{D_0}}} \quad (\text{C-12})$$

APPENDIX D

DERIVATION OF INCREMENTAL VELOCITY DUE TO BOOST

D-1. VACUUM (DRAG-FREE CONDITION)

The incremental velocity the missile attained during its accelerating phase of flight can be expressed mathematically as follows:

$$\Delta V_b = \int_0^{t_b} a \, dt \quad (D-1)$$

where ΔV_b = incremental velocity
 a = axial acceleration of missile
 t_b = burning time of rocket motor

From Fig. D-1, the axial acceleration may be expressed in terms of rocket-motor thrust T and weight W as follows:

$$a = \frac{Tg}{W} + g \sin \gamma_L \quad (D-2)$$

Hence

$$\Delta V_b = g \int_0^{t_b} \frac{T}{W} \, dt + g \int_0^{t_b} \sin \gamma_L \, dt \quad (D-3)$$

Since $W = W_L - W_P(t/t_b)$, we get (D-4)

$$\Delta V_b = g \int_0^{t_b} \frac{T}{W_L - W_P(t/t_b)} \, dt + g \int_0^{t_b} \sin \gamma_L \, dt \quad (D-5)$$

where W_L = missile weight at launch
 W_P = propellant weight

Assuming T , γ_L , and t_b are constants, Eq. (D-5) becomes

$$\Delta V_b = Tg \int_0^{t_b} \frac{t_b}{W_L t_b - W_P t} \, dt + g \sin \gamma_L \int_0^{t_b} dt \quad (D-6)$$

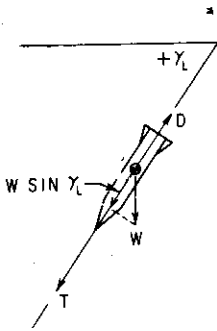


FIG. D-1. Force diagram.

Integrating Eq. (D-6), we get

$$\Delta V_b = Tg \left(-\frac{t_b}{W_P} \right) \left[\ln (W_{L^{t_b}} - W_{P^{t_b}}) \right]_{t=0}^{t=t_b} + g \sin \gamma_L \left[t \right]_{t=0}^{t=t_b} \quad (\text{D-7})$$

$$\text{or } \Delta V_b = -\frac{Tt_b}{W_P} g [\ln (W_{L^{t_b}} - W_{P^{t_b}}) - \ln (W_{L^{t_b}})] + gt_b \sin \gamma_L \quad (\text{D-8})$$

Since $Tt_b/W_P = I/W_P = I_{sp}$ [see Eq. (13-13)], Eq. (D-8) becomes

$$\Delta V_b = I_{sp} g \ln \left(\frac{W_L}{W_E} \right) + gt_b \sin \gamma_L \quad (\text{D-9})$$

where $W_E = W_L - W_P$

D-2. GENERAL SOLUTION

For the general solution, the drag term must be included in Eq. (D-2). Hence

$$a = \frac{Tg}{W} - \frac{Dg}{W} + g \sin \gamma_L \quad (\text{D-10})$$

$$\text{or } a = \frac{Tg}{W} - \frac{C_D \frac{1}{2} \rho V^2 S g}{W} + g \sin \gamma_L \quad (\text{D-10a})$$

Because of the nature of the drag term, a closed analytical solution cannot be obtained. Hence, for most analysis, Eq. (D-10a) must be solved by a method of iteration such as that described in Sec. 4-6 or on the automatic computing machines. However, for certain applications whereby the thrust-to-weight ratio is relatively high (i.e., high axial acceleration), it is permissible to use an approximation for the drag effect in calculating a value of ΔV_b . For these cases, an estimated average drag \bar{D} is used in Eq. (D-10). Hence Eq. (D-6) may be modified as follows:

$$\Delta V_b = (T - \bar{D})g \int_0^{t_b} \frac{t_b}{W_{L^{t_b}} - W_{P^{t_b}}} dt + g \sin \gamma_L \int_0^{t_b} dt \quad (\text{D-11})$$

Hence Eq. (D-11) becomes

$$\Delta V_b = - \left[(T - \bar{D}) \frac{t_b g}{W_P} \right] [\ln (W_{L^{t_b}} - W_{P^{t_b}}) - \ln (W_{L^{t_b}})] + gt_b \sin \gamma_L \quad (\text{D-12})$$

Multiplying Eq. (D-12) by T/T and rearranging, we get

$$\Delta V_b = \frac{T - \bar{D}}{T} I_{sp} g \ln \frac{W_L}{W_E} + g t_b \sin \gamma_L \quad (\text{D-13})$$

or

$$\Delta V_b = K' I_{sp} g \ln \frac{W_L}{W_E} + g t_b \sin \gamma_L \quad (\text{D-13a})$$

where $K' = (T - \bar{D}/T)$ as used in Eq. (4-12)

APPENDIX E

DERIVATION OF EXPRESSION FOR ΔV FOR ITERATION METHOD

In the derivation of ΔV [see Eq. (4-21)] for the iteration method used to calculate missile performance, two basic assumptions are made: (1) the acceleration vs. time curve (see Fig. E-1) is linear over the time interval Δt used, and (2) the time interval used throughout the procedure is a constant value. From Fig. E-1, the value of velocity V at any time t may be expressed as

$$V = V_{n-1} + a_{av} \Delta t \quad (\text{E-1})$$

where the subscript $n - 1$ denotes the first interval previous to t (and $n - 2$ is the second interval previous to t , etc.). Hence Eq. (E-1) becomes

$$V = V_{n-1} + (a + a_{n-1}) \frac{\Delta t}{2} \quad (\text{E-2})$$

But for a constant Δt , we get

$$a - a_{n-1} = a_{n-1} - a_{n-2} \quad (\text{E-3})$$

or
$$a = 2a_{n-1} - a_{n-2} \quad (\text{E-4})$$

Substituting Eq. (E-4) into Eq. (E-2), we get

$$V = V_{n-1} + (3a_{n-1} - a_{n-2}) \frac{\Delta t}{2} \quad (\text{E-5})$$

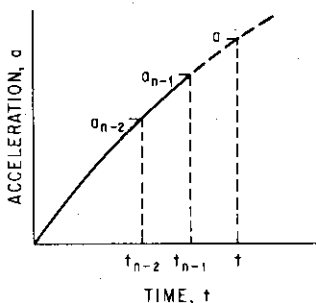


FIG. E-1. Acceleration vs. time.

APPENDIX F

DETERMINATION OF DOWNWASH FROM WIND-TUNNEL-TEST RESULTS

F-1. ANALYTICAL SOLUTION

For the purpose of illustration, a canard configuration has been arbitrarily selected. Hence, from Fig. (F-1), the complete model pitching moment M_{CM} may be expressed as

$$M_{CM} = N_B x_B + N_C x_C + N_T x_T \quad (\text{F-1})$$

where N_B , N_C , and N_T = normal force on body, canard, and tail surfaces

x_B , x_C , and x_T = center-of-pressure location of N_B , N_C , and N_T

Expressed in coefficient form, Eq. (F-1) becomes

$$M_{CM} = (M_\alpha)_{CM} = [(C_{N_\alpha})_B \alpha x_B + (C_{N_\alpha})_C \alpha x_C + (C_{N_\alpha})_T (\alpha - \epsilon) x_T] q S_\tau \quad (\text{F-2})$$

Dividing by $q S_\tau d$, Eq. (F-2) becomes

$$(C_m)_{CM} = \frac{M_{CM}}{q S_\tau d} = (C_{N_\alpha})_B \alpha \left(\frac{x}{d}\right)_B + (C_{N_\alpha})_C \alpha \left(\frac{x}{d}\right)_C + (C_{N_\alpha})_T (\alpha - \epsilon) \left(\frac{x}{d}\right)_T \quad (\text{F-3})$$

Hence
$$(C_m)_{CM} = (C_m)_{BC} + (C_m)_T (\alpha - \epsilon) \quad (\text{F-4})$$

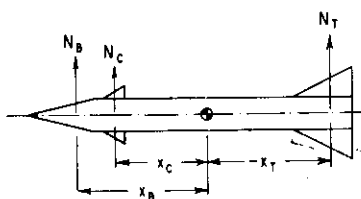


FIG. F-1. Analytical solution of downwash.

where the subscript BC denotes body-plus-tail configuration, etc. Therefore, at a given α , we get

$$\begin{aligned} \frac{\alpha - \epsilon}{\alpha} &= \frac{(C_m)_{CM} - (C_m)_{BC}}{(C_m)_T} \\ &= \frac{(C_m)_{CM} - (C_m)_{BC}}{(C_m)_{BT} - (C_m)_B} \quad (\text{F-5}) \end{aligned}$$

Equation (F-5) may be described as

$$\frac{\alpha - \epsilon}{\alpha} = \frac{\text{tail contribution in the presence of downwash}}{\text{tail contribution in the absence of downwash}} \quad (\text{F-5}\alpha)$$

If the moment curves are linear, then the slopes of C_m vs. α may be used as follows:

$$1 - \epsilon_\alpha = \frac{(C_{m_\alpha})_{CM} - (C_{m_\alpha})_{BC}}{(C_{m_\alpha})_{BT} - (C_{m_\alpha})_B} = \frac{(\Delta C_{m_\alpha})'_T}{(\Delta C_{m_\alpha})_T} \quad (\text{F-6})$$

where $(\Delta C_{m_\alpha})'_T$ = tail contribution in presence of downwash
 $(\Delta C_{m_\alpha})_T$ = tail contribution in absence of downwash

Similarly, it can be shown that the downwash due to control (canard) surface deflection ϵ_δ , may be expressed as

$$(1 - \epsilon_\delta) = \frac{(\Delta C_{m_\delta})_T}{(\Delta C_{m_\alpha})_T} \quad (\text{F-7})$$

F-2. GRAPHICAL SOLUTION

The downwash angle ϵ may also be determined graphically from wind-tunnel-test results. This is done by plotting the pitching-moment contributions of the tail in the presence of and absence of downwash vs. angle of attack as shown in Fig. F-2. It is apparent that, at a given α (i.e., α_1), the value of ΔC_{m_T} in the absence of downwash (i.e., $BT-B$) is point B in Fig. F-2. The value of ΔC_{m_T} in the presence of downwash is A ($BCT-BC$) at α_1 . This represents a loss of ΔC_{m_T} of $B-A$, which is equivalent to a downwash angle ϵ as shown in Fig. F-2. Hence the value of ϵ can be readily determined at any or all values of α desired. Hence non-linearity imposes no limitation on this graphical solution.

The normal-force coefficients may also be used in lieu of the pitching-moment coefficients. However, since the moment coefficients are generally somewhat more accurate than the normal-force coefficients, the former are preferred.

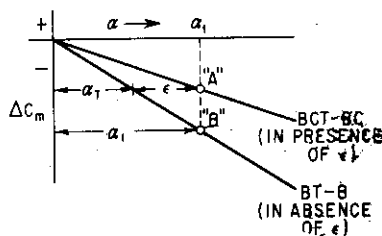


FIG. F-2. Graphical solution of downwash.

APPENDIX G

DETERMINATION OF DAMPING DERIVATIVES FROM WIND-TUNNEL-TEST RESULTS

G-1. DAMPING IN PITCH

The value of the pitch damping or rotary derivatives $C_{m\dot{\theta}}$, $C_{m\dot{\alpha}}$, and $C_{m\dot{\delta}}$, as discussed in Sec. 9-3, may be determined from the static derivatives (i.e., $C_{N\alpha}$ and $C_{m\alpha}$) which are obtained from wind-tunnel tests. In Sec. 9-3 it was shown that the value of $C_{m\dot{\theta}}$ for the complete model configuration consists of contributions from the forebody, canard (or any other control surfaces ahead of the tail), and tail surfaces as expressed below:

$$(C_{m\dot{\theta}})_{CM} = -2 \left\{ (C_{N\alpha})_B \left(\frac{x}{d} \right)_B^2 + (C_{N\alpha})_C [K_{C(B)} + K_{B(C)}] \frac{S_c}{S_r} \left(\frac{x}{d} \right)_C^2 + (C_{N\alpha})_T \times [K_{T(B)} + K_{B(T)}] \frac{S_T}{S_r} \left(\frac{x}{d} \right)_T^2 \right\} \quad (G-1)$$

From Eq. (G-1) [which is identical to Eq. (9-39)], it is apparent that the first two terms represent the contributions from the combined effects of the body and canards. The third or last term represents the tail contribution which includes the mutual interference between the body and tail. These contributions may also be expressed in terms of the moment derivative $C_{m\alpha}$, in the following general form:

$$(C_{N\alpha})_B \left(\frac{x}{d} \right)_B^2 \rightarrow (C_{N\alpha})_B \frac{(C_{m\alpha})_B^2}{(C_{N\alpha})_B} \rightarrow \frac{(C_{m\alpha})_B^2}{(C_{N\alpha})_B}$$

Hence Eq. (G-1) becomes

$$(C_{m\dot{\theta}})_{CM} = -2 \left\{ \frac{(C_{m\alpha})_{BC}^2}{(C_{N\alpha})_{BC}} + \frac{[(C_{m\alpha})_{BT} - (C_{m\alpha})_B]^2}{(C_{N\alpha})_{BT} - (C_{N\alpha})_B} \right\} \quad (G-2)$$

where the subscripts denote the components of the configuration (i.e., B body, T tail, etc.).

Similarly, the expressions for $C_{m_{\alpha}}$ and $C_{m_{\delta}}$ [see Eqs. (9-44) and (9-46)] become

$$(C_{m_{\alpha}})_{CM} = -2[(C_{m_{\alpha}})_{BT} - (C_{m_{\alpha}})_B] \frac{x_{C-T}}{d} \epsilon_{\alpha} \quad (G-3)$$

and
$$(C_{m_{\delta}})_{CM} = -2[(C_{m_{\alpha}})_{BT} - (C_{m_{\alpha}})_B] \frac{x_{C-T}}{d} \epsilon_{\delta} \quad (G-4)$$

where x_{C-T} is the distance between the canard and the tail surfaces as shown in Fig. 9-4, and ϵ_{α} and ϵ_{δ} are determined in Appendix F.

G-2. DAMPING IN ROLL

In order to determine the damping-in-roll derivative C_{l_p} [see Sec. 8-5 or Eq. (8-4)] in the wind tunnel, several techniques may be employed. Perhaps the simplest method is to roll the model on the mounting

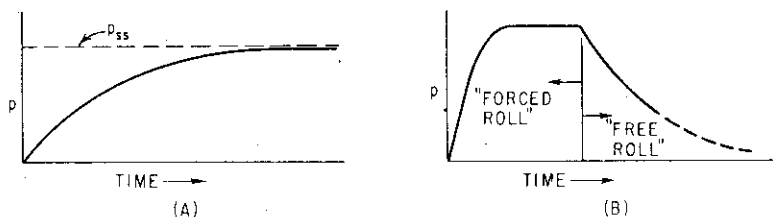


FIG. G-1. Damping-in-roll tests.

sting by means of fixed aerodynamic lateral-control surfaces. In this technique, the model is initially restrained from rolling while the tunnel builds up to speed, whereupon the model is released and commences to spin up to its steady-state rolling velocity, as indicated in Fig. G-1a.

The transient response of the missile in roll is expressed as

$$I_x \dot{p} - C_{l_{\delta}} \delta q S d + C_{l_p} p \frac{q S d^2}{2V} + L_0 \quad (G-5)$$

where I_x = moment of inertia of model in roll

$C_{l_{\delta}}$ = lateral-control effectiveness which is determined from conventional wind-tunnel test

L_0 = term to account for friction in the system and may be accounted for or, if it is small, neglected

From the time history of the measured rolling velocity as shown in Fig. G-1a, the roll acceleration \dot{p} and hence C_{l_p} may be calculated. However, the value of C_{l_p} is more accurately calculated for the steady-state rolling condition, i.e., $\dot{p} = 0$. For this condition, C_{l_p} is

determined by setting Eq. (G-5) equal to zero. Hence, if friction is neglected, we get

$$C_{i_p} = \frac{C_{i_\delta} \delta}{p_{ss} d / 2V} \quad (\text{G-6})$$

where p_{ss} = steady-state rolling velocity

Another method of determining C_{i_p} is to spin the model mechanically. In this technique, a driving device is employed to spin the model with the aerodynamic lateral-control surfaces in their neutral position. By measuring the rolling moment required to spin the model at various constant rolling velocities, the value of C_{i_p} is calculated as follows (again, assuming $L_0 = 0$):

$$C_{i_p} = \frac{\mathcal{L}_p}{qSd^2/2V} \quad (\text{G-7})$$

where \mathcal{L}_p = measured variation of required rolling moment with rolling velocity, ft-lb/radian/sec

A third method of determining C_{i_p} is simply to spin the model to an arbitrary rolling velocity and then allow the spin rate of the model to decrease toward zero velocity as shown in Fig. G-1B. In this technique, the aerodynamic lateral-control surfaces are set in their neutral positions. The value of C_{i_p} may be calculated by Eq. (G-5), which may be simplified to the following expression:

$$C_{i_p} = \frac{I_x \dot{p}}{pqSd^2/2V} \quad (\text{G-8})$$

APPENDIX H

DETERMINATION OF AERODYNAMIC DERIVATIVES FROM FLIGHT-TEST DATA

H-1. "PULSED MODEL"

One technique most commonly used in scaled-model flight testing is the "pulsed-model" method. In this method, the model is usually ground-launched and accelerated to the desired speed by means of a booster rocket which drops off at the end of its burning. The model then commences its free flight wherein small rocket charges are set off at fixed time intervals which provide the desired impulse to "disturb" the model in pitch and/or in yaw during its zero-lift flight trajectory. The model used in this technique is generally completely uncontrolled and must be statically stable. By carefully controlling the manufacturing and installation fin misalignments, the rolling velocity of the model is kept low in order to reduce the cross-coupling effects during the "disturbed" conditions. A typical plot of the model transient response in the "disturbed" condition is shown in Fig. 9-3. Telemetered data for this technique generally consist of time history of axial acceleration, normal acceleration about the model center of gravity, and angle of attack. A history of the model speed, Mach number, and dynamic pressure is also required and may be obtained from external coverage such as radar, theodolite, and radiosonde data.

The aerodynamic derivatives obtained from this method are C_{D_0} , C_{N_α} , C_{m_α} , and $(C_{m_\delta} + C_{m_z})$. The value of C_{D_0} may be determined when the model is flying in the undisturbed conditions.

$$C_{D_0} = \frac{n_x W}{qS} \quad (\text{H-1})$$

where n_x = axial acceleration
 W = weight of model

The value of C_{N_α} may be determined from the telemetered data of

normal acceleration and angle of attack during the "disturbed" condition of the model. The value of C_N is evaluated as follows:

$$C_N = \frac{nW}{qS} \quad (\text{H-2})$$

where n is the normal acceleration at the model center of gravity. By plotting the value of C_N vs. α , the value of C_{N_α} may be determined throughout the speed or Mach-number range of the model. Since the angle of attack is generally measured by an α indicator located at or ahead of the nose of the model (see Fig. H-1), the telemetered data of α must be corrected for the incremental



FIG. H-1. Angle-of-attack correction.

angle of attack $\Delta\alpha$ induced by the angular motion of the model. The induced angle of attack may be expressed as [see Eq. (9-34)]

$$\Delta\alpha = \tan^{-1} \frac{\dot{\theta}l}{V} \quad (\text{H-3})$$

For small angles, Eq. (H-3) becomes

$$\Delta\alpha \cong \frac{\dot{\theta}l}{V} \quad (\text{H-3a})$$

Since $\dot{\theta} = \dot{\alpha} + \dot{\gamma}$ [see Eq. (5-3)] and

$$\dot{\gamma} = \frac{g}{WV} (nW - W \cos \theta)$$

we get

$$\Delta\alpha = \frac{l}{V} \left(\dot{\alpha} + g \frac{n - \cos \theta}{V} \right) \quad (\text{H-4})$$

Hence

$$\alpha_{cg} = \alpha_{\text{measured}} - \Delta\alpha \quad (\text{H-5})$$

The value of C_{m_α} and $(C_{m_\dot{\theta}} + C_{m_\dot{\alpha}})$ may be determined by solving the equation of motion assuming a single degree of freedom. Hence

$$I\ddot{\theta} = M_\alpha \dot{\alpha} + M_\dot{\theta} \dot{\theta} + M_\alpha \dot{\alpha} \quad (\text{H-6})$$

Since $\dot{\theta} \cong \dot{\alpha}$ (assumption of single degree of freedom), we may rewrite Eq. (H-6) as follows:

$$I\ddot{\theta} - (M_\dot{\theta} + M_\alpha)\dot{\theta} - M_\theta \dot{\theta} = 0 \quad (\text{H-7})$$

or

$$\ddot{\theta} - (m_\dot{\theta} + m_\alpha)\dot{\theta} - m_\theta \dot{\theta} = 0 \quad (\text{H-7a})$$

Solving for the roots of Eq. (H-7a), we get

$$\lambda_{1,2} = \frac{1}{2}(m_{\dot{\theta}} + m_{\dot{\alpha}}) \pm \frac{1}{2}\sqrt{(m_{\dot{\theta}} + m_{\dot{\alpha}})^2 + 4m_{\theta}} \quad (\text{H-8})$$

From Sec. 9-3, it is apparent that

$$T_{1/2} = -\frac{2 \ln 2}{m_{\dot{\theta}} + m_{\dot{\alpha}}} \quad (\text{H-9})$$

and

$$P = \frac{4\pi}{\sqrt{(m_{\dot{\theta}} + m_{\dot{\alpha}})^2 + 4m_{\theta}}} \quad (\text{H-10})$$

From Eq. (H-9), the values of $(M_{\dot{\theta}} + M_{\dot{\alpha}})$ become

$$M_{\dot{\theta}} + M_{\dot{\alpha}} = \frac{-2I \ln 2}{T_{1/2}} = (C_{m_{\dot{\theta}}} + C_{m_{\dot{\alpha}}}) \frac{qSd^2}{2V} \quad (\text{H-9a})$$

Hence

$$C_{m_{\dot{\theta}}} + C_{m_{\dot{\alpha}}} = \frac{-4IV \ln 2}{qSd^2 T_{1/2}} \quad (\text{H-9b})$$

The value of $C_{m_{\dot{\alpha}}}$ may be determined by first squaring both sides of Eq. (H-10) and rearranging terms as shown below:

$$\left(\frac{4\pi}{P}\right)^2 = (m_{\dot{\theta}} + m_{\dot{\alpha}})^2 + 4m_{\theta} \quad (\text{H-10a})$$

or

$$m_{\theta} = \left(\frac{2\pi}{P}\right)^2 - \frac{(m_{\dot{\theta}} + m_{\dot{\alpha}})^2}{4} \quad (\text{H-10b})$$

Substituting Eq. (H-9) into Eq. (H-10b), we get

$$m_{\theta} = \frac{M_{\theta}}{I} = \left(\frac{2\pi}{P}\right)^2 - \left(\frac{\ln 2}{T_{1/2}}\right)^2 \quad (\text{H-11})$$

Since M_{θ} is equal to M_{α} for this single-degree-of-freedom analysis and is negative we get

$$C_{m_{\dot{\alpha}}} = \frac{M_{\alpha}}{qSd} = \frac{-I}{qSd} \left[\left(\frac{2\pi}{P}\right)^2 - \left(\frac{\ln 2}{T_{1/2}}\right)^2 \right] \quad (\text{H-11a})$$

Hence the value of $C_{m_{\dot{\alpha}}}$ and $(C_{m_{\dot{\theta}}} + C_{m_{\dot{\alpha}}})$ may be readily calculated by Eqs. (H-11a) and (H-9b) by measuring the period of oscillation P and time to damp to half amplitude $T_{1/2}$ from the telemetered record of the model transient response as shown in Fig. 9-3. The change in Mach number, dynamic pressure, etc., during this transient is assumed to be negligible.

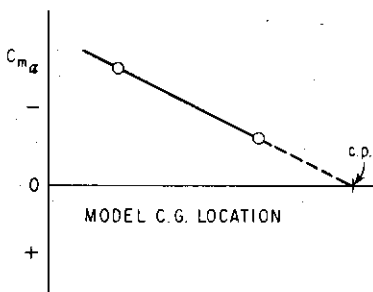


FIG. H-2. Determination of $C_{N\alpha}$.

extrapolating the curve of $C_{m\alpha}$ vs. center of gravity to $C_{m\alpha}$ equal to zero. Hence, from Eq. (5-19) and Fig. H-2, we get

$$cp = cg - \frac{\bar{X}}{d} = cg - \frac{C_{m\alpha}}{C'_{N\alpha}} \quad (\text{H-12})$$

or

$$C_{N\alpha} = \frac{C_{m\alpha}}{cg - cp} \quad (\text{H-12a})$$

It is therefore apparent that $C_{N\alpha}$ is simply the slope of the $C_{m\alpha}$ vs. center-of-gravity curve shown in Fig. H-2.

H-2. STEP-COMMAND INPUT

Another method commonly used consists of programming step-control surface deflections of sufficient duration to assure that the model or missile approaches its steady-state trimmed condition. In conditions wherein the missile is continually decelerating, the duration of command may be reduced somewhat in order that the change in Mach number, q , etc., be small. In these cases, the missile may not reach its steady-state trimmed condition but will have experienced a sufficient number of oscillations about its nominal trimmed condition to permit an accurate determination of the period of oscillation and time to damp to half amplitude. For this type of command a two-degree-of-freedom analysis is generally acceptable.

From the analysis presented in Sec. 9-5, it was shown that the period of oscillation P and the time to damp to half amplitude $T_{1/2}$ may be related to the aerodynamic coefficient as follows [see Eqs. (9-91) and (9-92)]:

$$P = \frac{2\pi}{\sqrt{-\omega^2(1 - \zeta^2)}} \quad (\text{H-13})$$

and

$$T_{1/4} = \frac{\ln 2}{\zeta\omega} \quad (\text{H-13a})$$

Equation (H-13) may be rewritten as

$$-\omega^2(1 - \zeta^2) = \left(\frac{2\pi}{P}\right)^2 \quad (\text{H-13b})$$

From Eq. (9-77) and the definition of ω and ζ (see Sec. 9-5), we may rewrite Eq. (H-13a) as

$$\omega^2(1 - \zeta^2) = -\left(\frac{2\pi}{P}\right)^2 = (m_\alpha + m_\delta f_\alpha) \left[1 - \frac{(-f_\alpha + m_\delta + m_\alpha)^2}{4(m_\alpha + m_\delta f_\alpha)} \right] \quad (\text{H-14})$$

Defining $\sqrt{-\omega^2(1 - \zeta^2)}$ as the damped natural frequency of the missile ω_d , we may write Eq. (H-14) as follows:

$$\omega_d^2 = (m_\alpha + m_\delta f_\alpha) \left[1 - \frac{(-f_\alpha + m_\delta + m_\alpha)^2}{4(m_\alpha + m_\delta f_\alpha)} \right] \quad (\text{H-15})$$

$$\text{or} \quad \omega_d^2 = m_\alpha + m_\delta f_\alpha - \frac{1}{4}(-f_\alpha + m_\delta + m_\alpha)^2 \quad (\text{H-15a})$$

$$\text{Hence} \quad m_\alpha = \omega_d^2 + \left(\frac{-f_\alpha + m_\delta + m_\alpha}{2}\right)^2 - m_\delta f_\alpha \quad (\text{H-16})$$

$$\text{or} \quad m_\alpha = \left(\frac{2\pi}{P}\right)^2 + \left(\frac{-f_\alpha + m_\delta + m_\alpha}{2}\right)^2 - m_\delta f_\alpha \quad (\text{H-16a})$$

From Sec. 9-5 and Eq. (9-77), we get

$$\zeta\omega = \frac{-e}{2} = -\frac{m_\delta + m_\alpha - f_\alpha}{2} = \frac{\ln 2}{T_{1/4}} \quad (\text{H-17})$$

Rearranging, we get

$$m_\delta + m_\alpha = -2\zeta\omega + f_\alpha \quad (\text{H-18})$$

Substituting Eq. (H-17) into Eq. (H-18), we get

$$m_\delta + m_\alpha = \frac{-2 \ln 2}{T_{1/4}} + f_\alpha \quad (\text{H-19})$$

$$\text{Hence} \quad C_{m_\delta} + C_{m_\alpha} = \frac{-2VI}{qSd^2} \left(\frac{2 \ln 2}{T_{1/4}} - \frac{C_{N_\alpha} qS}{mV} \right) \quad (\text{H-20})$$

Substituting Eq. (H-17) into Eq. (H-16a), we get

$$C_{m_\alpha} = \frac{-I}{qSd} \left[\left(\frac{2\pi}{P}\right)^2 - \left(\frac{\ln 2}{T_{1/4}}\right)^2 \right] + C_{m_\delta} \frac{qSd^2 C_{N_\alpha} qS}{2VI mV} \quad (\text{H-21})$$

In most practical cases, the last term in Eq. (H-21) may be neglected. Hence

$$C_{m_x} = \frac{-I}{qSd} \left[\left(\frac{2\pi}{P} \right)^2 - \left(\frac{\ln 2}{T_{1/2}} \right)^2 \right] \quad (\text{H-21a})$$

Other aerodynamic coefficients obtainable from this method include C_{D_0} , C_{N_α} , C_{N_δ} , and C_{m_δ} . The values of C_{D_0} and C_{N_α} may be determined by the methods previously described. The value of C_{N_δ} may be calculated from Eq. (5-23) as follows:

$$C_{N_\delta} = \frac{C_{N_{TR}} - C_{N_\alpha} \alpha_{TR}}{\delta} \quad (\text{H-22})$$

where α_{TR} , δ , C_{N_α} are known and

$$C_{N_{TR}} = \frac{n_{ss} W}{qS} \quad (\text{H-23})$$

The value of C_{m_δ} may be determined from Eq. (5-21) as follows:

$$C_{m_\delta} = - \frac{C_{m_x} \alpha_{TR}}{\delta} \quad (\text{H-24})$$

Aerodynamic hinge-moment characteristics of the control surfaces may also be determined from flight by telemetered strain-gauge data.

H-3. FORCED OSCILLATION

The forced-oscillation technique is commonly used to determine the combined lateral-control effectiveness and damping-in-roll characteristic of the missile. In this method the model or missile is forced to roll by deflecting the lateral-control surfaces throughout the missile flight trajectory. The combined effect of the lateral-control effectiveness and damping in roll may be determined from Eq. (9-93) as follows:

$$I_x \dot{p} = C_{l_p} p \frac{qSd^2}{2V} + C_{l_\delta} \delta qSd \quad (\text{H-25})$$

From the telemetered trace of rolling velocity (measured by a roll-rate gyro) vs. time, the value of $pd/2V$ per degree of lateral control deflection δ may be determined by assuming $\dot{p} = 0$. Hence Eq. (H-25) becomes

$$\frac{pd/2V}{\delta} = \frac{-C_{l_\delta}}{C_{l_p}} \quad (\text{H-26})$$

The assumption that $\dot{p} = 0$ at any instant of flight is generally valid, particularly for cases where the moment of inertia I_x is low or the

damping-in-roll derivative is large. This is readily apparent if the dynamic response of the missile in roll is treated essentially as a first-order system as indicated below [see Eq. (9-96)],

$$\frac{p}{\delta} = \frac{l_\delta}{-l_p + s} = -\frac{l_\delta l_p}{1 + (l/l_p)s} \rightarrow \frac{K}{1 + Ts} \quad (\text{H-27})$$

where
$$T = \frac{I_x}{C_{l_p} q S d^2 / 2V} \quad (\text{H-28})$$

Hence, for low values of I_x or large values of C_{l_p} , the value of T is also small. Hence, for most designs, the value of T is sufficiently low that it is generally valid to assume $\dot{p} = 0$ or that steady-state rolling velocity is realized throughout the flight of the missile.

H-4. MACH-NUMBER DETERMINATION

In order to reduce the flight-test data to aerodynamic coefficients, it is necessary that the Mach number, velocity, and dynamic-pressure history be known. The Mach number may be determined either from telemetered stagnation and static-pressure data from a pitot-static tube as shown in Fig. H-3, or from external data such as radar, theodolite coverage, and radiosonde information. From telemetered pressure data, the Mach number may be determined as follows:

1. For $M < 1$,

$$\frac{p_{\text{stagnation}}}{p_{\text{static}}} = \left(1 + \frac{\gamma - 1}{2} M^2 \right)^{\gamma/\gamma - 1} \quad (\text{H-29})$$

Substituting $\gamma = 1.4$ for air, Eq. (H-29) becomes

$$\frac{p_{\text{stagnation}}}{p_{\text{static}}} = (1 + 0.2M^2)^{3.5} \quad (\text{H-29a})$$

2. For $M > 1$ (see Fig. H-3),

$$\frac{p_{\text{stagnation}}}{p_{\text{static}}} = \frac{p_3}{p_2} \frac{p_2}{p_1} = \frac{p_3}{p_1} \quad (\text{H-30})$$

where p_3 = stagnation pressure.

p_1 = free-stream static pressure

p_2 = pressure behind a normal shock

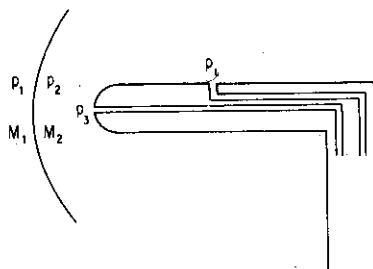


FIG. H-3. Pitot-static tube.

From the normal shock equations, we get

$$\frac{p_2}{p_1} = \frac{7M_1^2 - 1}{6} \quad (\text{H-31})$$

From isentropic compression [see Eq. (H-29a) we get

$$\frac{p_3}{p_2} = (1 + 0.2M_2^2)^{3.5} \quad (\text{H-32})$$

$$\text{Since } M_2 = \frac{M_1^2 + 5}{7M_1^2 - 1} \quad (\text{H-33})$$

Eq. (H-32) becomes

$$\frac{p_3}{p_2} = \left[1 + 0.2 \left(\frac{M_1^2 + 5}{7M_1^2 - 1} \right)^2 \right]^{3.5} \quad (\text{H-34})$$

Substituting Eqs. (H-31) and (H-34) into Eq. (H-30), we get

$$\frac{p_{\text{stagnation}}}{p_{\text{static}}} = \frac{p_3}{p_1} = \frac{7M_1^2 - 1}{6} \times \left[1 + 0.2 \left(\frac{M_1^2 + 5}{7M_1^2 - 1} \right)^2 \right]^{3.5} \quad (\text{H-35})$$

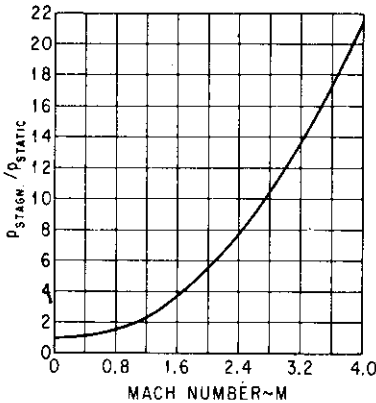


FIG. H-4. Variation of ratio of stagnation pressure to static pressure with Mach number.

Equation (H-35) is commonly known as the Rayleigh pitot-tube formula. A plot of Eqs. (H-29a) and (H-35) is presented in Fig. H-4. It is noted that Eq. (H-29a) may be used for Mach number up to 1.3 without appreciable error.

The velocity of the missile may be calculated from the Mach number as

$$V = Ma \quad (\text{H-36})$$

where a is the speed of sound and is related to the outside air temperature as follows:

$$a = 49.02\sqrt{T_{(\text{°F})} + 459.7} \quad (\text{H-37})$$

The velocity of the missile may also be determined from radar or theodolite data.

The dynamic pressure q , may be calculated as follows:

$$q = \frac{1}{2}\gamma p_1 M_1^2 \quad (\text{H-38})$$

or

$$q = \frac{1}{2}\rho V^2 \quad (\text{H-38a})$$

where ρ is the density of the air and may be determined from radio-sonde data.

INDEX

- AAM (air-to-air missile), 4-7, 70, 142
Ablation, 208
Accelerometer, body-mounted, 197
Ackeret, J., 33-35
Ackeret theory, 33-35
Adiabatic wall temperature, 166
Aerodynamic cross-coupling, 113, 118
Aerodynamic forces, definition of, 17
Aerodynamic gain, 77, 108, 147
Aerodynamic heating, 77, 165-168, 208
Aft control, 10, 11, 52, 53, 102-104, 158
Afterbody extension, effect of, 11, 12
Afterburner, 214
Ailerons, 10, 52, 53, 122-128
Air-breathing engines, 6, 8, 211
Air launch, 5, 173-183
Air loads, 12, 84, 155-164, 233
Air turbo rocket, 213, 214
Airflow interference, 5, 174-178, 182, 183
Airfoil characteristics, 32-51
 center of pressure, 36, 40, 51
 double-wedge, 35-37
 effective aspect ratio, 39-43
 $(L/D)_{\max}$, 42
 moments, 36
 normal-force-curve slope, 34-47
 effect of aspect ratio, 37-43, 51
 effect of Mach number, 34
 strength, 47
 sweepback, 43-47, 51
Allen, H. J., 28
Ambient exit pressure, 84, 215-218, 225
Angle of attack, 7, 18
Angular acceleration, 157, 158, 235, 236
Aperiodic mode, 130
Area moment of inertia, 240-242
Area ratio of nozzle, 218
ASM (air-to-surface missile), 6, 70
Aspect ratio, 32, 37-43, 51
Automatic control, 130-152
Axial force, 17, 18, 28, 50
Axial load, 241, 242
Axial stress, 241, 242
Axis systems, 130-134
 Euler, 133
 inertial, 133
Ballistic factor, 207, 208
Ballistic trajectory, 7, 83-90
Ballistic winds, 194, 195
Base area, 29
Base pressure (base drag), 11, 29-31, 68
Base-pressure coefficient, 30, 31
Beam analogy, simple, 236, 237
Beam rider, 6, 173, 182
Bending moments, 234-242
Beskin, L., 99
Beskin's body-upwash theory, 99
Bipropellant, 220
Blasius, H., 49
Blasius' equation, 49
Boattail, types of, 29, 30
Boattail drag, 29, 30, 68
Bodies of revolution, 18-32
 center of pressure, 30, 32
 conical, 18-22
 hemispherical, 18, 25-27
 ogival, 18, 23-25
 power series, 18, 27, 250, 251

- Body bending moment, 10, 15, 234-242
 Body carry-over lift (normal force), 96-103, 137
 Body extension, 11, 12
 Body pressure distribution, 29, 30
 Body upwash, 97-102, 163
 Body-wing interference factors, 96-103, 159-165
 Boltzmann, L., 167
 (See also Stefan-Boltzmann constant)
 Boost-glide trajectory, 4, 70-77
 Boost-sustain trajectory, 4, 6, 77, 78
 Booster, 6, 49
 Boundary layer, 31, 41, 50
 Boundary-layer temperature, 166, 167
 Buford, W. E., 28
 Burning, types of, 221-224
 Burning time of rocket motor, 71, 218, 219
 Busemann, A., 22, 33, 44
 Busemann constants, 33-35

 Caliber of ogive, 248
 Canard control, 9, 10, 48, 52, 96-102
 Captive flight balance, 176, 177
 Captive flight loads, 176-178, 238
 Carry-over force, 28, 29
 Casting material, 244
 Cathedral, 127
 Center of gravity, effect on stability, 7, 8, 94-104, 110, 111
 Center of pressure, boattail, 29
 body of revolution, 30, 32
 cone, 22
 delta wing, 45
 for hinge moment determination, 162-165
 location of, 22-51, 99, 162
 ogive, 23
 rectangular wing of finite aspect ratio, 40, 41
 subsonic airfoil, 51
 two-dimensional, 36
 Centripetal force, 107-110
 Chamber pressure, rocket motor, 90, 216-218, 224
 Chapman, D. R., 30, 47

 Characteristic solution, 131
 Characteristic velocity, 218, 219
 Chemical reaction, 215
 Chordwise pressure distribution, 163
 Circular probable error, 201
 Climb, optimum schedule, 80, 81
 rate of, 78-82
 time to, 80-82
 Coles, D., 65
 Combustion chamber, 213, 214, 220
 Composite propellant, 221-229
 Compressibility, 51, 66, 67, 160
 Compressible flow, 51
 Compressive load, 241, 242
 Compressive stress, 240-242
 Compressive wave, 33
 Compressor, 213
 Cone, flow over, 19-22
 Conical-flow theory, 20-22, 44
 Conical forebody, 18-22
 Control, effectiveness, 5-8, 52-56, 185
 reversal, 9, 52, 123
 types of, 7-13
 Canard, 9, 10
 jet, 12, 13
 nose-flap, 12
 tail, 10, 11
 wing, 7-11
 Control-stability relationship, 94-104, 107-111
 Control system, 9, 77, 134
 Cooling, regenerative, 220
 Cope, W. F., 67
 Critical damping, 147
 Critical design loads, 155-159, 178
 Cross-coupling, 113, 118, 142
 aerodynamic, 113, 118
 inertia, 113, 142
 Cross-flow, viscous, 28, 29, 160
 Cross-wind effects, 191, 196-203
 Cruciform design, 13-15, 107-109, 113-125
 Cruise trajectory, 7, 13, 78-83
 Cut-off altitude, 87, 88
 Cut-off angle, optimum, 87, 88
 Cut-off velocity, 87-90

 D'Alembert, J. Le R., 234
 D'Alembert's principle, 234

- Damping characteristics, 94, 136-139, 208
 Damping constant, 143, 147-150
 Damping-in-pitch, 11, 107-112, 136-138, 260
 Damping-in-roll, 125-127, 261, 262, 268, 269
 Datum missile, 195, 196
 DeLaval nozzle, 218
 Delta wings, 43-47, 68, 69, 99
 Dennis, D. H., 25
 Design criteria, 155-159
 Design loads, critical, 155-159, 178
 Diffuser, 213
 Dihedral effects, 117, 127
 Directional control, 113-119
 Directional stability, 113-119
 Dispersion, 5, 174-187, 190-208
 Divergence angle of nozzle, 217, 225, 230
 Divergence coefficient, 217, 230
 Divergent oscillation, 131
 Diving flight trajectory, 70-77
 Dorsal, 12
 Double-base propellant, 221-229
 Downwash, 7-15, 52, 258, 259
 contribution, to damping, 136-139
 to stability, 7-11, 97-103
 Drag, base, 21, 29-31
 boattail, 29, 30
 component of, 17, 18
 of cones, 19-22
 definition of, 17
 due to normal force, 40, 41, 50, 69
 form (*see* Wave drag)
 of ogives, 23-25
 pressure (*see* Wave drag)
 skin-friction, 17, 49, 50, 64-67
 Drag-rise factor, 50
 Drift, dispersion, 190, 196-200
 Dynamic overshoot, 123, 124, 149-152, 156-159
 Dynamic pressure, 12, 53, 83, 153-157
 Dynamic response, 130-152
 Dynamic stability, 11, 130-152

 Effective aspect ratio, 39-43
 Effective cross-sectional area, 241
 Elliptical lift distribution, 50
 Elliptical probable error, 201
 Emissivity factor, 168
 End-burning grain design, 224
 Ethylene oxide, 213, 214
 Euler, L., 133
 Eulerian axes, 133
 Evvard, J. C., 38
 Excess thrust, 79-82
 Exhaust velocity, jet, 84
 Exit flight, 83, 84, 185
 Exit pressure, ambient, 84, 215-218, 224
 Exit velocity, 84
 Expansion wave, 33

 Ferrari, C., 22
 First-order linear system, 150, 151
 First- and second-order theories, 29
 Flare tail, 12
 Flat earth, 201, 204-206
 Flat turn, 107-110
 Flight loads, 155-164, 238
 Flight-path angle, 75, 80-82, 95, 108-111
 Flow-field interference, 174-178, 182, 183
 Flow separation, 41-47, 160, 165, 215
 Flow types, laminar, 50, 64-67, 166, 167
 turbulent, 50, 64-67, 166, 167
 Forebody types, 18-28, 250, 251
 conical, 19-22
 Haack series, 27, 250, 251
 hemispherical, 25-27
 ogival, 23-25
 parabolic, 27, 250, 251
 power series, 27, 250, 251
 Form drag (*see* Wave drag)
 Forward control, 7-11, 96-102, 157
 Frankl, F., 67
 Frankl-Voishel theory, extended, 67
 Free-flight loads, 155-164, 238
 Free-stream Mach number, 20-45, 166
 Free-stream temperature, 166, 167
 Frequency, natural, 147-152
 Friction coefficient, 28, 49, 50, 167
 Friction drag, 17, 21, 49, 50, 64-67
 Fuel-air mixture, 212
 Fuel consumption, 82, 83, 213, 214
 Full expansion, 215-218

- g*-sensing device, 5
 Gas generator, 213, 221
 Glauert, H., 34, 51
 (See also Prandtl-Glauert factor)
 Grain configuration, 221-224
 Gravitational units, 234
 Gravity component, 75, 144, 184
 Gravity turn, 83-88
 Ground clearance (see Terrain clearance)
 Ground-handling loads, 238
 Ground launching, 184-186
 Ground-wind-induced loads, 185, 186
 Guidance systems, types of, 6, 84
 Gust effects on airloads, 156-159
- Haack, W., 27, 250, 251
 Haack series nose, 27, 250, 251
 Harmonic motion, simple, 130-132
 Heat-balance equation, 167, 168
 Heat sink, 208
 Heat-transfer coefficient, 167
 Heat-transfer rate, 165-168, 208
 Heating, aerodynamic, 77, 165-168, 208
 Heaviside, O., 135
 Heaviside factor, 135
 Hemispherical forebody, 18, 25-27
 Hinge moments, 8-11, 164, 165, 176
 Hollow cast, 244
 Honeycomb cross section, 244
 Horizontal flight (see Level flight trajectory)
 Hybrid theory (Van Dyke), 29
 Hypersonic similarity parameter, 25
- ICBM, 6, 7, 219
 Igniter, 221
 Ignition, rocket motor, 187
 Impulse, over-all specific, 218, 219
 specific, 77, 78, 88-90, 218, 219
 Impulse loss due to jet vanes, 13, 56
 Incompressible flow, 50, 51, 66, 67
 Induced drag, 40-50, 69
 subsonic, 40, 50
 supersonic, 40, 41
 Induced loads, ground-wind, 185, 186
 Induced roll, source of, 9, 121-128
 Induced rolling moments, 9, 15, 121-128
 Inertia cross-coupling, 113, 142
 Inertia forces and moments, 130-134
 Inertia loads, 233-237, 240-242
 Inertial axes, 133
 Infrared guidance, 6, 18, 25
 Inlet, 8, 79
 In-line tail, 14, 15
 Integral rocket motor, 211
 Interdigitated tail, 14, 15
 Interference drag, 67, 69
 Internal-burning grain design, 221-224
 Inviscid fluid-flow theory, 30
 IRBM, 7
 Isentropic flow, 215-218
- Jack, J. R., 30
 Jet control, type of, 12, 13, 53-56, 83
 Jet effect on base pressure, 11, 12, 31, 32, 55
 Jet exhaust velocity, 84
 Jet pressure ratio, 31
 Jet vanes, 12, 13, 54
 Jetavators, 12, 13, 54-56
- Kármán-Schoenherr equation, 50
 Kepler, J., 86
 Kepler's planetary ellipses, 86-88
- Laminar flow, 50, 64-67, 166, 167
 Laplace, P. S., 143
 Laplace transform, 143
 Lateral control, effectiveness, 10, 15, 52, 53, 121-128
 type of, 8
 Lateral-directional motions, 113, 142, 143
 Lateral stability, 121-128
 Launcher dynamics, 184, 191
 Launcher setting, 191
 Launching problems, 5, 6, 173-187
 airflow interference, 5
 airplane safety, 5
 dispersion, 5, 7, 173-187
 Leading-edge condition, 41-45
 subsonic, 43-45
 supersonic, 41-45

- Leading-edge suction, 69
 Level flight trajectory, 70-83, 236
 Lift (*see* Normal force)
 Lift-to-drag ratio, 42, 43, 46, 48, 187
 Limit stress, 239
 Lin, S., 140, 141
 Linearized theory, 29-41, 98, 162
 Lin's method, 140, 141
 Liquid propellant rocket, 4-6, 219-221
 Load factor, 8-11, 42, 94-104
 Loading distribution, 160-164
 Loads, 159-164
 Local angle of attack, 35, 162
 Local normal force coefficient, 161
 Long-range ballistic trajectory, 83-90
 Long-range cruise trajectory, 78-83
 Longitudinal dynamics, 130-142

 Maccoll, J. W., 20, 29
 (*See also* Taylor-Maccoll theory)
 Mach, E., 8
 Mach angle, 44, 162
 Mach cone, 37, 38, 41
 Mach number, 8, 20-46
 Malalignment, effect on dispersion, 177-185, 191-194
 Maneuverability requirement, 5-7, 11, 42
 Margins of safety, 239
 Mass ratio, 88-90, 222-231
 Material density, 243
 Material strength, 13, 243
 Maximum lift coefficient, 46, 49
 Maximum range, 82-90
 Maximum speed, 78-80
 Meyer, Th., 29
 (*See also* Prandtl-Meyer equation)
 Midsection, 28, 29
 Mid-wing design, 117
 Miles, E. R. C., 23
 Missiles, classes of, 4-7
 Mixing-length theory, 66, 67
 Model build-up, 96-104
 Modes, oscillatory, 130-142
 Moment of inertia, 133, 134, 142, 235
 Momentum flux, 216
 Momentum theorem, 216
 Monocoque construction, 240
 Monopropellant, 213, 220
 Monowing, 13, 14, 109, 113-119, 127, 128
 MRBM, 7
 Multistaging (*see* Staging)
 Natural frequency, 147-152, 266-268
 Navier, C. L. M. H., 49
 Navier-Stokes equation, 49
 Net thrust, 79, 80
 Newton, Sir Isaac, 132, 215, 234
 Newton's laws of motion, second, 132-134
 third, 215, 216, 234
 Nitrocellulose, 221-229
 Nonlinearity, 9, 15, 51
 Normal force, 7-11, 17
 due to angle of attack, 7-11
 due to control deflection, 7-11, 48, 97-103
 Normal-force coefficient, 28, 32-47
 bodies of revolution, 28, 32
 wings, 34-47
 Normal-force curve slope, 21, 22, 34-47, 97-103
 bodies of revolution, 21, 22
 wings, 34-47
 Nose-flap control, 12
 Nozzle, 214-231
 Nozzle angle, 31, 217, 225, 230
 Nozzle discharge coefficient, 230
 Nozzle divergence coefficient, 217, 230
 Nozzle exit area, 84
 Nozzle exit pressure, 84
 Nyquist, H., 148
 Nyquist technique, 148

 Oblique shock, 19, 33, 54
 Ogival forebody, 18, 23-25
 Ogive, properties of, 247-249
 Optimum climbing schedule, 80, 81
 Optimum cut-off angle, 87, 88, 207
 Optimum wing area, 48, 252, 253
 Oscillatory modes, 130-142
 Oswald, W. B., 50
 Oswald efficiency factor, 50
 Over-all specific impulse, 218, 219, 230, 231
 Oversustained trajectory, 77
 Oxidizer, 211, 221

- Parabolic nose, 27, 250, 251
 Particular solution, 131
 Performance degradation, 6, 182, 183
 Period of oscillation, 136-148, 265-268
 Peripheral pressure distribution, 161, 182, 183
 Perkins, E. W., 28
 Phugoid motion, 132, 139-142
 Pitching-moment coefficient, 14, 15, 36, 97-103
 Pitot tube, Rayleigh formula, 270
 Planform, wings, 32, 43-47, 68
 Potential-flow theory, 160
 Power-series nose, 18, 27, 250, 251
 Powered flight, 8, 71-90
 Prandtl, L., 29, 34, 51, 66
 Prandtl-Glauert factor, 34, 51
 Prandtl-Meyer equation, 29
 Prepackaged-liquid-propellant rocket motor, 4, 221
 Pressure, base, 11, 21, 29-31, 55, 68
 chamber, 90
 differential, 11, 17, 34-36
 dynamic, 12, 53, 83, 155-157
 Pressure coefficient, 21-23
 cone, 21
 ogive, 23
 Pressure distribution, 160-164
 Pressure drag (*see* Wave drag)
 Pressure gradient, 65
 Products of inertia, 133, 134
 Propellant flow rate, 84, 216-219
 Propellant properties, 13, 192, 226-229
 Propeller, 213

 Quadratic differential equation, 132, 139-142
 Quartic differential equation, 132, 139

 Radius of tangent ogive, 247-249
 Rail launchers, 182, 191
 Raked tips, effect of, 37-43
 Ramjets, 6, 214
 Range, 70-90
 Range safety, 186
 Rate of climb, 78-82
 Rayleigh, Lord, 270
 Rayleigh pitot-tube formula, 270

 Reciprocating engine, 212, 213
 Recovery factor, temperature, 166
 Recovery temperature, 166
 Rectangular wings, 32-43, 68, 99
 Reentry body, 11, 12, 207, 208
 Regenerative cooling, 220
 Regressive burning, 221-224
 Retrofit, missile aircraft, 174-183
 Retrolaunch, 5
 Reynolds, O., 30, 31, 45, 49, 64, 65, 167
 Reynolds analogy factor, 167
 Reynolds number, 30-49, 64, 65
 Rocket motors, types of, 4-54, 211-231
 boost-sustainer, 4, 6
 liquid-propellant, 6, 12, 54, 219-221
 prepackaged-liquid, 4, 211, 221
 solid-propellant, 192, 221-231
 Roll reversal, 9, 52, 123
 Roll stabilization, 10, 121-128
 Rolling motion, transfer function, 148
 Root-locus method, 148
 Roots of characteristic equation, 130-132, 140-142
 Routh, E. J., 139-141
 Routh's discriminant, 139-141

 Safety criteria, 173-182
 SAM (surface-to-air missile), 5, 6, 70
 Satellite velocity, 87, 88, 206, 207
 Schoenherr, K. E., 50
 Sea state, effect on launching, 187
 Second-order degree of accuracy, 35
 Second-order linear system, 143, 147-152
 Second-order shock expansion, 25
 Second-order theory, 29
 Section normal-force coefficient, 125
 Semimonocoque structure, 243
 Sensitivity factors in dispersion, 190-196
 Servo lag, 149-152
 Servo power requirement, 1, 8-11, 119
 Servo system, 8
 Shear loads, 234-240
 Shipboard launching, 187
 Shock angle, 19-21

- Shock-expansion method, 25, 37
 Shock formation, 41, 216
 Shock wave, 19, 20, 33
 Short-period oscillation, 132
 Sideslip, angle of, 114-117
 Sidewash, 116-118
 Simple beam analogy, 236, 237
 Six degrees of freedom, 130-134
 Skin friction drag, 49, 50, 64-67
 Slender-body theory, 22-25, 99
 Solid-propellant rockets, 4, 13, 221-231
 Solid rectangular cross section, 241
 Spanwise pressure distribution, 38-42, 163, 164
 Specific heat, 166, 167, 225
 Specific impulse, 70+90, 218, 219, 224
 Speed, for best rate of climb, 80, 81
 of sound, 37, 38, 74
 SSM (surface-to-surface missile), 6, 7, 70
 Stability, dynamic, 11, 130-152
 static, 8-12, 94-104, 193
 Stability margin, 8, 9, 48, 94-104, 193
 Staging, 6, 7, 88-90
 Stagnation temperature, 166
 Stall speed, 48, 49, 82
 Standard deviation, 201
 Stanton, T. E., 167
 Stanton number, 167
 Static gain, 150, 151
 Static pressure, effect on air loads, 166
 Static stability, 94-104, 193
 Stefan, J., 167
 Stefan-Boltzmann constant, 167
 Step rocket (*see* Staging)
 Stiffness requirement, 243
 Stokes, G. G., 49
 (*See also* Navier-Stokes equation)
 Straight wing, 32-43, 69
 Stress, axial (or compressive), 241, 242
 Structural integrity, 18, 23, 28, 178
 Structural weight trade-off, 5
 Subsonic airfoil characteristics, 34, 40, 49-51
 Subsonic leading edge, 43-45
 Supersonic area rule, 69
 Supersonic leading edge, 41-45, 162
 Supersonic speeds, 19-46
 Supersonic wing theory, 32-47
 Surface smoothness, 67, 168, 195
 Surface winds, 194, 195
 Sweepback, effect of, 43-47, 51
 Syvertson, C. A., 25
 T tail, 119
 Tail arrangement, 14, 15
 Tail contribution, to damping, 136-139
 to stability, 8-15, 117, 118, 124
 Tail control, 10, 11, 52, 53, 102-104
 Tail loads, 10, 15
 Tail-less configuration, 11
 Tangent ogive nose, 23-25
 Tangent ogive properties, 247-249
 Taylor, G. I., 20, 29
 Taylor-Maccoll theory, 20, 29
 Temperature, boundary-layer, 166, 167
 free-stream, 166
 stagnation, 166
 Temperature recovery factor, 166
 Temperature sensitivity, 192, 193, 223, 224
 Tensile stress, 240-242
 Terminal guidance, 6
 Terminal phase of flight, 130, 190, 207, 208
 Terrain clearance, 179-182
 Theories, Ackeret, 33-35
 Beskin's body-upwash, 99
 conical-flow, 20-22, 44
 extended Frankl-Voishel, 67
 first- and second-order, 29
 inviscid-fluid flow, 30
 linearized, 29-41, 98, 162
 mixing-length, 66, 67
 potential-flow, 160
 second-order, 29
 second-order shock-expansion, 25
 slender-body, 22-25, 99
 supersonic wing, 32-47
 Taylor-Maccoll, 20, 29
 Van Dyke's hybrid, 29
 Thermal loading (*see* Aerodynamic heating)
 Thermochemical equilibrium, 215
 Thickness, wing, 36, 68

- Thin-walled cylinder, 240-242
 Three degrees of freedom, 139-142
 Three-dimensional flow, 19, 20
 Thrust, 79-82, 216-219
 Thrust coefficient, 217, 230
 Thrust termination, 84, 222, 223
 Time, to climb, 80-82
 to damp to half amplitude, 136-142, 148, 265-268
 Time lag, of control system, 149-152
 downwash, 138, 139
 Tip control, 122, 123
 Tip effects, 37-43
 Tip losses, 37-43
 Tip-off, effect on dispersion, 184, 191
 Tolerances, aerodynamic smoothness, 195, 196
 Total impulse, 77, 191, 192, 218, 219
 Trailing edge, effect of, 47
 Trajectory, types of, 4-13, 70-90
 ballistic, 7, 83-90
 boost-glide, 4, 70-77
 boost-sustain, 4, 6, 77, 78
 cruise, 7, 13, 78-83
 diving, 70-77
 level flight, 70-83, 236
 Transfer function, 143-152
 Transform integral, 143
 Transition point, 65
 Transonic area rule, 69
 Triangular wings (*see* Delta wings)
 Triform, 13, 14
 Trim angle of attack, 8-15, 101-103, 110-112, 115-119
 Trim load factor, 101-103, 108-112, 157, 158
 Trim normal-force coefficient, 101-103, 108-112, 157, 158
 Tsien, H. S., 22
 Tucker, M., 67
 Turbine, 213
 Turbojet engine, 213
 Turboprop engine, 213
 Turbulent flow, 50, 64-67, 166, 167
 Turn radius, 108-110, 179-182
 Two degrees of freedom, 94-96, 134-139, 144-152, 266-268
 Two-dimensional flow, 19, 20, 29, 33-37
 Ultimate strength, 238, 239
 Undamped natural frequency, 149
 Underexpansion, 215-218
 Undersustained trajectory, 77
 Unguided ballistic missiles, 185, 190-208
 Unit cost, 233, 243
 Universal skin-friction constant, 65
 Unpowered flight, 71-90

 V tail, 119
 Van Dyke, M. D., 29
 Van Dyke's hybrid theory, 29
 Vapor pressure, 214
 Velocity at burnout, 70, 71, 75
 Ventral fins, 119
 Vertical launch, 6, 7
 Vertical tail size, 117-119
 Viscous force, 28-45, 160, 165
 Voishel, V., 67
 Volumetric loading, 224
 Von Kármán, Th., 27, 50, 66, 250, 251
 Von Kármán nose, 27, 250, 251
 Vortices, forebody, 185, 186

 Wall temperature, adiabatic, 166
 Wave drag, 17-43, 67, 68
 conical boattail, 29, 30, 68
 conical forebody, 21
 hemispherical forebody, 25-27
 ogival forebody, 23-25, 68
 wings, 33-43, 68
 Wedge semivertex angle, 33
 Wetted area, 49, 66, 67, 249
 Wilson, R. E., 67
 Wind shear, 7, 200, 207
 Winds, effect on dispersion, 184-186, 196-203
 Wing area, 8-14, 47-49
 Wing arrangement, 13-15
 Wing-body interference factors, 96-103, 159-165
 Wing characteristics, 32-47
 Wing control, 7-11, 52, 96-102, 121-124
 Wing location, 8-11, 48

- Wing planform, 32, 43-47, 68
- Wing-tail interference, 10, 97-103, 121-126
- Wing theory, supersonic, 32-47
- Wing-tip ailerons, 10, 52, 53, 122-128
- Wings, types of, 32-47
 - delta (or triangular), 43-47
 - rectangular, 32-43
 - sweptback, 43-47, 51
- X tail, 119
- Yaw, angle of, 114, 115
- Yawing moment, 113-119
- Yield strength, 238, 239
- Zero lift drag, 28, 50
 - of bodies of revolution, 28
 - of wings, 50

